**Study of the Electrostatic Shielding and
Environmental Interactions in Carbon
Nanotubes by Resonance Raman Spectroscopy**

Paulo Antônio Trindade Araújo

August 2010

Study of the Electrostatic Shielding and Environmental Interactions in Carbon Nanotubes by Resonance Raman Spectroscopy

Paulo Antônio Trindade Araújo

Orientador: Prof. Ado Jório de Vasconcelos

Tese de doutorado apresentada ao Departamento de Física da Universidade Federal de Minas Gerais como requisito parcial para a obtenção do grau de Doutor em Física.

August 2010

Dedico esta tese de doutorado à minha família.

Acknowledgments

- Agradeço ao meu orientador Prof. Dr. Ado Jório de Vasconcelos pelo apoio, pelas oportunidades concedidas e, principalmente, pela amizade.

- Agradeço ao Prof. Dr. Luiz Gustavo Cançado pelas valiosas discussões técnicas e teóricas sobre o campo próximo ($Near-field$) e suas aplicações. Agradeço também por, juntamente com a Lú e o Linus, ter me recebido maravilhosamente bem em Rochester.

- Agradeço ao Prof. Dr Marcos Assunção Pimenta, pelo apoio e gentileza, deixando as portas do Raman sempre abertas pra mim.

- Agradeço aos meus pais e irmãs pelo amor e compreensão.

- Agradeço a Sandra Donato por me mostrar que o auto-conhecimento é, definitivamente, essencial para se viver bem.

- Agradeço a Maíra e ao Luca, meu filhinho lindo. Os dois representam muito para mim.

- Agradeço aos meus queridos amigos, Mario, Dandan, Xubaca, Newton, Leonardo, Marcelo, Patrick e Dani pelo apoio e compreensão.

- Agradeço aos amigos do departamento de física pela ótima convivência.

- Agradeço à todos os meus colaboradores que, logicamente, foram fundamentais. É uma honra trabalhar com vocês.

- Ich moechte Prof. Achim Hartschuh danken. Er hat mir die Grundregel von NahFeld gelehrt. Vielen danke!

- Ich moechte Die NahFeld gruppe im Muenchen danken. Besonders moechte Ich meine Freunde, Huihong und Nicolai, danken. Aufrichtig, vielen danke!

Contents

Resumo

Na última década, muitos avanços experimentais e teóricos foram feitos na fotofísica dos nanotubos de carbono de parede única (SWNT). Tais conquistas nos permitiram alcançar um profundo conhecimento da física por trás da dependência com os índices (n, m) das energias de transição ópticas (E_{ii}) e da frequência do modo de respiração (ω_{RBM}). A primeira parte deste trabalho discute a pesquisa que tenho feito, baseado na espectroscopia Raman ressonante do modo radial de respiração, sobre as propriedades eletrônicas e vibracionais dos SWNTs. Estas pesquisas foi direcionada para o entendimento de como uma mudança no ambiente em torno dos SWNTs muda a relação existente entre $(E_{ii}, \omega_{\mathrm{RBM}})$ e (n, m). Será mostrado que mudanças ambientais fazem com que as frequências do modo radial de respiração aumentem. Isto acontece porque as paredes dos SWNTs interagem com o ambiente em torno dela através de forças de Van der Waals, que adicionam uma constante de mola extra, em paralelo ao sistema dos SWNTs. As mudanças nas E_{ii} são explicadas em termos das mudanças na constante dielétrica κ, que é formada por duas comtribuições: a constante dielétrica κ_{tube}, que depende das propriedades intrínsecas de cada SWNT e a constante dielétrica κ_{env}, que depende somente do ambiente. Hoje em dia, a comunidade científica enfrenta o desafio de fazer experimentos na escala nanométrica. Portanto, a construção de sistemas para experimentos de nano-manipulação (por exemplo, construção de nano-devices e litografia em escala nanométrica) e nano-caracterização (por exemplo, caracterização ótica e medidas de transporte) tornou-se uma necessidade. Na segunda parte deste trabalho, um sistema de microscopia confocal foi unido a um sistema de microscopia de força atômica (AFM). Com o sistema confocal, somos capazes de fazer espectroscopia com resoluções óticas próximas de $\lambda/2$, onde λ é o comprimento de onda da excitação. O sistema de AFM nos permite fazer imagens e manipular sistemas na escala nanométrica. Os dois juntos nos permite a realização simultânea de experimentos de espectroscopia e nano-manipulação. Se a ponta para o AFM for metálica, é possível realizar experimentos óticos com resoluções determinadas apenas pelo diâmetro das pontas, indo além dos limites de difração. Este sistema foi utilizado para entender mudanças nas estruturas eletrônicas e de fônons dos SWNTs quando estes são precionados por uma ponta de ouro e, além disto, entender as influências de segmentos de DNA na fotoluminescência de sistemas de SWNTs@DNA.

Abstract

In the last decade, many theoretical and experimental achievements have been made in the photophysics of single wall carbon nanotubes (SWNTs). Such accomplishments allowed us to gain a deep understanding of the physics behind the otical transition energy (E_{ii}) and the radial breathing mode frequency (ω_{RBM}) dependence on nanotube chiral indices (n, m). The first part of this work is devoted to assemble and discuss what I have done on the research of the SWNT electronic and vibrational properties, based on the radial breathing mode (RBM) measured by resonance Raman spectroscopy. Attention is directed to the understanding of how a change in the environment changes the correlation between ($E_{ii}, \omega_{\mathrm{RBM}}$) and ($n, m$). It will be shown that the changes on the ω_{RBM} due to a changing environment makes the frequency to increase. This happens because the SWNT's wall interacts with the environment through Van der Waals interactions, which add an extra spring constant in parallel to the SWNT system. The changes in E_{ii} are explained in terms of changes in the dielectric constant κ which, in our model, comprises both, the dielectric constant κ_{tube}, that is intrinsically dependent of the SWNT structure, and the dielectric constant κ_{env}, that depends on the environment. Nowadays, the scientific community faces at the challenge of performing experiments in the nanometer scale. Therefore, to build systems for nano-manipulation (i.e. nanoscaled device's construction and nanoscaled lithography) and nano-characterization (i.e. optical characterization and transport measurements) experiments has become a major need. In the second part of this work, a confocal microscopy setup was joined to an atomic force microscopy (AFM) setup. With the confocal system, we are able to perform spectroscopy with optical resolutions coming close to $\lambda/2$, where λ is the light source wavelength. The AFM system allows us to image and manipulate nano-scaled systems. Together They allow simultaneous experiments of spectroscopy and nano-manipulation. If the AFM tip is metallic, it is possible to perform optical experiments with resolutions delimited only by the tip diameter, going beyond the diffraction limits. Such a system has been utilized to understand the changes on the electronic and vibrational structures of SWNTs due to pressures imposed by a gold tip, and, besides this, to understand the influences of segments of DNA in the photoluminescence signal of SWNTs@DNA systems.

Chapter 1

Introduction

Due to their one-dimensional character, single-walled carbon nanotubes (SWNTs) exhibit unique electronic and vibrational properties that make them an interesting material for technological applications in electronics and optoelectronics [1, 2, 3, 4, 5, 6, 7, 8, 9]. Associated with each individual SWNT is a unique pair of indices (n, m) that fingerprints all of its properties [10]. Therefore, the knowledge of (n, m) is of great importance for defining the properties and applications for each SWNT [9, 10]. Quantum confinement is responsible for the rise of van Hove singularities in the SWNTs electronic and vibrational density of states, resulting in (n, m)-dependent optical properties [9, 10]. The most frequently used optically-based experimental technique to properly assign the (n, m) indices is resonance Raman spectroscopy (RRS). By knowing (1) the SWNT optical transition energy (E_{ii}) and (2) the radial breathing mode frequency (ω_{RBM}) as measured by RRS, together with their $(E_{ii}, \omega_{\mathrm{RBM}})$ changes with a changing environment it is possible to uniquely assign the (n, m) for an individual SWNT [11].

The last decade has been marked by an impressive development in understanding the nature of E_{ii} in quasi one-dimensional SWNTs, where $i = 1, 2, 3, ...$ denotes the inter-subband transitions between the ith valence and the ith conduction band for a given SWNT [11]. While the interest in the excitonic nature of E_{ii} and the dielectric screening in one-dimensional structures dates back to research in π-conjugated polymers [10], in carbon nanotubes the interest to these topics started in 2003 with the identification of the so-called "ratio problem" [12]. In 2007, Araujo *et al.* [13] and Michel *et al.* [14] showed that the scaling law for the exciton energies explaining the "ratio problem" breaks down for transitions with energies greater than E_{11}^M. The superscripts S and M of $E_{ii}^{S,M}$ for $i = 1, 2, 3, ...$ stand, respectively, for semiconducting and metallic SWNTs. These results led to the discussion of the excitonic nature of the higher energy levels, where

quantum-chemistry calculations and solid-state physics (tight-bind and first-principles) calculations give contradictory pictures [13, 15] due to a lack of knowledge about the dielectric screening in SWNTs. A large amount of information about the E_{ii} transitions is now available for a large range of tube diameters ($0.7 < d_t < 6\,\text{nm}$) [11], and the E_{ii} for SWNTs are now understood theoretically in terms of the bright exciton energy [10, 15, 16]. The E_{ii} can now be accurately described by tight-binding calculations, including corrections for curvature optimization and many-body effects [11], plus an empirically-based diameter and exciton size dependence for the dielectric screening in SWNTs [17, 18].

Parallel to the progress on understanding the E_{ii} in greater detail, was the development of the physics behind the radial breathing mode (RBM) frequency (ω_{RBM}). The RBM provides the spectroscopic signature of SWNTs [9, 10, 19], and the ω_{RBM} depends on the SWNT diameter (d_t), which is related to the SWNT (n, m) structural indices by $d_t = 0.142\sqrt{3(n^2 + mn + m^2)}/\pi$ [19]. The experimental results in the literature have been fitted with the relation $\omega_{\text{RBM}} = \mathbf{A}/d_t + \mathbf{B}$, with values for $\mathbf{A}$ and $\mathbf{B}$ varying from paper to paper [11]. The empirical constant factor $\mathbf{B}$ prevents the expected limit of a graphene sheet from being achieved, where the ω_{RBM} should go to zero when d_t approaches infinity. Therefore, $\mathbf{B}$ is supposedly associated with an environmental effect on ω_{RBM}, rather than an intrinsic property of SWNTs. An environmental effect here implies the effect of the surrounding medium, such as bundling, molecules adsorbed from the air, surfactant used for SWNT bundles dispersion, or substrates on which the tubes are sitting. Nowadays, the relation between ω_{RBM} and d_t is described by $\omega_{\text{RBM}} = (227/d_t)\sqrt{1 + C_e \cdot d_t^2}$, where C_e is the only adjustable constant that weights the effect of the medium surrounding the SWNTs [11].

It is worth to comment that the findings above were all done in SWNT samples which contains lots of SWNT of different species. What we were looking at would be something like a "global" perspective of the SWNTs properties, i.e. we were looking at an ensemble of SWNTs to extract properties regarding each (n, m) tube species. Besides the difficulty of finding good samples containing isolated tubes of a unique specie, we also had limitations in the capability of most of experimental setups to go beyond the micrometer scale. Nowadays, to perform experiments in the nanometer scale has become a major need. The second approach of this thesis is performing the instrumentation needed to build a system which is able to perform both, spectroscopy and manipulation, in the nanometer scale. The purpose of the system is joining a confocal microscopy setup to an atomic force microscopy (AFM) setup. With the confocal system, we are able to perform spectroscopy with optical resolutions coming close to $\lambda/2$, where λ is the light source

wavelength. The AFM system allows us to image and manipulate nano-scaled systems. Together They allow simultaneous experiments of spectroscopy and nano-manipulation. If the tip used is metallic, the system also allows "Tip Enhanced Spectroscopy" (TES) to be done. As a consequence, optical resolutions beyond the diffraction limit can be achieved, where the resolution is totaly related to the diameter of the tip. This makes the equipment ideal to study, for example, the specific changes in the SWNTs properties caused by structural defects and local dopants [20]. Such a system has been utilized, in this work, to understand the changes on the electronic and vibrational structures of SWNTs due to pressures imposed by a gold tip, and, besides this, to understand the influences of segments of DNA in the photoluminescence signal of SWNTs@DNA systems.

This thesis is arranged as follows: In Chapter 2, a brief discussion about the SWNTs electronic and vibrational properties and resonant Raman spectroscopy is presented. In the last section of Chapter 2, a recipe for the SWNT (n, m) assignment is given. Chapter 3 gives an overview of the influences of the shielding caused by the environment on the excitonic transitions. Chapter 4 explains, in details, the nano-spectroscopy an manipulation experimental apparatus as well as the major needs to build one of it. In Chapters 5 and 6 the experimental achievements to understand how the ω_{RBM} and the E_{ii} change with a changing environment will be given. Chapter 7 shows how the TES can be used to discriminate between the parts of carbon nanotube covered and not covered by DNA segments. We also showed that, by pressing a SWNT with an AFM gold tip, it is possible to reversely modulate its G-band Raman frequencies. Chapter 8 summarizes this thesis contents.

Part I

Theoretical Background
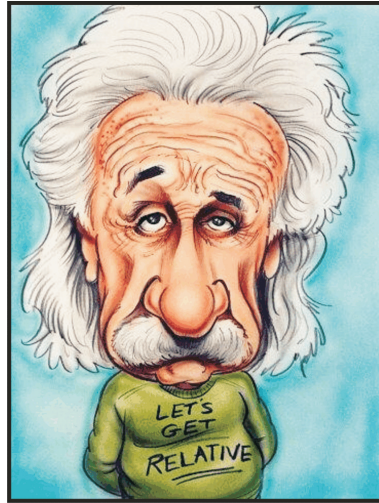
Figure 1.1: Albert Einstein's cartoon[1].

"I'm not an atheist and I don't think I can call myself a pantheist. We are in the position of a little child entering a huge library filled with books in many different languages. The child knows someone must have written those books. It does not know how. The child dimly suspects a mysterious order in the arrangement of the books but doesn't know what it is. That, it seems to me, is the attitude of even the most intelligent human being toward God."

Albert Einstein in a interview to the Time magazine.

[1]Credits: www.enlazandoweb.com

Chapter 2

Carbon Nanotubes and Raman Scattering: Basic Concepts

This chapter brings an overview of the electronic and vibrational structures of single wall carbon nanotubes (SWNTs) highlighting the main consequences of their circumferential confinement, in special, the rise of the van Hove singularities. A special focus will be given to the radial breathing mode (RBM), which gives the main SWNT spectroscopic signature, and its dependence with the tube diameter (d_t). A brief introduction to the Raman scattering theory will be addressed. In the last section, a recipe to use the Raman scattering spectroscopy to perform the SWNTs (n, m) indices will be given.

2.1   What is a SWNT?

A single-walled carbon nanotube (SWNT) can be described as a single graphene sheet rolled up in a cylinder form, one atom thick [10, 19]. Each SWNT can be associated with a unique chiral vector, $\vec{C_h}$:

$$\vec{C_h} = n\vec{a_1} + m\vec{a_2} \,, \tag{2.1}$$

which gives us the direction the graphene sheet is rolled up. As figure 2.1 shows, the $\vec{C_h}$ is obtained by a linear combination of n times $\vec{a_1}$ and m times $\vec{a_2}$, where $\vec{a_1}$ and $\vec{a_2}$ are the unit vectors used to describe the honeycomb lattice of the graphene.

The angle that $\vec{C_h}$ makes with relation to the unit vector $\vec{a_1}$ (see the Fig. 2.1) defines the called chiral angle (θ), which can vary from $\theta = 0°$ (zigzag SWNTs) to $\theta = 30°$ (armchair SWNTs). Each SWNT has its own pair (d_t, θ) of d_t and θ. The $\vec{C_h}$ modulus
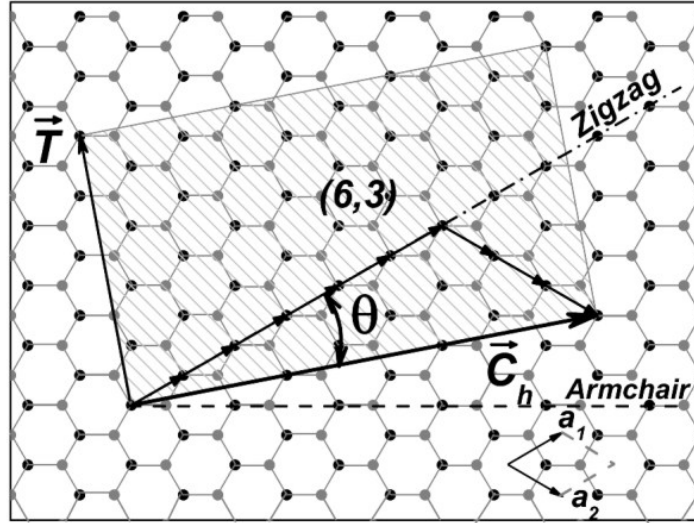
Figure 2.1: The dashed rectangle represents the unit cell of a carbon nanotube $(6,5)$. Two vectors are necessary to describe this unit cell and, therefore, the carbon nanotube structure: the chiral vector $\vec{C}_h$ and the translation vector $\vec{T}$, both of them described in terms of $\vec{a_1}$ and $\vec{a_2}$ that are the unit vectors used to describe the honeycomb lattice of the graphene. [21]

$(|\vec{C}_h|)$ also gives the SWNT diameter, d_t:

$$d_t = \frac{|\vec{C}_h|}{\pi} = \frac{a_{c-c}\sqrt{3}}{\pi}(m^2 + n^2 + mn)^{1/2}, \tag{2.2}$$

where a_{c-c} is the nearest-neighbor Carbon-Carbon distance ($1.421\,\mathring{A}$ in graphite). The chiral angle is obtained by:

$$\tan\theta = \frac{|\vec{a_1} \times \vec{C}_h|}{|\vec{a_1} \cdot \vec{C}_h|} = \frac{\sqrt{3}m}{m + 2n} \Rightarrow \theta = \tan^{-1}[\sqrt{3}m/(m+2n)]. \tag{2.3}$$

The indices (n, m) or the two parameters $(d_t,\ \theta)$ completely determine a specific SWNT and, therefore, its electronic and vibrational properties [9, 10, 19]. Besides the $\vec{C}_h$, the translation vector is also important to describe the SWNT's unit cell. It gives the periodicity of the unit cell along the SWNT axis and is defined by:

$$\vec{T} = t_1\vec{a_1} + t_2\vec{a_2} \equiv (t_1, t_2), \tag{2.4}$$

where the coefficient t_1 and t_2 are given by,

$$t_1 = \frac{(2n+m)}{d_R} \quad \text{and} \quad t_2 = \frac{-(2n+m)}{d_R}. \tag{2.5}$$

7

The denominator d_R is the greatest common divisor of $(2n + m,\ 2m + n)$ and is equals to d, if $n - m$ is not a multiple of $3d$, and $3d$ if $n - m$ is a multiple of $3d$. Here, d is the greatest common divisor of (n, m).

The unit cell of the SWNT is defined as the area delineated by the vectors $\vec{T}$ and $\vec{C_h}$. Since the real-space unit cell is much larger than that for a 2D graphene sheet, the 1D Brillouin zone (BZ) for the nanotube is much smaller than the BZ for a graphene 2D unit cell. Because the local crystal structure of the nanotube is so close to that of a graphene sheet, and because the Brillouin zone is small, Brillouin zone-folding techniques have been commonly used to obtain approximate electron $E(\vec{k})$ and phonon $E(\vec{q})$ dispersion relations for carbon nanotubes with specific (n, m) geometrical structures. The vectors to describe the SWNT BZ are obtained with the relation,

$$\vec{R_i} \cdot \vec{K_j} = 2\pi \delta_{ij}\,. \tag{2.6}$$

It follows that: $\vec{C_h} \cdot \vec{K_1} = 2\pi$, $\vec{T} \cdot \vec{K_1} = 0$, $\vec{C_h} \cdot \vec{K_2} = 0$ e $\vec{T} \cdot \vec{K_2} = 2\pi$. The vectors $\vec{K_1}$ and $\vec{K_2}$ are related to the vectors b_1 and b_2 of the graphene's BZ by,

$$\vec{K_1} = \frac{1}{N}(-t_2\vec{b_1} + t_2\vec{b_2}) \tag{2.7}$$

and

$$\vec{K_2} = \frac{1}{N}(m\vec{b_1} - n\vec{b_2})\,. \tag{2.8}$$

The N wave vectors $\mu\vec{K_1}$ ($\mu = 1$-$N/2$, . . . , $N/2$) give rise to N discrete $\vec{k}$ vectors or cutting lines in the circumferential direction (see Fig. 2.2). Here, N means the number of hexagons comprised by the SWNT unit cell. For each of the μ discrete values of the circumferential wave vectors, 1D electronic energy bands appears (one π-band and one π^*-band), whereas each μ gives rise to 6 branches in the phonon dispersion relations. Because of the translational symmetry of $\vec{T}$, we have continuous wave vectors in the direction of $\vec{K_2}$ for a carbon nanotube of infinite length. However, for a nanotube of finite length (L_t), the spacing between wave vectors is $2\pi/L_t$, and effects on the electronic structure associated with the finite nanotube length have been observed experimentally [9].

2.1.1 The electronic structure

As a first approximation, the electronic structure of a SWNT can be obtained from its parent material, graphene, whose electronic structure is well described by tight-bind calculations considering interactions just with first neighbors [19]. The problem consists
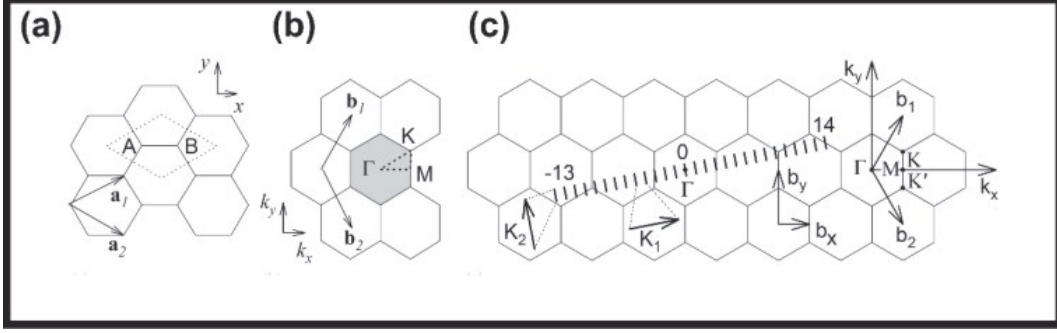
Figure 2.2: (a) The graphene unit cell (dotted rhombus), containing sites A and B where carbon atoms are located, and (b) the graphene first Brillouin zone (shaded hexagon). $\vec{a_i}$ and $\vec{b_i}$ (i = 1, 2) are basis vectors and reciprocal lattice vectors, respectively. The high symmetry points, Γ, K and M are indicated. (c) Parallel equidistant lines represent the cutting lines for the (4, 2) nanotube. The cutting lines are labeled by the cutting line index μ, which assumes integer values from 1 - $N/2$=-13 to $N/2 = 14$, where N is the number of hexagons inside the SWNT unit shell [9].

of solving the equation,

$$E_j(\vec{k}) = \frac{\langle \psi_j | H | \psi_j \rangle}{\langle \psi_j | \psi_j \rangle} , \tag{2.9}$$

where ψ_i and ψ_j are the Bloch's functions given by:

$$\psi_{\vec{k}}(\vec{r}) = \sum_j c_j(\vec{k}) \varphi_{\vec{k}j}(\vec{r}) , \tag{2.10}$$

where $\varphi_{\vec{k}j}(\vec{r})$ is given by:

$$\varphi_{\vec{k}j}(\vec{r}) = \frac{1}{\sqrt{M}} \sum_l e^{i\vec{k}.\vec{R}(\vec{l})} \phi_j(\vec{R}(\vec{l}) - \vec{r}) . \tag{2.11}$$

M is the number of unit cells, $\vec{R}(l)$ is the vector giving the position of an atom in the $l - th$ unit cell and ϕ_j is the $j - th$ atomic orbital of the atom. It follows that the electronic dispersion of the graphene is given by,

$$E_{g2D}(\vec{k}) = \frac{\epsilon_{2p} \pm \gamma_0 \omega(\vec{k})}{1 \pm s\omega(\vec{k})} , \tag{2.12}$$

where the function $\omega(\vec{k})$ is given by,

$$\omega(\vec{k}) = \sqrt{|f(\vec{k})|^2} = \sqrt{1 + 4\cos\frac{\sqrt{3}k_x a}{2}\cos\frac{k_y a}{2} + 4\cos^2\frac{k_y a}{2}} . \tag{2.13}$$

Figure 2.3: The graphene's π and π^* electronic dispersion calculated over the first BZ. The inset shows the dispersion along the high-symmetry points. The values used for γ_0 and s are, respectively, 3.033 eV and 0.129. [19]
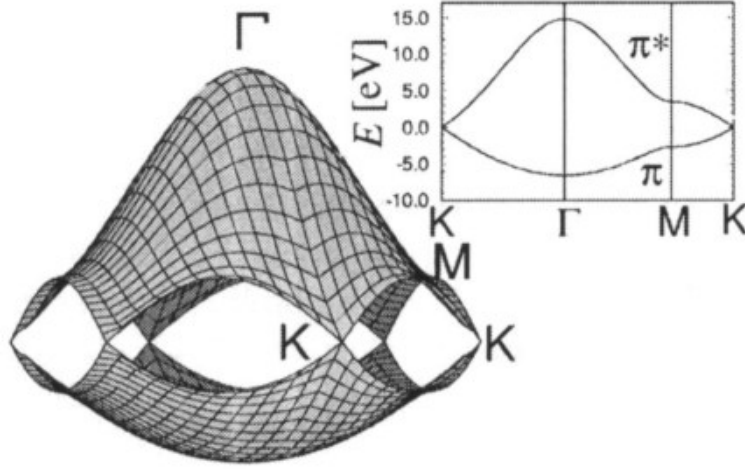
The Eq. 2.12 is plotted as a function of $\vec{k}$, as exhibited in the figure 2.3.

However, in the case of SWNTs, the quantum confinement of the 1D electronic states must be taken into account [9]. The electronic σ bands are responsible for the strong in-plane covalent bonds within the 2D graphene sheets, while the π bands are responsible for weak van der Waals interactions between such graphene sheets in 3D graphite. The π bands are close to the Fermi level and then electrons can be optically excited from the valence to the conduction band. While in a graphene sheet we have a quasi-continuum of possibilities to choose wavevectors in the 2D reciprocal space, for SWNTs we have to consider the boundary conditions in the circumferential direction which limit us to certain wavevectors in the radial direction, giving rise to the cutting lines (see figure 2.2) [9, 19]. Then, by "cutting" the 2D graphene electronic dispersion with those allowed radial wavevectors, we obtain the SWNTs electronic dispersion as showed in the Fig. 2.4. Observe that, in the case of SWNTs, the condition $e^{\vec{k}\cdot\vec{C}_h} = 1$ must be fulfilled. Therefore, k(πd_t)=$\mu 2\pi$ and then $|\vec{K}_1|$=2/d_t. It is worth to comment that $N\vec{K}_1$=$-t_2\vec{b}_1 + t_1\vec{b}_2$ is a vector of the graphene's reciprocal lattice. Since t_1 and t_2 do not have common multiples, it follows that μ=0, 1,...,$N-1$ or, equivalently, μ=1-$N/2$,...,$N/2$.

Then, the electronic dispersion for SWNTs will be given by:

$$E_\mu(\vec{k}) = E_{g2D}\left[k\frac{\vec{K}_2}{|\vec{K}_2|} + \mu\vec{K}_1\right],\tag{2.14}$$

where $\mu = 1 - N/2, ..., N/2$ and $-\pi/|\vec{T}| < k < \pi/|\vec{T}|$. The N possible values are

10
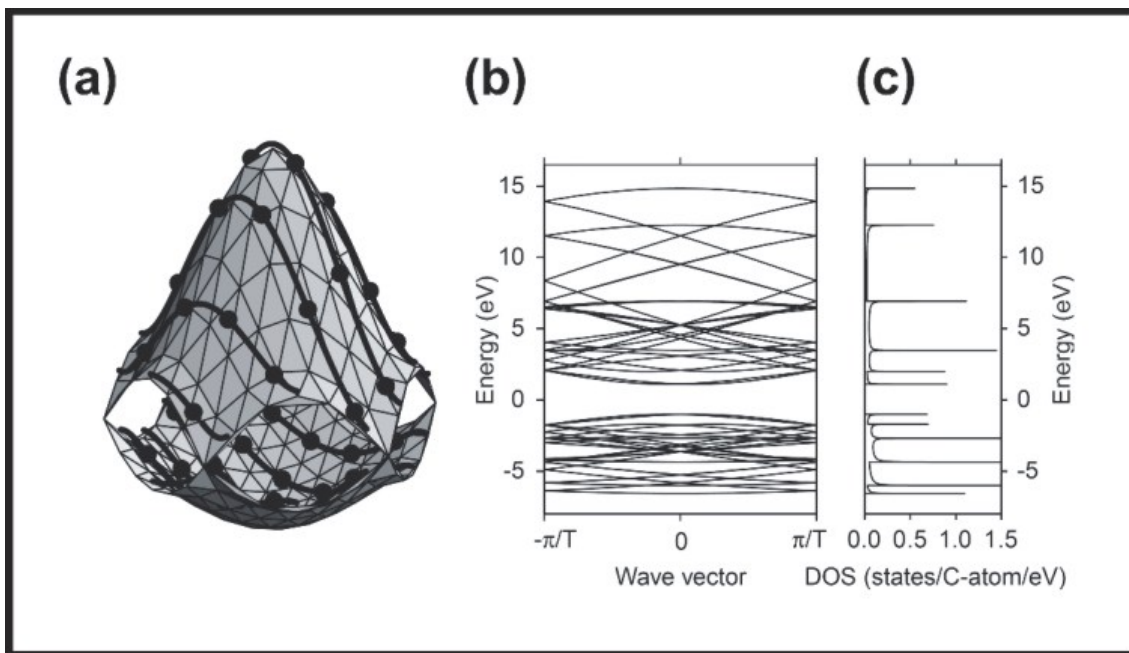
Figure 2.4: (a) The calculated energy contours for the conduction and valence bands of a 2D graphene layer in the first Brillouin zone using the π-band nearest neighbor tight binding model [19]. The valence and conduction bands touch each other at the high symmetry K points. Thick solid curves show the cutting lines for the $(4, 2)$ nanotube, but translated to the first Brillouin zone of the graphene, the dark points indicating the connection between cutting lines. (b) Electronic energy band diagram for the $(4, 2)$ nanotube obtained by zone-folding from (a). (c) Density of electronic states for the band diagram shown in (b). [9]

transversal sections of the graphene's electronic dispersion and the cuts are done every time the wavevectors obey the condition:

$$\vec{k} = k\frac{\vec{K_2}}{|\vec{K_2}|} + \mu\vec{K_1} \, , \tag{2.15}$$

to each μ (see the Fig. 2.4). The electronic dispersion for SWNTs are usually very hard to interpret, which can be simplified by its electronic density of state, as showed in the Fig. 2.4(c). A close inspection shows the van Hove singularities, which are responsible for strong SWNTs band to band electronic transitions. These band to band transitions are baptized $E_{ii}^{S,M}$ for $i = 1, 2, 3, ...$ The subscript "ii" means that one electron is being promoted from the $i - th$ valence sub-band to the $i - th$ conduction sub-band, ordered by energy from the Fermi level. The superscripts S and M stand for semiconducting and metallic SWNTs, respectively. As showed in Fig. 2.5, a SWNT is metallic every time a cutting line touches the K point in the brillouin zone and it is a semiconducting

otherwise [9, 10]. The condition to have a metallic SWNT is that $[(2n + m)mod3]=0$. If $[(2n + m)mod3]=1$, the SWNT will be semiconducting type I. If $[(2n + m)mod3]=2$, the SWNT will be semiconducting type II.
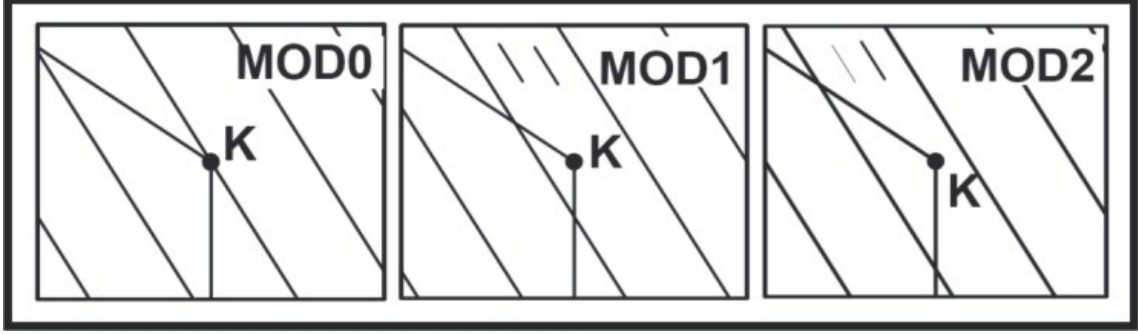
Figure 2.5: Different types of SWNT: A SWNT is metallic ($[(2n + m)mod3]=0$) every time a cutting line touches the K point in the brillouin zone and it is a semiconducting otherwise ($[(2n + m)mod3]=1(2)$) [9, 10].

The optical transitions will occur around the high symmetry K points, where the expression for E_{ii} can, by approximation, be given as,

$$E_{ii}(d_t) \approx 2a_{C-C}\gamma_0 \frac{p}{d_t} , \qquad (2.16)$$

where $p = 1, 2, 3, 4, ...$ for E_{11}^S, E_{22}^S, E_{11}^M, E_{33}^S.... Because of the trigonal warping effect [9, 19], E_{ii} also presents a chiral angle dependence, which can be described by $\beta_p \cos 3\theta/d_t$. The Eq. 2.16 becomes:

$$E_{ii}(d_t, \theta) \approx 2a_{C-C}\gamma_0 \frac{p}{d_t} + \frac{\beta_p \cos 3\theta}{d_t^2} , \qquad (2.17)$$

where β_p is a parameter which must be adjusted to each E_{ii}.

The $\sigma - \pi$ orbitals mixing

The first-neighbor tight-binding model, together with the zone-folding method, are good enough to describe most of properties for carbon nanotubes with large diameters ($d_t > 1.2$ nm). However, for small diameters ($d_t < 1.2$ nm) it is necessary to consider effects of hybridization and mixing of the σ and π orbitals. Nowadays, this drawback is solved by the extended tight-binding model (ETB) [22, 23]. This is a symmetry-adapted non-orthogonal method that considers both, the π-orbitals and the σ-orbitals in

12

its calculations. In analogy to what is done for graphene, two carbon atoms together with two screw-axis symmetry operation, are used to describe the SWNT. Then, adapting this symmetry in the first-neighbor π tight-binding, and considering as much neighbors as possible[1], the one find the electronic dispersion for each SWNT specie. Next, the energy is optimized allowing the bonding angles between the atoms to vary. This bonding angles variation appear very important for small diameter tubes. Besides this, the ETB is able to predict the metallic SWNT mini-gap, which appears due to curvatures effects.

Among several examples, the metallic-semiconducting transition due to $\sigma - \pi$ orbitals mixing is an important one to be considered. Although this effect has been predicted back to 1999 [24, 25, 26], only in 2008 it was directly observed through an electric force microscopy experiment (EFM) [27]. In this case, isolated SWNTs grown by chemical vapor deposition (CVD) on a 100-nm thick SiO_2 layer on top of a p-doped Si substrate using Fe nanoparticles as catalyzers were studied. Next, the sample was characterized via resonant Raman scattering allowing distinction between semiconducting and metallic species as well as a probable (n, m) assignment. After this characterization, AFM is utilized to check on the tubes morphology. As illustrated in Fig. 2.6, during the experiments, the SWNT is charged through contact with a properly biased AFM tip. Both tip bias and tip-SWNT force during the charging process can be easily controlled, while tip-SWNT contact time is kept fixed to 1s. Because no bias is applied between tip and sample during the EFM imaging, the extra SWNT charges induce image charges of opposite sign in the EFM tip, leading to an attractive tip-sample interaction which shifts the cantilever oscillation frequencies to lower values. These shifts demonstrate the presence of unbalanced charges in the SWNTs. In order to search for the semiconductor-metal transition in SWNTs, two experiments were devised: initially, a pair of Raman-labeled metallic and semiconducting SWNTs with similar diameters is chosen and a survey of the injected charge on each SWNT as a function of tip bias is carried out. This step allowed us to realize that for metallic tubes the charge-bias plots are always symmetric and a minimum bias of $\pm 2\,\mathrm{V}$ is necessary for unbalanced charges to be detected.

Next, keeping both bias and tip-SWNT contact time constant, the injected charge density on each nanotube is monitored as a function of the compressive tip-SWNT force during injection. In particular (even though that the conclusions extent to metallic and semiconducting SWNTs in general), it is observed that the (12,6) metallic SWNT presents a weak dependence of the tip force on the charging process. However, in (18,7) semicon-

---

[1]For computational calculations, one must find the best of two worlds: Time consumption and good results.
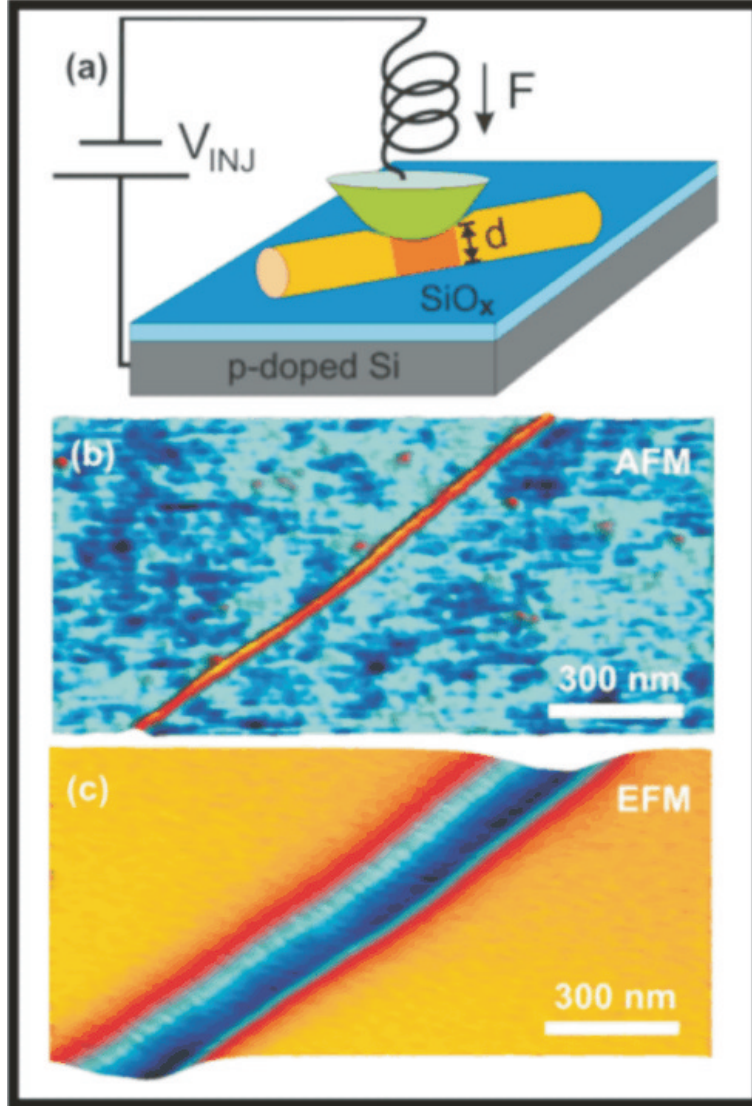
Figure 2.6: (a) A SWNT (in orange) on top a silicon oxide layer (in blue) is charged through the contact with an AFM tip (in green) biased at V_{INJ} while it is pressed with a controlled force per unit length F. (b) 3D AFM image of a (14,6) semiconducting SWNT atop the SiOx layer. (c) 3D EFM image of the same nanotube after it has been charged (V_{INJ}=6 V, lift height=50 nm) evidencing the negative frequency shift of the cantilever. [27]

ducting tube the charging is strongly tip force dependent: for small forces ($\approx 2\,\mathrm{N/m}$), no charge is detected at the SWNTs. When the force is increased between $3\,\mathrm{N/m}$ and $7\,\mathrm{N/m}$, a steady increase of the stored charge per unit length is observed. When the force is increased further (above $8\,\mathrm{N/m}$) a saturation is observed and similar charge densities of the metallic SWNT are achieved. This is an evidence that, due to compression, the

SWNT underwent a transition from its semiconducting behavior to a metallic behavior. At this point, the band gap presented in the semiconducting system vanishes and the tube becomes metallic. These results are all supported by theory, which predicts band-gap closure of semiconducting tubes upon radial compression (deformation) [24, 25, 26]. It is important to note that all the transitions observed are reversible.

Considering many-body interactions in E_{ii}

A paper published in 1999 by Ishida *et.al.* presented for the first time experimental evidences showing that many-body effects are important and play important changes in SWNTs electronic structure [28]. The experiment was performed in thin films of SWNTs from where a near-infrared absorption spectrum was obtained. A comparison between the experimental E_{ii} obtained and E_{ii} calculated through the tight-binding method suggested that excitonic effects should be taken into account. However, only in 2005, with the two-photons experiments evidences [29, 30], the E_{ii} transitions were proven to be excitonic in nature. The ETB does not consider exciton formation! One way to explain the excitonic contributions is considering them in first-principle (ab-initio) calculations methods [10].

Among several existing ab-initio methods, that one based in density functional theory (DFT) is mostly used to study SWNTs. The theory is based on a theorem where the electronic density ($n(\vec{r})$) is taken as a basic variable so that all the properties of the system's ground state are functional of It. These assumptions conduct us to the called Kohn-Sham equations:

$$\left[-\frac{\nabla^2}{2} + V_{ion} + V_{hartree} + V_{xc}^{LDA} \right] \psi_{n\vec{k}} = E_{n\vec{k}}^{LDA} \psi_{n\vec{k}}. \tag{2.18}$$

This equation is formally exact for the ground state description. It is an equation that describes independent particles i.e. it describes the movements of an electron described by the wave-function $\psi_{n\vec{k}}$ under the influence of an effective potential in which the interactions with other electrons are included. This potential is therefore composed by: (1) a term (V_{ion}) representing the interaction between an electron and its nuclear potential; (2) a term ($V_{Hartree}$) which provides the mean Coulomb interaction between electrons and (3) a term (V_{xc}) which is the exchange potential. The description of V_{xc} demands some approximations where the most common are the local density approximation (LDA) and the generalized gradient approximation (GGA). In the LDA approach, the exchange energy between two electrons in a given point $\vec{r}$ is replaced by the value it would assume in a homogeneous gas of electrons with the same density in $\vec{r}$. In the GGA

approach the gradient of the density in $\vec{r}$ is also taken into account.

The equation 2.18 is solved auto-consistently considering an initial proposition for $n(\vec{r})$ which is used to build the Hamiltonian. After the equation is solved and a set of $\psi_{n\vec{k}}$ is found, a new $n(\vec{r})$ and a new Hamiltonian are built. This interactive process happens until the convergence of $n(\vec{r})$ is achieved. The vector $\vec{k}$ in the equation is a parameter introduced by the Block theorem. For each $\vec{k}$ we have a family of continuous functions $E_n(\vec{k})$ that together give the band structure of the material.

A limitation of this method is that It only gives the ground state's properties. In order to describe, for example, the excited states, another approximations must be considered. Usually this is done through perturbation theory in many-body systems. In particles, the GW approximation (G is the Green function, W is the shielded Coulomb interaction and the product GW describes the electron self-energy) corrects the Kohn-Sham wave-functions appropriately describing charged excitations. However, in an experiment of optical absorption, an electron-hole pair is created. The strong interaction between them should be taken into account. This is done through the Bethe-Salpeter equation. It worth to comment that besides all the approximations described above, because of the Coulomb nature of the electron-electron and electron-hole interactions, we still have to model the effective dielectric constant which comprises contribution from the material itself and from the environment in which the material is. In chapter 3 we propose a model for the effective dielectric constant in SWNT+environment systems.

In the case of carbon nanotubes, the electron-electron repulsion and electron-hole attraction are similar in strength. One closely cancel the other. Using this argument, it is possible to simplify all the statement above. Kane and Mele showed [12, 31] that the many-body interactions in carbon nanotubes can be described by a logarithmic correction to the E_{ii} diameter dependence. The Eq. 2.19 then reads:

$$E_{ii}(d_t, \theta) = 2a_{C-C}\gamma_0 \frac{p}{d_t}\left[1 + b\log\frac{c}{p/d_t}\right] + \frac{\beta_p \cos 3\theta}{d_t^2}, \qquad (2.19)$$

where b is an environment-dependent adjustable parameter and $c = 0.812\,\text{nm}^{-1}$ [12]. For E_{ii} higher than E_{11}^M an additional term $\gamma p/d_t$ must be taken into account because the excitonic contributions are not the same for every transition [13]. We use this approach in several parts of this work because this equation contains parameter which can be easily adjusted with basis on experiments.

2.1.2 The vibrational structure

Phonons denote the quantized normal mode vibrations that strongly affect many processes in condensed matter systems, including thermal, transport and mechanical properties [9]. The 2D graphene sheet has two atoms per unit cell, thus having 6 phonon branches, as shown in the Fig.2.7(a). These phonon branches can be calculated by using a simple harmonic oscillator model which lead us to solve a couple of equations like,

$$M_i \ddot{\vec{r}}_i = \sum_j K^{ij} (\vec{r}_i - \vec{r}_j) \ (i = 1, ..., N) , \tag{2.20}$$

where $\vec{r}_i$'s are the displacements of the atoms in the unit cell, M_i is the mass for the atom i and K^{ij} is an element of the force constant tensor which, gives us the interaction strength between atoms i and j [19]. Similar to what has been done to find the SWNT electronic dispersion, the zone-folding procedure can be used, as first approximation, to generate the SWNT phonon dispersion, as shown in Fig.2.7(c). The graphene has two atoms in the unit cell. This generates six phonon branches in its dispersion. Applying the zone-folding method to this branches, the SWNT's phonon dispersion will be given by:

$$\omega_{1D}^{m\mu}(k) = \omega_{2D}^m \left(k \frac{\vec{K}_2}{|\vec{K}_2|} + \mu \vec{K}_1 \right) , \tag{2.21}$$

where, again, μ=0, 1,...,$N-1$ and $-\pi/|\vec{T}| < k < \pi/|\vec{T}|$. The index $m = 1, 2, ..., 6$ represents each graphene phonon branch.

The phonon for the phonon dispersion in Fig. 2.7 density of states is shown in Fig.2.7(d). Again, the van Hove singularities are the most important features. Although the zone-folding procedure describes most of the phonon dispersion, it cannot predict the ω_{RBM} because in the zone-folding method the radial breathing mode is treated as a translation, whose frequency is zero. Therefore, to model ω_{RBM}, more complex treatments based on tight-bind calculations, first principles or elasticity theory are needed [10, 19]. From now on, I will focus on the radial breathing mode that is, together with E_{ii}, the main scope of this thesis.

The radial breathing mode

The radial breathing mode (see Fig. 2.8) is a symmetric vibrational mode where all the SWNT's atoms move, in phase, in the radial direction. Here, the SWNT will be considered as a hollow cylinder and the radial breathing frequency (ω_{RBM}) will be
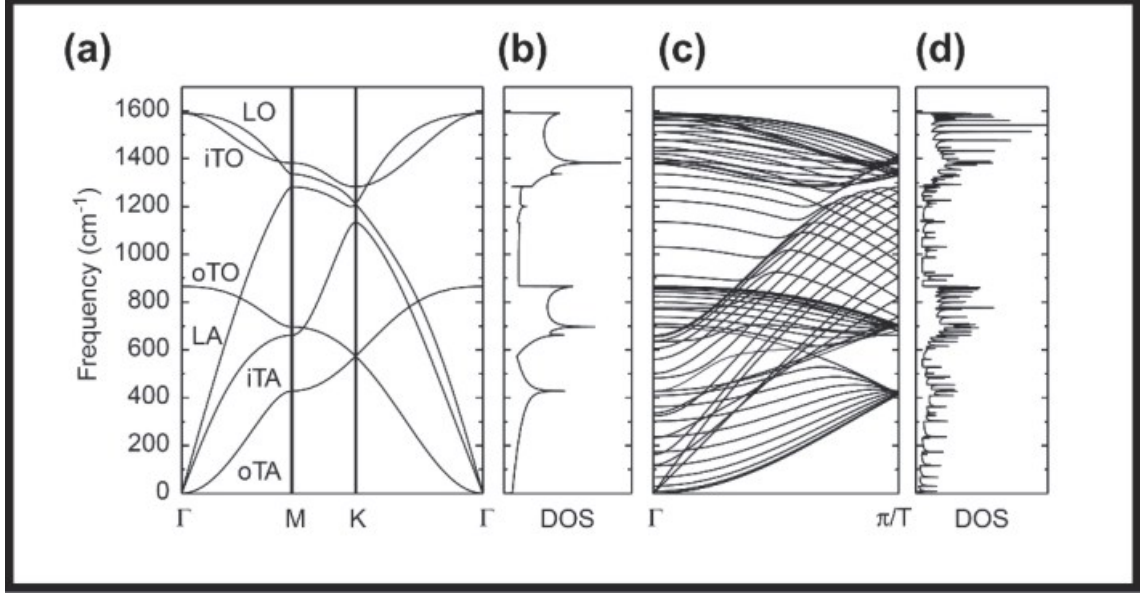
Figure 2.7: (a) Phonon dispersion of graphene using the force constants method. The phonon branches are labeled: out-of-plane transverse acoustic (oTA); in-plane transverse acoustic (iTA); longitudinal acoustic (LA); out-of-plane transverse optic (oTO); in-plane transverse optic (iTO); longitudinal optic (LO). (b) The phonon density of states for a 2D graphene sheet. (c) The calculated phonon dispersion relations of an armchair carbon nanotube with $(n, m) = (10,10)$, for which there are 120 degrees of freedom and 66 distinct phonon branches, calculated from (a) by using the zone folding procedure. (d) The corresponding phonon density of states for a (10,10) nanotube [9].

deduced with basis on the elasticity theory. The elasticity theory is nothing more than the study of the solid body's dynamics. Following the principles of elasticity theory [32], with respect to some referential, a given point in a solid can be described by the vector $\vec{r} = x_1\mathbf{i} + x_2\mathbf{j} + x_3\mathbf{k}$. When the body is deformed, the point described by $\vec{r}$ is displaced to $\vec{r'} = x_1'\mathbf{i} + x_2'\mathbf{j} + x_3'\mathbf{k}$. The displacement vector is, therefore,

$$\vec{u} = \vec{r'} - \vec{r} = (x_1' - x_1)\mathbf{i} + (x_2' - x_2)\mathbf{j} + (x_3' - x_3)\mathbf{k}. \tag{2.22}$$

Note that x_i' for $i = 1, 2, 3$ is dependent of x_i for $i = 1, 2, 3$. Considering only small displacements, we find that the distances between two points before and after the deformation are related by

$$dl'^2 = dl^2 + 2u_{ik}dx_k dx_i, \tag{2.23}$$

where,

$$u_{ik} = \frac{1}{2}\sum_{l=1,2,3}\left[\frac{\partial u_i}{\partial x_k} + \frac{\partial u_k}{\partial x_i} + \frac{\partial u_l}{\partial x_k}\frac{\partial u_l}{\partial x_k}\right], \tag{2.24}$$

18
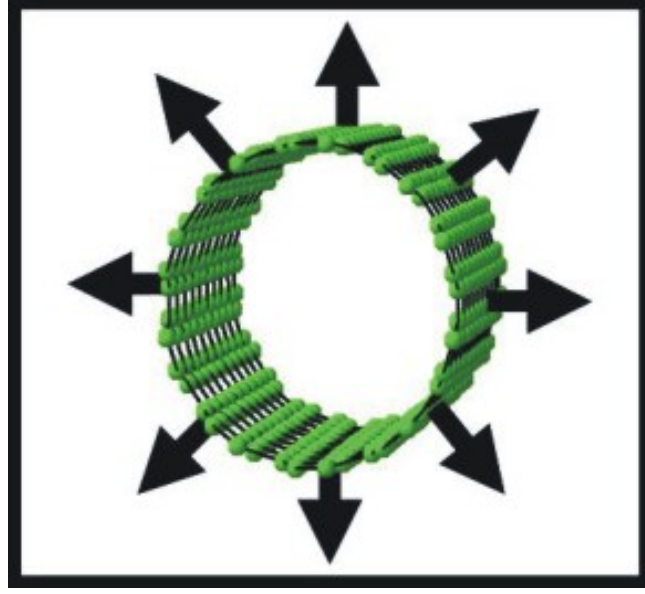
Figure 2.8: The radial breathing mode is a symmetric vibrational mode where all the SWNT's atoms harmonically move, in phase, in the radial direction.

is called "strain tensor".

If a body is not deformed or is not under action of external forces, this means that its molecules are found in a thermal equilibrium state. The body is in mechanical equilibrium. This means that, if we consider a small portion of this body, the resultant force due to the neighbors must be[2]:

$$\vec{F}_t = \int \vec{F} dV \,, \tag{2.25}$$

where $\vec{F}$ is the force per unit of volume. This tell us that the forces act on the surface of the portion, and so the resultant force can be represented as the sum of forces acting on all the surface elements, i.e. as an integral over the surface. For each component of $\vec{F}$, namely, F_i for $i = 1, 2, 3$ we have:

$$\int F_i dV = \int \frac{\partial \sigma_{ik}}{\partial x_k} dV = \oint \sigma_{ik} d\mathrm{a}_k \,. \tag{2.26}$$

The quantity σ_{ik} is called "stress tensor". As we see from Eq. 2.26, $\sigma_{ik} da_k$ is the $i - th$ component of the force on the surface element $d\vec{a}$. It can be shown that the strain tensor and the stress tensor are dependent one on another by [32]:

$$\sigma_{ik} = \frac{E}{1+\nu} \left[u_{ik}^2 + \frac{\nu}{1-2\nu} u_{ll} \delta_{ik} \right] \,, \tag{2.27}$$

---

[2]Remember that, according to the Newton's third law, the forces with which various parts of the portion considered act on one another cannot give anything but zero in the total resultant force.

and

$$u_{ik} = [(1 + \nu)\sigma_{ik} - \nu\sigma_{ll}\delta_{ik}]/E \,, \tag{2.28}$$

where there is a summation over the index l. E is the Young's modulus and ν is poisson ratio.

Now, considering that we are dealing with isotropic bodies, the equations of equilibrium must read:

$$\frac{\partial \sigma_{ik}}{\partial x_k} = 0 \,. \tag{2.29}$$

It follows that the equations of motion in a elastic body can be recapped:

$$\frac{\partial \sigma_{ik}}{\partial x_k} = \rho\frac{\partial^2 u_i}{\partial t^2} \,, \tag{2.30}$$

where ρ is the density.

Considering the relations given by Eqs. 2.27 and 2.28 and some vectorial identities we obtain:

$$\frac{E}{2(1+\nu)}\nabla^2\vec{u} + \frac{E}{2(1+\nu)(1-2\sigma)}\vec{\nabla}\vec{\nabla}\vec{u} = \rho\frac{\partial^2\vec{u}}{\partial t^2} \,. \tag{2.31}$$

In a general case, the solution $\vec{u}$ can be separate into two components (one longitudinal and another transversal) which propagates independently with different velocities. The Eq. 2.31 can be rewritten as:

$$\frac{\partial^2\vec{u}}{\partial t^2} = c_t^2\nabla^2\vec{u} + (c_l^2 + c_t^2)\vec{\nabla}\vec{\nabla}\vec{u} \,, \tag{2.32}$$

where $\vec{u} = \vec{u}_l + \vec{u}_t$. One satisfy $\vec{\nabla} \cdot \vec{u}_t = 0$ and the another satisfy $\vec{\nabla} \times \vec{u}_l = 0$. It is also true that:

$$c_t = \left[\frac{E}{2\rho(1+\nu)}\right]^{\frac{1}{2}} \,, \tag{2.33}$$

and

$$c_l = \left[\frac{E(1-\nu)}{\rho(1+\nu)(1-2\nu)}\right]^{\frac{1}{2}} \,. \tag{2.34}$$

Assuming that $\vec{u} = \vec{u}(\vec{r})e^{-i\omega t}$ the Eq. 2.32 becomes:

$$-\omega^2\vec{u} = c_t^2\nabla^2\vec{u} + (c_l^2 + c_t^2)\vec{\nabla}\vec{\nabla}\vec{u} \,, \tag{2.35}$$

Considering we are using the polar coordinates (ξ, ϕ, z), it follows that the angular dependence is always of the form $[\cos(n\phi), \text{sen}(n\phi)]$, and n is the angular eigenvalue. The z dependence is always e^{ikz} and (n, z) are the two principal quantum numbers. Looking strictly at the radial breathing mode, where the carbon atoms move, in phase, in the

radial direction, and using the method proposed by Mahan [33] to solve the Eq. 2.35, we find that the radial breathing mode frequency (ω_{RBM}) is given by:

$$\omega_{RBM} = \frac{4c_t}{d_t} \left[1 - \left(\frac{c_t}{c_l} \right)^{\frac{1}{2}} \right]^{\frac{1}{2}} . \tag{2.36}$$

In the case of carbon nanotubes, it follows that $c_l = (C_{11}/\rho)^{\frac{1}{2}}$ and $c_t = (C_{66}/\rho)^{\frac{1}{2}}$ [33]. Most theories and experiments give $C_{66} = (44 \pm 3) \times 10^{11}$ dynes/cm². The C_{11} values range from 106 to 146×10^{11} dynes/cm². Choosing $C_{11} = 106 \times 10^{11}$ dynes/cm² we obtain:

$$\omega_{RBM} = \frac{227}{d_t} \, cm^{-1} . \tag{2.37}$$

How does ω_{RBM} change with changing environment?

The RBM of nanotubes which interact with their surroundings can be modeled by two spring constants, one relating to the intrinsic properties of the nanotube (as stated in the last subsection), i.e., the $C - C$ bond strength, and one relating to the interaction strength between the nanotube and its surroundings. If the RBM is modeled as a cylindrical shell (see Fig. 2.9) with one degree of freedom, $x(t)$, which corresponds to the spatially uniform radial deflection from its equilibrium position, the Eq. 2.35 can be easily simplified. The RBM for the shell is therefore governed by:

$$\frac{x(t)}{R^2} + \frac{\rho h}{Eh}(1 - \nu^2)\frac{\partial^2 x(t)}{\partial t^2} = 0 , \tag{2.38}$$

where where t is time, R is the radius, E is the Young's modulus, ρ is the mass density per unit volume, ν is Poisson's ratio, and h represents the thickness of the shell.

Comparing Eq. 2.38 to the standard equation of the harmonic oscillator:

$$\frac{\partial^2 x(t)}{\partial t^2} + \omega^2 x(t) = 0 , \tag{2.39}$$

we easily find that:

$$\omega_0 = \frac{1}{R} \left[\frac{Eh}{\rho h(1 - \nu^2)} \right]^{\frac{1}{2}} , \tag{2.40}$$

which gives the radial breathing mode frequency for a cylinder free of external forces. Let us now suppose that a rigid shell, with radius $R_s = R + s_0$, is concentrically coupled to the cylinder (see Fig. 2.10).

21
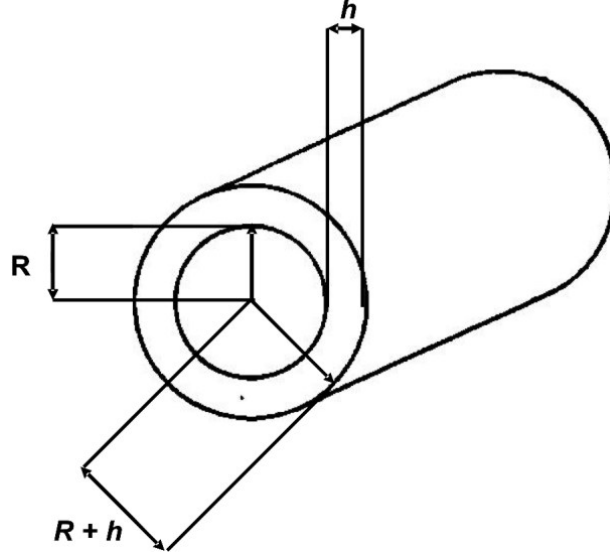
Figure 2.9: Schematics of the hollow cylinder with radius R and thickness h. In the case of Single Wall Carbon Nanotubes, h is comparable to the diameter of a carbon atom.

The interaction between the cylinder's wall and the rigid shell happens through Van der Waals forces, which are modeled by a Lennard-Jones potential given by:

$$U(x) = K \left[0.4 \left(\frac{s_0}{s_0 + x} \right)^{10} - \left(\frac{s_0}{s_0 + x} \right)^{4} \right], \tag{2.41}$$

where s_0 is the equilibrium separation with the cylinder. In the case that $x(t)$ undergoes small changes with relation to s_0, the potential can be approximated by a expansion around s_0 giving:

$$U(x) = U_0 + \left(\frac{dU}{dx} \right)_{s_o} (x - s_0) + \frac{1}{2} \left(\frac{d^2U}{dx^2} \right)_{s_o} (x - s_0)^2 + ... \tag{2.42}$$

Note that this potential generates a restorative force (per unit of area) in the cylinder's wall. This force is given by the gradient of the potential given by Eq. 2.42:

$$p(x) = -\nabla U(x) \approx -2 \left(\frac{d^2U}{dx^2} \right)_{s_o} (x - s_0) = \frac{24K}{s_0^2} (x - s_0), \tag{2.43}$$

where the higher order terms were neglected. The cylindrical shell subjected to a pressure given by Eq. 2.43 is governed by:

$$\frac{x(t)}{R^2} + \frac{\rho h}{Eh}(1 - \nu^2)\frac{\partial^2 x(t)}{\partial t^2} = -\frac{(1 - \nu^2)}{Eh}p(x). \tag{2.44}$$

22
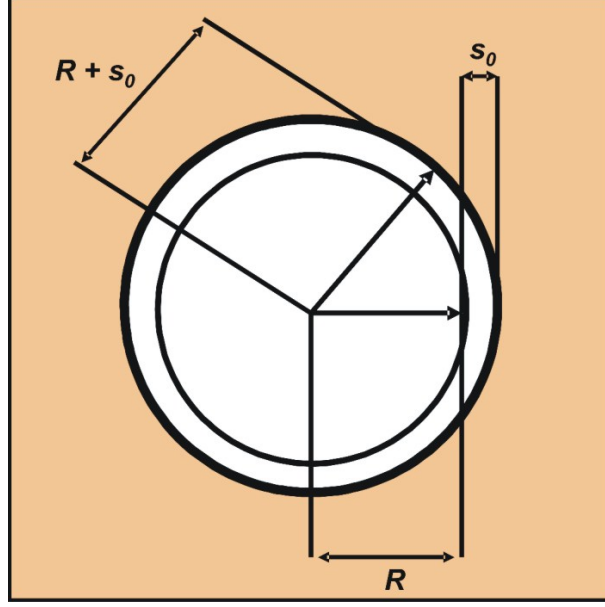
Figure 2.10: A top view of the hollow cylinder surrounded by some medium. This medium forms a rigid shell around the cylinder whose radius is $R + s_0$. The cylinder's wall interacts with the rigid shell by means of Van der Waals forces. The effect of such an interaction is upshifting the radial breathing mode frequency of the cylinder.

Rearranging Eq. 2.44 we find:

$$\frac{\partial^2 x(t)}{\partial t^2} + \frac{Eh}{\rho h(1-\nu^2)} \left[\frac{1}{R^2} + \frac{24(1-\nu^2)}{Eh}\frac{K}{s_0}\right] x(t) = 0 \,. \tag{2.45}$$

Finally, comparing Eq. 2.45 to Eq. 2.39 we find:

$$\omega = \left(\frac{Eh}{\rho h(1-\nu^2)}\right)^{\frac{1}{2}} \left[\frac{1}{R^2} + \frac{24(1-\nu^2)}{Eh}\frac{K}{s_0}\right]^{\frac{1}{2}} \,, \tag{2.46}$$

which gives the new cylinder's radial breathing mode frequency that is upshifted with respect to ω_0 given by Eq. 2.40. These findings will very important to explains the results presented further in chapter 5.

2.2 Resonance Raman spectroscopy and SWNT characterization

The Raman scattering, from a classical point of view, is related to the modulation of the polarizability α in the material by the vibrational mode Q. The electric dipole induced by the local field $\vec{E}$ can be described by:

$$\vec{P} = \alpha\vec{E} \,, \tag{2.47}$$

where α is the electronic polarizability that, in general, depends on the generalized coordinate Q of a given vibrational mode. Expanding α in terms of Q, we have:

$$\alpha = \alpha_0 + \left(\frac{\partial \alpha}{\partial Q}\right)_0 Q + \cdots, \tag{2.48}$$

where the derivative is made with relation to the equilibrium position. If ω_q is the frequency of the vibrational mode and ω_0 is the frequency of the incident light, we can rewrite $\vec{E}$ and Q as:

$$Q = Q_0 \cos \omega_q t \qquad \text{and} \qquad \vec{E} = \vec{E}_0 \cos \omega_0 t. \tag{2.49}$$

Considering just small oscillations, the Eq. 2.47 is recapped as:

$$\vec{P} = \alpha_0 \vec{E}_0 \cos \omega_0 t + \left(\frac{\partial \alpha}{\partial Q}\right)_0 Q_0 \vec{E}_0 \cos \omega_0 t \cos \omega_q t. \tag{2.50}$$

Using the trigonometric relation $2\cos(a)\cos(b) = \cos(a+b) + \cos(a-b)$, the Eq. 2.50 becomes:

$$\vec{P} = \alpha_0 \vec{E}_0 \cos \omega_0 t + \frac{1}{2}\left(\frac{\partial \alpha}{\partial Q}\right)_0 Q_0 \vec{E}_0 [\cos(\omega_0 - \omega_q)t + \cos(\omega_0 + \omega_q)t]. \tag{2.51}$$

The first term in the Eq. 2.51 is related to the Rayleigh scattering. The components with frequencies $(\omega + \omega_0)$ e $(\omega - \omega_0)$ are related to the Raman scattering. Note that the Raman scattering is possible only if

$$\left(\frac{\partial \alpha}{\partial Q}\right)_0 \neq 0, \tag{2.52}$$

which means that, in order to observe the Raman scattering, the polarizability must vary if the coordinate Q varies around the equilibrium. The Raman scattering is, therefore, the inelastic scattering of light.

Considering the quantum mechanics point of view, during a scattering event, (1) an electron is excited from the valence band to the conduction band by absorbing a photon, (2) the excited electron is scattered by emitting (or absorbing) phonons, and (3) the electron relaxes to the valence band by emitting a photon. If during the Raman process a phonon emission occurs, it means that a stokes process has taken place. Otherwise, if a phonon absorption occurs, it means that an anti-stokes process has happened [9]. The states $|i\rangle$, $|a\rangle$, $|b\rangle$ e $|f\rangle$ are defined as:

$$|i\rangle = |n_i, 0, n, \psi_0\rangle \tag{2.53}$$

$$|a\rangle = |n_i - 1, 0, n, \psi_a\rangle \tag{2.54}$$

$$|b\rangle = |n_i - 1, 0, n \pm 1, \psi_b\rangle \tag{2.55}$$

$$|f\rangle = |n_i - 1, 1, n \pm 1, \psi_0\rangle, \tag{2.56}$$

where each ket contains information about the number of incident photons, the number of scattered photons, the number of phonons and the electronic state, respectively. The signal $+$ stands for the Stokes process while the signal $-$ stands for the anti-Stokes process. The figure 2.11 show the diagram of the Raman scattering Stokes process.
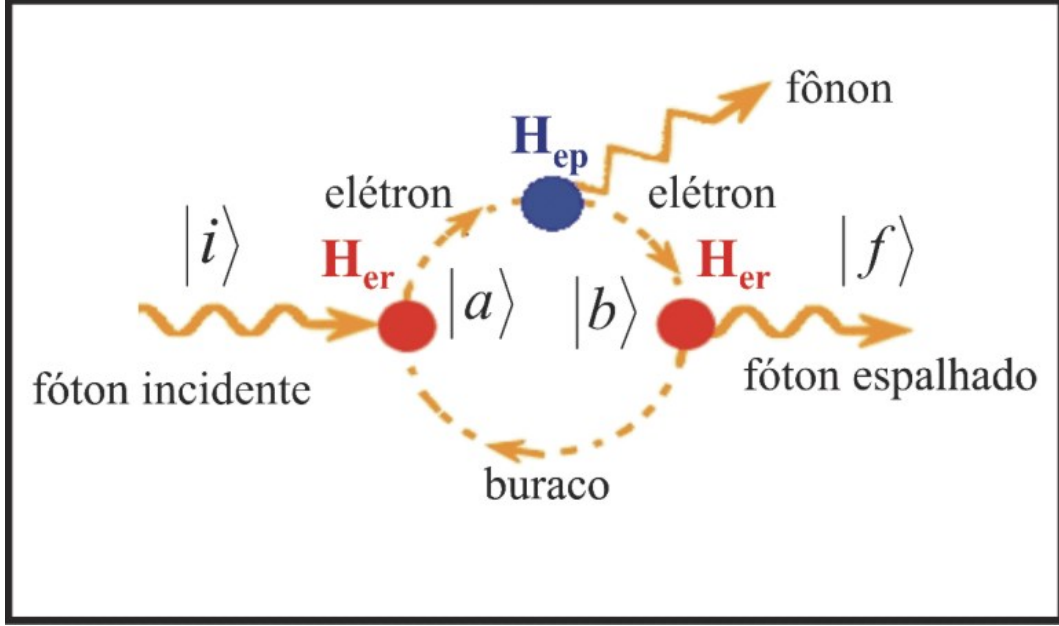
Figure 2.11: Diagram of the Raman scattering Stokes process. It worth to comment that, among the several possible diagrams for this process, this is the most likely one.

The energies associated to these states are:

$$
\begin{align}
E_i &= n_i\hbar\omega_i + n\hbar\omega_q + \varepsilon^{(v)}(k_0) \tag{2.57}\\
E_a &= (n_i - 1)\hbar\omega_i + n\hbar\omega_q + \varepsilon_a^{(c)}(k_0) \tag{2.58}\\
E_b &= (n_i - 1)\hbar\omega_i + (n \pm 1)\hbar\omega_q + \varepsilon_b^{(c)}(k_0) \tag{2.59}\\
E_f &= (n_i - 1)\hbar\omega_i + \hbar\omega_s + (n \pm 1)\hbar\omega_q + \varepsilon^{(v)}(k_0) \tag{2.60}
\end{align}
$$

where $\hbar\omega_q$ is the phonon energy, $\hbar\omega_i$ is the incident photon energy, $\hbar\omega_s$ is the scattered photon energy, $\varepsilon^{(v)}(k_0)$ and $\varepsilon_{a,b}^{(c)}(k_0)$ are the energies of the electron in the valence and conduction bands, respectively. The positive sign in the term which describes the phonon energy (see Eqs. 2.59 and 2.60), stands for an increase in the state's energy due to the creation of a phonon (Stokes process). The negative sign stands for a decrease in energy due to the annihilation of a phonon (anti-Stokes). In order to conserve the energy and

the momentum, it follows that: $\hbar\omega_i = \hbar\omega_s \pm \hbar\omega_q$ and $\vec{k}_i = \vec{k}_s \pm \vec{q}_q$, where the ω_q and $\vec{q}_q$ are, respectively, the frequency and the wavevector of the phonon. $\mathbf{k_i}$ and $\mathbf{k_s}$ are the wavevectors of the incident and scattered photons.

The number of emitted phonons before relaxation of the lattice can be one, two, and so on, which we call, respectively, one-phonon, two-phonon and multi-phonon Raman processes. The order of a scattering event is defined by the number of internal scattering events, including elastic scattering by an imperfection (such as a defect or an edge) of the crystal. The lowest order process is the first-order Raman scattering process which gives Raman spectra involving one-phonon emission. In graphene, the so-called G band around $1582\,\mathrm{cm}^{-1}$ is the only first-order Raman peak. In SWNTs, the G band spectra, which is split into many features around $1580\,\mathrm{cm}^{-1}$, and the lower frequency radial breathing mode (RBM) are usually the strongest features in SWNT Raman spectra, and they are both first-order Raman modes [9, 10].

Our target, the radial breathing mode, is a unique phonon mode, appearing only in carbon nanotubes and its observation in the Raman spectrum provides direct evidence that a sample contains SWNTs. Frequencies ω_{RBM} raging from 50 to $500\,\mathrm{cm}^{-1}$ can be expected. In fact, the radial breathing mode frequency ω_{RBM} is the most important SWNT spectroscopic signature because of its relation with SWNT diameter (d_t) given by $\omega_{RBM} = 227/d_t$ [34] (deviations from this relation can be attributed to environmental effects, as we will show in Chapter 5). These features make the resonance Raman spectroscopy a powerful tool to characterize SWNTs because, from a resonance Raman spectra (or a couple of them), we can extract information about $E_{ii}^{S,M}$ and ω_{RBM}. The pair $(E_{ii}^{S,M}, \omega_{RBM})$ is unique for each SWNT specie and, with help of the Kataura's plot, it is possible to identify each (n,m). The Kataura's plot brings $E_{ii}^{S,M}$ plotted as a function of d_t (see Fig.2.12), which is linked to ω_{RBM} through the relation $\omega_{RBM} = 227/d_t$. Using the $d_t(n,m)$ dependence given by Eq.2.2, it is possible to index a SWNT.

2.2.1 A guide to the Raman-based (n,m) assignment

The Raman-based (n,m) assignment is straightforward if the sample has isolated tubes or even bundles with small diameter tubes. In this case, the RBM spectra have well defined ω_{RBM} peaks [11, 13]. The (n,m) assignment becomes more difficult when the sample is composed of SWNTs with a broad range of d_t. The larger the d_t, the larger the overlap in the resonances among different RBMs for tubes of similar d_t. In this case, the assignment must be performed based on anchors, as discussed further in the text.
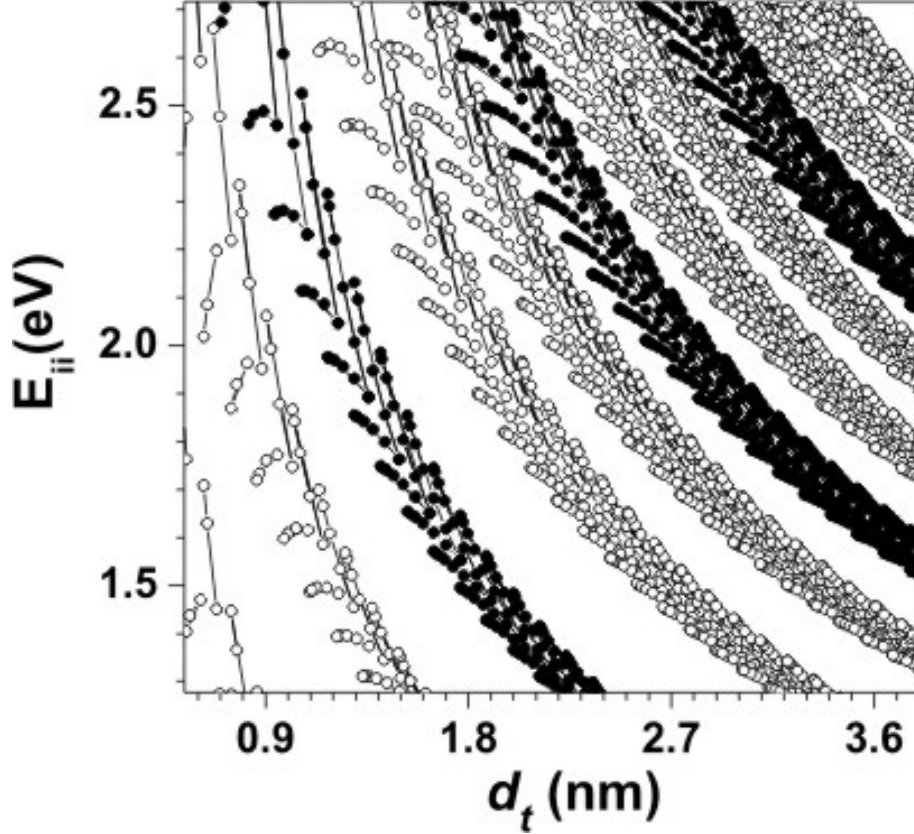
Figure 2.12: The Kataura's plot presents E_{ii} as a function of d_t. Each bullet represents an unique E_{ii} from a given SWNT specie. Black bullets stand for metallic SWNTs, while open bullets stand for semiconducting species. Using a pair $(E_{ii}^{S,M}, \omega_{RBM})$ experimentally obtained and with help of the relation $\omega_{RBM} = 227/d_t$ we can run over all the SWNTs presented in the plot, finding their (n,m) indices [11, 34, 35].

Let us begin with just one laser line. Figure 2.13(a) shows one RBM spectrum obtained using the 644 nm laser line ($E_{\text{laser}} = 1.925\,\text{eV}$). Figure 2.13(b) shows the Kataura plot used to analyze the spectra, obtained from Eq. 2.19 using the parameters for the "alcohol-assisted" CVD [3] grown SWNTs [13]. Each bullet represents one transition energy $(E_{ii}^{M,S})$. From the bottom to the top, the first group is associated with the E_{22}^{S} (E_{11}^{S} is below and only a single point can be seen at the right-bottom corner), the second group is the E_{11}^{M}, the third group is the E_{33}^{S}, and so on. The light green bullets are associated

---

[3]The nomenclatures "alcohol-assisted" ($A.A$) and "super-growth" ($S.G.$) carbon nanotubes will be employed throughout the text. The $A.A.$ tubes are grown by CVD method using Acetate Cobalt-Molybdenum as percussor and alcohol as catalyst. During the growth process the CVD chamber is kept under a Ar/H_2 flux. The $S.G.$ tubes are grown by CVD method using $Fecl_3$ (or Fe, Al/Fe, Al_2O_3/Fe, Al_2O_3/Co) as percussor and water as catalyst. During the growth process the CVD chamber is kept under a Ar/H_2 or He/H_2 flux.

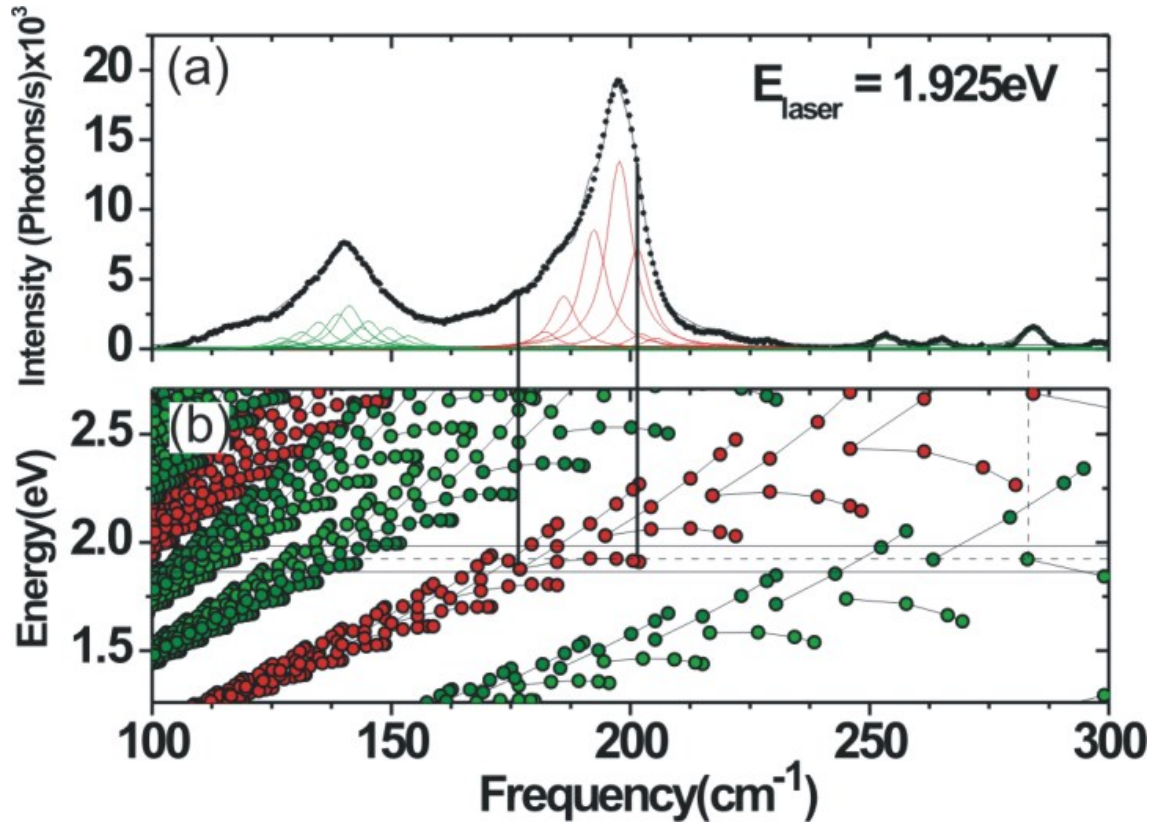**Figure 2.13**: (a) Raman spectrum (bullets) obtained with a 644 nm laser line. This spectrum was fitted by using 34 Lorentizians (curves under the spectra) and the solid line is the fitting result. (b) The Kataura plot from Eq. 2.19 with the parameters given in Ref. [13]. The dashed line indicates E_{laser} and the solid line gives the width of the resonance window $(E_{\text{laser}} \pm 0.06)\,\text{eV}$. [11, 13]

with semiconducting carbon nanotubes with $\mod(2n+m, 3) = 1$ (type one - SI), the olive bullets are associated with semiconducting carbon nanotubes with $\mod(2n + m, 3) = 2$ (type two - SII) and the red bullets are associated with metallic carbon nanotubes $(\mod(2n+m, 3) = 0)$. In each group, we can realize several branches, called families, that are characterized by $2n + m =$ const. The geometrical patterns are crucial for the fitting (mainly in case one has a map with many laser lines), and they work for larger diameter tubes as well.

In Fig. 2.13(a) the bullets show the data and the solid line shows the fit obtained using 34 Lorentzian curves (the peaks bellow the spectral curve). Each Lorentzian curve can be related to one RBM from one carbon nanotube. The red Lorentzians represent the RBM from metallic tubes and the green (olive) Lorentzians represent the RBM from semiconducting SI (SII) tubes. To know how many Lorentzians should be used to fit each resonance spectrum, we use the Kataura plot. Figure 2.13(b) has a dashed line that represents the excitation energy for the spectrum shown in Fig. 2.13(a), and the two bold lines (above and below the dashed line) give the approximate boundary for the RBM resonance profiles [36]. To fit the spectrum shown in Fig. 2.13(a) we expect that all the circles inside the rectangle $(E_{\text{laser}} \pm 0.06)\,\text{eV}$ made by the two bold lines should show up. The vertical bold lines connecting Fig. 2.13(a) and Fig. 2.13(b) indicate the metallic $2n+m = 30$ family in resonance. Note that while the Kataura plot usually presents E_{ii} as a function of d_t, in Fig. 2.13(b), we plot E_{ii} as a function of ω_{RBM} for a direct comparison with each spectrum. Here we have the first constraint:

- The conversion between ω_{RBM} and d_t must be performed considering the relation (see Chapter 5) $\omega_{\text{RBM}} = (227/d_t)\sqrt{1 + C_e \cdot d_t^2}$. By properly adjusting the constant C_e one can overlap the bullets in the Kataura's plot within $(E_{\text{laser}} \pm 0.06)\,\text{eV}$ and RBM peaks in the spectrum.

The difficulty in performing the spectral fitting occurs because a large number of Lorentzian curves are needed to fit a broad RBM profile. The fitting program tends to broaden and increase some peaks, while eliminating others. If for the same fit, one Lorentzian is shifted by a couple of cm^{-1}, the fitting program will return a completely different fitting result. Therefore, another constraint, this time for the linewidths (full width at half maximum - FWHM), must be adopted:

- We require all the Lorentzian peaks in one spectrum to share the same FWHM. The value is free to vary as a fitting parameter, but it should be the same for all

Lorentzian peaks. Fluctuations of the RBM FWHM with (n, m) can be expected. However, such fluctuations do not change the picture of the results obtained after a self-consistent, many-cycles, fitting procedure.

After the fitting, one is ready to associate each pair $(E_{laser}, \omega_{RBM})$ with a specific (n, m). With just one laser line $(E_{laser} \pm 0.06)$ eV, the assignment procedure is reliable enough to associate a given ω_{RBM} to a couple (n, m) if the E_{ii} values are well known. However, a change in the environmental conditions (see Chapter 6) changes E_{ii} and adds uncertainty in energy. For those using just one laser line this uncertainty is accounted for considering that a change in the environment changes E_{ii} by ~ 40 meV in average, although this value can go up to 100 meV (see Chapter 6), giving rise to a new freedom in the fitting [9, 11]. An additional anchor here, to decrease the uncertainty, is the fact that, as the chiral angle gets smaller $(\theta \rightarrow 0)$, the Raman signal gets more intense [36]. In fact, the uncertainty in E_{ii} is promptly overcome by using many laser lines, allowing measurement of resonance profiles of each SWNT. After analyzing all the spectra obtained experimentally using the procedure described above for one laser line, we select each RBM frequency and plot its intensity as a function of E_{laser}. Such a plot gives the resonance profile for the SWNT that has the specified RBM mode frequency. Figure 2.14 shows three Raman spectra for three E_{laser} values that are different but close to each other, so that the same RBMs should be close to resonance for the three spectra. In each spectrum we selected two Lorentzian curves (with frequencies around $192 \, \text{cm}^{-1}$ and $186 \, \text{cm}^{-1}$) and we show, in Figs. 2.14(d) and (e), their resonance profiles (Intensity vs E_{laser}). These resonance profiles should then be fit by using the RRS intensity equation:

$$I(E_{laser}, E_q) = \left| \frac{\mathcal{M}}{(E_{laser} - E_{ii} - i\gamma)(E_{laser} - E_{ii} - E_q - i\gamma)} \right|^2, \qquad (2.61)$$

where $\mathcal{M}$ represents the matrix elements, E_{laser} is the laser energy, E_{ii} is the optical transition energy, γ is the resonance window linewidth and E_q is the RBM energy. We assume the matrix elements and γ do not change within one resonance profile. From the fits it is then possible to obtain the E_{ii} for that specific RBM, i.e. for that specific (n, m) SWNT.

2.3 Summary

In this chapter we showed that each SWNT is totaly described by a pair of indices (n, m) or, equivalently, by the pair $(E_{ii}^{S,M}, \omega_{RBM})$, which is easily accessible with resonant
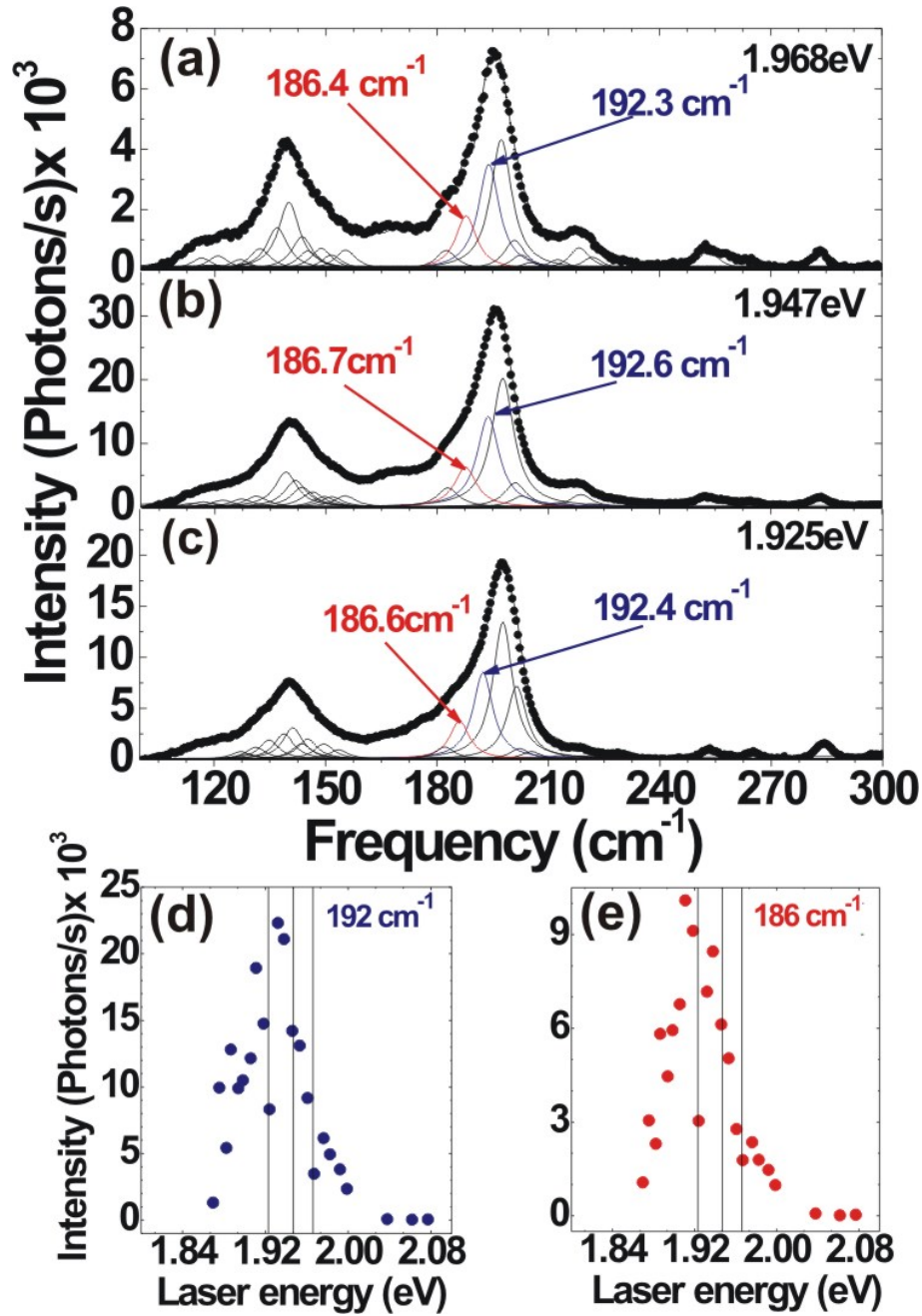
Figure 2.14: Raman spectra (bullets) obtained with a (a) 630 nm, (b) 637 nm and (c) 644 nm laser lines. All the spectra are fit with a sum of Lorentizians (solid line). (d) The resonance profile for the carbon nanotube with $\omega_{\text{RBM}} \sim 192\,\text{cm}^{-1}$, $(n, m) = (12, 6)$. (e) The resonance profile for the carbon nanotube with $\omega_{\text{RBM}} \sim 186\,\text{cm}^{-1}$, $(n, m) = (11, 8)$. The vertical lines indicate the three excitation energies used to measure the spectra displayed on panels (a), (b) and (c). [13]

Raman scattering. We also explained both, the electronic and the vibrational structure, emphasizing the importance of the circumferential confinement in the SWNT properties, where the most striking feature is the rising of the van Hove singularities. By means of the elasticity theory, an expression for the radial breathing mode frequency was deduced as $\omega_{RBM} = 227/d_t$. Next, a simple model based on van der Waals forces was employed to explain how ω_{RBM} changes with changing environment. In sequence, a brief introduction of the Raman scattering, highlighting its main features, was addressed. Finally, a recipe for performing the (n, m) assignment using resonant Raman spectroscopy was described.

Chapter 3

The Historical Overview of E_{ii}: van Hove singularities, Excitons and the Screening Problem

In this chapter, a summary of the historical evolution of the research behind the E_{ii} is addressed. It is seen that E_{ii} clearly depends on intrinsic and extrinsic properties (e.g. a change in the environment). This dependence is attributed to the dielectric screening effect, which is connected to the dielectric constant κ. Usually, the excitonic transitions are calculated by means of the Bethe-Salpeter equation (see Chapter 2) and the dielectric screening within the random phase approximation (RPA). Finally, a simple method to describe κ is proposed.

3.1 The evolution of the experimental determination of E_{ii}

As briefly stated in Chapter 2, quantum confinement is responsible for the occurrence of van-Hove singularities in the electronic structure of SWNTs, resulting in strong resonance processes. In general, the electronic density of states (DOS) is given by:

$$D(E) = \frac{2}{N} \sum_{\mu=1}^{N} \int \frac{1}{\frac{dE_\mu(\vec{k})}{d\vec{k}}} \delta(E_\mu(\vec{k}) - E) d\vec{k}. \tag{3.1}$$

From Eq. 3.1 one can see that every time the derivative $\frac{dE_\mu(\vec{k})}{d\vec{k}}$ is equal to zero the equation diverts. All the points where Eq. 3.1 diverts are called van Hove singularities.

The last decade assembled much important experimental information about E_{ii} that, piece by piece, was supported by theoretical approaches by means of tight-binding and first-principles calculations [10, 12, 15, 16, 22, 23, 31, 37, 38]. In 2001, Jorio *et al.* [39] described E_{ii} in terms of a first-neighbor tight-binding calculation combined with a zone-folding procedure. They successfully explained their resonance Raman experimental results using this simple model because the range of tube diameters ($1 < d_t < 3$ nm) and laser energy ($E_{\text{laser}} = 1.58$ eV) covered a region where curvature and excitonic effects were not evident [39]. In 2002, Bachilo *et al.* [40] performed Raman scattering and photoluminescence experiments on high-pressure carbon monoxide (HiPco) grown SWNTs dispersed in Sodium Dodecyl Sulfate (SDS) and, by analyzing the experimental E_{11}^S and E_{22}^S values for semiconducting SWNTs, they figured out that the simple first-neighbor tight-binding calculation was not able to accurately describe the experimental E_{11}^S and E_{22}^S transition energies for SWNTs within the ($0.7 < d_t < 1.3$ nm) range.

For this reason, the so-called "ratio-problem" and the curvature effect were introduced, providing evidence that excitons and the σ-π hybridization should be take into account. As explained in Chapter 2, Popov *et al.* [22, 37] and Samsonidze *et al.* [23] described the curvature effects using the ETB model, while Spataru *et al.* [38], performing first-principle calculations, described the exciton structure directly. The ETB model was efficient in describing all $(2n+m)$-family trends, as reported by Telg *et al.* [41] and Fantini *et al.* [42]. Telg *et al.* and Fantini *et al.* used resonance Raman spectroscopy with a set of tunable lasers to map the RBM signal from HiPco SWNTs dispersed in SDS, building a 3D plot (see Fig. 3.1) from which they experimentally assigned more than 45 SWNTs, including S-SWNTs and M-SWNTs. Later, Wang *et al.* [29] and Maultzsch *et al.* [30] performed two-photons experiments giving rise to unquestionable experimental evidence that the electronic transitions in SWNTs arise from excitons.

In 2007, the RBM spectra of as-grown vertically aligned SWNTs synthesized by the chemical vapor deposition method from alcohol (the $A.A.$ tubes previously described) were measured over a broad diameter (0.7 to 2.3 nm) and energy (1.26 to 2.71 eV) ranges [13]. Over 200 different SWNT species and about 380 different optical transition energies were probed, going up to the fourth optical transition of semiconducting SWNTs, thus establishing the (n, m) dependence of the poorly studied E_{33}^S and E_{44}^S transitions [13]. Over 95 different laser lines were used to generate the two-dimensional plot giving the Raman intensity as a function of the laser excitation energy (E_{laser}) and the inverse of Raman frequency shift, as showed in Fig. 3.2. As stated in Chapter 2, the d_t is known to be related to the inverse ω_{RBM}, so that the resonance profile of each RBM Raman peak
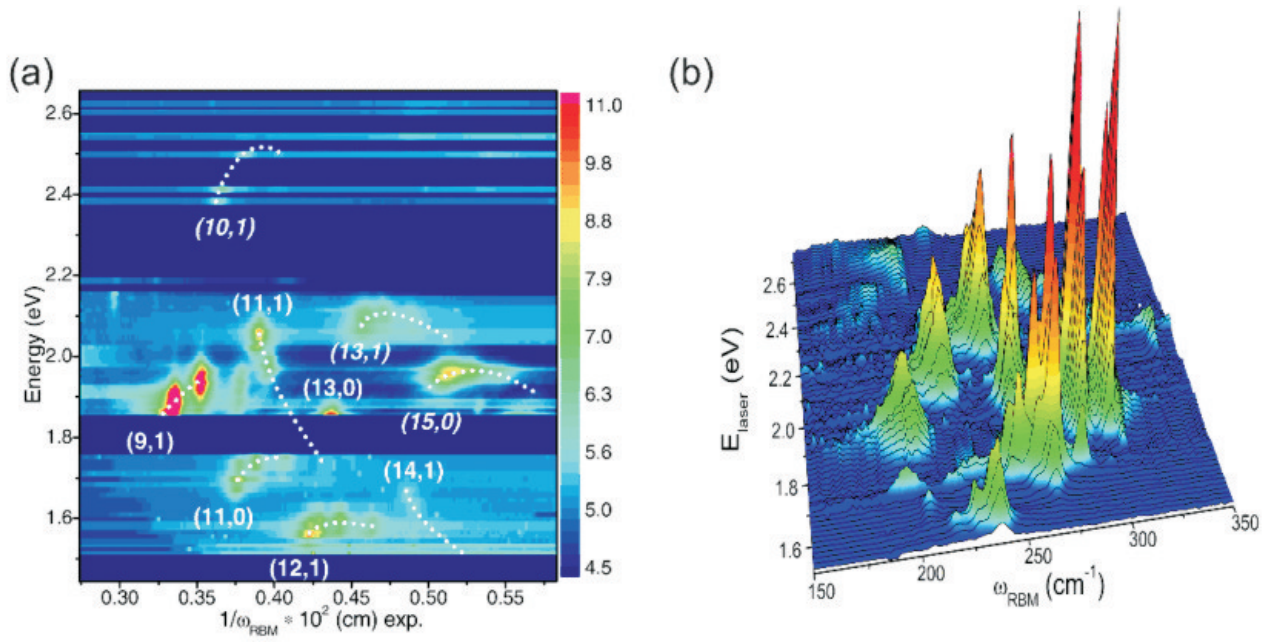
Figure 3.1: (a) Contour plot of the Raman intensity of the RBM from HiPco SWNTs dispersed in a SDS aqueous solution as a function of excitation energy and reciprocal RBM frequency. The dotted and dashed lines connect maxima originating from tubes of the same $(2n + m) = const.$ branch. In each branch the member with the smallest chiral angle $(\theta \to 0)$ is labeled.[41] (b) RBM Raman measurements of a similar sample, measured with 76 different laser lines E_{laser} and showing results consistent with (a). [42]
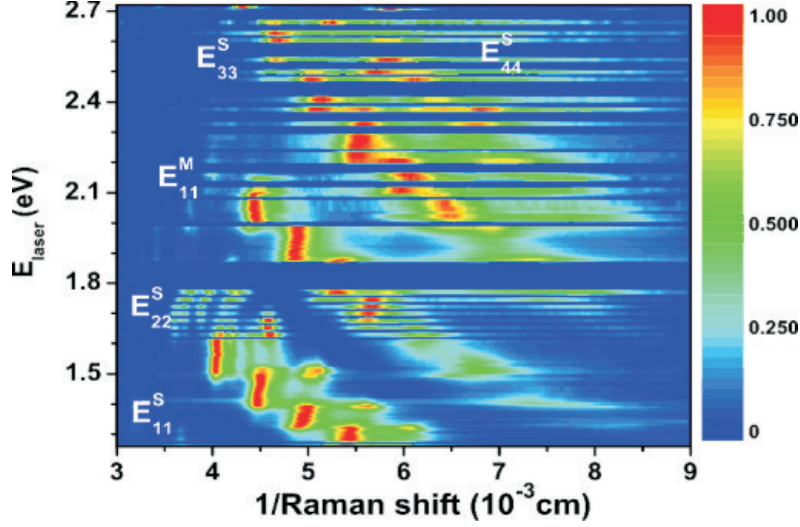
Figure 3.2: 95 different laser lines were used to generate a 2D color map showing the RBM spectral evolution as a function of excitation laser energy for SWNTs growth by the alcohol assisted CVD method. The intensity of each spectrum is normalized to the strongest peak, and we plot the inverse Raman shift. The E_{ii} subbands are labeled with S/M superscripts standing for semiconducting/metal tubes. [13]

can be directly related to a given SWNT diameter.

Using the 2D plot exhibited in Fig. 3.2, 84 different SWNTs species were unambiguously indexed, allowing a careful analysis of E_{ii} to be made from E_{22}^S to E_{44}^S. For a fixed SWNT chirality, the E_{ii} values are expected to exhibit a simple scaling behavior (see Eq. 2.16 in Chapter 2) when plotted as a function of p/d_t, where $p = 1, 2, 3, 4, 5$ for E_{11}^S, E_{22}^S, E_{11}^M, E_{33}^S, E_{44}^S, respectively [31].

Figure 3.3(a) shows a plot of the assigned transition energies E_{11}^S, E_{22}^S, E_{11}^M, E_{33}^S, E_{44}^S as a function of p/d_t, after correction for their chirality dependence obtained by subtracting $(\beta_p \cos 3\theta/d_t^2)$ from the experimentally obtained E_{ii} values (see inset to Fig. 3.3(a) and respective caption for β_p values, $1 \leq p \leq 5$). Such a chirality correction is expected to collapse all E_{ii} values onto a single (p/d_t) dependent curve [31]. Note that the points do not scale linearly as p/d_t. As discussed by Kane and Mele [31] (and recapped in Chapter 2), the non-linear scaling is due to many-body effects and can be fit with a logarithmic correction (see Eq. 2.19). It is noticeable that the E_{33}^S and E_{44}^S transitions do not follow the same scaling law as the E_{11}^S and E_{22}^S transitions, indicating that there is something fundamentally different between the first two lowest energy optical transitions and the subsequent transitions in semiconducting SWNTs. Figure 3.3(b) shows evidence for the difference between the (E_{33}^S, E_{44}^S) and $(E_{11}^S, E_{22}^S, E_{11}^M)$ experimental data. The E_{11}^S, E_{22}^S and E_{11}^M val-
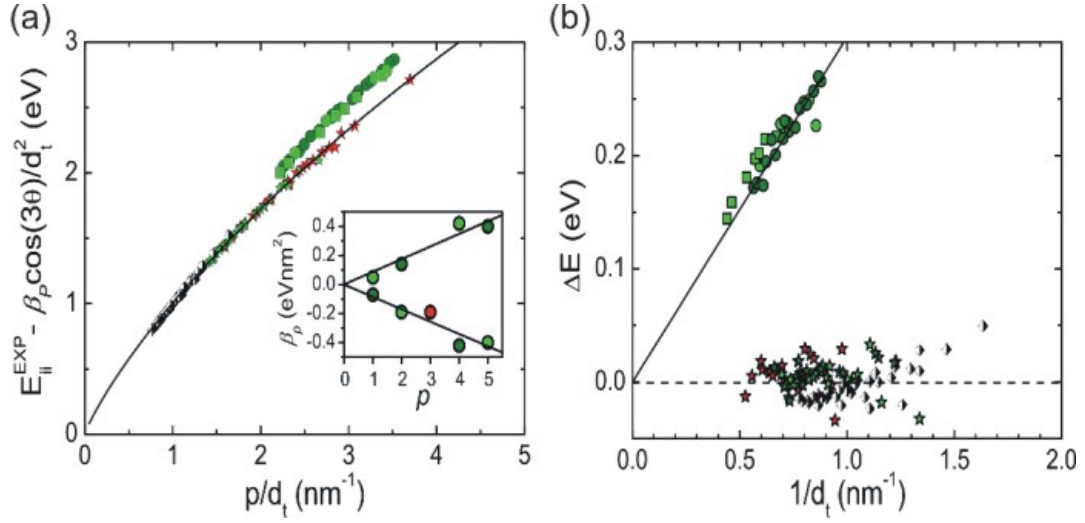
Figure 3.3: (a) Experimental optical transition energies obtained from analysis of Fig. 3.2 as a function of p/d_t, after correcting for the chiral angle dependence ($E_{ii}^{EXP} - \beta_p \cos 3\theta/d_t^2$). The chirality dependence corrected E_{11}^S (black and white diamonds from Ref. [40]), E_{22}^S (green/olive stars) and E_{11}^M (red stars) are fitted with Eq. (6.1). Inset: the experimental β_p values for the lower (upper) E_{ii} branches are -0.07(0.05), -0.19(0.14), -0.19(not measured), -0.42(0.42) and -0.4(0.4) for $p = 1, 2, 3, 4$ and 5, respectively. (b) Deviation (ΔE) of the ($E_{ii}^{EXP} - \beta_p \cos 3\theta/d_t^2$) data from the fitting curve in (a), versus $1/d_t$. The solid line ($\Delta E = 0.305/d_t$) fits the ΔE_{33}^S (green/olive circles) and ΔE_{44}^S (squares). [13]

ues plotted in Fig. 3.3(a) can be fitted by [31] the Eq. 2.19 with $2a_{C-C}\gamma_0 = 1.049\,\text{eV·nm}$, $b = 0.456$ and $c = 0.812\,\text{nm}^{-1}$.

Figure 3.3(b) shows the deviation (ΔE) of the chirality dependence corrected ($E_{ii} - \beta_p \cos 3\theta/d_t^2$) values from the right side of Eq. (2.19). The deviations ΔE_{33}^S and ΔE_{44}^S from the zero line in Fig. 3.3(b) shows a clear $1/d_t$ dependence, and can be successfully fit by a single expression $\Delta E = \gamma/d_t$, with $\gamma = (0.305 \pm 0.004)\text{eV·nm}$. Michel *et al.* [14] observed the same odd behavior finding also a $1/d_t$ dependent deviation.

3.2 The dielectric screening effect

The experimental evidences gave rise, so far, to the necessity of understanding how distinct states could shield each other, in the sense that this shielding could explain the scale break-down observed for E_{33}^S and E_{44}^S. Two approaches were made:

1. Quantum-chemistry calculations were used to explain the scaling-law breakdown showing that the excitons related to higher transitions (E_{33}^S, E_{44}^S,) are weakly bound (or are even unbounded e-h pairs) [13] due to the mixing of the DOS of E_{11}^S and E_{22}^S with E_{33}^S. At the bottom of the E_{33}^S zone there is a large DOS from E_{11}^S and E_{22}^S, corresponding to delocalized and unbound states. This effect is enhanced at the E_{33}^S and E_{44}^S levels compared to the E_{22}^S states (the latter overlaps only with the E_{11}^S band). The calculations estimate less than $0.001\,\text{eV}$ separation in the density of states at the E_{33}^S transition, attributed to other molecular states, compared to about an $0.02\,\text{eV}$ separation at the E_{22}^S transition. Any small perturbation (*e.g.* dielectric environment inhomogeneity, tube ends or vibrational coupling) will mix the nearly isoenergetic states at the E_{33}^S and E_{44}^S levels. Consequently the mixing of all these states and non-Condon effects might become important with E_{33}^S and E_{44}^S only marginally reflecting the character of "pure" states [13].

2. Predictions based on solid-state physics calculations, both tight binding and first-principles, actually give an opposite picture, *i.e.* that the excitons which are related to the higher transitions are more strongly bound than the lower ones, and the stronger many-body effects cause the breakdown of the scaling law [15, 16]. A reason why higher transitions exciton states are strongly bounded is that the effective mass of electron and hole in these higher transitions are heavier than in the lower transitions [15]. Thus the corresponding Coulomb energy (electron self-energy and

exciton biding energy) increases as a function of the exciton wavevector measured form the high symmetry K-point in the 2D brillouin zone.

Therefore, the opposite conclusions come from opposite pictures given by different theoretical models. While solid state physics based calculations impose periodic boundary conditions on a perfect tube and the exciton wavevector constitutes a good quantum number, which allows efficient separation of "pure" E_{11}^S, E_{22}^S, and E_{33}^S bands, quantum-chemistry calculations do not impose periodic boundary conditions and do not allow such separation. On the other hand, quantum chemistry calculations are based on a short SWNT segments (about 500 atoms in [13]). The experimental results themselves did not offer a conclusive answer towards one or the other theoretical model, which led us to a deep search for the missing physics; i.e. the problem of the dielectric screening in SWNTs. Besides this, the understanding of the dielectric screening is fundamental to properly explain and correlate the changes in the E_{ii} due to changes in the environment surrounding the SWNTs (see Fig. 3.4), e.g. when the tube in a surfactant solution [40, 41, 42], in bundles [42], sitting on silicon substrate [39] or isolated from each other [34, 35]. The highlighted areas in Fig. 3.4 delimit SWNT families that are common to the samples. A close inspection reveals that the E_{ii} varies from sample to sample.

Evidently, this search has attracted attention of the SWNT scientific community: the physical interpretation of the dielectric constant in the results from the two photons experiments (see Refs. [29, 30]) have considered that the exciton binding energies are much lower than the predicted by state-of-the-art first principles calculations by Spataru *et al.* [38]. A recent work from Steve Louie's group [43] showed that the mismatch could be solved by considering that the dielectric constant in carbon nanotubes exhibits an anti-screening behavior, which makes the exciton binding energy to be stronger than the ones reported by Wang *et al.*[29] and Maultzsch *et al.*[30]. They also conclude that the use of an electron-hole interaction model with a spatially constant dielectric function to estimate the exciton binding energy in isolated SWNTs leads to a large underestimation of the binding energy and, therefore, to accurately determine the electron-hole interaction a spatial-dependent dielectric screening is essential.

Within the extended tight-binding model [44], the transition energies from the ground state to the first bright exciton state are calculated by solving the BetheSalpeter equation [44, 45]. Inside this context, The unscreened Coulomb potential V between carbon π orbitals is modeled by the Ohno potential [46]. The dielectric screening effect is considered within the random phase approximation (RPA). In the RPA, the static
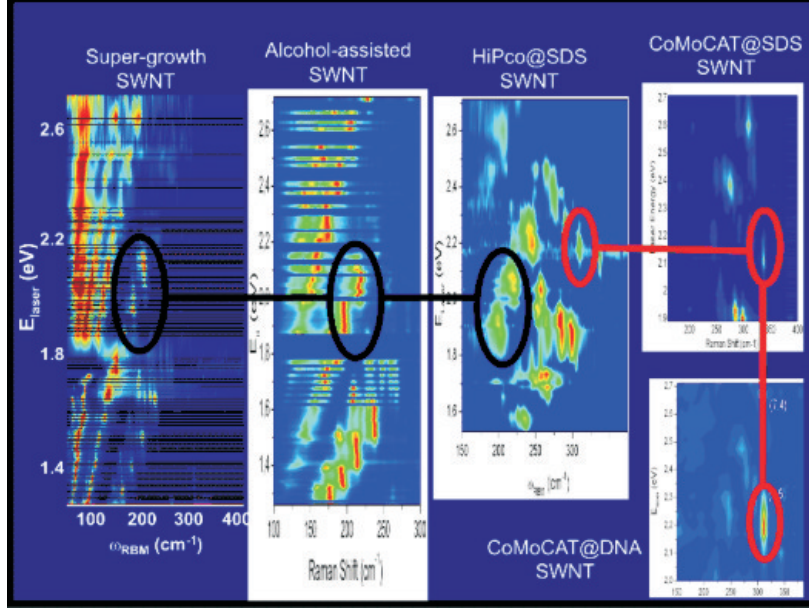
Figure 3.4: Comparison of the Raman maps for 5 different samples: the super-growth SWNTs [34], the alcohol-assisted SWNTs [13], HiPco@SDS and CoMoCat@SDS [42] and CoMoCat@DNA SWNTs [42]. The highlighted black and red areas delimit SWNTs families that are common to the samples.

screened Coulomb interaction W is expressed as:

$$W = \frac{V}{\kappa \varepsilon(\vec{q})} \,, \tag{3.2}$$

where $\varepsilon(\vec{q})$ is the dielectric function describing effects of the polarization of the π bands; κ is the static dielectric constant describing the effects of electrons in core states, the σ bonds, and surrounding materials. Only the polarization for the π band is directly calculated, while the effects of electrons in the core states, the σ bands, and the surrounding materials are represented by a single constant κ. The most correct description of the screening, the inhomogeneous and nonlocal dielectric response of the nanotube itself and the surrounding materials must be considered. However, this is not an easy task. A simple model to deal with the dielectric screening is considering that κ comprises two contribution: the κ_{tube} and the $\kappa_{\text{env.}}$. The term κ_{tube} is uniquely dependent of the SWNT's intrinsic properties while the term $\kappa_{\text{env.}}$ takes into account changes in the environment surrounding the tubes. The relation between κ, κ_{tube} and $\kappa_{\text{env.}}$ is given by:

$$\frac{1}{\kappa} = \frac{C_{\text{env.}}}{\kappa_{\text{env.}}} + \frac{C_{\text{tube}}}{\kappa_{\text{tube}}} \,, \tag{3.3}$$

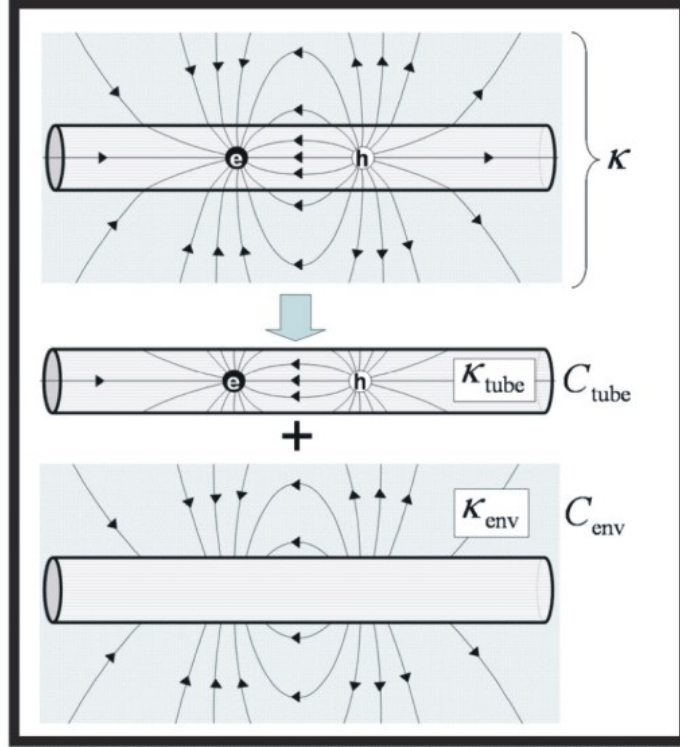where $C_{\text{env.}}$ and C_{tube} are coefficients weighting the contributions from inside and outside

Figure 3.5: A schematic of the connection of the net dielectric constant κ and the dielectric constant of the surrounding material $\kappa_{\text{env.}}$ and of the nanotube itself κ_{tube}. [44]

of a nanotube, respectively. Figure 3.5 illustrates this approach for κ.

In Chapter 6, we show that this method for describing κ is well succeeded, explaining the changes in the E_{ii} due to a changing environment.

3.3 Summary

In this chapter a historical overview of the evolution in the research of E_{ii} and its dielectric screening is presented. It is discussed that, to accurately determine the electron-hole interaction and, therefore, the E_{ii}, a spatial-dependent dielectric screening is essential. The excitonic energies are usually described by the Bethe-Salpeter equation within the context of tight-biding calculations (or ab-initio calculations). The dielectric screening effect is considered within the random phase approximation (RPA). In order to simplify the calculations, a successful and simple model for κ is presented, where κ is comprised of two terms: the κ_{tube} and the $\kappa_{\text{env.}}$. The term κ_{tube} is uniquely dependent of the SWNT's intrinsic properties while the term $\kappa_{\text{env.}}$ takes into account changes in the environment surrounding the tubes.

Part II

Instrumentation Development and Results

Figure 3.6: Richard P. Feynman's caricature[1].

"What is science? Of course you all must know, if you teach it. That's common sense. What can I say? If you don't know, every teacher's edition of every textbook gives a complete discussion of the subject. There is some kind of distorted distillation and watered-down and mixed-up words of Francis Bacon from some centuries ago, words which then were supposed to be the deep philosophy of science. But one of the greatest experimental scientists of the time who was really doing something, William Harvey, said that what Bacon said science was, was the science that a lord-chancellor would do. He [Bacon] spoke of making observations, but omitted the vital factor of judgment about what to observe and what to pay attention to...

...And so what science is, is not what the philosophers have said it is, and certainly not what the teacher editions say it is. What it is, is a problem which I set for myself after I said I would give this talk."

A small piece of Richard P. Feynman's talk presented at the fifteenth annual meeting of the National Science Teachers Association, 1966 in New York City.

[1]Credits: http://browse.deviantart.com

Chapter 4

Instrumentation Development: Going Beyond the Micrometer Scale

To perform experiments in the nanometer scale has become a major need. This chapter goes over the instrumentation needed to build a system which is able to perform both, spectroscopy and manipulation, in the nanometer scale. The purpose of the system is joining a confocal microscopy setup to an atomic force microscopy (AFM) setup. With the confocal system, we are able to perform spectroscopy with optical resolutions coming close to $\lambda/2$, where λ is the light source wavelength. The AFM system allows us to image and manipulate nano-scaled systems. Together They allow simultaneous experiments of spectroscopy and nano-manipulation. If the tip used is metallic, the system also allows "Tip Enhanced Spectroscopy" (TES) to be done. As a consequence, optical resolutions beyond the diffraction limit can be achieved, where the resolution is totaly related to the diameter of the tip. I would like to specially mention that this text was written doing mention to the specific equipments we have in our laboratory. However, any other equipment of any other brand and factory can be used if they have similar specifications compared to the ones we use. The reader which is not interested in instrumentation can skip this chapter without having trouble to understand the next chapters.

4.1 Nano-spectroscopy and manipulation - I

4.1.1 Classical Microscopy: theoretical foundations

Collection of Light and Resolution Limit

Our experiments are performed using a back-scattering geometry, where the illumination of the sample and the collection of the scattered light is done by means of an objective attached to the inverted microscope system. In an inverted microscope scheme, the illumination of the sample and the collection of the scattered light is done in an opposite direction of most commonly found upright microscopes. The geometrical characteristics of light collection (as well as the illumination of the sample) is totally dependent on the objective's features, which are basically synthesized by its numerical aperture ($N.A.$). The $N.A.$ is defined as a measure of the solid angle (Ω) covered by the objective. As shown in Fig. 4.1(a), the region covered by the objective reflects a cone, and as shown in Fig. 4.1(b) the solid angle of a cone with apex of 2θ is given by

$$\Omega = 2\pi \left(1 - \cos\theta\right) . \tag{4.1}$$

Figure 4.1(a) shows that θ is also the half-angle of collection and, therefore, the $N.A.$ can be described as:

$$N.A. = n\mathrm{sen}\theta , \tag{4.2}$$

where n is the refractive index of the medium between the sample and the objective.

Using Eqs. 4.1 and 4.2 we obtain

$$\theta = \mathrm{sen}^{-1}\left(\frac{N.A.}{n}\right) \quad \text{and} \quad \Omega = 2\pi\left[1 - \cos\left[\mathrm{sen}^{-1}\left(\frac{N.A.}{n}\right)\right]\right] . \tag{4.3}$$

Commercial objective specifications

Usually the $N.A.$, as well as other objective's specifications are engraved on its barrel. Figure 4.2 brings a picture of a commercial objective and teaches us how to interpret the labels engraved on it. Most of the labels are clear enough, however some of them need to be clarified:

- **Specialized optical properties**: Microscope objectives often have design parameters that optimize performance under certain conditions. For example, there are special objectives designed for polarized illumination (signified by the abbreviations **P**, **Po**, **Pol**, or SF, and/or having all barrel engravings painted red), phase contrast (**PH**, and/or green barrel engravings), differential interference contrast (**DIC**), and many other abbreviations for additional applications.
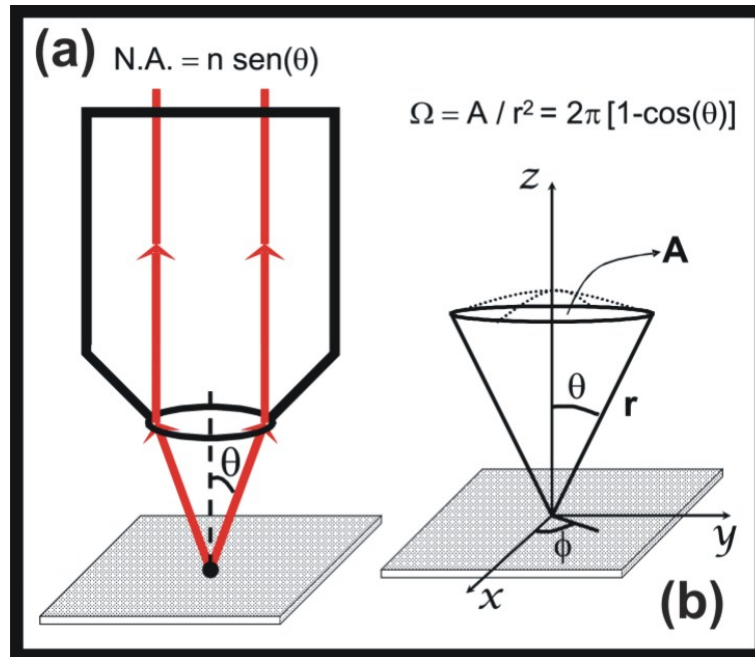
Figure 4.1: (a) The scheme of the objective's sample illumination and scattered light collection. (b) The geometric construction to obtain the cone's solid angle (Ω).

- **Color code**: Many microscope manufacturers label their objectives with color codes to help in rapid identification of the magnification. The dark blue color code on the objective illustrated in Fig. 4.2 indicates that the linear magnification is 60x. Table 4.1 shows a list of color codes and their respective meanings.

- **Working distance**: This is the distance between the objective front lens and the top of the cover glass when the specimen is in focus. In most instances, the working distance of an objective decreases as magnification increases.

- **Cover slip thickness**: Most transmitted light objectives are designed to image specimens that are covered by a cover slip. The thickness of these small glass plates are currently standardized at $0.17\,\text{mm}$ for most applications, although there is some variation in thickness within a batch of cover slips. The specification on the commercial objective gives the maximum cover slip thickness in which the objective will work adequately.

In our experiments we use two types of objectives: (1) an immersion oil Nikon objective flat field, aberration and infinity corrected with $60\,\text{x}$ magnification ($N.A. = 1.4$) and (2) an air Nikon objective flat field, aberration and infinity corrected with $60\,\text{x}$
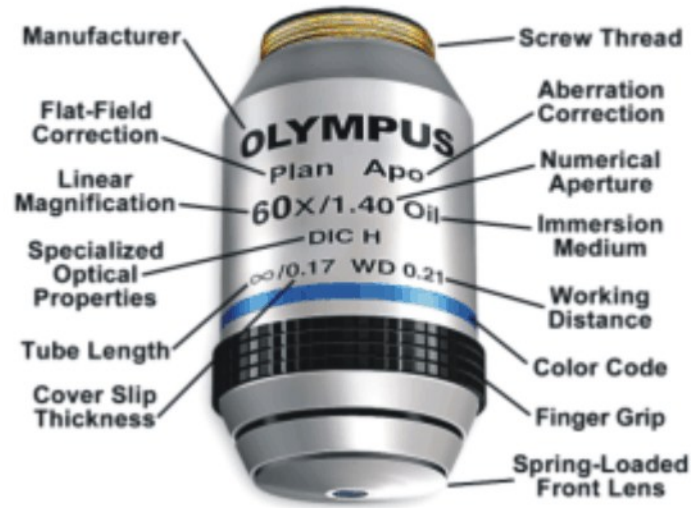
Objective Specifications

Figure 4.2: Specifications engraved on the barrel of a typical microscope objective. These include the manufacturer, correction levels, magnification, numerical aperture, immersion requirements, tube length, working distance, and specialized optical properties. [47]

magnification ($N.A. = 0.95$). Table 4.2 summarizes the $N.A.$, θ and Ω of both types of objectives. The immersion oil specifications we used were: non-drying immersion oil type DF manufactured by Cargille Laboratories, with diffraction index $n = (1.5150 \pm 0.0002)$.

Working principles of immersion oil objectives

When an object is illuminated in an optical microscope, some of this light passes through the object with no change in their optical paths. This is called undeviated light (See Fig. 4.3(b)). However, some of the light is deviated form its original path and is rendered 180° out of phase in comparison to the undeviated light (See Fig. 4.3(b)). This situation generates diffraction patterns which reflects the object characteristics. Figure 4.3(a) shows the diffraction pattern of an illuminated line grid. As seen, the central bright spot is the undeviated light contribution (0th order of diffraction) and the adjacent spots are the 1st and 2nd orders of diffraction (deviated light contribution). Obviously, all the captured diffraction orders form the diffraction pattern of the illuminated object. Microscope specimens can be considered as complex gratings with details and openings of various sizes. The details of a specimen will be resolved if the objective captures the 0th order of the light and at least the 1st order (or any two orders). Therefore, the greater the

47

Immersion color code	Immersion type
Black	Oil immersion
Orange	Glycerol immersion
White	Water immersion
Red	Special

Magnification color code	Magnification
Black	1 x, 1.25 x
Brown	2 x, 2.5 x
Red	4 x, 5 x
Yellow	10 x
Green	16 x, 20 x
Turquoise blue	25 x, 32 x
Light blue	40 x, 50 x
Cobalt (dark) blue	60 x, 63 x
White (cream)	100 x

Table 4.1: Color-Coded Rings on Microscope Objectives. [47]

Objective	$N.A.$	θ	Ω
Oil immersion 60 x	1.4	68.9	4.02
Air 60 x	0.95	71.8	4.32

Table 4.2: Numerical Aperture ($N.A.$) and calculated θ and Ω of the objectives used in our equipment.

number of diffracted orders that gain admittance to the objective, the more accurately the image will represent the original object.

The reader may ask now: Why do we use immersion oil objectives? If a medium of higher refractive index than air (such as immersion oil) is used in the space between the front lens of the objective and the top of the cover slip (see Fig. 4.3(c)), the angles of the diffracted orders are reduced and the diffracted pattern is compressed. As a result, an oil immersion objective can capture more diffracted orders and yield better specimen's image construction than a dry objective as shown in Fig. 4.3(d).

It is important to note that, once we have access to higher diffraction orders (by using immersion oil objectives as stated above) we still need to resolve the features among them, allowing for a good image resolution. The image resolution is limited by the spatial diffraction limit (Δx) that gives the minimum distance between two objects in which their features can still be unraveled. We observe that we are specially limited if the light is in
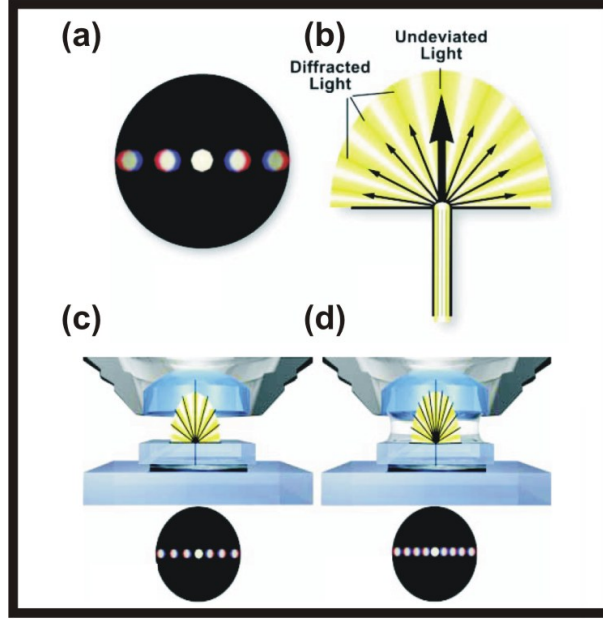
Figure 4.3: (a) Diffraction pattern of a illuminated line grid and (b) a illustration of the undeviated and deviated light after the object's illumination.(c) and (d) show the effect of imaging medium refractive index on diffracted orders captured by the objective. As one can see in (d), if a immersion oil with refractive index close to the coverslip's refractive index, more diffraction orders can be captured and a better resolution can be achieved. [47]

the blue region, whose diffraction angle is smaller than for green or red. This eventually causes the features (mainly those in the blue region) to overlap. As we see next, Δx relies on the objectives features and for most of standard optical microscopes is roughly given by the Abbe criterion [48]:

$$\Delta x = \frac{0.61\lambda}{N.A.}, \tag{4.4}$$

where λ is the wavelength of light. The maximum resolution that conventional microscopes can achieve is $\lambda/2 \geqslant 200\,\text{nm}$. An inspection of Eq. 4.4 shows that the higher the $N.A.$, the greater the spatial resolution. This is why the immersion oil objective we use has a high $N.A.$. With high $N.A.$ we are able to compensate the fact of having more diffraction lines(and consequently more overlapping) getting into the objective. All these strategies to improve the image's reconstruction are originated from the same practical fact: The knowledge of information, we currently possess, concerning how to improve image reconstruction stems from a well-know truth that conventional optical systems are not able to collect the whole spectrum of spatial frequencies associated with optical fields generated by a light source located in a distance sufficiently far from the detector (the

called far-field regime).
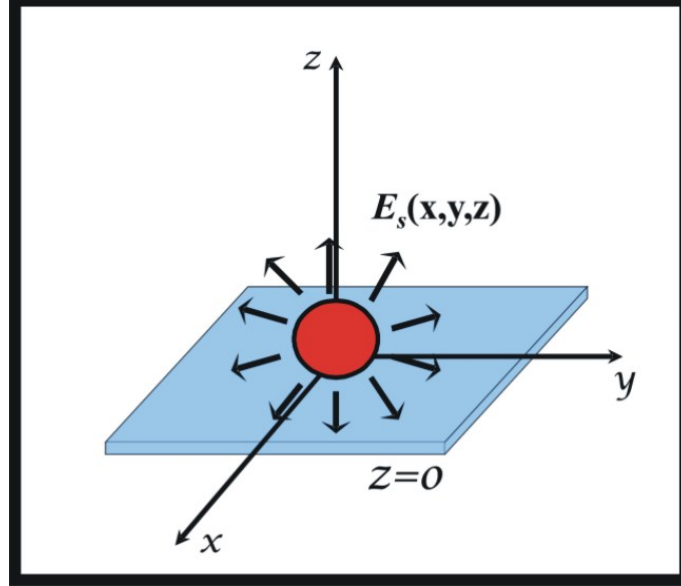
4.1.2 The Angular Spectrum Representation

Figure 4.4: The electric field E_s is evaluated in a plane z =const. transverse to an arbitrarily chosen z axis.

To clarify the statement above, let's consider an electric field $E_S(x, y, z)$ in the real space emitted by some material [located at $(x, y, z = 0)$] in an optical experiment. Considering that $E_S(x, y, z)$ is propagating in an arbitrary z direction, as shown in Fig.4.4, we can describe the electric field $E_S(k_x, k_y; z)$ in the wavevector space via Fourier transform:

$$E'_S(k_x, k_y; z) = \frac{1}{4\pi^2} \int\int_{-\infty}^{\infty} E_S(x, y, z) e^{i(k_x x + k_y y)} dx dy \,, \tag{4.5}$$

where k_x and k_y are the wavevectors related to the cartesian coordinates x and y. Analogously, we describe $E_S(x, y, z)$ according to:

$$E_S(x, y, z) = \frac{1}{4\pi^2} \int\int_{-\infty}^{\infty} E'_S(k_x, k_y; z) e^{-i(k_x x + k_y y)} dk_x dk_y \,. \tag{4.6}$$

Considering a homogeneous, isotropic, linear and source free medium, the Maxwell's equation must read:

$$\nabla \cdot \vec{E} = 0 \,, \nabla \cdot \vec{B} = 0 \,, \nabla \times \vec{E} = -\frac{\partial \vec{B}}{\partial t} \,, \nabla \times \vec{B} = \mu_\circ \varepsilon_\circ \frac{\partial \vec{E}}{\partial t} \,, \tag{4.7}$$

where $\mu_\circ$ and $\varepsilon_\circ$ are, respectively, the permeability and permittivity of vacuum. Using the vectorial identity $\vec{\nabla} \times \left(\vec{\nabla} \times \vec{A} \right) = \vec{\nabla} \left(\vec{\nabla} \vec{A} \right) - \nabla^2 \vec{A}$ and the Eqs. 4.7 we find the wave equations that rule the $\vec{E}$ and $\vec{B}$ dynamics,

$$\nabla^2 \vec{E} - \frac{1}{\mu_\circ \varepsilon_\circ} \frac{\partial^2 \vec{E}}{\partial t^2} = 0 \,, \nabla^2 \vec{B} - \frac{1}{\mu_\circ \varepsilon_\circ} \frac{\partial^2 \vec{B}}{\partial t^2} = 0 \,. \tag{4.8}$$

Supposing that the fields have a time dependence $e^{i\omega t}$, we obtain the Helmholtz equations for $\vec{E}$ and $\vec{B}$ which are:

$$(\nabla^2 + k^2)\vec{E} = 0 \,, (\nabla^2 + k^2)\vec{B} = 0 \,, \tag{4.9}$$

where $k = 2\pi n/\lambda$, λ is the electric field wavelength and n is refractive index of the medium. It is clear that the representation given by Eq. 4.6 must obey the Helmholtz equation. It follows that:

$$(\nabla^2 + k^2) \int \int_{-\infty}^{\infty} E'_S(k_x, k_y; z) e^{i(k_x x + k_y y)} dk_x dk_y = 0 \,, \tag{4.10}$$

which evolves to:

$$\left(\frac{\partial^2}{\partial z^2} + \left[k^2 - \left(k_x^2 + k_y^2 \right) \right] \right) E'_S(k_x, k_y; z) = 0 \,. \tag{4.11}$$

For a given initial condition, $E_S(x, y, 0)$, it follows that

$$E_S(x, y, z) = E_S(x, y, 0) e^{\mp i k_z z} \,, \tag{4.12}$$

where,

$$k_z = \sqrt{k^2 - (k_x^2 + k_y^2)} \,. \tag{4.13}$$

Observe that in order to ensure that the electric field will not diverge, the condition Im[k_z]≥ 0 must occur. Then $E_S(x, y, z)$ is written, for any arbitrary z as:

$$E_S(x, y, z) = \frac{1}{4\pi^2} \int \int_{-\infty}^{\infty} E_S(x, y, 0) e^{-i(k_x x + k_y y)} e^{-i k_z z} dx dy \,. \tag{4.14}$$

Let's define $k_{||} \equiv k_x^2 + k_y^2$. Then we have,

$$k_z = \sqrt{k^2 - (k_{||}^2)} \,. \tag{4.15}$$

The next step is to figure out how $e^{-i k_z z}$ rules the propagation of $E_S(x, y, z)$ in the z direction. See that if $k_{||} \leq 2\pi n/\lambda$, k_z is real and the electric field is propagating over the space, generating what is called far-field. On the other hand, if $k_{||} \geq 2\pi n/\lambda$, the electric

field is now evanescent and it decays exponentially generating what is called near-field. Those two conditions observed above tell us that if some detector is far enough from the source, it happens a loss of information since the near-field component is lost in the way. This, therefore, is the reason for the existence of the diffraction limit in standard optical experiments. Furthermore, we will show that by using a metallic tip, under certain conditions, it is possible to recover information coming from evanescent waves.

4.1.3 Confocal microscopy: the experimental setup

The system in our laboratory works like a Scanning Confocal Microscope (SCM). In this case, the interaction of the light with the object occurs in the following way: The light source is focused onto the object plane. Usually the object will be sitting on a cover slip sitting on a XY-stage which can move the object along the X and Y directions. After interacting to the sample, the light, containing information about the whole specimen, goes to the detector systems (whose details will be given further in the text). Figure 4.5 shows the scheme of a confocal microscope setup.

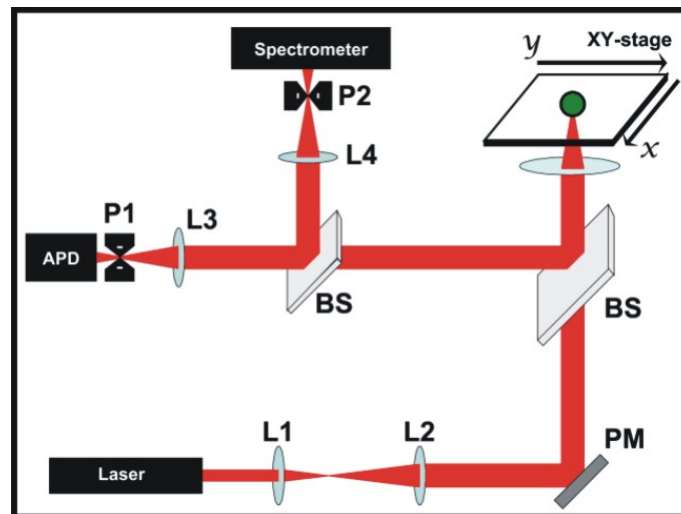**Figure 4.5**: Scheme of a confocal microscope setup. L stands for lens, PM stands for plane mirror, BS stands for beam-splitter and P stands for pinhole. The pinholes in front of the detectors are the key to successfully perform SCM.

In a conventional microscope we usually detect information coming from several points. By contrast, an object in a confocal scheme is irradiated in a point-wise fashion

and the physical interaction between the laser light and the object detail irradiated is measured point by point. To obtain information about the entire object, it is necessary to guide it across the laser beam, or to move the laser relative to the object (this is what the XY-stage does). Depending on the diameter of the pinhole, the light coming from object points outside the focal plane is obstructed and thus excluded from detection. As the laser beam is focused to a diffraction-limited spot, which illuminates only a small portion of the focal plane at a time, the point illuminated and the point observed (i.e. image and object points) are situated in conjugate planes which means that they are focused onto each other. This is what is called a confocal beam path (see Fig. 4.5). By varying the pinhole diameter, the degree of confocality can be adapted to practical requirements, and with the aperture fully open, the image is nonconfocal.

It is fundamental to comment that the laser beam has to be expanded to achieve full convergence of the objective lens just before reaching the objective in order to achieve a diameter compatible with the objective's $N.A.$ (compatible with the area in the rear part of the objective). To make the expansion, one needs to combine two lenses with different focal distances. The first lens in the optical path should have the smaller focal distance (see the two lenses just after the laser-source in Fig. 4.5). In order to achieve a good combination of lenses, which do not need large optical paths, the first lens should have a focal distance of 30 mm and the second one should have a focal distance of 80 mm. This gives an expansion factor of 3 times and for lasers whose the beam diameter is about 1 mm this expansion fulfill the requirements to cover the whole rear entrance area of a objective with $N.A. = 1.4$.

The system in our laboratory uses the inverted microscope ECLIPSE-Ti-U, manufactured by Nikon which has attached to its body a 60× air/immersion oil objectives (for details see the subsection 4.1.1). The laser is a cylindrical He-Ne (HRP120) which emits at 632.8 nm manufactured by Thorlabs. The laser beam output power is 12 mW. After the laser output exit we use an interference filter centered at (633±1 nm) blocking most of plasm frequencies and allowing a very monochromatic light to reach the microscope.

Inside the microscope we use a dichroic beam-splitter manufactured by the Semrock optics (The beam-splitter reflectance and transmittance must be chosen according to the users needs). Our microscope counts with a specially designed stainless steel base that holds the XY-stage (and also the AFM scan-head, as explained further in the text). It is a home-made piece that is coupled to the microscope body. Figure 4.6 shows a technical drawing of the base, highlighting its fundamental aspects.
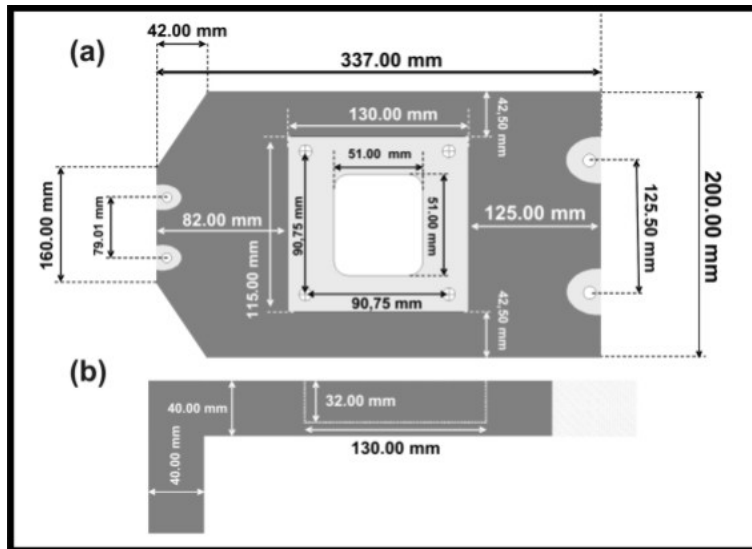
Figure 4.6: Technical drawing of the microscope plate. (a) The microscope plate's top view and (b) the microscope plate's side view.

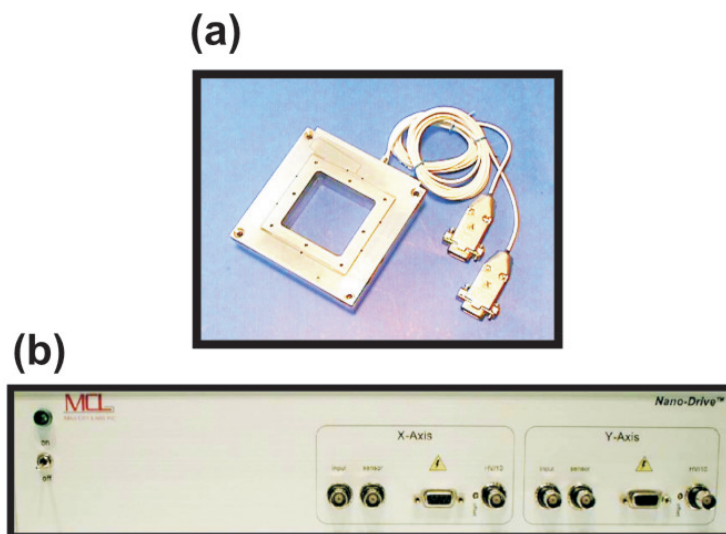## The XY-stage system

Figure 4.7: (a) The Nano-H50 nanopositioning stage and (b) the Nano-Drive^{TM} that is required for operating the Nano-H50 nanopositioning.

Our system uses a XY-stage device manufactured by Mad City Labs, Inc. This XY-

stage system is composed of a Nano-H50, which is a piezoelectric (PZT) actuated linear nanopositioning stage (see Fig. 4.7), and a Nano-Drive$^{\text{TM}}$, which is the complete control package required for operating all Mad City Labs, Inc. nanopositioning systems (see Fig. 4.7). The Nano-H50 comes complete with position sensitive detectors for closed loop operation. The Nano-H50 is a nanopositioning stage of exceptional resolution and stability. Table 4.3 summarizes its technical characteristics. The Nano-H50 is manufactured from a high performance Al alloy.

As shown in Fig. 4.8, PZT actuators are preloaded within the Nano-H50 and supply the driving force for stage movement. The flexure hinges, which form the guidance mechanism, are cut into the stage using electric discharge machining (EDM). EDM is also used to form an integrated amplifier that increases the range of motion of the PZT actuators. The PZT actuators are oriented perpendicular to the stage motion direction and within the amplifier.

Two single axis stages are stacked with an adapter plate to form the Nano-H50. The bottom stage (y-axis) has a lower resonant frequency than the top stage (x-axis) due to the mass of the top stage. A stage direction arrow is located on the side of each axis. This arrow indicates which direction the stage moves when a positive voltage is applied. Two DB-9 connectors are labeled X or Y for identification (see Fig. 4.7(a)). This identification describes which driver axis that particular stage should be connected to (see Fig. 4.7(b)).

Specifications	Closed Loop
Translation (μm) (XY)	50$\pm$10%
Voltage Range (V)	-5 V to +150 V
Resonant Frequency Unloaded X-Axis (Hz)	500$\pm$20%
Resonant Frequency Unloaded Y-Axis (Hz)	250$\pm$20%
Stiffness (N/μm)	0.8$\pm$20%
Maximum load (hor/vert) (kg)	1/0.25
Inplane Tilt (μrad)	15 (TYP)
Mass (g)	700
Cable length (ft)	6
Cable connection	DB-9

Table 4.3: Nano-H50 nanopositioning specifications.

The Nano-Drive$^{\text{TM}}$ includes a low noise, low drift 150 V driver, position sensing electronics, and closed loop proportional-integral feedback control. The driver is capable
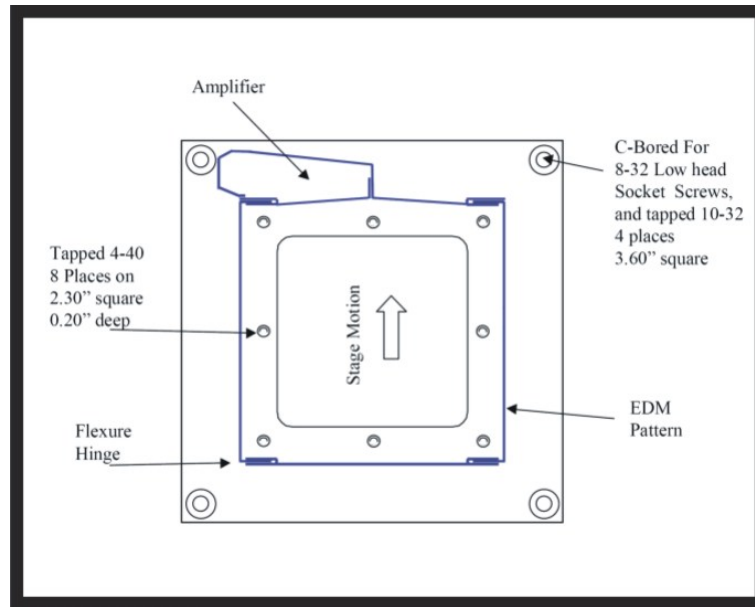
Figure 4.8: The Nano-H50 schematics.

of supplying $150\,\mathrm{mA}$ at $150\,\mathrm{V}$. The Nano-Drive$^{\mathrm{TM}}$ has been factory adjusted for its complementary nanopositioning device (the Nano-H50). This adjustment includes setting the gain (not user accessible), bandwidth, and offset of the position sensing electronics. Note that the command signal (cmd) is used to control the displacement of the nanopositioning device. The Bayonet Nut Connector (BNC) input signal in the front panel of the Nano-Drive$^{\mathrm{TM}}$ will receive a signal coming from the RHK system (the RHK will be discussed further in the text). Table 4.4 summarizes its technical details.

4.1.4 The detection systems

The Avalanche Photodiode - APD

In general, the Avalanche Photodiode Device (APD) works as follows (see Fig. 4.9). A photocathode captures photons and emits a photoelectron into the APD cavity. In general (and this applies to our APD device), the photocathode is a silicon photodiode which has its efficiency mostly defined by the silicon's work function. The generated photoelectron is a result of the photoelectric effect. After leaving the photocathode area, the photoelectron reaches a series of dynodes (with each dynode experiencing a potential higher than its predecessor) which, by means of the impact ionization effect, generates several others photoelectrons and therefore amplifies the signal. This impact ionization

Function	Specifications
Output Voltage Range	-5 to 150 V
Output Current	150 mA
Analog Interface (Input BNC)	-10.0 to +10.0 V
Connector Type	DB-9
Power Requirement	90-260 VAC
Digital Interface (OPTION)	USB 16 or 20 Bit
Other Accessible Signals (ISS Option)	TTL(4)
Front Panel Accessible Output Signals	
Output Voltage ÷ 10 (HV/10)	-0.5 to 15.0 V
Position Sensor Signal	0.0 to 10.0 V
Front Panel Adjustments	
(Standard)	Sensor Offset
(SO Option)	Scan Offset
(OCL Option)	Open/Closed Loop

Table 4.4: Nano-Driver$^{\text{TM}}$ specifications.

effect is a result of a secondary emission where an electron (or the photoelectron) has enough energy to strip electrons of the dynode. After the last dynode, the amplified photocurrent is captured by an anode and then converted to a Transistor-Transistor Logic (TTL)-pulse. The dynode is so named because it acts as a middle point between the (photo)cathode and the anode. It is an electrode made of a polished metal.

Our APD device is a SPCM-AQRH-14 manufactured by PerkinElmer$^{\circledR}$. This APD is a self-contained module that detects single photons of light over the 400 nm to 1060 nm wavelength range. Although it works similarly to a photomultiplier, it presents a range and sensitivity that often outperforms the later. It has a circular active area that achieves a peak photon detection efficiency of more than 65% at 650 nm over a 180 μm diameter. The photodiode is both thermoelectrically cooled and temperature controlled, ensuring stabilized performance despite ambient temperature changes. As each photon is detected, a TTL pulse of 2.5 Volts (minimum) high in a 50 load and 15 ns wide is output at the rear BNC connector. The signal delivered by this BNC output is processed by the RHK controller (see its description further in the text). The APD device needs a power supply of 5 V. Table 4.5 summarizes some of its technical information.

The APD will receive any signal coming from the microscope, which is a result of the interaction between the light and the sample. In order to map some desired range of wavelengths (or, equivalently, frequencies) the user has to introduce a set of band-pass or
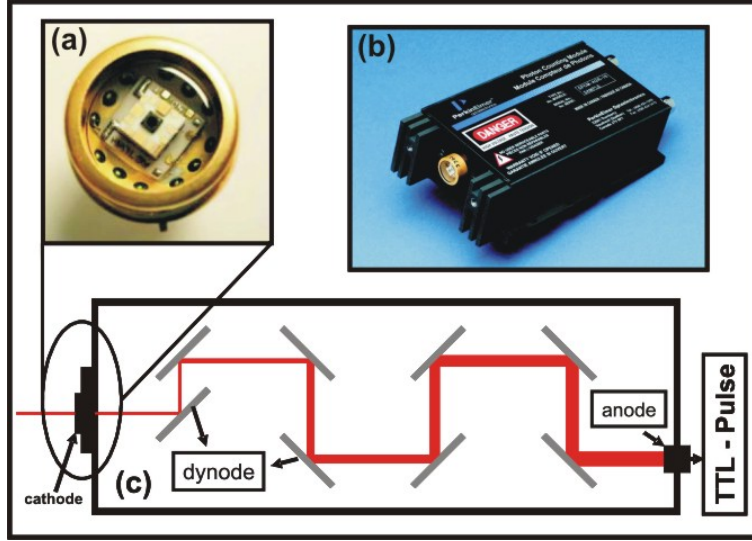
Figure 4.9: Scheme of a Avalanche Photodiode Device (APD). Our APD is the SPCM-AQRH-14 manufactured by PerkinElmer®. (a) A zoom of the APD's electrodiode. (b) An overview of SPMC-AQRH-14 device. (c) A schematics of the photoavalanche process. A photon reaches the photocathode which generates a photoelectron. Next, each photoelectron reaches a series of dynodes, generating other electrons. At the end, the amplified signal reaches an anode and the photocurrent is converted into a TTL-pulse.

Parameter	Min.	Typical	Max.	Unit
Supply current		0.3	1.2	A
Supply voltage	4.75	5	5.25	V
Case operating temperature	5		40	°C
Active area (diameter) at minimum Pd	170	180		μm
Photon detection efficiency (Pd) at:				
400 nm	2	5		%
650 nm	50	65		%
830 nm	35	45		%
1060 nm	1	2		%
Dark Count			100	counts/s
Single photon timing resolution				ps
Output pulse width			15	ns

Table 4.5: SPCM-AQRH-14 specifications.

long-pass filters. Note that, when performing Raman or photoluminescence experiments, it is always interesting to set a long-pass filter centered at the laser's excitation wavelength because the Rayleigh contributions are all suppressed (reminding that the Rayleigh signal is much stronger than Raman or photoluminescence signals). Table 4.6 summarizes

the appropriated filters to perform Raman and photoluminescence of carbon nanotubes excited at 632.8 nm. According to our experiences the filters manufactured by Semrock are the best of both worlds, being economical and of high quality.

Type	Centered at	FWHM	Spectral region
Band-pass	640 nm	10	RBM stokes
Band-pass	690 nm	10	D-band stokes
Band-pass	700 nm	10	G-band stokes
Band-pass	760 nm	10	G'-band stokes
Long-pass	830 nm		Photoluminescence[a]

Table 4.6: Appropriated filters to perform Raman and photoluminescence of carbon nanotubes excited at 632.8 nm

[a]In this case all luminescence signal from all type of tube will be collected. If The user desires to see a contribution from a specific specie, this filter can be replaced by an appropriated band-pass.

The Coupled Charged Device - CCD and the spectrometer

Besides the APD device, our system also counts with a spectrometer with a Coupled Charged Device - CCD connected to it. The spectrometer is a Shamrock sr-303i manufactured by Andor^{TM} Technology and the CCD is a iDus DU401A-BR-DD also manufactured by Andor^{TM} Technology. Figure 4.10 (a) shows the system as a whole and (b) shows the Shamrock sr-303i's scheme. Light enters the spectrometer cavity and is reflected by the plane mirror (PM1) and into the spherical mirror (SM1). Next, the reflected light reaches the diffraction grating (Grs) being dispersed into its wavelength components. By a convenient Grs position (chosen from the software provided by Andor^{TM} Technology), the user can select each wavelength range of the dispersed light that will be reflected by the spherical mirror SM2. After the reflection, the chosen portion of the reflected light is focused into the CCD silicon photodiode. The signal acquired by the CCD is further converted into digital signal and interpreted by the system's software.

The Shamrock sr-303i is equipped with a triple grating turret which can be easily and speedily removed, and replaced by an alternative turret with new gratings. This design means that only a simple offset command is required to change between the gratings at the turret.

Our spectrometer works with 3 diffraction gratings providing different spectral res-
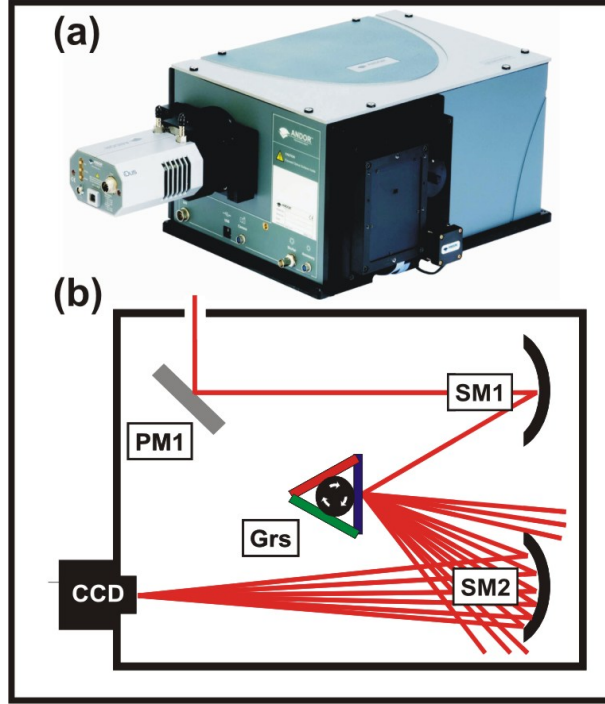
Figure 4.10: (a) The iDus DU401A-BR-DD CCD attached to the Shamrock sr-303i spectrometer. (b) The Shamrock sr-303i scheme. This spectrometer has three different diffraction gratings which can be chosen by rotating the GRs triple-turret support.

olutions. Table 4.7 summarizes some information about the gratings. It is a spectrometer with a focal Length of 303 mm, wavelength resolution of 0.1 nm ($<$0.2 nm with 26 μm pixel CCD detector) and an accuracy of $\pm$0.2 nm. The iDus DU401A-BR-DD ccontains pixels with dimensions 26$\times$26 μm arranged in a array of 1024$\times$128 pixels. Its image area is 26.6$\times$3.3 mm^2. It has a thermoelectric cooling device to -75C (it is a cooler installed inside the CCD box), enabling negligible dark current.

Lines/mm	Blazed (nm)	Recom. Spec. Region (nm)	Peak Efficiency
600	500	330-900	72
1200	1000	600-1400	69
2400	Holographic	190-800	68

Table 4.7: Technical information of the three gratings in our system's spectrometer.

4.2   Nano-spectroscopy and manipulation - II

In the last section we reviewed some basic concepts of classical optics, for instance, spatial resolution and discussed the division of the light into propagating and evanescent waves. It was also discussed the principles of confocal spectroscopy as well as the experimental instrumentation needed to perform it. In this section we will discuss the instrumentation needed to perform, simultaneously, nano-manipulation and nano-spectroscopy, i.e. how to go beyond the classical diffraction limits. Basically, we have an Atomic Force Microscope (AFM) system combined with a confocal microscopy system. If the user is utilizing a metallic tip, as will be shown, then it is possible to recover the information contained in the evanescent waves and make the optical resolution reach nanometric scale. The tip also can be used for nano-manipulation, e.g. cut of tubes, twist of tubes and bend of tube and simultaneous spectroscopy measurements.

4.2.1   The scanning probe microscope control - RHK

The RHK scanning probe microscope control is, in fact, the main nucleus of the system as a whole. It is responsible for sending voltages to the XY-stage system, interpreting signals coming from the APD, receiving signals coming from the easy-PLL (the easy-PLL will be explained in the next section) and running the feedback-loop mechanism, which is essential in systems working with scanning probe techniques. Figure 4.11(a) shows the RHK front panel and (b) shows the RHK rear panel.

I will restrict this discussion to what is strictly necessary to make the RHK work as an atomic force microscope (AFM). Let us have a look at Fig. 4.11(a)[1]. The RHK generates or processes voltages to control the X,Y and Z directions of a device and this is done with the help of a software dedicated to assisting the RHK (the XPMPro$^{\text{TM}}$).

The RHK can provide offset voltages ($V_{off.}$) or scan voltages ($V_{scn.}$). The $V_{off.}$ and the $V_{scn.}$ are electrically summed to each other. This means that if $V_{off.}$ is set zero, $V_{scn.}$ can sweep $\pm130\,\text{V}$ (yielding a total range of $260\,\text{V}$)[2]. On the other hand, if $V_{off.}$ is set $120\,\text{V}$, the $V_{scn.}$ can sweep just $\pm10\,\text{V}$. The X and Y voltages operate independently of the feedback-loop, which controls the distance between the tip and the sample and prevents from tip-crashing (the feedback loop will be better explained elsewhere). The Z voltages operate in connection to the feedback loop.

---

[1]From now on, I will direct the discussion to explain how the RHK is used to head our system's configuration. To other applications, the user must read its manual.

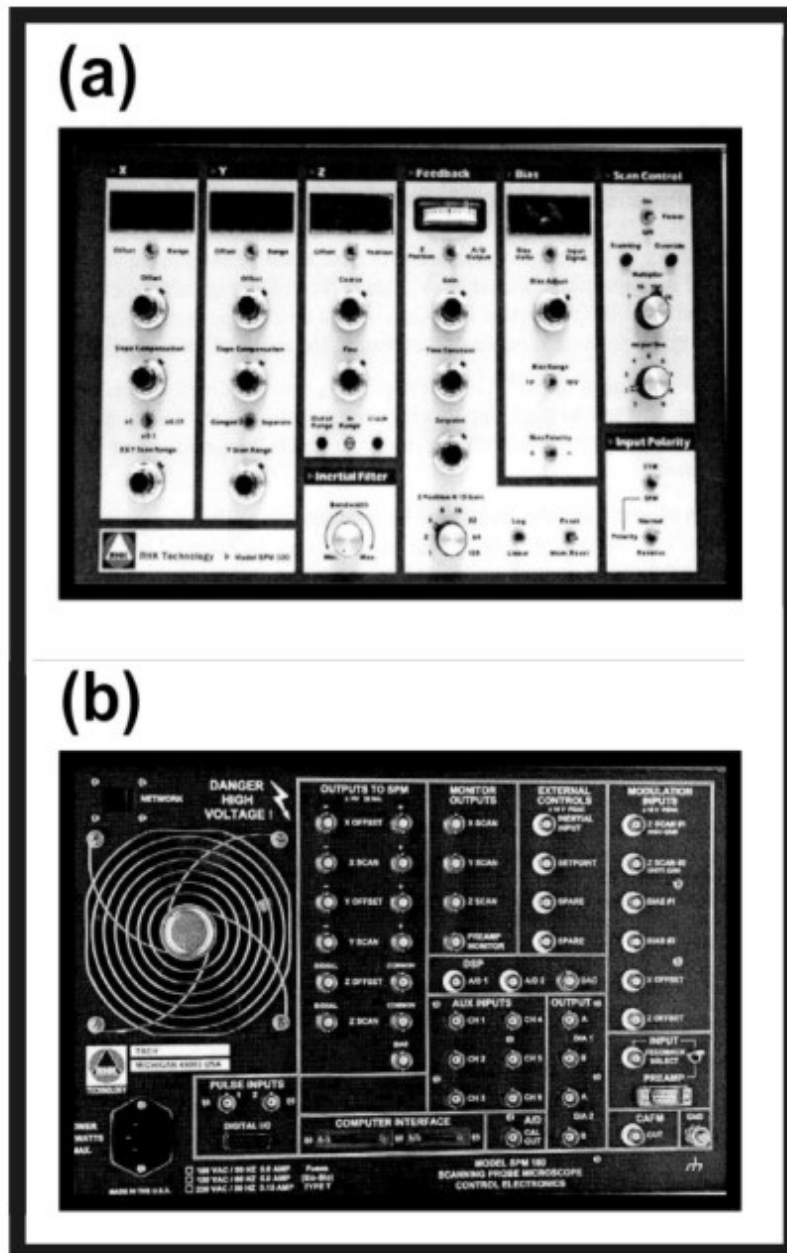[2]Considering that the RHK is being suppied with $130\,\text{V}$.

Figure 4.11: (a) The RHK's front panel and (b) the RHK's rear panel.

The Bayonet Nut Connector (BNC) outputs of the column "OUTPUT TO SPM" (see Fig. 4.11(b)) outputs offset and scan voltages to the scan-head's piezos. The BNC outputs of the column "MONITOR OUTPUTS" (see Fig. 4.11(b)) are responsible to output scanned voltages to the Nano-Drive™ and consequently to the Nano-H50 positioning. *It is important to comment that no scan-head configuration will need to use all the BNCs*

outputs! As to be explained in Section 4.2.2, we have two piezos connected to each other: one responsible for the positioning of the X and Y directions and another responsible for the positioning of the Z direction. In our scan-head's configuration the XY-piezos will receive only $V_{off.}$ from the X and Y "+ and -" offsets outputs located at the column "OUTPUTS TO SPM". The Z piezo will receive a mixing of $V_{off.}$ and $V_{scn.}$ from the "signal and common" BNC outputs[3].

The X and Y $V_{off.}$ are selected through the X and Y potentiometers[4] located at the RHK's front panel (see Fig. 4.11(a)). These values can be monitored through the digital volt meters (DVMs) with the DMVs selectors in the offset position (the DVMs will display the $V_{scn.}$ if the selectors are in the range position). The Z $V_{off.}$ can be coarsely applied by means of the "coarse" potentiometer and softly adjusted with the "fine" potentiometer. The DVM selector in the offset position will make the DVM display the offset voltages (if the selector is set to the range position, the DVM will display the piezo's voltage relative to the feedback dynamical range). Figures 4.12(a) and (b) show how to connect the signals from the RHK to the scan-head's piezos. In the halfway point from the RHK to the piezos, the X and Y offset voltages undergo a low-pass filter whose cutoff frequency is 30.3 kHz. This filter is essential because it prevents noise (in the tuning-fork resonance frequency range) from reaching the piezos and consequently supply the system with noise frequencies. The Z signal undergoes a notch-filter centered at 32.7 kHz, which is the tuning-fork's natural resonance frequency. The Z common must be grounded in the scan head. The connections to the XY-piezo are more elaborate because, for each direction, the piezo's walls should experience opposite voltages in order to properly expand or retract in the X and Y directions (or combined X and Y positioning).

The "X SCAN" and "Y SCAN" BNC outputs of the column "MONITOR OUT-PUTS" (see Fig. 4.11(b)) supply scan voltages to the Nano-Drive™ and consequently to the nano-H50 positioning. Figure 4.14 shows how to connect the RHK outputs to the Nano-Drive™'s inputs. These outputs supply ± 130 V to the Nano-Drive™ inputs resulting in a 260 V piezos swing in the X and Y direction[5].

The area swept by the stage is set by the potentiometer "X&Y Scan Range" (see

---

[3]The Z $V_{scn.}$ is related to the feedback loop control and the Z $V_{off.}$ is used to garantee that the Z voltage will be inside the feedback voltage range. Note that the $V_{off.}$ is independent of the feedback loop control.

[4]When the potentiometer is in the position 5 no $V_{off.}$ is apllied. If it is in the position 10 a $V_{off.}$=130 V is applied while in the position 0 a $V_{off.}$=-130 V is applied.

[5]The probe in our system's configuration stay stopped while the sample moves in accordance to the XY-stage movement.
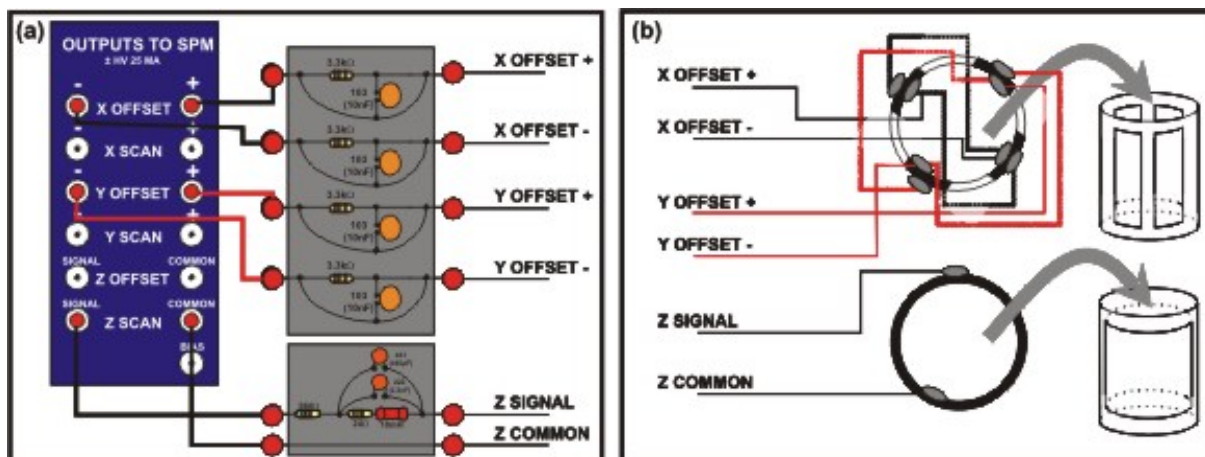
Figure 4.12: (a) The X and Y V_{off} leave the RHK BNC outputs and undergo a low-pass filter while the Z signal voltage undergoes a notch-filter centered at 32.7 kHz which is the tuning-fork's natural resonance frequency. Afterwards each signal is carefully directed to a specific XY- and Z- piezos sections, as diagramed in (b). All the filters circuit are diagramed as they are in our system. The values are also the ones we use.

Fig. 4.11(a)). When the knob is set to 0, no voltages are being applied while in the position 10 the maximum voltage range of 260 V is being applied. The selector sweeping from 1 to 0.01 gives the maximum voltage ranges. If the selector "Ganged/Separate" is set to Ganged, the x and y directions will be equally dimensioned and only squared areas will be swept. If the selector is set to Separate, rectangular areas can be swept and in this case the potentiometer "X&Y Scan Range" navigates the x direction and the potentiometer "Y Scan Range" navigates the y direction. The conversion from voltages to angstroms is performed by the software XPMPro™. Figure 4.13 shows how to connect the RHK to a computer.

When the XPMPro™ is activated the voltage to angstroms conversion factor must be set in the "configure hardware" option. Figure 4.15(a) works as a guide for the reader. The X and Y conversion factors are usually set by taking the general specifications of the XY-stage[6]. The Z scan conversion factor is usually set after scanning a standard grating which gives the height calibration of the system. Another possibility is to write a .prm file including information concerning conversion factors, feedback loop configurations etc. The "X&Y Scan Range" potentiometer sets the maximum voltage range and consequently the maximum scan area. However, by means of the XPMpro™ software we can define

---

[6]The Nano-Drive™ can sweep a maximum range of $50 \times 50\,\mu$m and receive an maximum input voltage range of 155 V. For safety reasons, the "X&Y Scan Range" is set to 4.5 and the RHK applies a voltage range of 117 V. Therefore, the conversion factor is $45\,\mu$m/117 V=0.385 nm
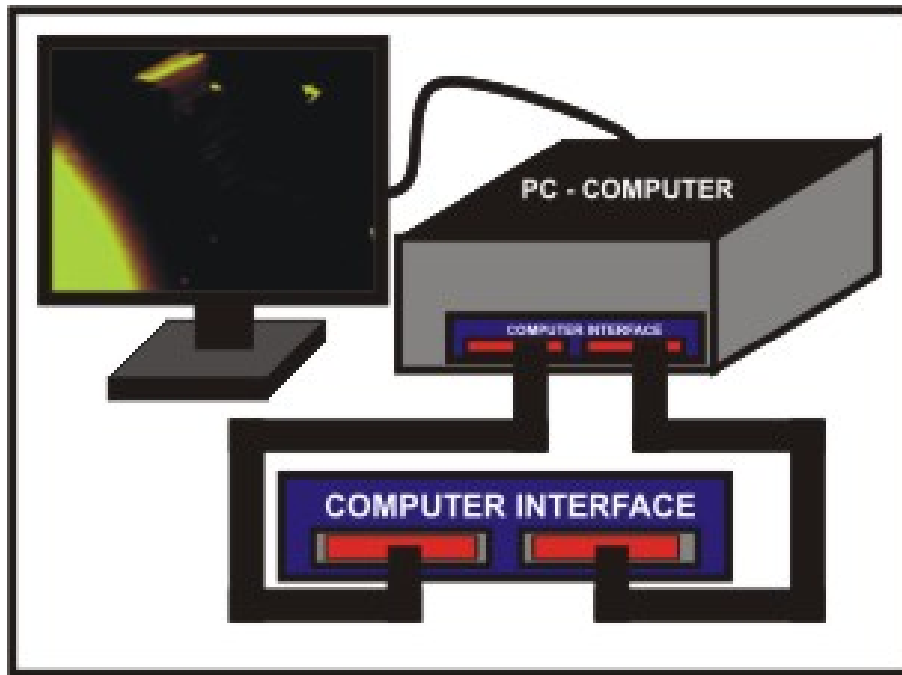
Figure 4.13: The computer and the RHK system are connected through the computer interface terminals. The cables are supplied by the RHK company.

smaller scan areas applying offset voltages (using the commands in the scan-area window) which gives a new dimension to the area that should be scanned. This can be seen in Figure 4.15(b). In the right panel, the red square represents the maximum scan area set by the "X&Y Scan Range" potentiometer and the yellow square represents the resized area. It is important to note that giving additional offset voltages, the resized area can be placed anywhere inside the red square.

The Z voltages are feedback-loop dependent. When the RHK system is used in the AFM mode, the "STM/SPM" input selector must be in the SPM position (the position STM is used in the case that the RHK system is doing scanning tunneling microscopy). The "normal/reverse" polarity selector must be set to normal because the feedback signal is larger when the tip/sample interaction is present. In this configuration, with no tip/sample interaction, when the analog meter needle is fully to the left, it means that the Z piezo is fully extended and if the needle is fully to the right it means that the Z piezo is fully retracted[7]. In AFM systems, a tip sweeps a determined area while map-

---

[7]If the selector Z Position/A/D output is in the Z Position, the analog meter is measuring the feedback voltage range. While the voltages in the feedback mechanism are in the range, a green led remains lightning. If the voltages are out of the feedback range, the red leds "out of range" or "crash" will be lightning.
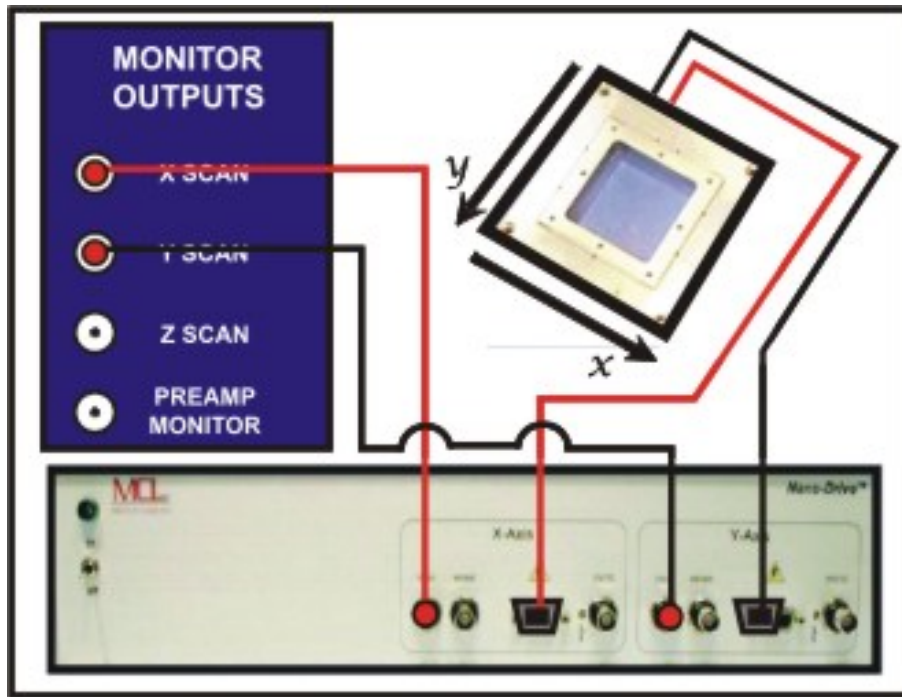
Figure 4.14: Connections from the RHK's outputs to the Nano-Drive$^{\text{TM}}$ voltages inputs. The Nano-Drive$^{\text{TM}}$ and the Nano-H50 positioning are connected by means of DB-9 plugs.

ping its surface. This tip is attached to the Z piezo that is responsible for controlling the tip height while scanning the surface ground. During this process, it is important to prevent the tip from crashing into the surface. This is done by means of a setpoint and a feedback-loop scheme. The setpoint value is responsible to determine the intensity of the interaction between the tip and the sample's surface. In our case, the setpoint value will inform how close to the sample surface the tip is positioned. To guarantee that the tip/surface interaction will always be the one established by the setpoint, the AFM system counts with a feedback mechanism which receives voltage signals which results from the tip/sample interactions and interprets if this signal is higher or lower than the setpoint value. Next, the feedback sends to the Z piezo a voltage that will retract or expand the piezo adjusting tip/sample interaction to the setpoint value. As mentioned in Section 4.2.4 the tuning-fork's resonance frequency is monitored by the Easy-Pll and each time that the tuning-fork experiences changes in its resonance frequency (due to different interactions strengths), the Easy-PLL converts this frequency change into voltage signals. Afterwards, this voltage signal goes to the RHK. The RHK sends the voltage signal to the Z piezo and then it brings the tip/sample interaction back to the setpoint value. Figure 4.16 shows how to connect the Easy-PLL output signal to the RHK's preamplifier
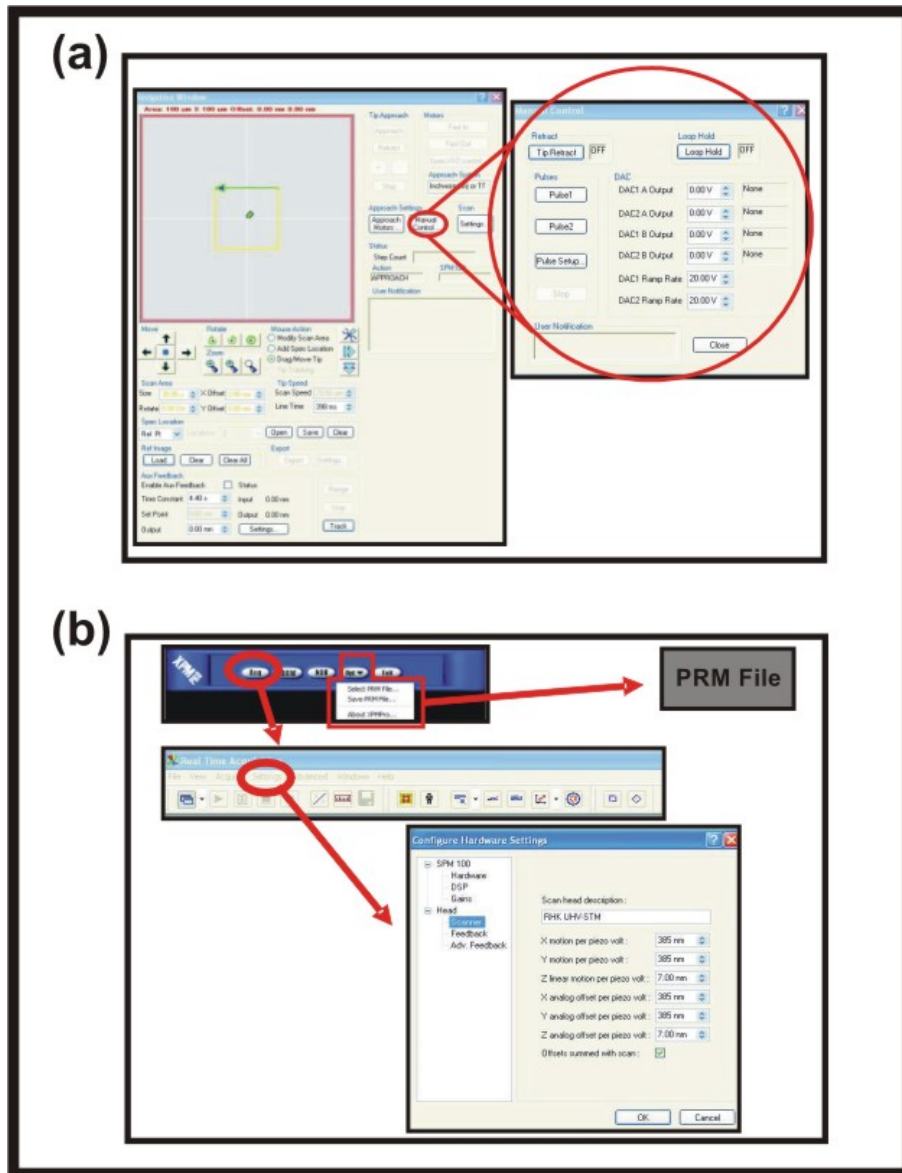
Figure 4.15: (a) Diagram showing the maximum area set by the RHK (red square) and the resized area (yellow square). Below are the scan-area window commands used to resize scan areas. (b) Diagram showing how to set the X,Y and Z conversion factors.

input.

Looking at the column "FeedBack" of the RHK's front panel (see Fig. 4.11(a)), the potentiometer "setpoint" sets the setpoint value of the experiment. The potentiometer set to the position 5 symbolizes that there are no setpoint voltages. In the position 10 a setpoint of 1 V is set. Finally, in the position 0 a setpoint of -1 V is set. The potentiometer "Gain" assumes any value between 0 (with the potentiometer in the position 0) and 2
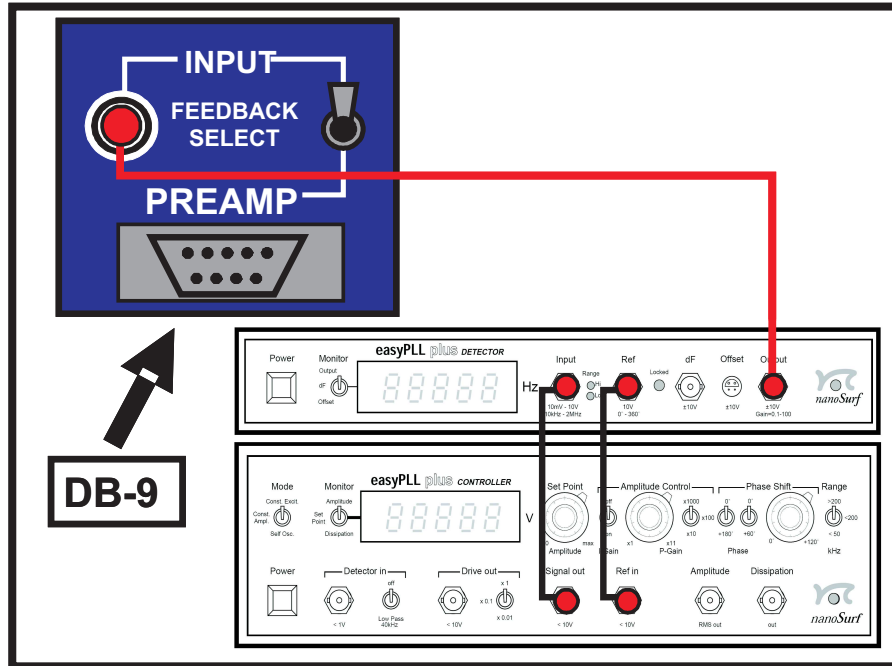
Figure 4.16: Diagram showing how to connect the Easy-PLL output signal to the RHK's preamplifier input. The selector must be set to the BNC terminal once the information is being carried by BNC cables.

(with the potentiometer in the position 10). It is a parameter which determines how fast the feedback mechanism will respond to some interaction between the tip and sample space (how fast the feedback mechanism will retract or extend the Z piezo).

The "Time Constant" potentiometer is related to the integral gain. The integral gain works to eliminate errors accumulated due to the use of the gain. It varies from 0 (with the potentiometer in the position 0) to 20 ms (with the potentiometer in the position 10).

The "Z position A/D" potentiometer is used to increase the resolution of the Z piezo. The A/D converter in the XPMpro™ has resolution of 16 bits. This means that if the range which the AFM system can cover in the Z axis is 500 nm and the A/D potentiometer is in the position 1, the Z piezo will translate about 12.7 nm/bit. If its set to 128 the Z piezo will translate 0.1 nm/bit. When the A/D potentiometer is not in the position 1, the selector "Z position/A/D output" must be in the position "A/D output" because now the range that should be monitored is the A/D converter range and not the feedback loop range[8]. The selector "reset/mom. reset" set in the position "reset" will

---

[8]Looking at the analog meter measuring the A/D converter range, if the needle is fully to the left or

reset the feedback circuit and let it switch off. When performing experiments, position the selector halfway! This ensures that the feedback mechanism works properly. Finally, the "Log/linear" selector must be in the linear position (the Log position is used in the STM mode because the tunneling currents are exponential as well as to linearize the values of the equation which the Log operation is being applied).

The APD's TTL digital pulses are also interpreted by the RHK system. As showed in Figure 4.17, the APD's output signals must be sent to the "PULSE INPUTS" BNC inputs in the RHK rear panel (see Fig. 4.11(b)). The I/O 15 pin connector is available to synchronize the scanning with some external equipment. It is used, for example, to synchronize the spectrometer and the scanning in order to form spectroscopic images.

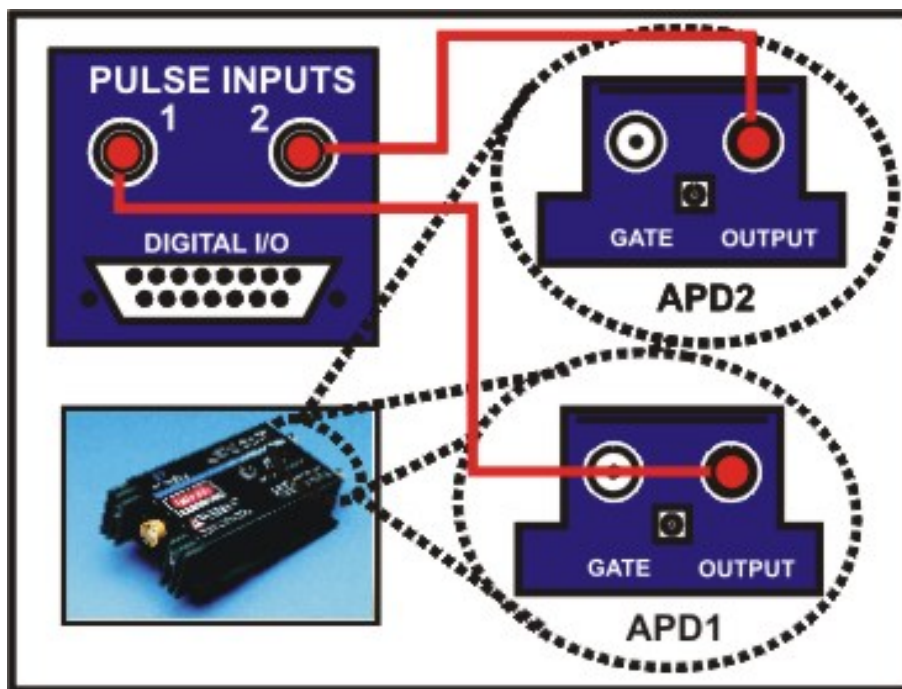**Figure 4.17**: Diagram showing how to connect the APD devices to the RHK pulse inputs. The I/O 15 pin connector is used to synchronize the scanning with external equipment.

4.2.2 The scan-head configuration

The AFM scan-head used in our system's configuration is home-made and specially

---

to the right we lose the A/D conversion information although the piezo voltages are still in the feedback loop range!

designed to perfectly couple the AFM system to the confocal spectroscopy system. In this section, I will try to describe, in detail, how to construct a similar system, in order to make the reader comfortable enough to build their own system scan-head. I will separate the text in parts that will represent the steps needed in order to build the head.

First step: the scan-head base

The first step is building the scan-head's base. The base must be built with stainless steel and must be very carefully machined to guarantee the smoothness of the piece. Figure 4.18(b) shows a technical drawing of the scan-head base and gives the dimensions needed to build it.

Once the base is ready, we must install the picomotor and the height-adjustable screws. As shown in Fig. 4.18(a), the picomotor will be installed in the hole on the top of the scan-head while the height-adjustable screws will be installed in the holes at the bottom of the head. The picomotor must be smooth enough to allow for very precise positioning while allowing the user to leave a certain position for a period of time and return to same initial position. The picomotor is an essential component because in our scan-head design, the tip-approach mechanism is composed of two steps:

1. A coarse approach is performed by the picomotor. This is done by means of a TTL/Analog picomotor driver which is connected to the XPMpro$^{\text{TM}}$ software. With the software, the user can set how many steps per cycle the picomotor will bring the head down. The computer sends a TTL pulse to the picomotor driver circuit which is interpreted and transformed into mechanical motion.

2. A fine approach is done by the Z piezo component. For each picomotor cycle, the Z piezo is fully extended to try to find the setpoint. If it does not find the setpoint, the picomotor goes another cycle again, fully extending the Z piezo. This procedure repeats until the approach is done.

Our system's pico-motor is the Model ♯8302 manufactured by New Focus$^{\text{TM}}$. Its minimum incremental motion is $<30\,\text{nm}$ with a maximum angular resolution of $<0.6\,\text{mrad}$. The maximum frequency drive allowed is $2\,\text{kHz}$ and its total screw range is $50.8\,\text{mm}$. The height-adjustable screws are essential in order to align the head as close as possible to the microscope base. Our system's height-adjustable screws are the Model ♯9303 manufactured by New Focus$^{\text{TM}}$. Its tip style is spherical (ball) and has 80 threads/inch with a total screw range of $50.8\,\text{mm}$.
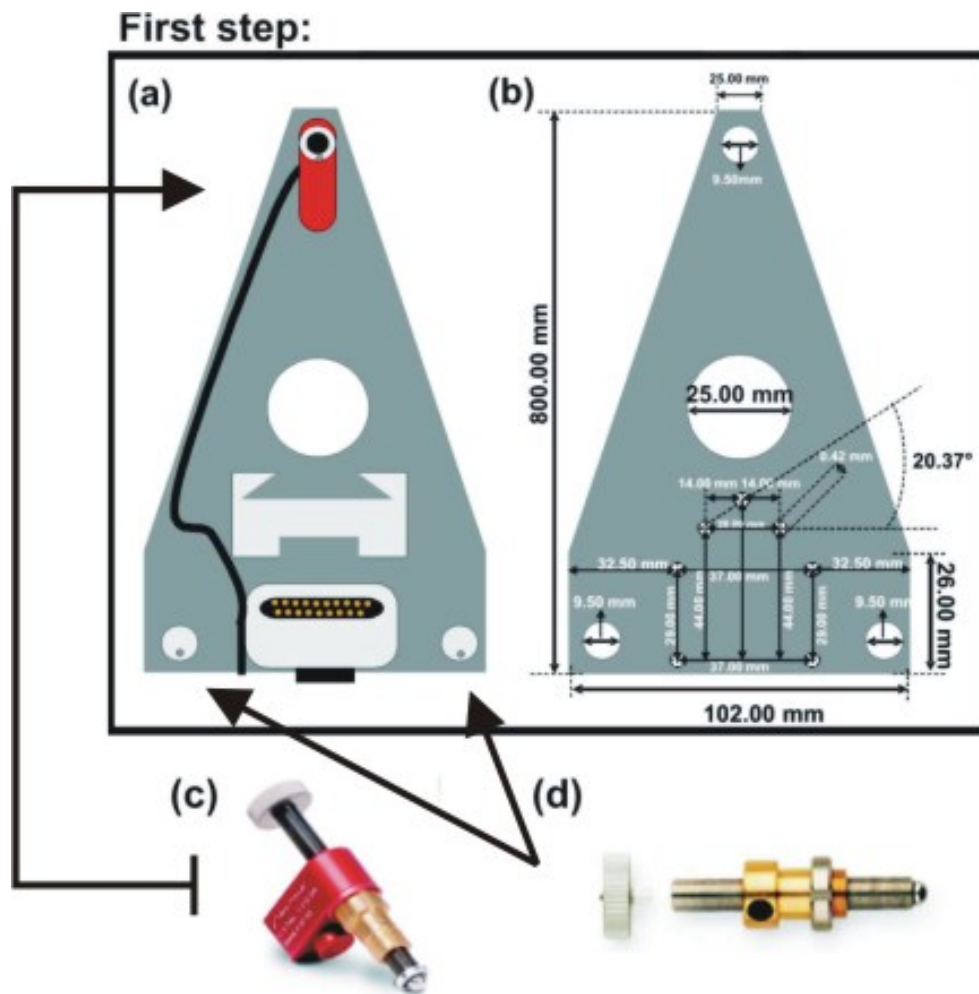
Figure 4.18: (a) Scan-head's base mounted with its main components: the picomotor (red component in the top of the head) and the height adjustable screws (in the bottom of the head). (b) Technical drawing of the scan-head's base with all the dimensions needed to build it.

The TTL/Analog picomotor driver is the Model ♯8703 manufactured by New Focus™. Table 4.8 summarizes its main features. In order to make the picomotor drive work properly some connections must be done. Figure 4.19 diagrams these connections. Fig. 4.19(a) and Fig. 4.19(b) show the model ♯8703 picomotor driver and the circuit board beneath the picomotor driver. Figure 4.19(c) shows the OB29 connector that connects the picomotor driver to the computer interface. All the drawings and diagrams accurately portray the characteristics or details of the equipment necessary to generate our system. In the bottom place of the picomotor driver the red and black wires must be soldered. Otherwise, the drive will not work adequately.

Model ♯8703 Single axis driver			
Channels	Control	Max. PR	Inp. Volt.
1	TTL, Analog	2 kHz	12 V

Table 4.8: Technical information of the TTL/Analog picomotor driver Model ♯8703.
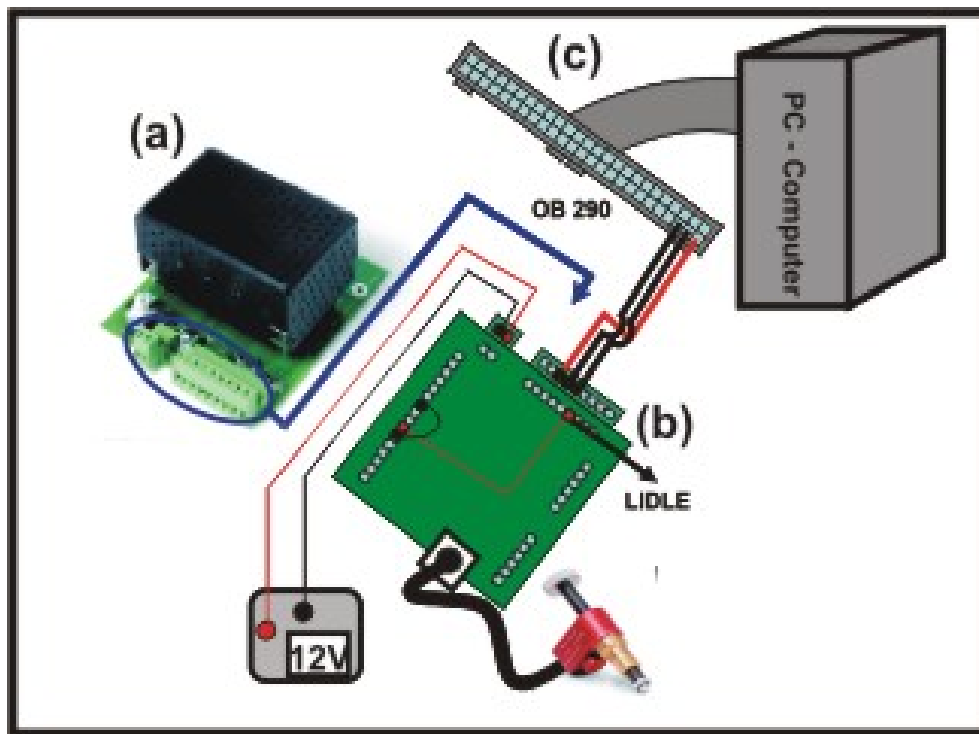

Figure 4.19: (a) The Model ♯8703 picomotor driver. (b) A bottom view of the picomotor driver in (a). In the voltage source, the black line is the ground while the red is the signal. It is important to comment that the drawings are designed to represent the system as it is.

Second step: the "column holder"

The second step is mounting the "column holder" for the piezos and the circuit amplifiers. The "column holder" must be built using stainless steel. Figure 4.20 shows a technical drawing of the holder. Figure 4.20(a) shows a top view of the holder, Fig. 4.20(b) shows a bottom view of the holder and the Fig. 4.20(c) shows a side view of the holder[9]. The holes in the bottom face hold M4 screws while the holes in the lateral of the holder hold M4 screws. The "column holder" has a groove where a "slide holder" is held. This is important because it allows the user to adjust the height of the piezo's column in relation

---

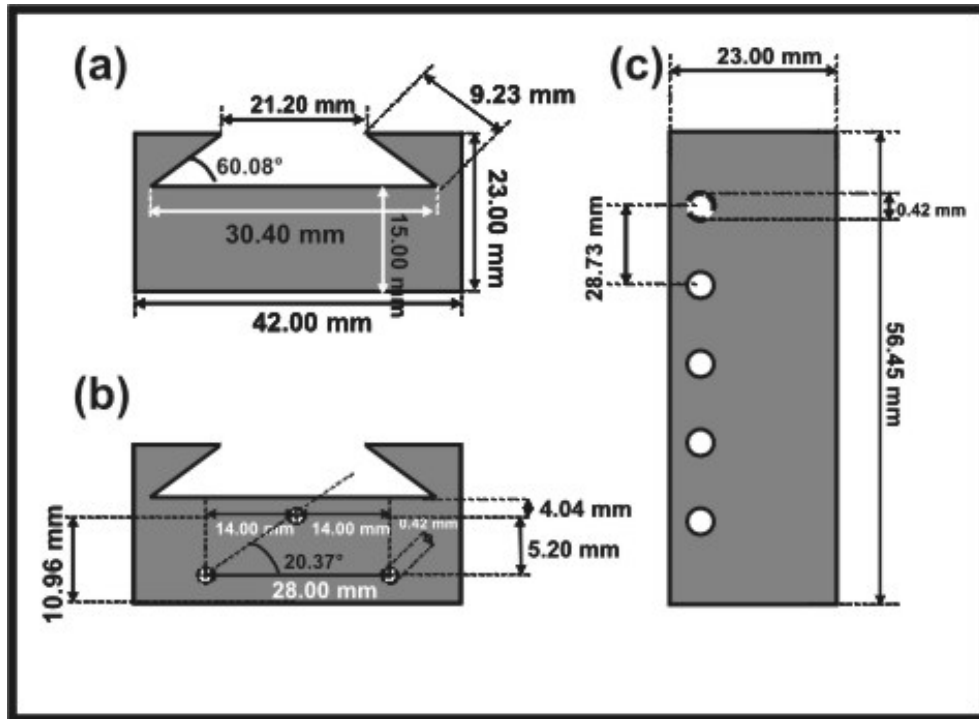[9]Both sides of the holder have the same shape and dimensions.

to the microscope base.

Figure 4.20: Technical drawing of the "column holder". (a) Top view, (b) bottom view and (c) side view.

Third step: the "slide holder"

The third step is mounting the "slide holder" which allows the user to control the height of the piezo's column in relation to the microscope's base. It must be built using stainless steel. Attached to the "slide holder" will be the "main holder" where the amplifier circuits and the piezos are attached. Figure 4.21 shows a technical drawing of the "slide holder". Fig. 4.21(a) shows the top view of the "slide holder" (the bottom view is the same), Fig. 4.21(b) shows the front view of the "slide holder" and Fig. 4.21(c) shows the side view of the "slide holder". The two holes in the holder hold M4 screws. Once completing the "slide holder", we now need to construct an important attachment: the "main holder".
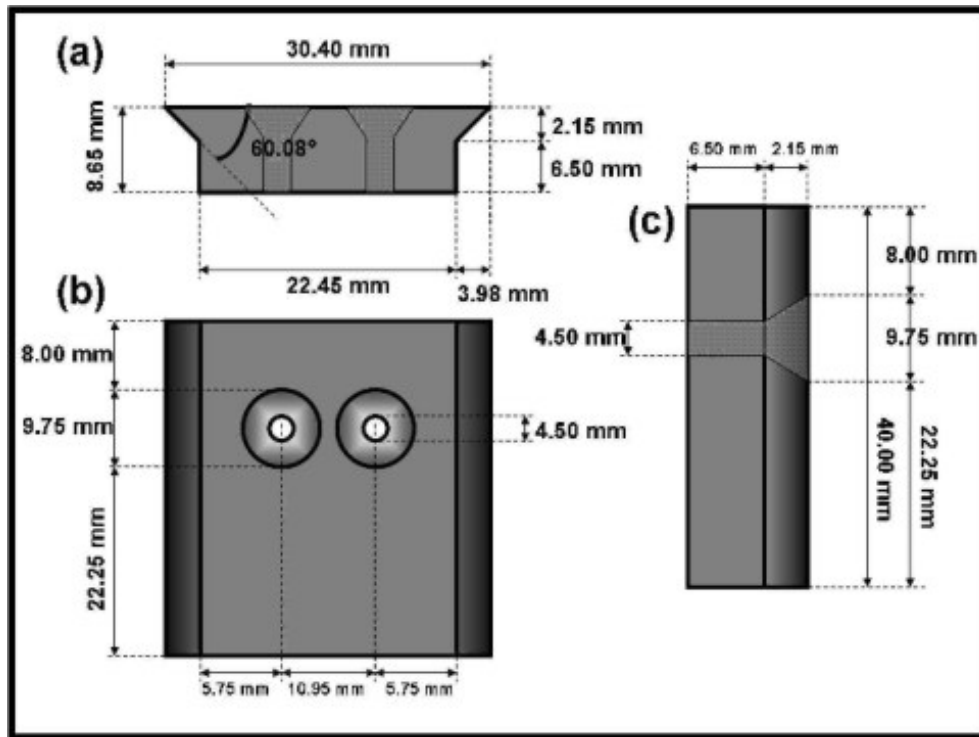
Figure 4.21: Technical drawing of the "slide holder". (a) Top view (the bottom view is the same), (b) front view and (c) side view.

Fourth step: the "main holder"

The fourth step is mounting the "main holder" which will hold the piezos and the amplifier circuits. It must be built using stainless steel. Figure 4.22 shows a technical drawing of the "main holder". One side of the "main holder" will be connected to the previously constructed "slide holder". The opposing side will hold the dither's piezo. In our system, the dither is built using a small piece of a broken piezo. One side of the piezo will be ground referenced and the other side will receive the signal. Under an AC signal, the piezo will begin shaking and automatically it will shake the whole scan-head and will, therefore, shake the tuning-fork in its resonance frequency. The dither's piezo is connected to the "main holder" with epoxy glue. The other two sides will be connected to a Z signal notch-filter (see the Section 4.2.1) and a I/V amplifier converter (this I/V amplifier will be explained further in the text).

Fifth step: the "piezo's base"

The fifth step is mounting the "piezo's base", which basically protects the piezo's
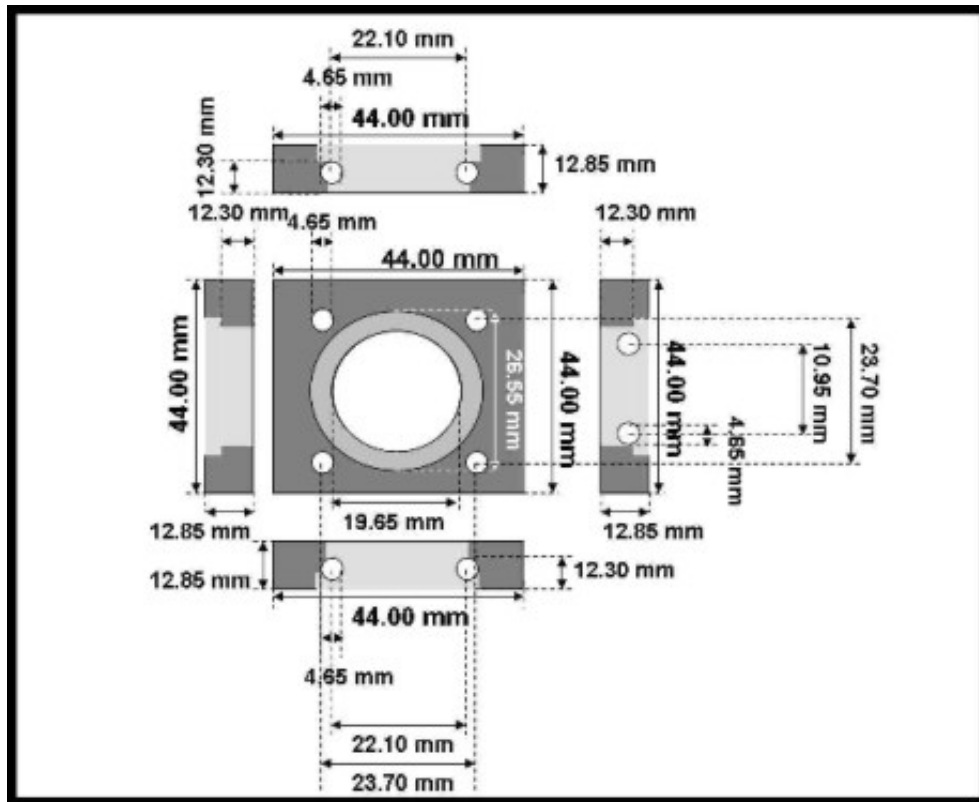
Figure 4.22: Technical drawing of the "main holder".

column. It must be built using stainless steel. Figure 4.23 shows a technical drawing of the "piezo's base". It is a hollow cylinder which houses the piezos. Fig. 4.23(a) shows the top view of the "piezo's base" , Fig. 4.23(b) shows the side view of the "piezo's base" and Fig. 4.23(b) shows the bottom view of the "piezo's base".

Sixth step: connecting the XY-piezo to the Z-piezo.

As stated before, in our system's configuration the XY-piezo is independent of the Z-piezo. It is necessary to remember that the XY-piezo receives only offset voltages and is totally independent of the feedback-loop mechanism. The Z-piezo is connected to the feedback-loop and therefore receives offset and scan voltages. The best configuration to build a piezo structure (at least in our case) whose X, Y and Z signals will interfere as little as possible is one where the XY-piezo is independent of the Z-piezo. Both, the XY- and the Z-piezos are manufactured by EBL precision. The XY-piezo is the Model EBL♯3 and the Z-piezo is the Model EBL♯4. Their main technical descriptions are summarized in Table 4.9.
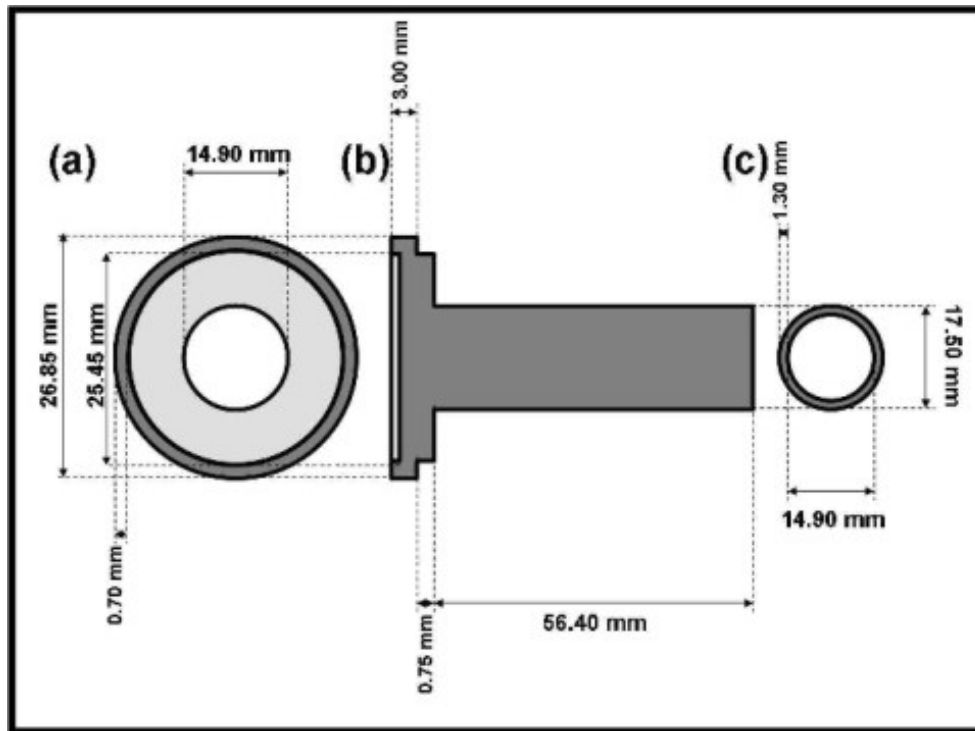
Figure 4.23: Technical drawing of the "piezo's base". (a) Top view, (b) side view and (c) bottom view.

The piezos are connected to each other by using epoxy glue but they are not directly glued to each other. First, the XY-piezo is glued into an insulating ceramic ring (see Fig. 4.24(b)) and then the pair is glued in the Z-piezo. A metallic ring with holes to fit precision's screws (see Fig. 4.24(c)) is also glued to the bottom of the Z piece. This piece is fundamental because we will fix the tuning-fork's circuit-board (the first amplification stage) on it. On the top of the XY-piezo an insulating ceramic ring (see Fig. 4.24(a)) is attached and works as a support to make the piezos column more stable and isolated from the "piezo's base". Figure 4.24 gives the technical drawings the aforementioned pieces.

The ring attached to the top of the XY-piezo must be connected to a stainless steel ring. This stainless ring will lay on the top of the "piezo's base" tube. Figure 4.25 shows a technical drawing of this attachment.

Figure 4.26 outlines a routine to build the whole piezo setup which is described as follows:

1. Both, XY- and Z-piezos, must be rolled up with a Scotch brand tape 3M until the thickness of the piezo matches that of the "piezo's base" cylinder inner diameter.

76

XY-piezo EBL♯3			
κ	**E**	ν	ρ
3450 (K_3^T)	6.3 (10^{10} N/m^2)	0.31	7.45 (g/cm^3)
Therm. cond.	**Therm. exp.**	$\mathbf{d_{31}}$	$\mathbf{d_{33}}$
1.5 (W/m°C)	4.7 (ppm/°C)	-2.62 (Å/V@293°K)	5.83 Å/V@293°K
XY-piezo EBL♯4			
κ	**E**	ν	ρ
1050 (K_3^T)	8.5 (10^{10} N/m^2)	0.31	7.5 (g/cm^3)
Therm. cond.	**Therm. exp.**	$\mathbf{d_{31}}$	$\mathbf{d_{33}}$
2.1 (W/m°C)	3.0 (ppm/°C)	-0.95 (Å/V@293°K)	2.20 (Å/V@293°K)

Table 4.9: Technical specifications of the EBL♯3 and EBL♯4 piezoelectric tubes. κ is the dielectric constant, E is the young's modulus, ν is the poisso's ratio and ρ is the density. Additional information are available at http://www.eblproducts.com.

2. The ceramic ring ♯02 must be glued to the stainless steel ring ♯01.

3. Turn the pieces up side down and glue the XY-piezo ♯03 onto the ceramic ring ♯02. A small portion (~ 2 mm) must be above the ceramic ring in order to connect the wires that apply the X and Y offset voltages.

4. The ceramic ring ♯04 must be glued in on the bottom of the XY-piezo ♯03.

5. The top of the Z-piezo ♯05 must be glued to the ceramic ring ♯04.

6. The object created so far must be covered with the "piezo's base" hollow cylinder. Next, let the epoxy glue dry.

7. After drying, the metallic ring ♯06 must be glued to the bottom of the Z-piezo.

8. Drill a small hole across the ceramic ring ♯02. This is important in order to connect a wire to the Z-piezo inner wall.

9. The first amplification stage ♯07 can now be attached.

With the complete set, another stainless steel ring, which will stand on the top of the stainless steel ring ♯01,must be built. This ring will be tightly screwed to the "main holder" of the scan-head giving stability to the piezo's set. Figure 4.27 shows a technical drawing of the ring.
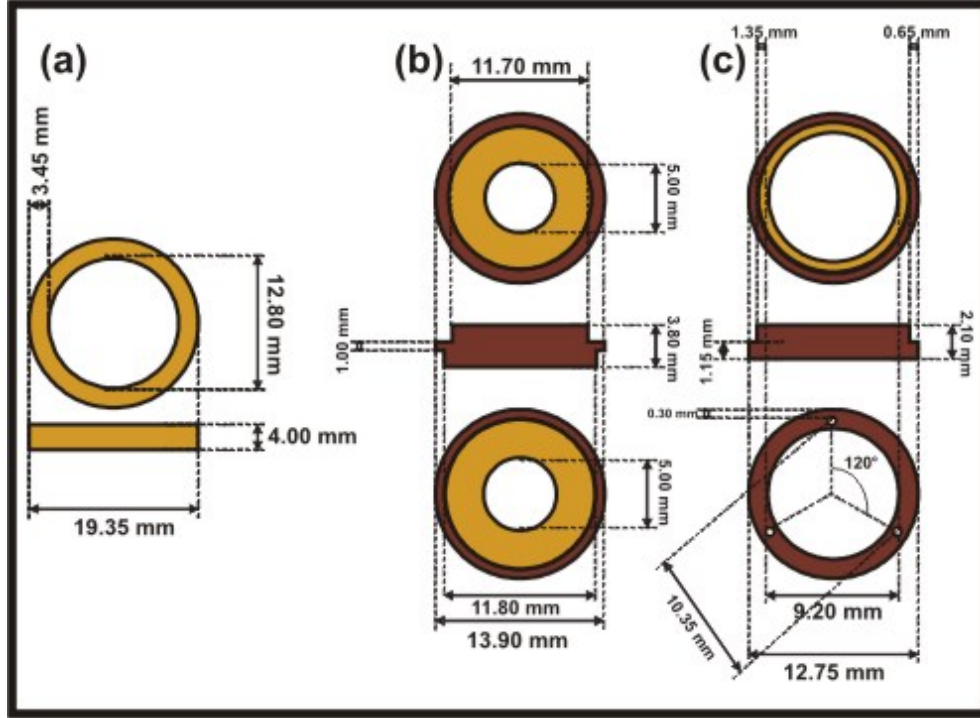
Figure 4.24: Technical drawings of the pieces needed to mount the XYZ-piezo's mechanism. (a) Ceramic ring which is attached on the top of the XY-piezo, (b) ceramic ring to connect the XY-piezo and the Z-piezo and (c) metallic ring which is glued on the bottom of the Z-piezo.

Seventh step: building the amplification stages

The scan-head has two amplification stages: the first one is a JFET-based amplifier that amplifies the current generated by the tuning-fork oscillation, and a second one is an OP. based amplifier that converts the current into voltage and amplifies the result signal. Figure 4.28 shows the amplifiers circuit and diagrams the tuning-fork's signal path from the tuning-fork to the Easy-PLL's signal input.

To understand what happens during the amplification, I am going to break the diagram into the two parts mentioned above. Figure 4.29 shows the first amplification stage with the currents and voltages in it. The voltage V only ensures that we are in a regime that the transistor works as an amplifier. When the transistor is reverse-biased like in the circuit, the transistor's input impedance is too high in the way that we can set $I_G \approx 0$. We have that:

$$I_\mathrm{S} = I_\mathrm{G} + I_\mathrm{D} \quad \text{and} \quad V_\mathrm{DS} = V_\mathrm{GS} + V_\mathrm{GD}, \tag{4.16}$$

where V_DS is the voltage drop between the source and the drain, V_GS is the voltage
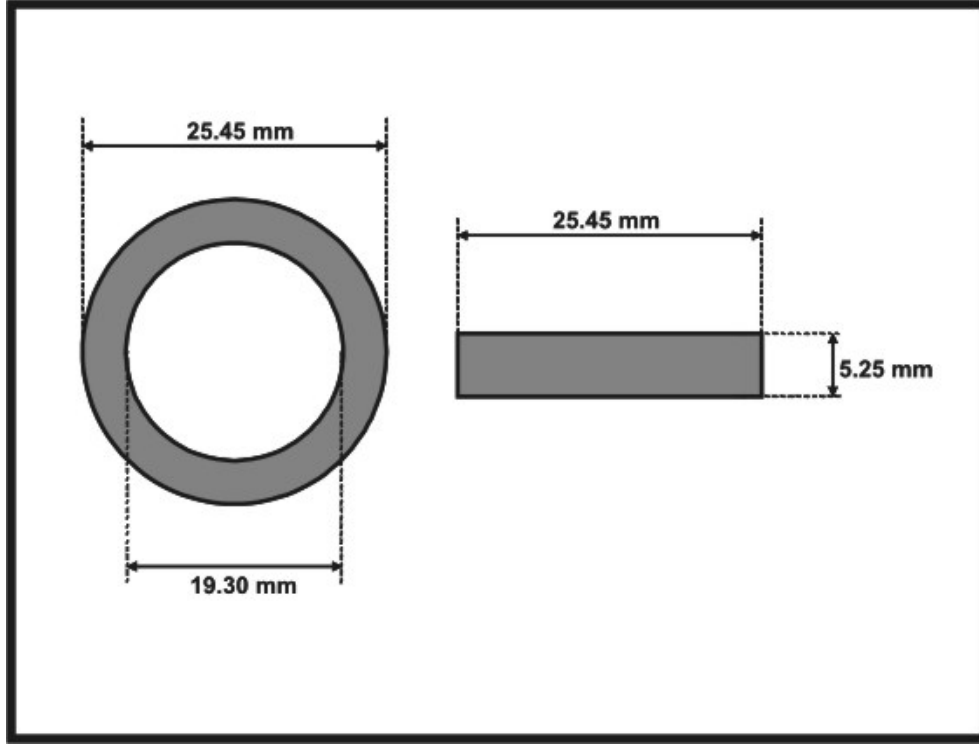
Figure 4.25: Technical drawing of the stainless steel ring which supports the whole piezo's setup.

drop between the source and teh gate and V_{GD} is the voltage drop between the gate and the drain. Using these relations and $I_G \approx 0$ it is found that $V_{GS}=I_D R_S$. It follows that $V_{OUT}=V_{IN}+I_D R_S$ and for oscillating signals:

$$\Delta V_{\text{OUT}} = \Delta V_{\text{IN}} + I_D R_{\text{S}}, \tag{4.17}$$

giving the voltage amplification. It is a direct result that $\Delta I_{\text{OUT}}=\Delta V_{OUT}/R_{\text{S}}$.

Keeping our analysis, the figure 4.30 shows a general overview of the second amplification stage. This is actually a two steps operational amplifier circuit and it will be analyzed in three parts. The first and the second parts (the (01) and (02) in the Fig. 4.30) gives:

$$V_{\text{IN}} = \frac{R_{\text{a}}}{R_1}V_1 + R_{\text{a}}C_1\frac{dV_1}{dt}, V_1 = \frac{R_{\text{b}}}{R_2}V_2 + R_{\text{b}}C_2\frac{dV_2}{dt}. \tag{4.18}$$

By solving this set of equations we have the inhomogeneous second order differential equation:

$$\frac{d^2V_2}{dt^2} = \left[\frac{1}{R_1C_1} + \frac{1}{R_2C_2}\right]\frac{dV_2}{dt} + \frac{1}{R_1C_1R_2C_2}V_2 = \frac{1}{R_{\text{a}}R_{\text{b}}C_1C_2}V_{\text{IN}}. \tag{4.19}$$
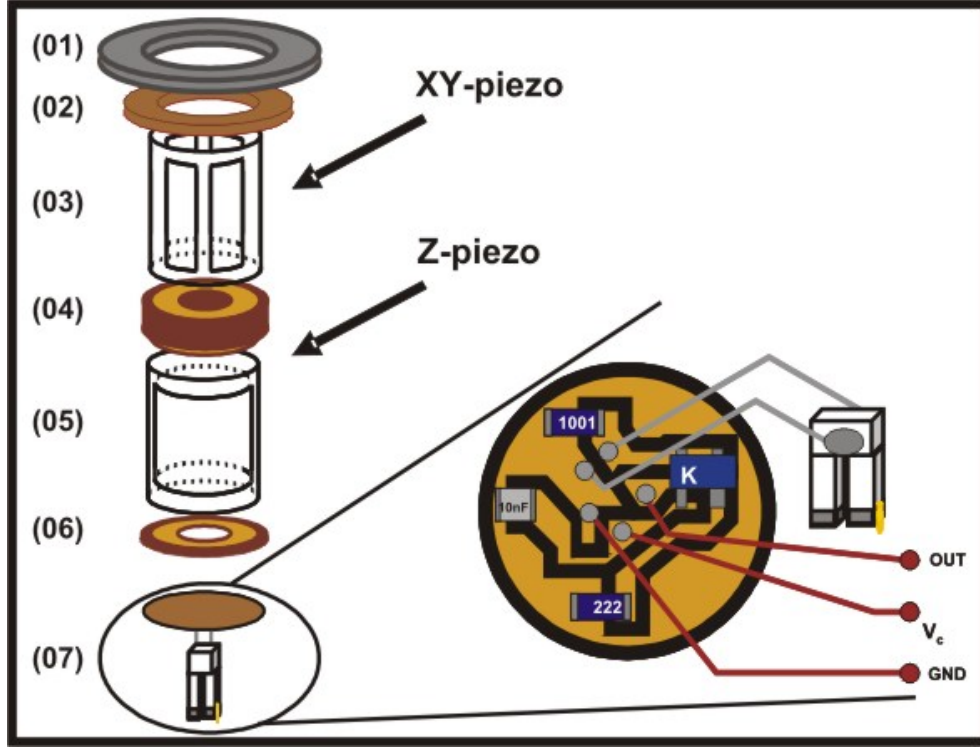
Figure 4.26: This figure illustrate the sequence which must be followed in order to mount the piezo's set and fix it to the scan-head. An accurate description is given in the text.

It is solution is:

$$V_2 = \frac{R_1 R_2}{R_a R_b} V_{\text{IN}} \left[\frac{R_1 C_1}{R_2 C_2 - R_1 C_1} e^{\frac{-t}{R_1 C_1}} - \frac{R_2 C_2}{R_2 C_2 - R_1 C_1} e^{\frac{-t}{R_2 C_2}} \right]. \qquad (4.20)$$

Finally, the amplification is found equals to:

$$V_{\text{OUT}} = \frac{C_2 \frac{dV_2}{dt} + \left[\frac{1}{R_2} + \frac{e^{\frac{-t}{R_C C_3}}}{R_C} \right] V_2}{\frac{e^{\frac{-t}{R_C C_3}}}{R_C}}. \qquad (4.21)$$

Now that we quantitatively understand what is going on with the amplification stages, we must bring them working out in a real circuit. The first amplification stage will be attached to the bottom part of the Z piezo. Precisely speaking, the circuit must have the dimensions of the metallic ring in Fig. 4.24(c) where it will be screwed. The circuit is all done with superficial mounting device (SMD) components which are manually soldered in a printed circuit-board. The components are: one $10\,\text{M}\Omega$ SMD resistor, one $2.2\,\text{k}\Omega$ SMD resistor, one $10\,\text{nF}$ SMD capacitor, one SMD JFET transistor model
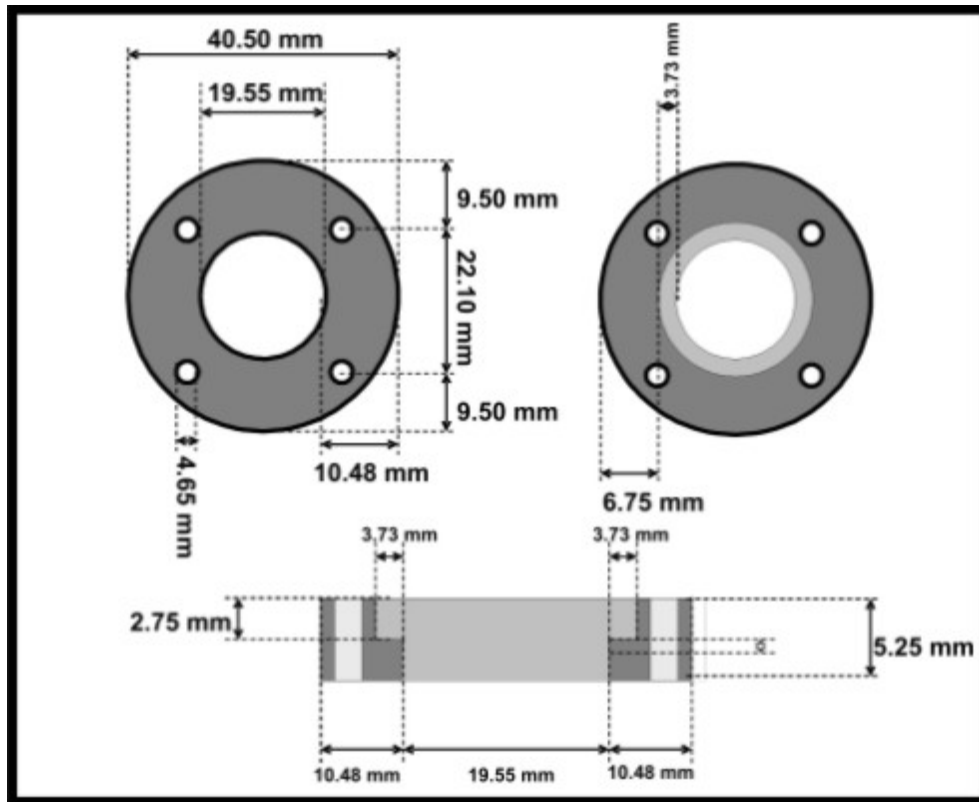
Figure 4.27: Technical drawing of the stainless steel ring which fixes the piezo's set onto the "main holder" of the scan-head.

3SK166A manufactured by SONY and one tuning-fork[10]. The next step is soldering the components into the printed circuit-board. Figure 4.31(a) illustrates the circuit's design and Fig. 4.31(b) illustrates the position of all the components of the circuit. The connections for OUT, V_C and GND are made using copper wires[11] with diameter of 0.113 mm and covered by an insulating resin[12].

The second amplification (also called OPAmp circuits) stage is more conceptual, although its design is somewhat more elaborate. The circuit is made with more robust components. It is composed of the following materials: two $2\,k\Omega$ resistors, one $200\,k\Omega$ resistor, one $20\,k\Omega$ resistor, one $50\,\Omega$ resistor, four $30\,\mu F$ electrolytic capacitors, five $100\,nF$

---

[10]The tuning-forks we use are made of quartz prongs which oscillates $180°$ out of phase. The prongs move against each other.

[11]The one we use is manufactured by PIRELLI and its model is PIREFORM R.

[12]Hint: All the components, except the JFET transistor are very robust and usually their are not burned during the soldering. When the circuit is ready, an easy test to verify if the JFET still works is: the resistance between the channels DRAIN and SOURCE must be something about 18-23Ω. With V_C applied, the voltage drop between the DRAIN and the GND must be 3 V and the voltage drop between the SOURCE and the GND must be 1.5 V.
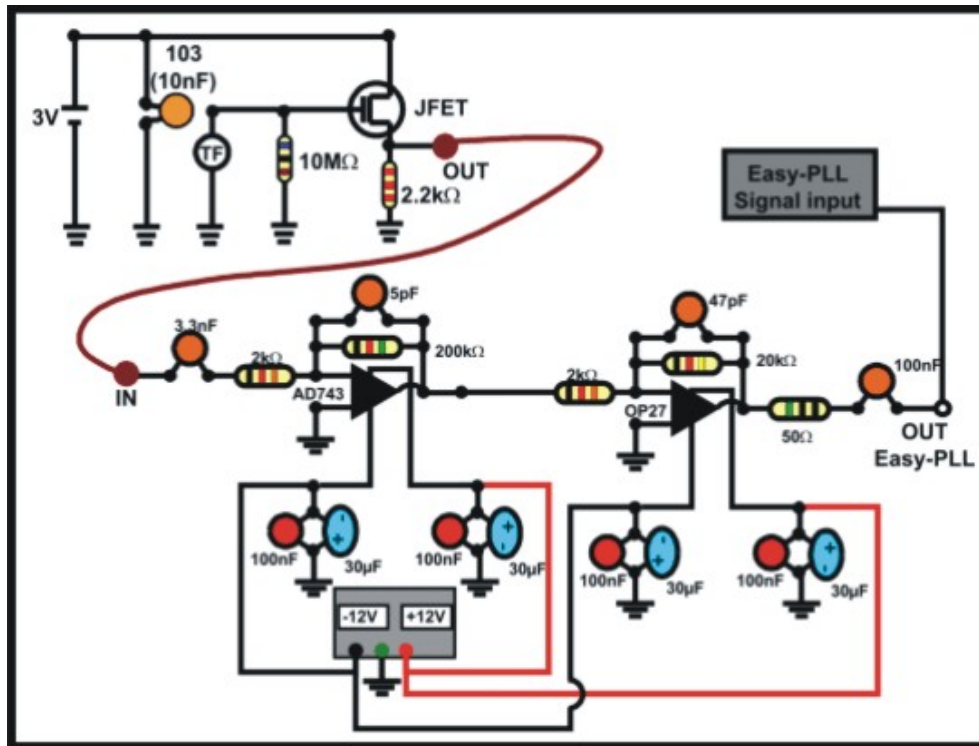
Figure 4.28: Circuit diagram for the first and second amplification stages. The values for all the components are the ones we use in our circuits.

capacitors, one 3.3 nF capacitor, one 47 pF capacitor, one 5 pf capacitor, one AD743 operational amplifier and one OP27 operational amplifier. The circuit is constructed on a conventional circuit-board. The design suggested is given in Fig. 4.32 but, of course, the reader can feel free to redesign the circuit since there exists more than one way of designing the circuit. Figure 4.32(a) shows a frontal view of the circuit and Fig. 4.32(b) shows a back view. One useful hint is taking advantage of the circuit components prongs to make the connections showed in Fig. 4.32(b). The gray/white colored lines are the circuit's ground. Fig. 4.32(b) is a mirrored vision of the circuit's back in Fig. 4.32(a). A direct correspondence between the frontal and back views of the components must be consider.

It is convenient to take advantage of the circuit-board design and use it as an shortcut to connect the RHK's ±X and ±Y offset voltages to the XY-piezo, connect the AC voltage from the Easy-PLL's drive out channel to the dither, as well as connect the 3 V power supply to the first amplification stage. All the connections (from the XY-piezo, first amplification stage, dither to the OPAmp circuit-board) must be done with resin-covered copper wire (0.113 mm of diameter). Then the OPAmp stage must be attached to
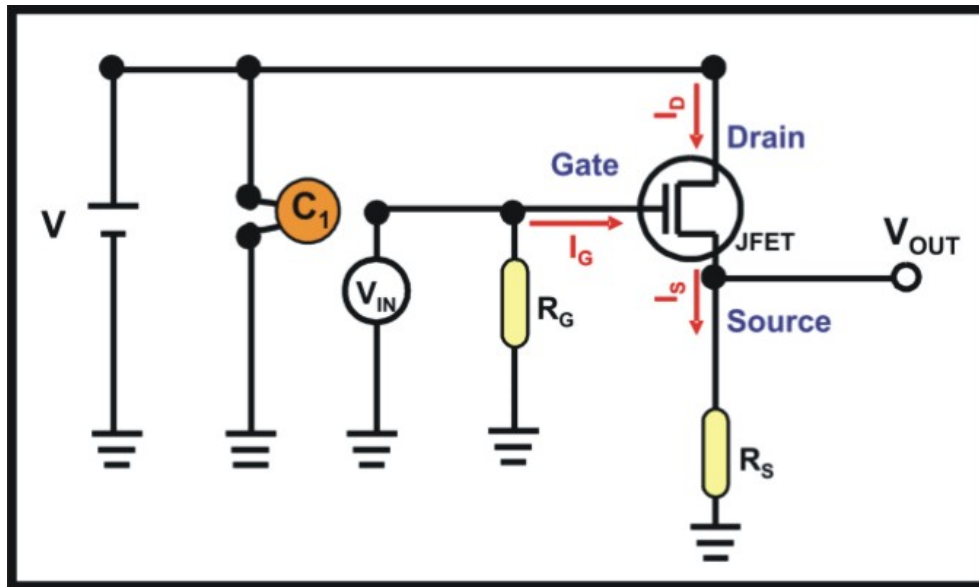
Figure 4.29: A general circuit diagram for the first amplification stage. It amplifies the current signal coming from the tuning-fork.
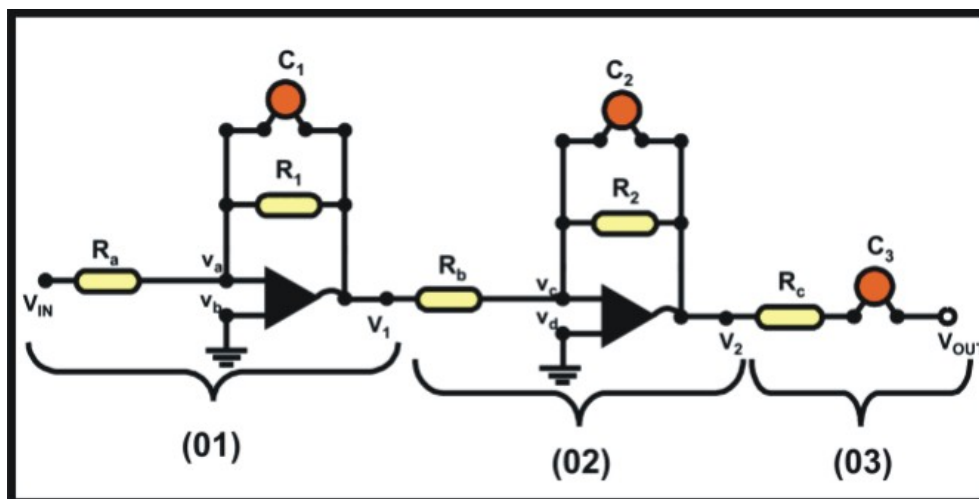
Figure 4.30: A general circuit diagram for the second amplification stage. It converts current into voltage signal and send to the Easy-PLL a amplified voltage signal.

one side of the "main holder" (see the fourth step). Note that in both, Figs. 4.32(a) and (b), the channels BIAS, Z common and Z signal will not be used in this configuration. The Z's connections will be done directly from the RHK to the Z piezo and the channel BIAS is used only for STM purposes.

Figure 4.31: (a) Design of the printed SMD circuit-board. (b) The circuit-board with all the SMD components. Inset: The SMD JFET transistor model 3SK166A. In the illustration the drain, source and gate channels are labeled.

Eighth step: the scan-head communicates with the external devices by means of a DB-15 plug

The scan-head must be as stable as possible in order to properly perform experiments in the atomic resolution scale. The idea is letting the head be as 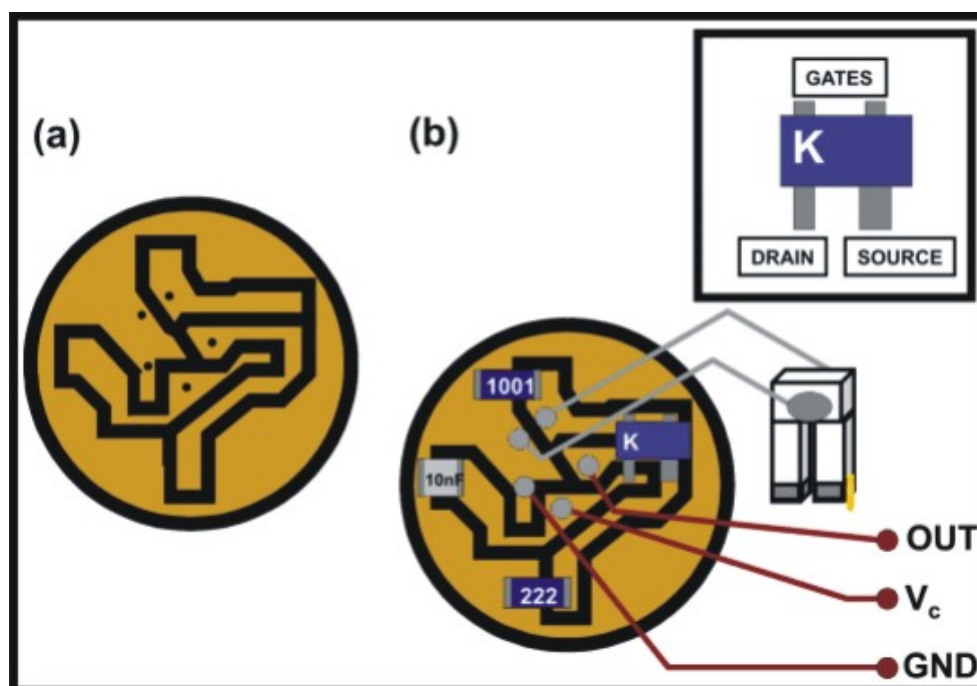isolate as possible from external influences, whatever they are. All the signals that need to reach the external devices and the scan-head must be driven to a 17-pin female plug and from this 17-pin female plug to a DB-15 plug. From this DB-15 plug the cables must be connect to a 17-pin male plug attached to the break-out box (the break-out box will be explained later in the text). The break-out box converts the 17-pin plug outputs into BNC outputs. These BNC outputs are then connected to the RHK, Easy-PLL and so on. The figure 4.33 shows how to connect the OPAmp channels to the 17-pin male-plug. The diagram adopts a color code which designates a particular color to a particular wire[13]. In the diagram, three different cables are shown, with each cable possessing 5 wires (each colored differently) and a shied. The cables are Model P/N 1211/5 manufactured by BRIM Electronics

---

[13]Although this could seem useless at first glance, this wires color code is very practical to hunt for signal problems, for example.
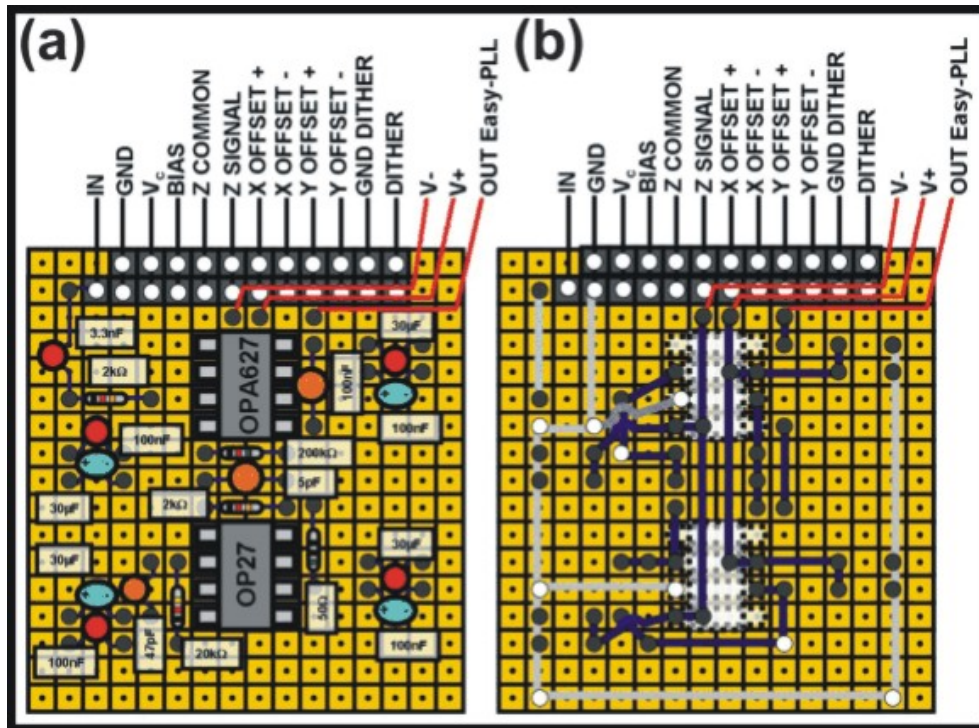
Figure 4.32: (a) The OPAmp circuit's front view and (b) the OPAmp circuit's back view. (b) is a mirrored vision of the circuit's back view in (a) and so a direct correspondence between the front and back views must be taken into account.

Inc. The 17-pin male and female connectors are manufactured by WPI wire-pro. Inc.

The 17-pin male-plug is then connected to its female counterpart and finally converted into a DB-15 male-plug. Figure 4.34 shows how to perform the conversion. Note that the color code is maintained.

Next, the DB-15 male-plug must be converted back into the 17-pin female plug. This 17-pin female-plug will be connect to its male counterpart which in turn is attached to the break-out box. Figure 4.35 shows how to perform this conversion. Note that the color code is again maintained.

Now a conversion from 17-pin male to BNC connectors is performed by means of the break-out box. The break-out box is a metallic box which works much like a faraday's cage which prevents electromagnetic noises. Once more, this conversion maintains wire color code convention. Figure 4.36 shows the schematics of the break-out box. Utilizing BNC cables, the break-out box's terminals are now connected to the RHK, Easy-PLL, power supplies etc.
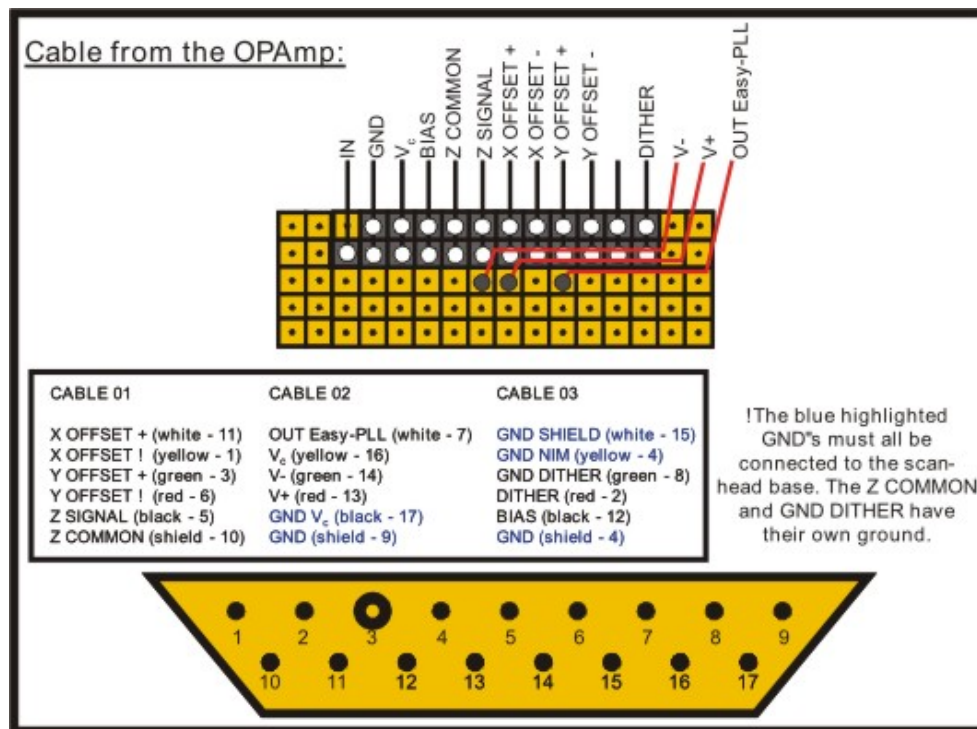
Figure 4.33: The OPAmp circuit channels are connected to a 17-pin male-plug. The cables connecting the circuit to the plug obey the color code portrayed in the diagram.

Ninth step: bringing every step together

It is now time to bring every step together and see the result. Figure 4.37 shows an overview of how the scan-head should appear after it is mounted. Figure 4.37(a) shows an illustration of the back panel of the scan-head, Fig. 4.37(b) shows the top view of the scan-head. Fig. 4.37(c) shows the front and side views of column with the "slide holder", "main holder" and the "piezo's base" joined together. Finally, Fig. 4.37(d) shows a real picture of the side, front and back views of the scan-head.

Next, Fig. 4.38 gives an overview of a system ready to perform experiments. The ±X and ±Y offset voltages are connected to their low-pass filters. The offset voltages then travel to the break-out box and finally to the scan-head. The Z common goes directly to the scan-head while the Z signal undergoes a notch-filter and then goes to the scan-head. The Easy-PLL's drive-out signal supplies the dither's channel in the break-out box and afterwards it travels to the scan-head.

The amplified tuning-fork signal leaves the scan-head and goes to the break-out box. Next it goes to the Easy-PLL's "detector in" input. The Easy-PLL's output signal goes directly to the RHK. A ±12 V DC power supply is connected to the break-out box's
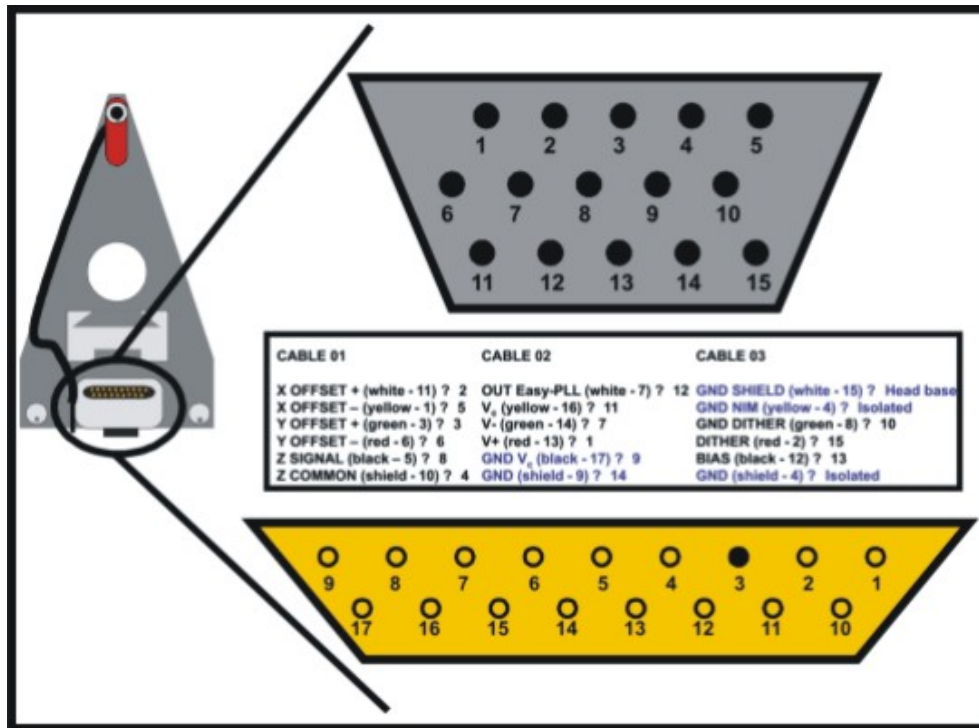
Figure 4.34: Scheme of the conversion from a 17-pin female plug into a DB-15 female connector. Note that the same wires color code is applied. The scan-head is showed in the left. The connector's conversion wires are protected by a metallic box as highlighted on the bottom of the scan-head.

V_+ and V_- inputs. These voltages travels from the break-out box to the OPAmp circuit. A 3 V DC power supply is connected to the break-out box's V_C input and then it goes to the scan-head, feeding the first amplification stage. The "pico-motor driver" controls the pico-motor.

4.2.3   The Shear-force mechanism

Tuning-fork sensors

Commercial AFM microscopes usually detects the probe's depletions (due to tip/sample interactions) by means of optical detection. A laser beam is aimed into the tip's arm and reflected from the arm to a photo-detector. This photo-detector monitors the laser beam's path changes and relates this to the changes in the arm's movement. However, this kind of detection is not appropriate for near-field experiments because of possible light signal
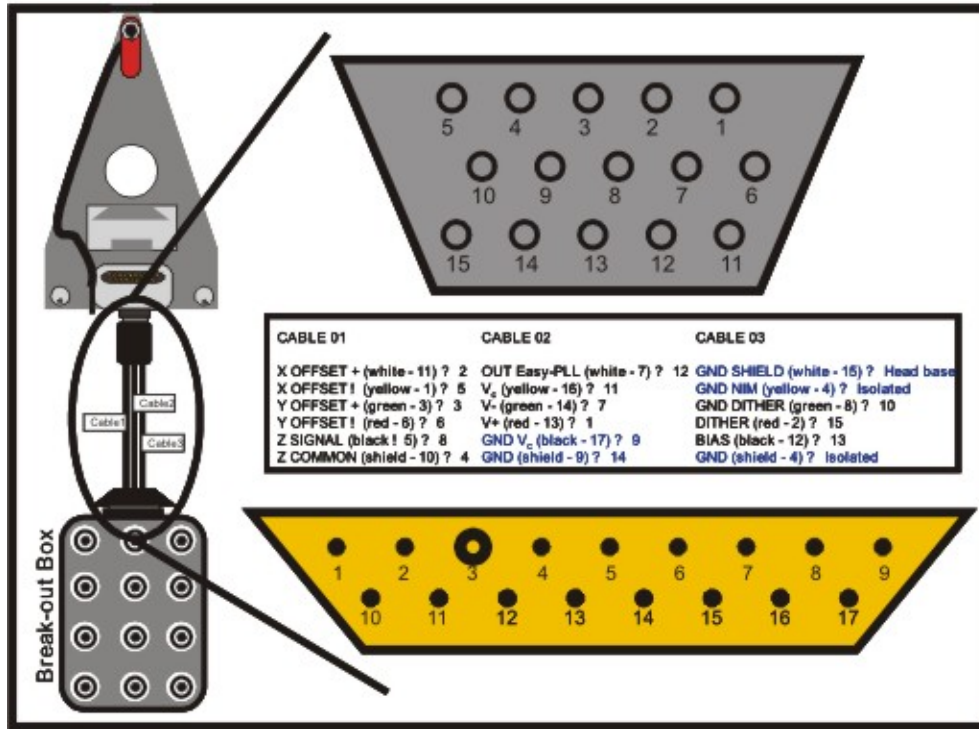
Figure 4.35: Scheme of the conversion from a DB-15 male plug into a 17-pin female plug. Note that the same wire color code is applied.

interactions. An alternative way is measuring changes in the admittance[14] of piezoelectric devices which will be related to changes in its resonance frequency due to tip/sample interactions.

The most successful method of shear-force detection has been the one based on microfabricated quartz tuning forks [49]. It consists of a quatz element shaped like a tuning-fork with electrodes deposited at its surface. The resonance frequency of the tuning-forks we use is 32,768 Hz (model TC38 manufactured by Buerklin electronics). The mechanical oscillations of the tuning-fork prongs induces surface charges that are detected by its electrodes and processed by an external electronic circuit. Therefore, the tuning-fork acts as a mechanical-electrical converter. The electrodes layout ensures that only movements of the prongs against each other will be excited and detected. For commercial purposes, the tuning-forks are utilized with a metallic protection cover (see inset in Fig. 4.39) which, for the shear-force scheme, needs to be removed. Figure 4.39

---

[14]The admittance is defined as the inverse of the impedance of a system. It is measured in siemens (℧). It is a measure of how easily a circuit or device will allow a current to flow. Resistance is a measure of the opposition of a circuit to the flow of a steady current, while impedance takes into account not only the resistance but also dynamic effects.
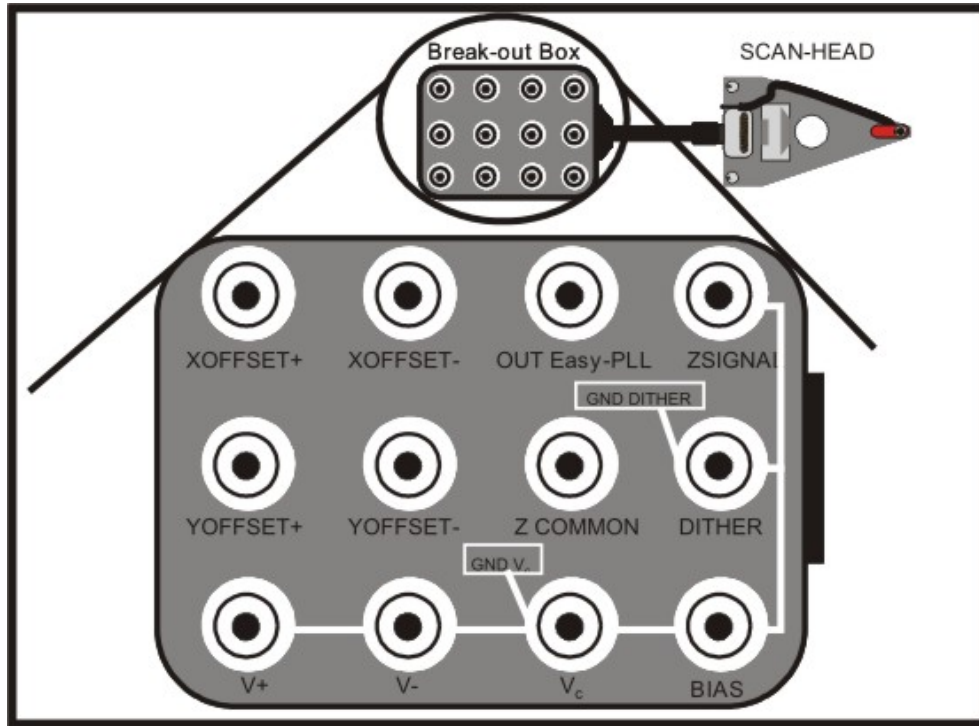
Figure 4.36: The break-out box scheme.

illustrates the way the protection cover can be removed.

As showed in Fig. 4.39(a), the tuning-fork is supported by an epoxy mounting. Using a pair of pliers (doing very smooth pressures), the epoxy mounting must be smashed, as showed in Fig. 4.39(b). Next, the tuning-fork must be carefully removed from the cover protection, as exhibited in Fig. 4.39(c).

For harmonic oscillations, the equation of motion that the tuning-fork is submitted to by an external driving force is:

$$\frac{d^2x}{dt^2} + 2\beta\frac{dx}{dt} + \omega_0^2 x = A\cos\omega t \,, \tag{4.22}$$

where β=b/2m is the damping parameter, ω_0^2=k/m is the natural oscillation frequency and A=A_0/m is the normalized driving force amplitude[15]. The solution for the homogeneous equation is:

$$x_h(t) = Be^{-\beta t}\cos(\omega_1 t - \phi) \,, \tag{4.23}$$

---

[15]It is worth to comment that b is the coefficient of the resisting force, k is the constant of spring and A_0 is the driving force amplitude
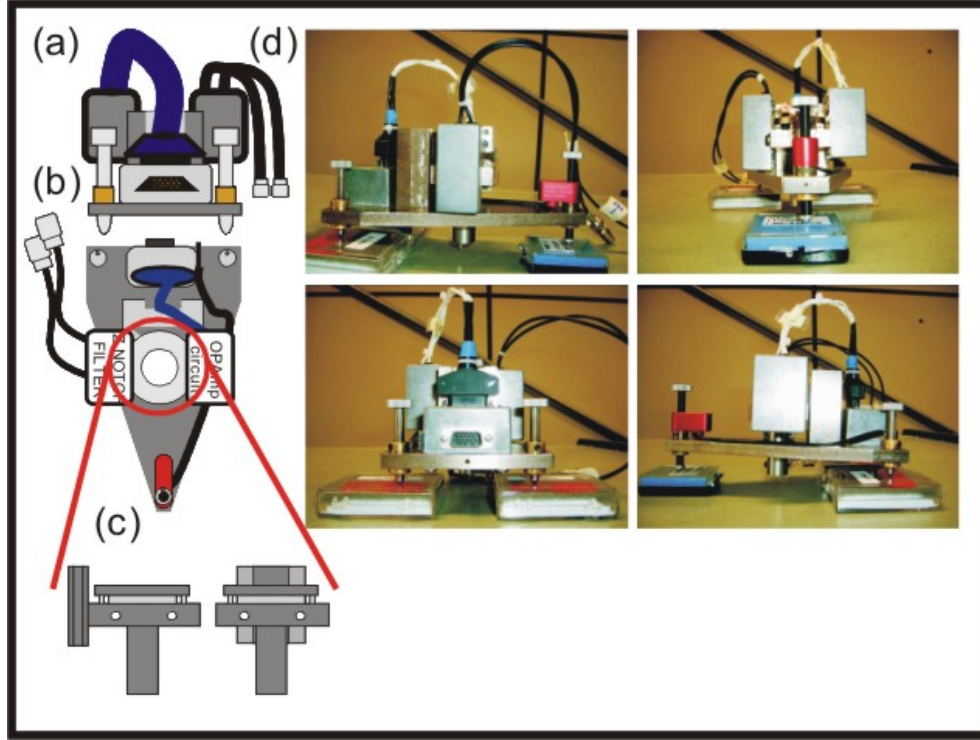
Figure 4.37: (a) Back view of the scan-head. (b) Top view of the scan-head. (c) The front and side views of column with the "slide holder", "main holder" and the "piezo's protector" joined together and (d) real picture of the side, front and back views of the scan-head.

where $\omega_1^2 = \omega_0^2 - \beta^2$. The particular solution is given by:

$$x_p(t) = \frac{A}{\left[(\omega_0^2 - \omega^2)^2 + 4\omega^2\beta^2\right]^{1/2}} \cos(\omega_1 t - \delta), \tag{4.24}$$

where δ is found:

$$\delta = tan^{-1}\left[\frac{2\omega\beta}{\omega_0^2 - \omega^2}\right]. \tag{4.25}$$

The general solution is:

$$x(t) = Be^{-\beta t}\cos(\omega_1 t - \phi) + \frac{A}{\left[(\omega_0^2 - \omega^2)^2 + 4\omega^2\beta^2\right]^2}\cos(\omega_1 t - \delta), \tag{4.26}$$

where the first term is a transient whose life-time is $\tau = 2Q/(\omega_0^2 - 2\beta^2)^{1/2}$ (also known as response time). Q is defined as quality factor which is given by $Q=(\omega_0^2 - 2\beta^2)^{1/2}/2\beta$. For slightly damped systems, it can be rewritten as $Q \approx \omega_0/\Delta\omega$. This gives us a life-time of $\tau = 2Q/\omega_0$. The higher the Q-factor of a system is, the longer it takes to respond to an

90
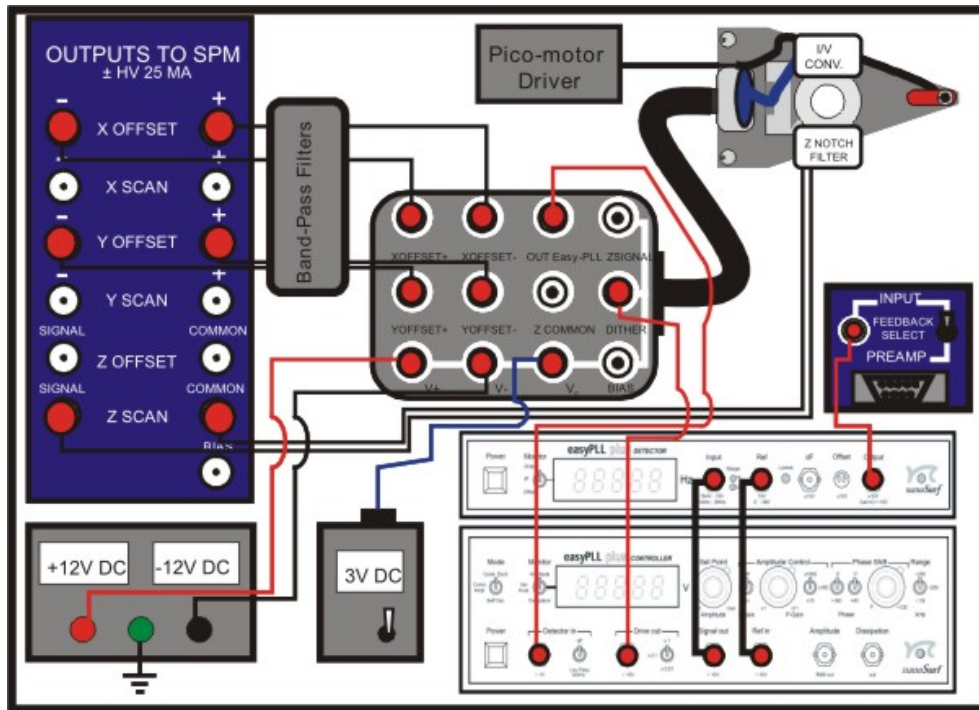
Figure 4.38: The general diagram of our system's connections.

external signal. On the other hand, a high Q-factor is a prerequisite for high sensitivity! The parameters of the tuning-fork used for tip/sample distance control must be adjusted to guarantee a certain level of sensitivity and prevent the tip from crashing into the sample. In principle, the resonance frequency responds instantaneously to an external perturbation. This shift in frequency is usually measured by a phase-locked loop device.

The gold tip probes

In principle, all kinds of tip, namely, glass tips or any metallic tip, can be used to probe a sample in an AFM experiment. However, for optical experiments such as near-field, it is fundamental to have an efficient metallic tip which can provide both, topographic and optical resolutions on the atomic scale. Gold tips have been revealed as the best option to fulfill those two requirements. The tips are home-made, fabricated by electrochemically etching a continuous metallic gold wire. This procedure can generate sharp tips with diameters varying from 10 to 30 nm. The gold wire used is manufactured by Alfa Aesar®. It has a diameter of 0.1 mm and is 99.998% pure. The etching process happens by passing an electrical current from the gold wire, which works as an electrode, to a platinum ring, which works as an counter electrode. Both, the gold wire and the
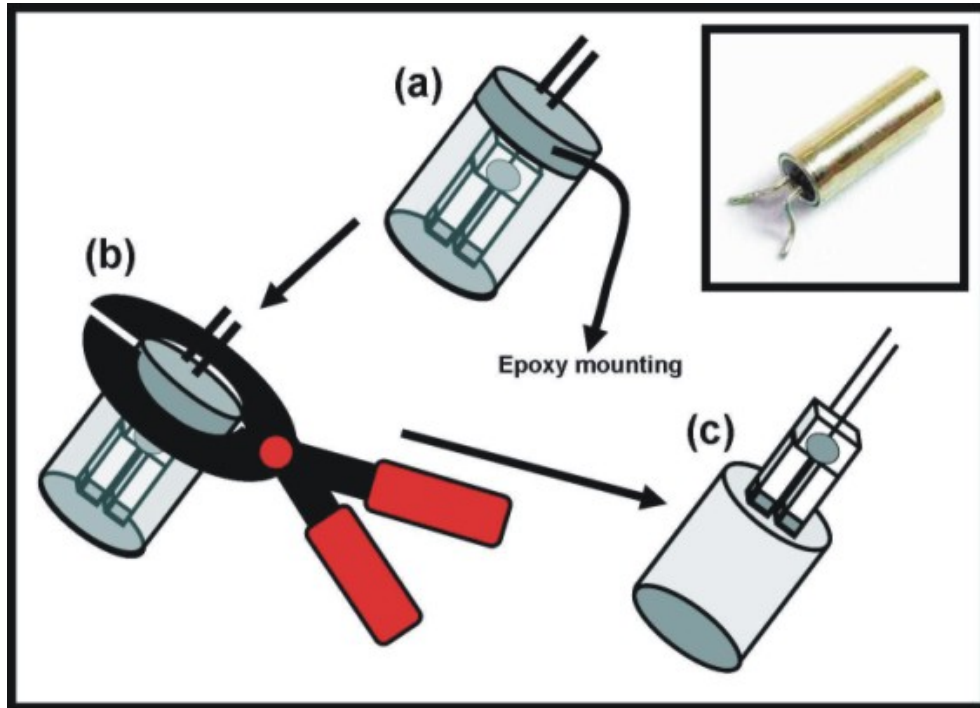
Figure 4.39: The tuning-forks are protected by a metallic cover. For shear-force purposes, this protection must be removed step by step as illustrated in (a), (b) and (c). The tuning-fork is supported by an epoxy mounting which must be carefully removed with a pair of pliers. Inset: a picture of a commercial tuning-fork.

platinum ring, are immersed into a 37% hydrochloric acid (HCl) solution to form a closed loop circuit. Figure 4.40 schematically shows the etching setup.

The platinum ring is ground referenced to the function generator while the function's generator signal is connected to a stainless stell tweezer which holds the gold wire. Both, the platinum ring and the gold wire, are inside of a quartz cuvette filled with a HCl solution. The tweezer is attached to a XYZ-stage allowing for an easier positioning of the gold wire. The function generator generates pulses with a width of $30\,\mu$s and period of $330\,\mu$s. The amplitude of each pulse is 8 V. A Push button controls the amount of pulses flowing in the circuit. During the process the following chemical reaction occurs [50]:

$$Au + 4Cl^- \longrightarrow AuCl_4^- + 3e^- \tag{4.27}$$

$$Au + 2Cl^- \longrightarrow AuCl_2^- + e^- \tag{4.28}$$

$$AuCl_2^- + 2e^- \longrightarrow AuCl_4^- + 2e^- \tag{4.29}$$
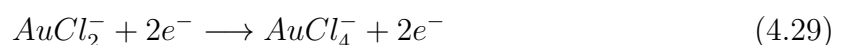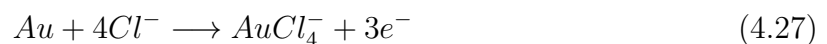
In this chemical reaction, gold material is being removed from the gold wire. The
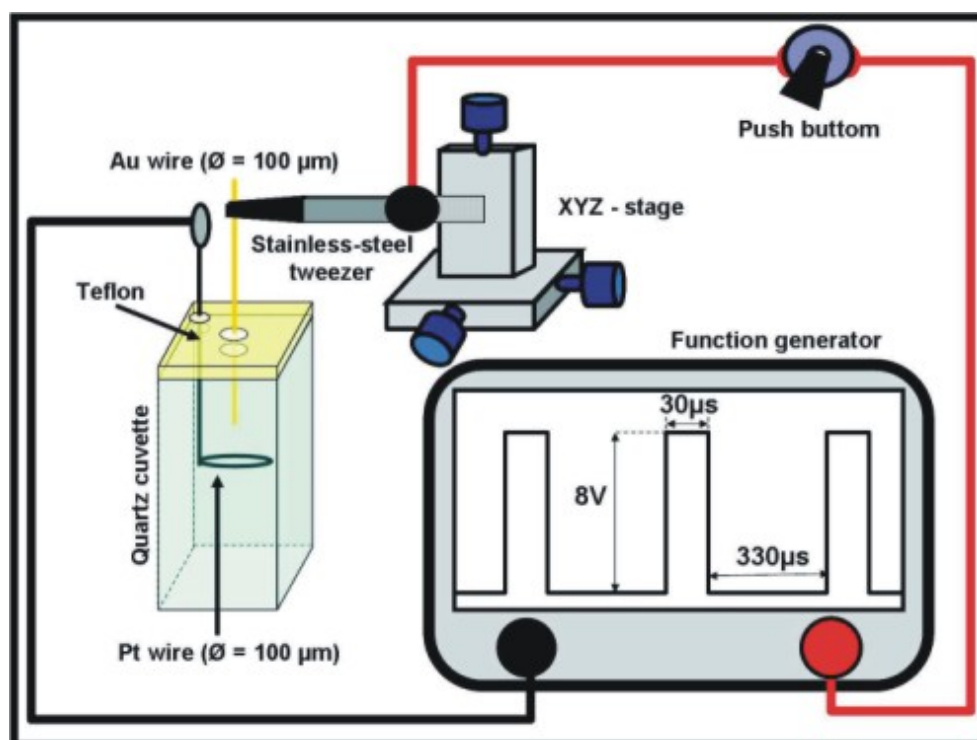
Figure 4.40: The platinum ring is ground referenced to the function generator while the function's generator signal is connected to a stainless steel tweezer which holds the gold wire. Both, the platinum ring and the gold wire, are inside a quartz cuvette with a 37% HCl solution. The tweezer is attached to a XYZ-stage allowing for an easier positioning of the gold wire. The function generator generates pulses with a width of 30 μs and period of 330 μs. The "push" button controls the amount of pulses flowing into the circuit.

diameter decreases faster at the end of the gold wire and, after continuous clicking of the "push" button (in general, something about 2 or 3 minutes), the gold tip is formed, acquiring a conical shape. The tip is drawn out of the HCl solution and must be rinsed by distilled water to remove any remaining acid residues. In order to make nice tips, it is only a matter of getting used to the etching process. Figure 4.41 gives an illustration of the procedure I usually perform to etch my tips. It may be useful for most of the readers.

First the platinum ring should be dipped to a depth which is about 7× the gold wire diameter and the gold wire should be dipped to a depth which is about 4× its diameter, as showed in Fig. 4.41(a). Next, the "push" button should be clicked until the the gold wire becomes long and thin (almost invisible), as roughly illustrated in Fig. 4.41(b). As exhibited in Fig. 4.41(c), the gold wire should be dipped again to a depth which is about 4× its diameter. The "push" button should be softly clicked to make the very thin gold wire disappear allowing just the conical-shaped gold tip remaining. Hint: during the
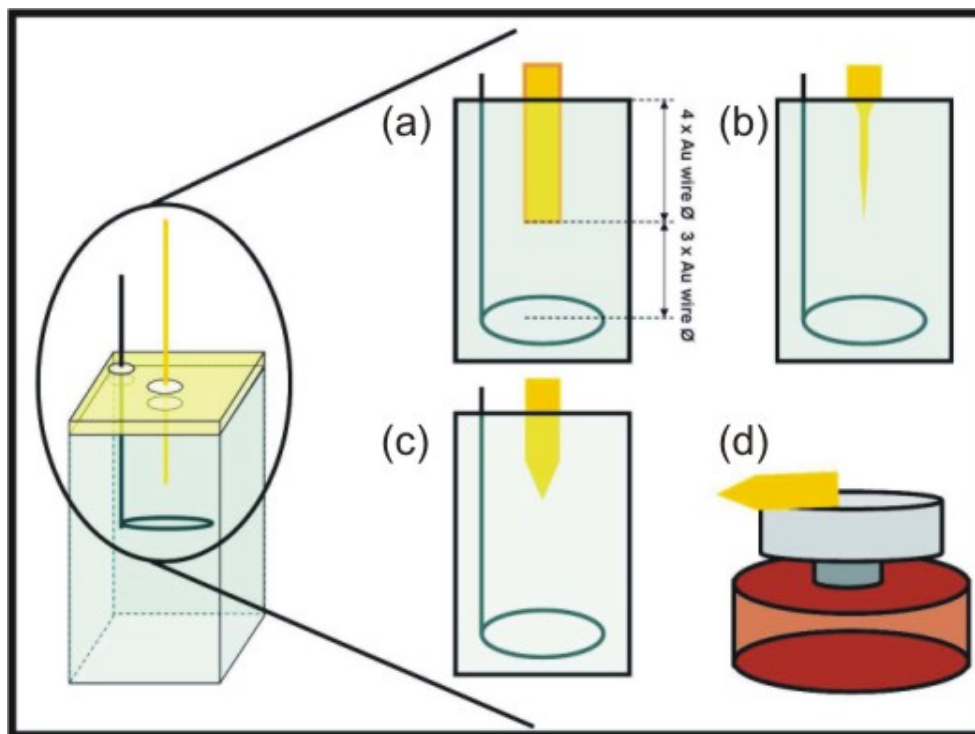
Figure 4.41: An illustration of the steps involved in producing small diameters gold tips. A complete description is given in the text.

etching lots of bubbles are formed around the gold wire end. When the pulse's flow is interrupted, these bubbles go down to the cuvette's ground but some of them get stuck to the end of the tip apex. When the space between a stuck bubble and the visible tip is "empty", it means the the gold tip is already thin enough. Usually, each 100 tips you etch in a single bath will give about 30 tips possibly good for near-field. There is no guarantee that all those 30 tips will work properly! In general, tips with diameters varying from 10 to 60 nm are appropriate to perform good topographies an near-field enhancements.

With a good set of gold tips, the next step is attaching a gold tip in one of the tuning-fork prongs. Once again, I will give an explanation of the method I used to attach a tip to a tuning-fork. The steps are:

1. Attach a microscope cover slip to a stable base. Next, attach a piece of double-sided tape creating a small angle with relation to the cover slip's edge. This is illustrated in Fig. 4.42(a).

2. With the help of a tweezer, take the desired gold tip and attach it to the double-sided tape. The tip apex must be outside the cover slip's edge [see Fig. 4.42(b)].
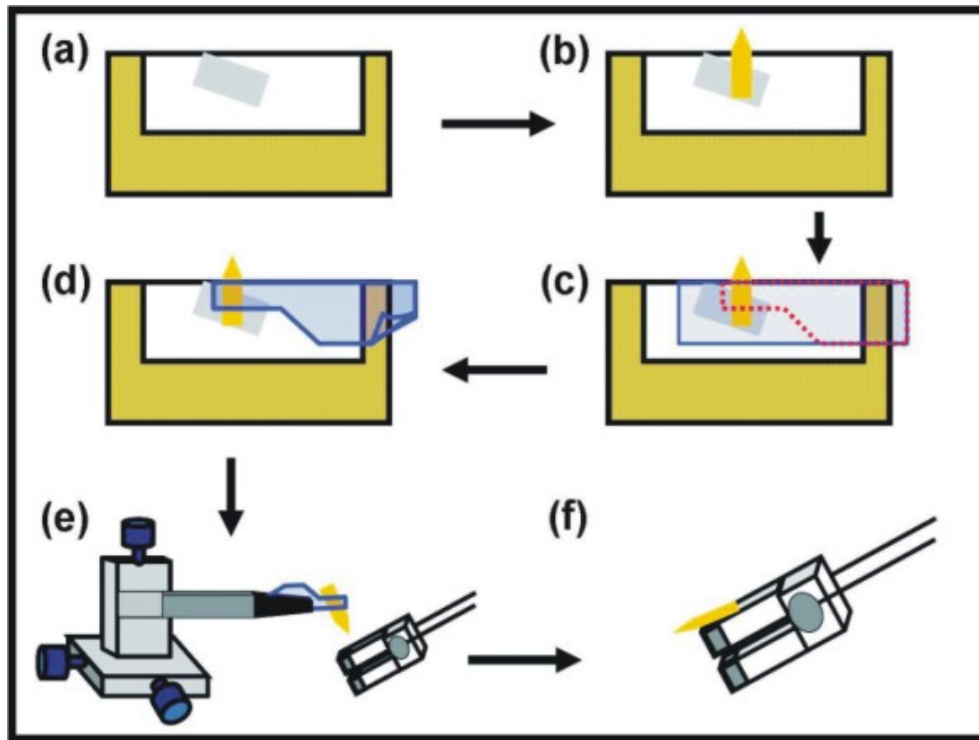
Figure 4.42: Steps to attach the gold tip in one of the tuning-fork's prongs.

3. Cover the tip with Scotch tape as showed in Fig. 4.42(c).

4. With help of a razor blade, cut the Scotch tape and a small piece of the gold tip according to the pattern showed in Fig. 4.42(d).

5. Stick the set to a inverted tweezer and put the tweezer in a XYZ-stage (see Fig. 4.42(e)).

6. Put a small amount of super glue on one of the tuning-fork's prongs and with the help of the XYZ-stage position the tip according to the illustration in Figs. 4.42(e) and (f).

7. Wait for the super glue to dry for two hours.

4.2.4 The Easy-PLL plus

As stated in the Section 4.2.3, our system uses a shear force feedback mechanism where a tuning fork has a tip (glass tips, gold tips, etc.) attached to one of its prongs. When the tip interacts with the sample, the fork experiences changes in its resonance frequency. This interaction will change both, the amplitude and the phase, besides the

tuning-fork resonance frequency. These changes are usually monitored by lock-in amplifiers or phase looked loop (PLL) systems which converts changes in the resonance frequencies into DC voltages that can be interpreted by the feedback mechanism. Our system uses a PLL (easyPLL plus Version 3.0 manufactured by nanoSurf®) to monitor the tuning-fork frequencies. To understand how a PLL works and its advantages compared to the conventional lock-in systems, it is worthwhile to understand the principles of a lock-in amplifier.

A lock-in system always receive an AC signal, which is usually sinusoidal, and outputs a DC signal. This conversion is made by a rectifier which works as a phase-sensitive convertor. The phase shifter usually feedbacks part of the incoming signal and because of this, it suppresses noises and rectifies only signals of interest. In order to function correctly, the lock-in must be programmed to recognize the signal of interest, otherwise it can not be able to recognize what is noise and what is not. This is achieved by providing it with a reference AC signal of the same frequency and with a well defined phase relationship to that of the interaction-free resonance tuning-fork frequency. Suppose that the input signal is of the form $V_{in} = Asin(\omega t)$ and the reference is $V_{ref.} = Bsin(\omega t + \phi)$. The phase-sensitive device multiplies the reference by the input signal. The result of this multiplication is:

$$V_{in} \cdot V_{ref.} = \frac{1}{2}AB\cos(\phi) + \frac{1}{2}AB\cos(2\omega t + \phi), \qquad (4.30)$$

where A is the amplitude of the input signal, B is the amplitude of the reference signal and ϕ is the relative phase between the input and reference signals. ϕ is, in fact, an user adjustable phase-shift[16] introduced within the lock-in. Some features must be highlighted. Consider that the amplitude, B, of the reference signal is kept constant. The output DC signal is:

- Proportional to the amplitude A of the input signal.

- Proportional to the cosine of the angle ϕ, between it and the reference signal.

- Modulated at 2ωt, i.e. it contains components at twice the reference frequency.

Next, the lock-in's output signal passes a low-pass filter which removes the AC component, leaving the lock-in amplifier output signal as the required DC signal. It follows that both, phase and amplitude, can be monitored. The advantage of working with a lock-in is its simple design and application. However, as stated in the Section 4.2.3, the Q-factor of

---

[16]The phase-sensitive has a phase shifter allowing for fine adjustments of the phase.

a resonant system defines its sensibility and how fast it is going to respond to a given stimulation. This raises some drawbacks in using lock-in systems because for high quality tuning-forks (that are very sensitive), the response time of the amplitude to changes in the resonance frequency increase and therefore, the maximum scan-speed decrease. The response time of the phase is still fast but not clearly in line with changes in the tip/sample distances. Besides this, both the amplitude and the phase signal contain information concerning tip/sample distances and the quality factor of the tuning-fork. Therefore, changes in the tip/sample distances and tuning-fork's quality factors can not be distinguished because both alter the phase. Finally, big differences in the resonance frequency compared to width of the resonance peak saturates the feedback signal or even changes its signal.

With modes based on the PLL principle, also called FM-modes, the sensor always vibrates at its resonance frequency, and changes in the vibration frequency and vibration/excitation amplitude are measured. In these modes, the vibration frequency is always adjusted in the sense that the phase shift corresponds to the phase shift at resonance, which is 90°. This resonance condition is independent of the Q-factor, the material or shape of the resonator[17]. It follows that FM-modes can efficiently use changes in the frequency and phase shift to monitor the tip/sample distance. Besides this, several drawbacks are eliminated and: (01) The scan speed can be very even if the tuning-fork has a high Q-factor, (02) there is no saturation of the feedback signal. It does not matter if the changes in frequency are much bigger in relation to the resonance peak width and (03) the changes in frequency and phase shift can be assigned only to changes in the tip/sample distances. In summary, The PLL method is excellent to monitor systems with all kinds of Q-factors and lock-in systems are interesting only to monitor systems with low Q-factors! In our case, the system tuning-fork plus gold tip present Q-factors of about 1000. Figure 4.43 illustrates how the FM-modes work.

The FM-mode we used is the "constant amplitude" mode. This mode is excellent for Q-factors between 500 and 100000, offering a better signal to noise ratio. The Easy-PLL has two components: the CONTROLLER (whose parameters are all manually set) and the DETECTOR, which is connected to the Easy-PLL's softwear interface. First, with the tip far-away from the sample surface, the Easy-PLL's DETECTOR uses its internal oscillator and send it to the CONTROLLER's drive out BNC. This procedure sweeps a given frequency range and obtains the tuning-fork resonance window, as showed

---

[17]Does not matter the Q-factor, the resonance curves intersect at the the resonance frequency at a 90° phase shift.
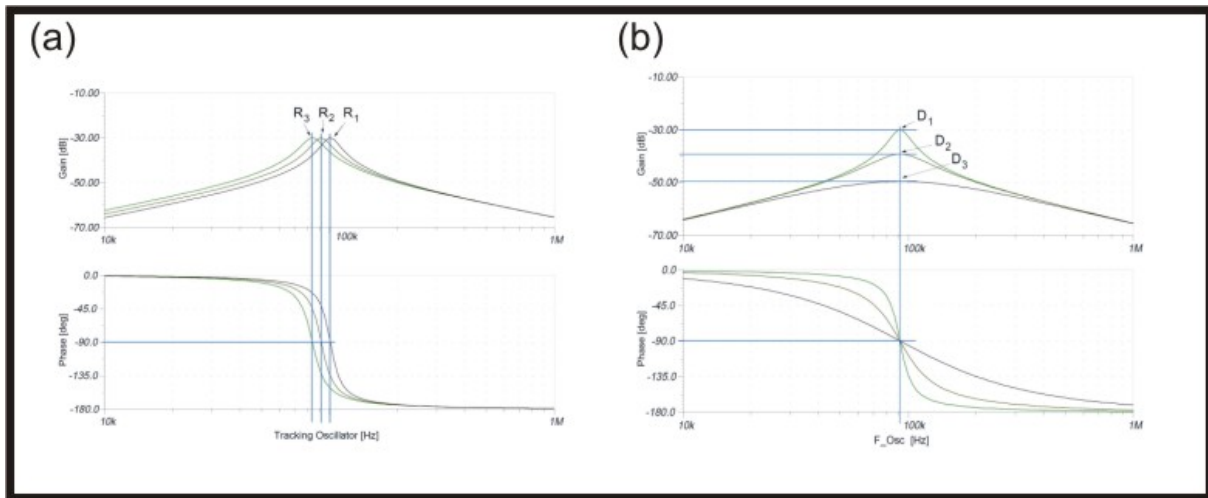
Figure 4.43: FM-Modes signals: (a) changes in resonance frequency only influence the tracking and (b) changes in Q-factor only influence the amplitude/dissipation. [51]

in Fig. 4.44. This resonance frequency is set as the DETECTOR's reference. Next, the CONTROLLER receives a signal coming from the tuning-fork, amplifies it and sends it to the DETECTOR and to its own amplitude PI-controller (this works like an amplitude feedback control), which has a given setpoint value for the amplitude. The DETECTOR compares the signal to its reference. The internal oscillator, by means of its PI-controller, varies its frequency and phase until the frequencies and phases of both, the signal and the reference, to be the same. The system is phase-locked at a minimum driving amplitude and/or at the steepest point of the phase-frequency characteristic. The DETECTOR converts this internal oscillator's changes into DC voltage that is sent to its BNC output.

The frequency generated by the internal oscillator also goes to the CONTROLLER mixer, which mixes the frequency with the CONTROLLER's feedback amplitude mechanism, adjusting the driving out amplitude which drives the tuning-fork.

4.2.5 Going beyond the classical optical limits: near-field optics

The idea of near-field sub-wavelength imaging

Basically, the design of near-field probes is a classical antenna problem. If the antenna is working as a receiver, electromagnetic waves must be channeled to near-field regime of the antenna. If the antenna is working as a sender, energy has to be released from the near-field zone. Antennas are excellent devices to establish an efficient coupling

98
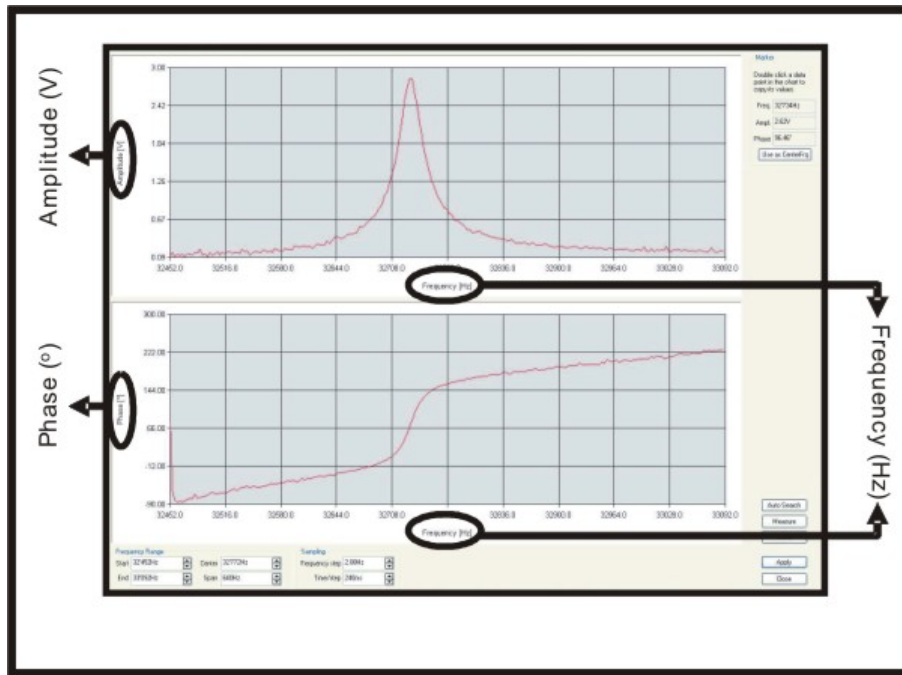
Figure 4.44: Tuning-fork resonance profile obtained with the Easy-PLL's softwear interface.[51]

between the near-field and the far-field. Near-field optical microscopy based on local field enhancement was proposed in 1985, even before the invention of atomic force microscopy [52]. Under certain conditions, a scattering object can act as a local source [52]. This light source is established by the field enhancement effect whose origin is similar to the lightning-rod effect in electrostatic. In this approach, the object acts not only as a scatterer of the sample's near-field but also acts providing a local near-field excitation source to record a local spectroscopy response. This allows for simultaneous spectral and sub-diffraction spatial measurements although it depends on the magnitude of the field enhancement.

The field enhancement magnitude is extremely dependent of the electric field polarization. The incident light is responsible for driving the free electrons into the metallic tip. Inside the wire, the electric field is null. However, charges accumulate on the tip's surface, giving rise to a considerable surface charge density. As shown in Fig. 4.45(a), if the incident light has its polarization perpendicular to the tip axis, diametrically opposite points on the tip surface will have opposite charges. In consequence, the foremost end of the tip will remain uncharged. A very different situation takes place if the light polarization is parallel to the tip axis. In this case, the surface charge density is axially

99
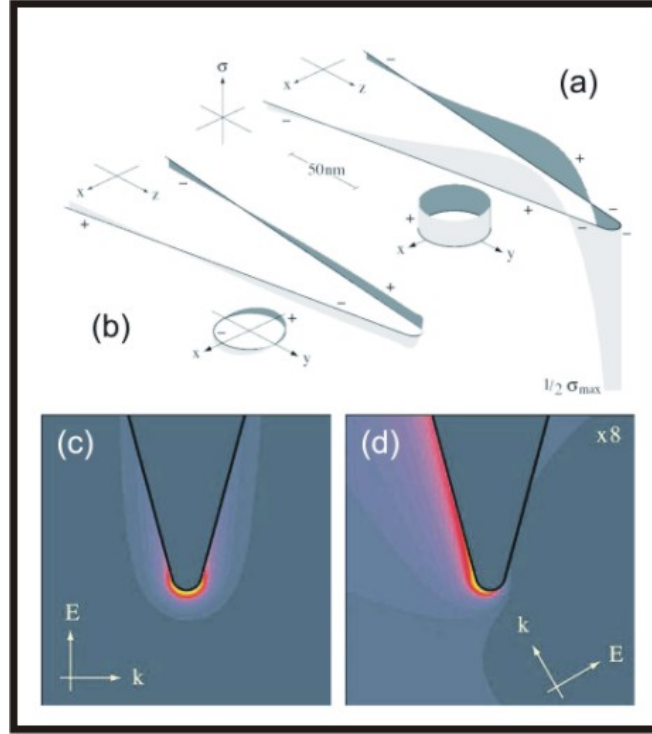
Figure 4.45: (a) and (b): Induced surface charge density at the surface of a sharp metal tip. In (a) the driving field is parallel to the tip shaft, whereas in (b) they are perpendicular to each other. In (a) there is a large surface charge accumulation at the foremost part, responsible for the field enhancement. In (b) the surface charge has a node at the end of the tip. (c) Calculated field distribution at a sharp Au tip for an incident electric field vector parallel to the tip shaft. The graphic shows the localization of the electric field at the tip apex. (d): Field distribution for an incident electric field orientated nonparallel to the tip shaft. The field is no longer confined to the tip apex.[48]

symmetric and has the highest amplitude at the end of the tip. Note that, in both cases, there is a formation of standing waves (surface plasmons) in the tip structure.

Independently of the tip's shape and the magnitude of the enhancement factor, the electric field at the vicinity of a sharp tip can be very well described by the fields of an effective dipole $\mu(\omega)$ located at the center of the tip apex and with the magnitude:

$$\mu(\omega) = \begin{bmatrix} \alpha_\perp & 0 & 0 \\ 0 & \alpha_\perp & 0 \\ 0 & 0 & \alpha_\parallel \end{bmatrix} \mathbf{E}_0(\omega) , \tag{4.31}$$

where the z-axis coincides with the tip axis. E_0 is the exciting electric field in the absence of the tip. $\alpha_\perp$ and $\alpha_\parallel$ are, respectively, the transverse and longitudinal polarizabilities.

$\alpha_\perp$ is defined as:

$$\alpha_\perp = 4\pi\varepsilon_0 r^3 \frac{\varepsilon(\omega) - 1}{\varepsilon(\omega) + 2} \,, \tag{4.32}$$

and $\alpha_\parallel$ is defined as:

$$\alpha_\parallel = 2\pi\varepsilon_0 r^3 f_e(\omega) \,. \tag{4.33}$$

Here, ε denotes the bulk dielectric constant of the tip, r is the tip radius and $f_e(\omega)$ is the complex field enhancement factor [48]. Once the tip's dipole is determined, the electric field E in the vicinity of the tip is calculated as:

$$\mathbf{E}(\mathbf{r}, \omega) = \mathbf{E}_0(\mathbf{r}, \omega) + \frac{\omega^2}{\varepsilon_0 c^2} \mathbf{G}(\mathbf{r}, \mathbf{r}_0, \omega)\mu(\omega) \,, \tag{4.34}$$

where $\mathbf{r}_0$ specifies the origin of μ and $\mathbf{G}$ is the dyadic Green's function.

The consequences of the field enhancement for Raman scattering and photoluminescence

Raman scattering and photoluminescence are distinct optical processes which interact somehow with the electronic and vibrational structure of a given material. The former is a coherent process and the later is a non-coherent process. The effects of field enhancement on each signal are expected to vary from each other.

In the case of tip enhanced Raman scattering (TERS), in order to achieve the maximum efficiency, it is important to obtain an enhancement of both, incident and scattered fields. For an incident light with frequency ω_i, the enhancement factor $f(\omega_i)$ is defined as:

$$f(\omega_i) = \frac{E_{tip}(\omega_i)}{E_i(\omega_i)} \,, \tag{4.35}$$

where $E_{tip}(\omega_i)$ is the electric field amplitude at the tip apex and $E_i(\omega_i)$ is the amplitude of the incident electric field. In the same way, it is defined an enhancement factor $f(\omega_S)$ for a scattered field:

$$f(\omega_S) = \frac{E_{tip}(\omega_S)}{E_S(\omega_S)} \,, \tag{4.36}$$

where $E_{tip}(\omega_S)$ is the electric field amplitude at the tip apex and $E_i(\omega_S)$ is the amplitude of the scattered electric field. In most of cases, in a Raman scattering experiment we can say that $\omega_i \sim \omega_S$ and the total field enhancement M is given by:

$$M = f(\omega_i)^2 f(\omega_S)^2 \sim f(\omega_i)^4 \,. \tag{4.37}$$

Eq.4.37 means that the total enhancement of the Raman intensity in a TERS experiment is proportional to the fourth power of the electric field enhancement [48]. In the case

of PL phenomena, the PL intensity is determined by the number of excitons relaxed radioactively from excited states to the ground state. The enhancement of PL therefore depends on the excitation rate and the quantum yield Q denoting the fraction of emitted photons. Accordingly, the PL enhancement due to the presence of the metal tip can be written as:

$$M_{PL} \approx M^{1/2} \frac{Q_{PL}}{Q_{PL0}} \,, \tag{4.38}$$

where Q_{PL} and Q_{PL0} denotes the quantum yield with and without tip, respectively. Finally we comment on Fig. 4.45(b). It should be noticed that no charges can be accumulated at the tip end if the driving field is polarized transverse to the tip axis, and hence no field enhancement is observed (see Figs. 4.45(b) and (d)) [48, 53]. It means that if the incident field is not polarized along the tip axis, only the scattered light can be effectively enhanced, and the maximum enhancement for the Raman intensity will be given by $M = f(\omega_i)^2$.

4.2.6 Converting Gaussian polarized beams into radially polarized beams

If the sample or object are excited in a backscattering geometry (which is the case for our system), unavoidably the major contribution of electric field of the laser light will be perpendicular to the tip and will generate a weak enhancement for both, Raman scattering and photoluminescence. As discussed, to establish a strong field enhancement at the tip, the electric field of the light must be parallel to the tip axis. To fulfill this condition in the backscattering illumination scheme, one should appeal to other polarization configurations. The so-called radially polarized mode offers solutions to all the requirements because it has an extremely strong longitudinal electrical field which is parallel to the tip axis.

Commonly, laser sources output a fundamental Gaussian beam profile. To convert this Gaussian beam into the radially polarized mode one needs to impose different phase shifts to different parts of the laser beam. It is necessary to use four $\lambda/2$ plates with their optical axis differently oriented. Figure 4.46(a) schematically shows how to build the radially polarized mode convertor. Two $\lambda/2$ plates must be carefully cut into four parts. One plate must be cut in the optical axis direction while the another plate must be cut in the direction that makes an angle of 45° with the optical axis direction. Next, two piece from each group must be joined together to form the mode convertor. The different pieces must be glued using UV-optical glue. During the collage, the pieces must stand over a very flat surface to guarantee that no part will be bent.
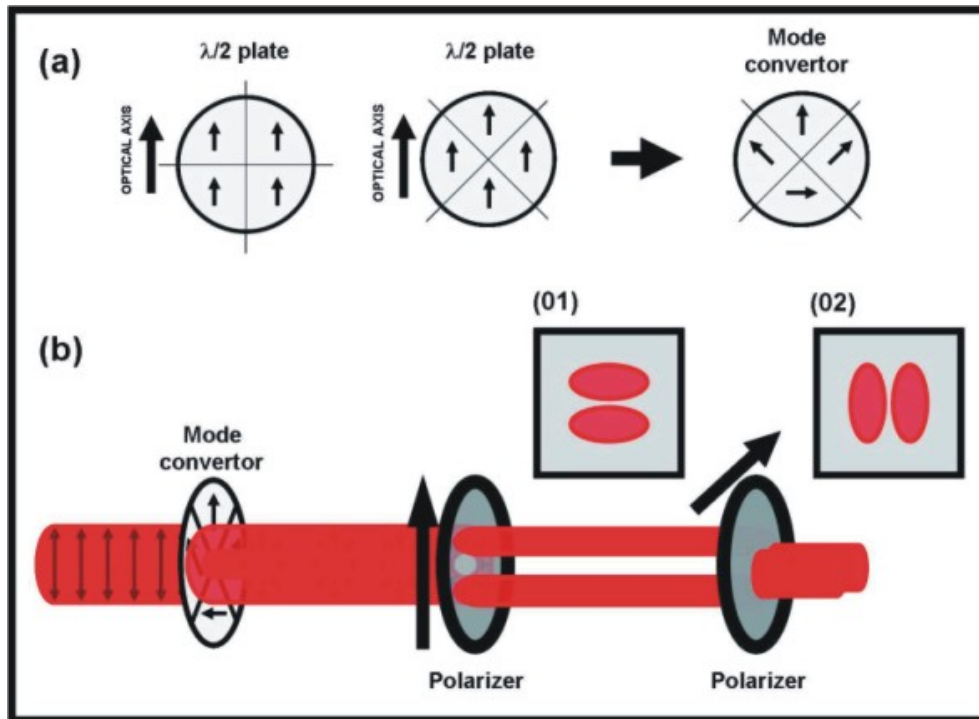
Figure 4.46: (a) Two $\lambda/2$ plates, cut in different directions, are needed to build the radially polarized mode convertor. One cut must be done in the optical axis direction while the another cut must be in the direction making 45° with relation to the optical axis. The mode convertor is built using two pieces of each group. (b) The radially polarized mode has the appearance of a doughnut. By rotating a polarizer continuously in front of the beam, two lobules will also rotate continuously.[48, 53]

Figure 4.46(b) shows how the laser beam must appear after undergoing the mode convertor. The radially polarized mode looks like a doughnut and when its beam is analyzed with the help of a polarizer, only the electrical field components oriented to the polarizer transmission axis will survive. The result is illustrated in panels (01) and (02) to the cases where two polarizers are oriented in 90° with relation to each other. Only two lobules remain and they rotate following the polarizer's transmission axis. By rotating the polarizers continuously, the lobules will also continuously rotate.

The next step is placing the radially polarized mode convertor in the optical path from the laser source to the microscope. Figure 4.47 illustrates the experimental setup. The laser beam must undergo a couple of lenses (L1 and L2) in order to be expanded. Next, the beam must undergo the mode convertor and become radially polarized. Afterwards, the radially polarized beam must be expanded again (by means of the lenses L3 and L4) to achieve a diameter equal to the objective's numerical aperture. A spa-

tial filter must be placed in the focus position in the path between the lenses L3 and L4. The spatial filter prevents any undesirable high diffraction to propagate (it filters the radially polarized mode allowing, basically, the first order to propagate). Finally, the laser mode obtained has a radial polarization in the transversal direction and a strong non-propagating component in the longitudinal direction, as showed by the inset in the Fig. 4.47.
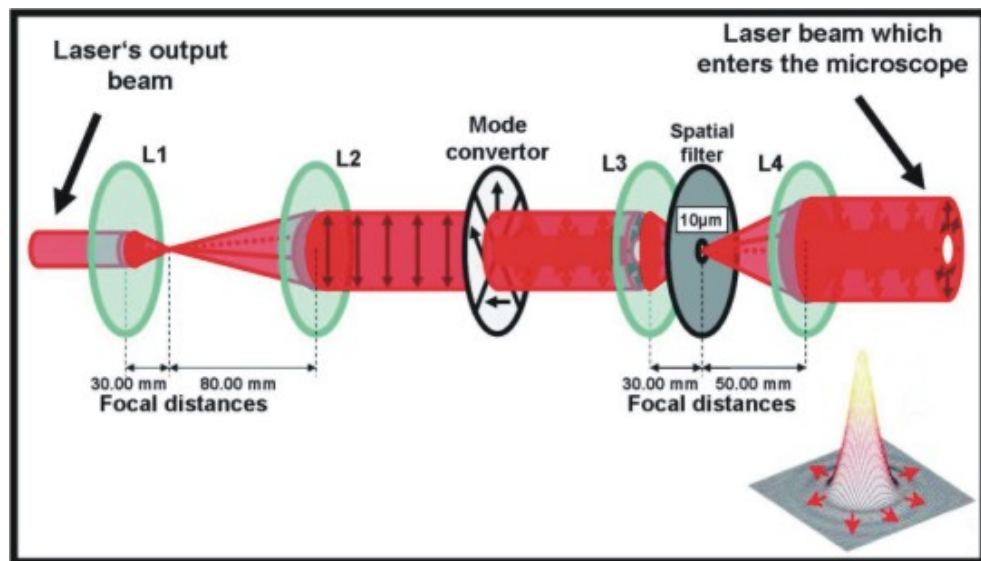
Figure 4.47: Experimental scheme for including the mode convertor in the halfway point of the optical path between the laser and the microscope. A detailed description is given in the text. Inset. Simulation of the field of radially polarized laser beam.[48, 53]

4.2.7 Shielding the system against noises

Near-field systems are very sensitive to undesirable mechanical, optical and electromagnetic noises. To prevent from mechanical noises, the optical table must stand over compressed air-based dampers that work like stabilizers. Our Model is a Stabilizer™ I-2000 manufactured by Newport. Supplied with controlled flow of compressed air at constant pressure, they provide one of the best methods of vibration isolation for critical applications. The system operates on the principle of air pistons, which are equivalent to soft springs. The system counts with leveling valves which control the height of the table, being readjusted every time the table's load varies. The stabilizers are extremely efficient

to block high-frequencies (short-wavelengths) vibrations in both, horizontal and vertical, directions. The microscope stands over pieces of silicone rubber with height of $\approx$30 mm. This piece of silicone must have an intermediate hardness[18]. In the case that this passive damping does not work, the user can try an active damping system. However, this kind of system can offer extra electromagnetic noises which can hamper the AFM electronics.

The whole system must be inside a metallic box which is covered by acoustic foams. Because of the foam, this box isolates the system from acoustic noises. This system, together with the stabilizers and the silicones, guarantees that almost no mechanical noises will reach the scan-head. The box is also efficient to prevent from electromagnetic noises. It must be grounded to prevent from electrostatic charges and because any electric field is null inside it, the box works as a Faraday's cage. Finally, all the sockets used to feed the system must be grounded at the same point to avoid ground loops in the system. High resolution systems have several sensitive instruments connected to each other and ground loops can transmit dramatic noises between these instruments, which is very critical when the system is prepared to process small signals.

4.3   Results: Testing the system

4.3.1   Confocal microscopy measurements

In the last sections a careful analysis of our system is presented. The main steps to set up the system, as well as its components, were explained in detail. The next step is exemplify what we can obtain with all this. Here, I will show two examples of images from experiments that are daily performed in our laboratory. Figure 4.48 shows a typical G-band confocal image of carbon nanotubes. According to Fig. 4.48(c), the resolution observed is 500 nm.

Figure 4.49 is a confocal image of the G-band of a carbon nanonotube serpentine [54]. The graphic in the upper right corner of the Fig. 4.49 shows the line profile along the whole serpentine while the graphic in the bottom right corner is the line profile of the region inside the dark circle shown in the confocal map. A close inspection reveal that the optical resolution achieved is 400 nm.

In both figures, a narrow band-pass filter centered at 700 nm and with a band width of 10 nm is used in front of the APD device. This guarantee that only the light scattered

---

[18]Hint: There is not a specific value for this hardness. Surgical silicones offers an excellent system for damping.
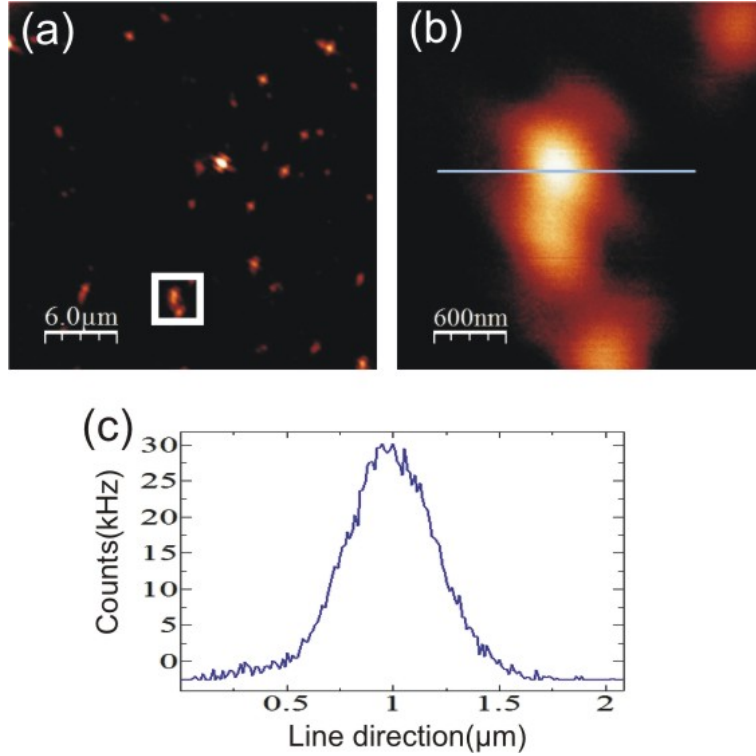
Figure 4.48: Typical G-band confocal image of SWNTs in bundles. (a) A scan area of $30 \times 30 \, \mu\text{m}^2$ was chosen. (b) shows a zoom of the squared region in (a) whose scan area is $3 \times 3 \, \mu\text{m}^2$. (c) The profile which was taken in the region limited by the blue line in (b). The resolution observed is $500 \, \text{nm}$.

referent to the G-band frequency will be mapped. Besides this, the APD accumulation time is set at $40 \, \text{ms}$ while the scan-speed is $200 \, \mu\text{m/s}$. The laser-power at the microscope rear entrance is $2 \, \text{mW}$.

4.3.2 Atomic force microscopy (AFM) measurements

It is evident that, in principle, each object studied by AFM requires the use of a specific set of parameters (feedback gain, time constant, line speed, etc...) that provides good images. However some parameters never change. The parameters for the tip-approaching procedure can be always used no matter the sample. Table 4.10 summarizes RHK's parameters during tip approach. The Easy-PLL parameters are given in Table 4.11.

When the approach is done, some parameters must be adjusted. In most cases, when the sample is deposited over a cover-slip or quartz, it is possible to set some standard parameters for topography scans. In the RHK's front panel the gain must be readjusted to
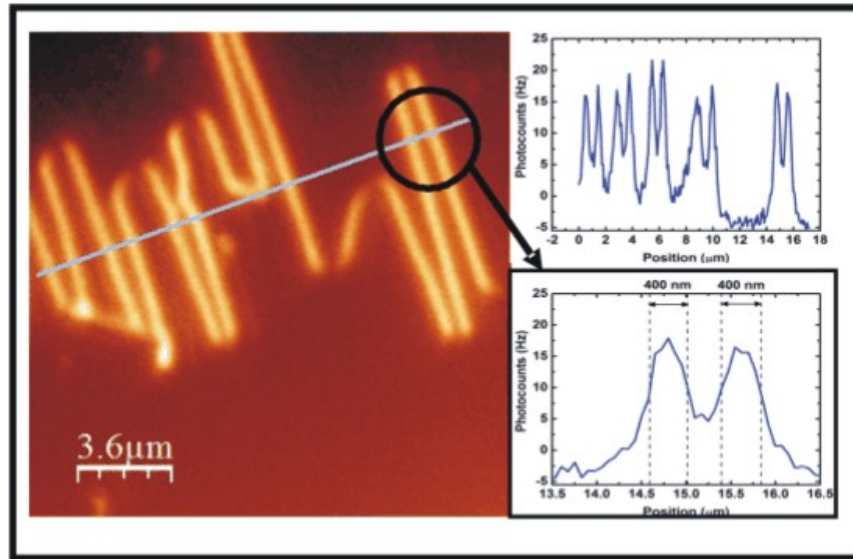
Figure 4.49: The confocal map of the G-band of a carbon nanotube serpentine. Its profile is exhibited by the graphic at the upper right corner. The graphic at the bottom right corner is a zoom of the circled region in the confocal map.

Front panel parameters			
X,Y offset	**X,Y Slope Comp.**	**Amp. Selec.**	**Z coarse**
5	5	1×	5
Z fine	**Bias range**	**Bias polarity**	**Inp. Polarity**
5	1 V	+	SPM/NORMAL
Gain	**Time const.**	**Setpoint**	**A/D Gain**
1.5	5	5.15	1

Table 4.10: RHK's parameters for the tip approach procedure. Note that the parameters which were not mentioned do not play any role to the approach. They can be at any value. The only exception is the "X and Y scan range" that can not be more than 5 V, otherwise the XY-stage can be burnt.

0.6. In case that the objects have small heights (<2 nm), the A/D gain can be readjusted to 4 or 8. The scan speed is set, in the XPMpro^{TM} software to 500 nm/s. In the Easy-Pll's hardware, the "Setpoint" should be readjusted to 3. It is important to say that, before

Hardwear parameters			
Mode	**Monitor**	**Setpoint**	**Amp. Control**
Const. Amp.	Amp.	5	On/1/×10
Phase Shift	**Range**	**Drive out**	**Detector in**
0°/0°/0	<50	Low-pass on	×0.01
Softwear parameters			
Input	**Output**	**Tip guard**	**Op. Mode**
Auto range	G. ×1/P.P on	R. T. on/P. D. on	Const. Amp.
Lock Range	**Bandwidth**		
±183 Hz	120 Hz		

Table 4.11: Easy-PLL's parameters for the tip approach procedure. Note that the software parameters are always the same for both, the tip approach and scan procedures. "G." stands for "Gain", "P.P." stands for "positive polarity", "R.T." stands for "Retract Tip" and "P.D." stands for "positive direction".

starting with the approach procedures, the user must:

- In the XPMpro™ (see Fig. 4.15), go to the navigation window and, in the approach setting commands, actuate the "manual control" command.

- In the "manual control" command, set the command "Tip Retract" ON.

- The Bias DVM must read between -0.1 and -0.3. If it does not, go to the Easy-PLL software and change the frequency offset until the DVM reads a desired value.

- Set "Tip Retract" OFF and start the approach procedure.

Next, some examples of typical topographic images obtained from our system. Figure 4.50 shows a topography image of a microscope glass where the tip used has a diameter of about 40 nm. Figures 4.50(a) and (b) show the trace and retrace, respectively, of an scan area of $3 \times 3 \, \mu m^2$ and Figures 4.50(c) and (d) are the zoom (whose scan area is $1 \times 1 \, \mu m^2$) of the region marked with squares in Figs.4.50(a) and (b), respectively. Figure 4.50(e) shows the profile for both, trace (blue solid line) and retrace (red solid line), that were taken in the region limited by the light blue lines in Figs.4.50(c) and (d). It is observed that the groove has a height of about 2 nm and a width of about 40 nm while the step has about 1.5 nm of height and a width of about 40 nm, which are in accordance with the tip dimensions.
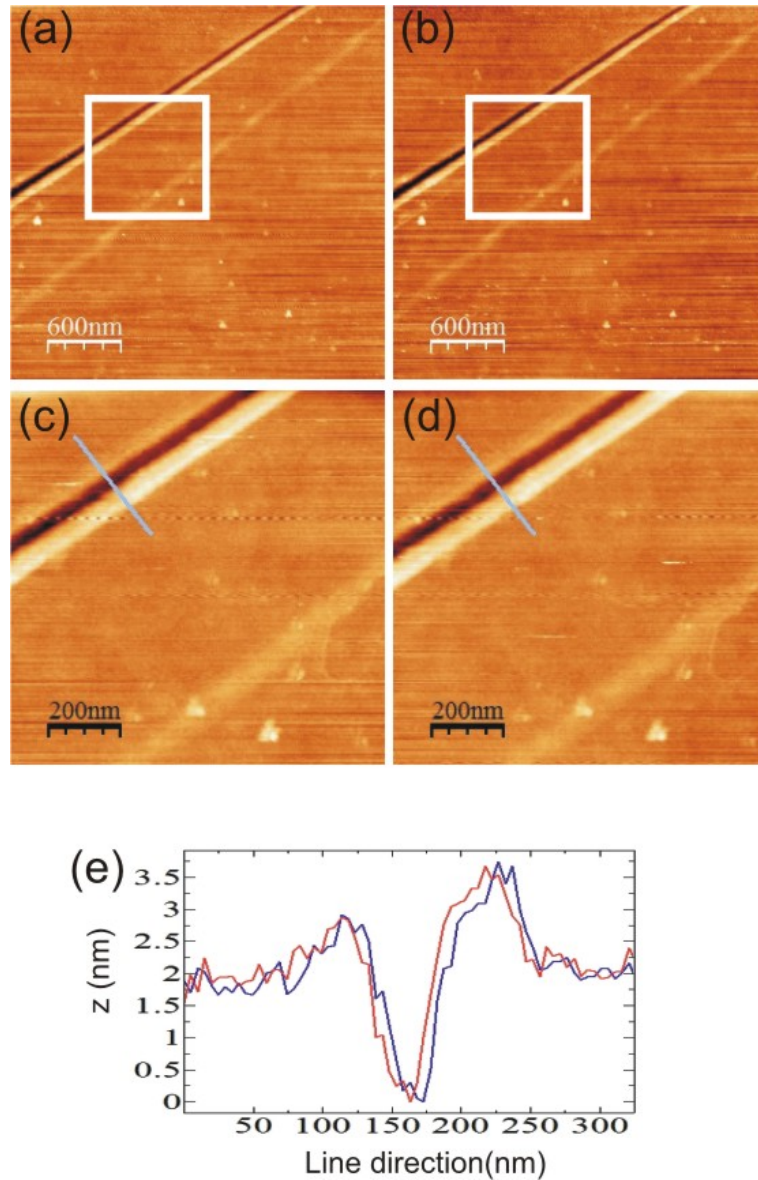
Figure 4.50: Topography image of a microscope glass. (a) and (b) are the trace and retrace image whose the scan area is $3 \times 3\,\mu\text{m}^2$. (c) and (d) are the zoom of the region marked with the squares in (a) and (b), whose scan area is $1 \times 1\,\mu\text{m}^2$. (e) shows the profile for both, trace (blue solid line) and retrace (red solid line), that were taken in the region limited by the light blue lines in (c) and (d).

Figure 4.51 shows the topographic image of a commercial standard sample used to calibrate the Z piezo displacement/voltage conversion. Figures 4.51(a) and (b) show the trace and retrace, respectively, of an scan area of $6 \times 6\,\mu\text{m}^2$ and Fig. 4.51 shows the profile for both, trace (black solid line) and retrace (red solid line), that were taken in the region

109

limited by the light blue lines in Figs.4.51(a) and (b). The width and heights delimited present values in agreement with the factory values.
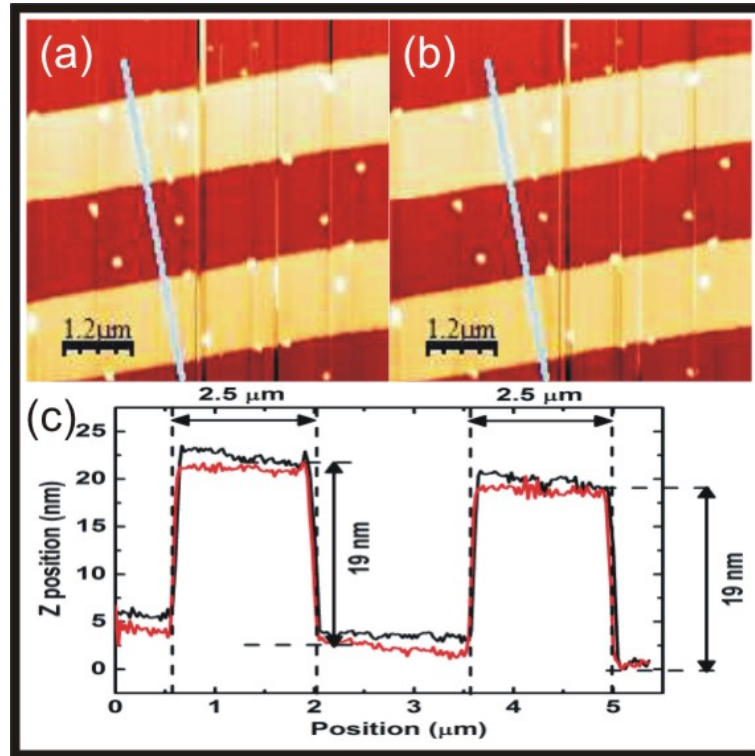
Figure 4.51: Topography image of a standard sample for Z displacement/voltage calibration. (a) and (b) are the trace and retrace image whose the scan area is $6 \times 6\,\mu\mathrm{m}^2$. (c) shows the profile for both, trace (black solid line) and retrace (red solid line), that were taken in the region limited by the light blue lines in (a) and (b).

Finally, Fig. 4.52 shows the topography image of a carbon nanotube after a treatment to remove the SDS solvent. Figures 4.52(a) and (b) show the trace and retrace, respectively, of a scan area of $0.8 \times 0.8\,\mu\mathrm{m}^2$ and Fig. 4.52 shows the profile for both, trace (black solid line) and retrace (red solid line), that were taken in the region limited by the light blue lines in Figs.4.52(a) and (b).

4.3.3 Near-field measurements

What is different when we are setting the parameters to perform near-field? Answer:
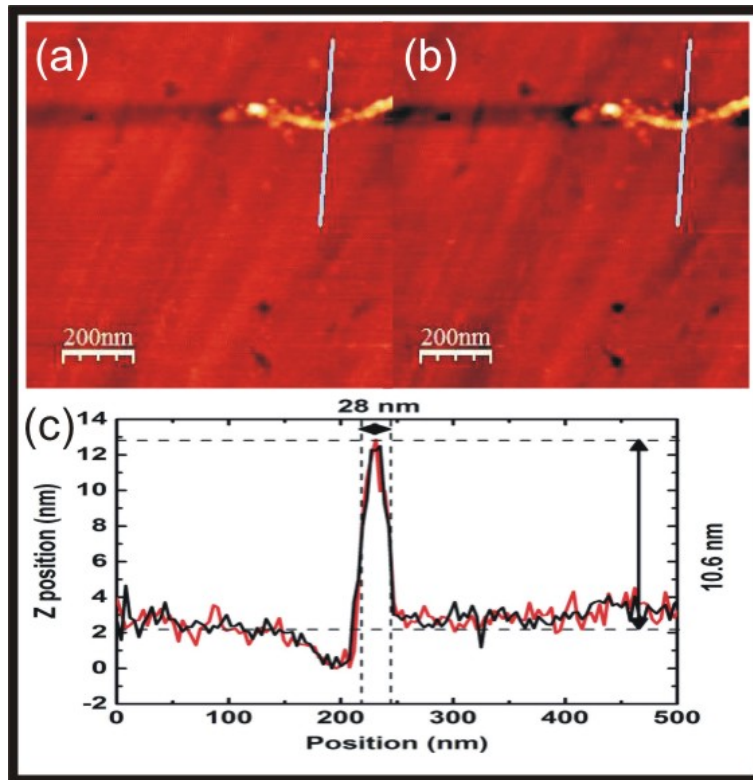
Figure 4.52: Topography image of a carbon nanotube after a treatment to remove the SDS solvent. (a) and (b) are the trace and retrace image whose scan area is $0.8 \times 0.8 \, \mu m^2$. (c) shows the profile for both, trace (black solid line) and retrace (red solid line), that were taken in the region limited by the light blue lines in (a) and (b).

nothing changes in the confocal microscopy parameter[19] and nothing changes in the AFM microscopy parameters. However, after the tip approach is done, the user must retract the tip a little (at about 300 steps of the picomotor) and place the tip end into the laser focus at the sample's surface. This can be done by adjusting the XY offset voltages and the linear micrometers where the "height-adjustable screws" are sitting (our stage is the model "411/422 Series Miniature Ball Bearing Linear Stages" manufacture by Newport®). The focus can be optimized following, with an oscilloscope, the light scattered by the tip when it passes over the laser focus.

Figure 4.53 (a) and (b) show, respectively, the topography image and the photoluminescence near-field signal of a $(6,5)$ SWNT wrapped with DNA. The scan area is $0.8 \times 0.8 \, \mu m^2$. Figs. 4.53 (c) and (d) show, respectively, the line profile for both, the

---

[19]Strictly speaking, the user must decrease the laser power reaching the tip. High powers can melt the gold tip apex.

topography and the near-field images, that were taken in the region limited by the light blue lines. The topography shows that the tube has a diameter of about 1.3 nm, which is obtained from the height of the line profile in the Fig. 4.53(c). The near-field profile shows that an optical resolution between 10 and 54 nm was achieved. Both, topographic and near-field images were simultaneously recorded.
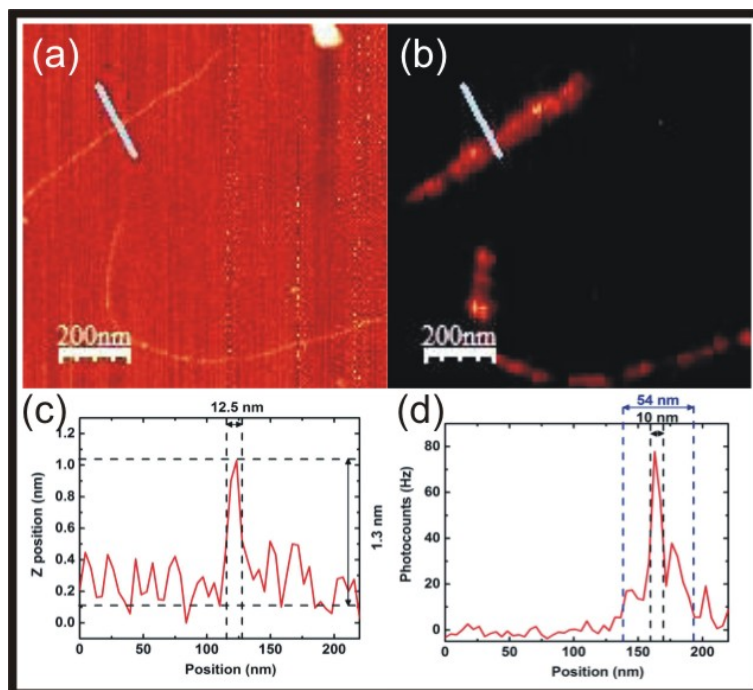
Figure 4.53: (a) and (b) show, respectively, the topography and the near-field images of a $(6, 5)$ SWNT wrapped with DNA. (c) and (d) show, respectively, the line profile for both, the topography and teh near-field images, that were taken in the region limited by the light blue lines. An optical resolution between 10 and 54 nm has been achieved.

Another example of near-field photoluminescence is given in Fig. 4.54. Again, the Figs. 4.54(a) and (b) show, respectively, the topography image and the photoluminescence near-field signal of a $(6, 5)$ SWNT wrapped with DNA. The scan area is $3 \times 3 \, \mu m^2$. In both, Figs. 4.54(a) and (b), in the graphics numbered from (01) to (04), the line profiles were taken in the region limited by the light blue lines. A close inspection of the profiles allows one to ensure that optical resolutions raging from 42 to 54 nm were achieved and the SWNT diameter is about 1.3 nm, which is obtained by measuring the line's profile height in Fig. 4.54(a). Again, the topographic and near-field images were simultaneously

112

recorded.
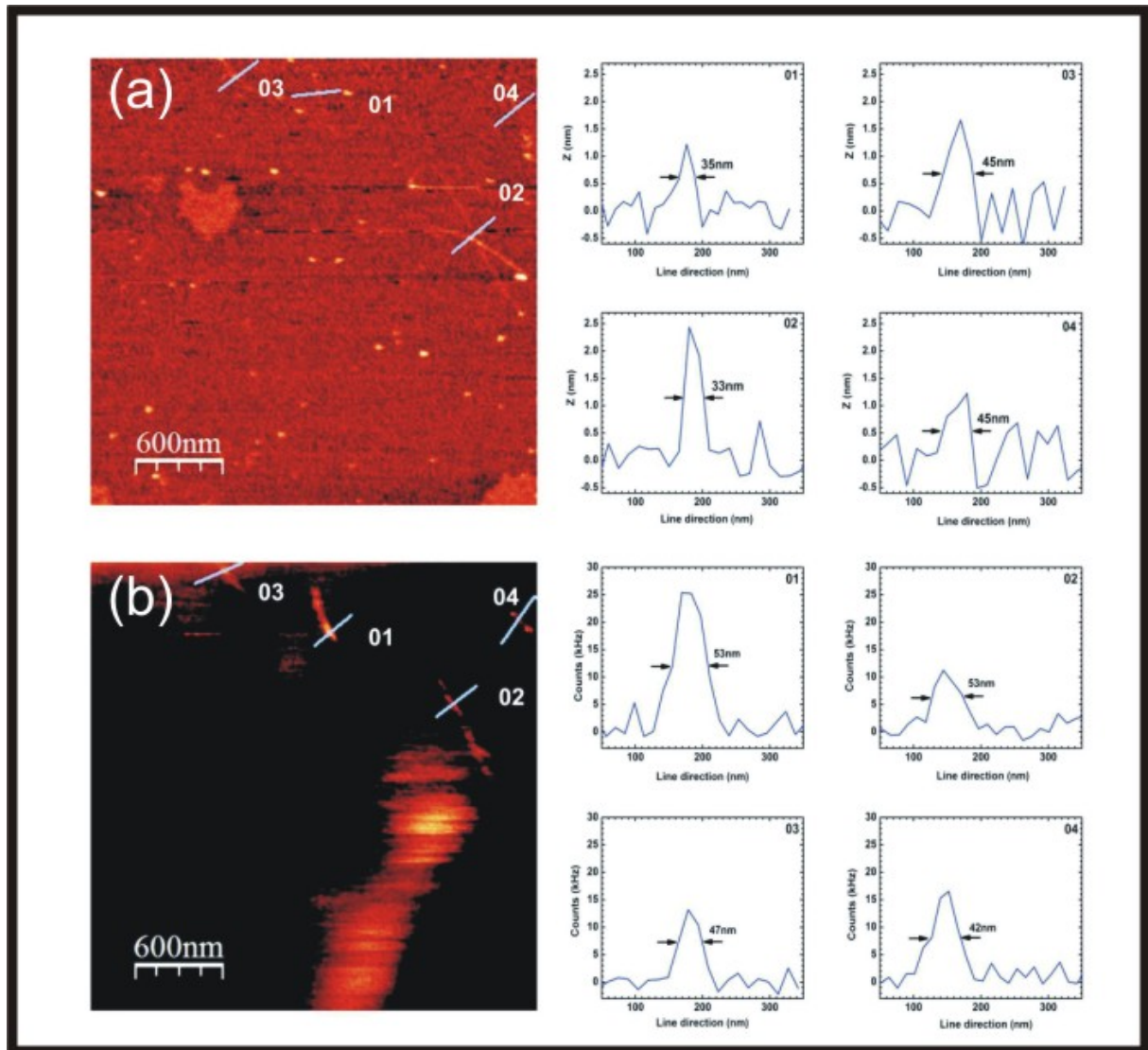
Figure 4.54: (a) and (b) show, respectively, the topography and the near-field images of a $(6,5)$ SWNT wrapped with DNA. In both, the Figs. 4.54(a) and (b), the graphics numbered from (01) to (04), the line profiles that were taken in the region limited by the light blue lines. Optical resolutions between 42 and 54 nm was been achieved.

In both the experiments, the APD accumulation time is set at 10 ms while the scan-speed is $0.5\,\mu$m/s. The laser-power at the microscope rear entrance is $100\,\mu$W.

4.4 Summary

In this technical report, a very detailed description of the optical, mechanical and electronic devices necessary to implement a system for nano-spectroscopy and - manipulation was given. The purpose of this system is joining a confocal microscopy setup to an atomic force microscopy (AFM) setup. With the confocal system, we are able to perform spectroscopy with optical resolutions coming close to $\lambda/2$, where λ is the light source wavelength. The AFM system allows us to photograph and manipulate nano-scaled systems. Both together allow simultaneous experiments of spectroscopy and nano-manipulation. By using a metallic tip, we also can go beyond the classical limit of diffraction and perform nano-spectroscopy. The attempt is to make this report a start-point to whom desires to build a similar experimental scheme. The last chapter exhibited several examples of confocal, topography and near-field images trying to guide the readers in how to obtain such an images.

Chapter 5

Environmental Effects on the SWNTs Radial Breathing Mode Frequency ω_{RBM}

Chapter 2 introduced some basic aspects of single wall carbon nanotubes (SWNTs) electronic and vibrational physics and how to use resonance Raman spectroscopy to characterize them. This chapter will present the role of environmental effects on the SWNTs radial breathing mode frequency (ω_{RBM}). By environmental effects one should understand as the effect of a changing medium surrounding the SWNTs, e.g. bundling, surfactant used for nanotubes dispersion, substrates, on their vibrational structure.

5.1 The ω_{RBM} vs. d_t relation and the role of a changing environment

In Chapter 2 it is shown that the radial breathing mode (RBM) provides the spectroscopic signature of single wall carbon nanotubes (SWNTs) [10, 55]. The RBM frequency (ω_{RBM}) depends on SWNTs diameter (d_t), which is related to their (n, m) structural indices by Eq. 2.2 [10].

The experimental results in the literature have been fitted with the relation,

$$\omega_{\mathrm{RBM}} = \mathbf{A}/d_t + \mathbf{B}\,, \tag{5.1}$$

with values for $\mathbf{A}$ and $\mathbf{B}$ varying from paper to paper [13, 39, 40, 41, 42, 56, 57, 58, 59, 60, 61]. Table 5.1 summarizes some of these values. The empirical constant factor $\mathbf{B}$ prevents the expected limit of a graphene sheet from being achieved, where the ω_{RBM} must go to

zero when d_t approaches infinity. Therefore, **B** is supposedly associated with an environmental effect on ω_{RBM}, rather then an intrinsic property of SWNTs. Environmental effect here means the effect of the surrounding medium, such as bundling, molecules adsorbed from the air, surfactant used for SWNT bundles dispersion, substrates where the tubes are sitting.

Sample	A	B
Laser ablation bundled SWNTs [56]	232	0
SWNTs at silicon substrate [39]	248	0
HiPco SWNTs SDS[a]-dispersed [40]	223.5	12.5
HiPco SWNTs SDS[a]-dispersed [41]	214.4	18.7
HiPco SWNTs SDS[a]-dispersed [42]	218	17
Free-hanging SWNTs [60]	204	27
Alcohol-assisted CVD SWNTs [13]	217	15
HiPco SWNTs SDS[a]-dispersed [61]	227	$7.3/11.8^b$

Table 5.1: Some important **A** and **B** values for the relation $\omega_{RBM} = \mathbf{A}/\mathbf{d_t} + \mathbf{B}$ reported in the literature.
[a]SDS stands for sodium dodecyl sulfate.
[b]Different values of **B** were found for semiconducting/metallic SWNTs.

Here, resonance Raman scattering is used to measure the RBMs of a sample composed of "super-growth" (*S.G.*) SWNTs. These SWNTs are grown by the water-assisted chemical vapor deposition (CVD) method [62, 63, 64, 65]. This water-assisted CVD process has been called "super-growth" because it generates millimeter-long isolated and high-purity SWNTs [62, 63, 64, 65]. The water in this case is the catalyst while $Fecl_3$ (or Fe, Al/Fe, Al_2O_3/Fe, Al_2O_3/Co)is used as percussor. The "super-growth" SWNTs exhibit a broad d_t distribution (d_t from 1 to 4 nm) and all tube chiralities ($0° \leq \theta \leq 30°$). The SWNTs are vertically aligned from a silicon substrate to form a very sparse material, where SWNTs represent only 3.6% of the total volume [64].

These SWNTs follow a simple linear relation between ω_{RBM} and d_t, with the proportionality constant $\mathbf{A} = 227.0\,\mathrm{cm}^{-1}\mathrm{nm}$, in agreement with the elastic property of graphite (see Section 2.1.2), and with a negligible environmental effect ($\mathbf{B} \approx \mathbf{0}$) [33, 34]. All the observed ω_{RBM} reported in the literature are upshifted from this fundamental relation [13, 39, 40, 41, 42, 56, 57, 58, 59, 60, 61]. The upshift exhibits a d_t dependence in quantitative agreement with recent predictions considering the Van der Waals interaction

between SWNTs and environment [66].

With the "super-growth" sample, 125 Raman spectra, each at a different E_{laser} excitation, are used to assign the (n, m) structure of 197 different SWNTs (of which 73 are metallic and 124 semiconducting) [10, 34, 35]. As explained in Chapter 2, each RBM spectrum exhibits bands that are composed by a convolution of Lorentzian peaks. Each Lorentzian corresponds to the RBM Stokes spectrum of one specific (n, m) SWNT. The SWNTs observed are that ones having an optical transition energy (usually called E_{ii}, $i = 1, 2, ...$) in resonance with the excitation laser energy. Although the (n, m) assignment is complex, it is a reliable procedure, and have already been extensively discussed in the literature (see references [41, 42, 59] and specially [13]). This analysis is important because all the 197 (n, m) tubes assigned in this work have their optical transition energies (E_{ii}) upshifted from others in the literature [13, 40, 41, 42, 57, 59, 67, 68, 69, 70].

Using all the 197 (n, m) SWNTs assigned and the relation given by Eq.2.2, the experimental ω_{RBM} can be plotted as a function of d_t, as shown in Fig.5.1. Fitting the data shown in Fig.5.1 using the relation $\omega_{\mathrm{RBM}} = \mathbf{A}/d_t + \mathbf{B}$ we obtain $\mathbf{A} = (\mathbf{227.0 \pm 0.3})\,\mathrm{cm}^{-1}\mathrm{nm}$ and $\mathbf{B} = (\mathbf{0.3 \pm 0.2})\,\mathrm{cm}^{-1}$. This result is unexpected for being different from all results in the literature [39, 40, 41, 13, 42, 56, 57, 58, 59, 60, 61], and it is remarkable because a standard relation between ω_{RBM} and d_t with a negligible environmental effect ($\mathbf{B} \approx \mathbf{0}$) has been obtained, so that $\omega_{RBM} \to 0$ as $d_t \to \infty$. Furthermore, the value of the constant $\mathbf{A} = 227.0\,\mathrm{cm}^{-1}\mathrm{nm}$, that accounts for the vibrational characteristics of SWNTs, exactly matches the value predicted by elasticity theory [33, 71] and is in excellent accordance with the value predicted by recent tight-binding method calculations for isolated SWNTs [72]. Both the theoretical methods are parameterized by the speed of sound in graphite. Therefore, this result directly connects one-dimensional carbon nanotubes and their two-dimensional counterpart graphene (see Chapter 2).

To understand why the ω_{RBM} dependence with d_t in "super-growth" SWNTs is unique, the results obtained here are compared to the results in the literature. Figure 5.2(a) shows the difference between several $\omega_{\mathrm{RBM}} = \mathbf{A}/d_t + \mathbf{B}$ found in the literature [13, 39, 40, 41, 42, 56, 60] and the $\omega_{RBM} = 227.0/d_t$ established here. All the curves in the literature converge within the 1 to 2 nm d_t range, that is where most of the experimental data were actually obtained. Figure 5.2(b) shows the difference between the ω_{RBM} experimental values from the literature $(\omega_{\mathrm{RBM}}^{Lit.})$[13, 39, 40, 41, 42, 57, 58, 59, 60] and from this work $(\omega_{\mathrm{RBM}}^{S.G.},\ S.G.$ stands for "super-growth") as a function of d_t. All the published results for $\omega_{\mathrm{RBM}}^{Lit.}$ are grouped in Fig.5.2(b) on a d_t dependent upshifted trend for $\Delta\omega_{\mathrm{RBM}} = \omega_{\mathrm{RBM}}^{Lit.} - \omega_{\mathrm{RBM}}^{S.G.}$. The down-triangles in Fig.5.2(b), that spread out from the
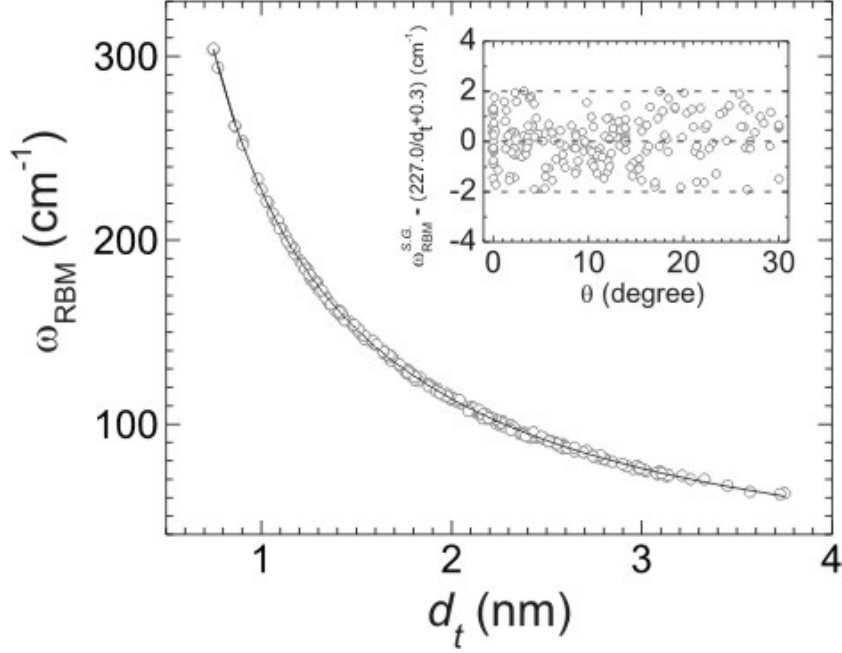
Figure 5.1: Experimental radial breathing mode frequency (ω_{RBM}) as a function of tube diameter (d_t). Open circles represent the SWNT data assigned in this work and the solid line is a fitting to the data given by ω_{RBM}=227.0/d_t + 0.3. The inset plots the difference between the experimental ω_{RBM} and 227.0/d_t + 0.3 as a function of SWNT chiral angle (θ). [34]

general trend, are related to the ω_{RBM}=248/d_t relation (dashed dark-grey curve from reference [39] in Fig.5.2(a)) proposed in 2001 [39, 55] by imposing the $\mathbf{B} = 0$ condition on the basis of $\omega_{\text{RBM}} \to 0$ as $d_t \to \infty$. The ω_{RBM}=248/d_t relation was obtained with an E_{ii} vs d_t relation that did not consider nanotube curvature effects (the first-neighbor tight-binding model), which are important for small d_t tubes (below d_t=1.2 nm) [10]. Therefore, the scatter in the data from the general trend in Fig.5.2(b) might be due to a wrong (n, m) assignment below d_t=1.2 nm. It is likely that the same argument is valid for the ω_{RBM} vs d_t relation obtained in Ref. [56] (black dash-dotted line in Fig.5.2(a)), since it is also based on the first-neighbor tight-binding model. Therefore, we demonstrated that the d_t dependence of the difference between the experimental data in the literature and the fundamental relation ω_{RBM}=227.0/d_t is always the same.

A recent molecular dynamics calculation considering Van der Waals interactions between SWNTs and a shell of adsorbed fluid [66] is now applied to explain the result shown in Fig. 5.2(b). Longhurst and Quirke considered SWNTs within the 1.03 to 1.73 nm range surrounded by water at 300 K, and showed a d_t dependent upshift on ω_{RBM} as compared to
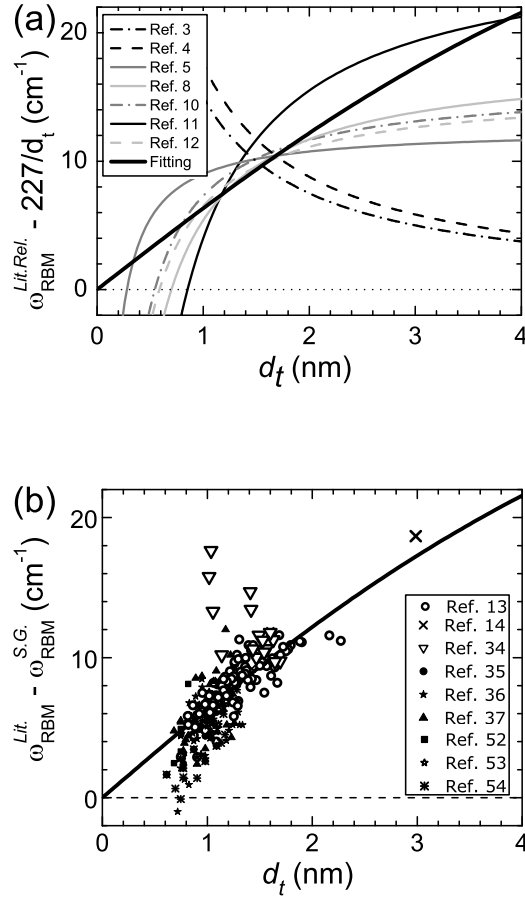
Figure 5.2: (a) Difference between ω_{RBM} relations from the literature ($\omega_{\mathrm{RBM}}^{Lit.Rel.}$) and $\omega_{\mathrm{RBM}}=227.0/d_t$ as a function of tube diameter (d_t). (b) Difference between ω_{RBM} data from the literature ($\omega_{\mathrm{RBM}}^{Lit.}$) and ω_{RBM} data from this work ($\omega_{\mathrm{RBM}}^{S.G.}$) as a function of d_t. Each symbol represents data from a different reference (see legends). The thick solid line is a fit to the data in (b), as discussed in the text, and it is also shown in (a). [34]

the tube in vacuum, ranging from 4 to $10\,\mathrm{cm}^{-1}$, in perfect agreement with our observation in Fig. 5.2(b). The shifts were explained by the interaction of the RBM with the adsorbed shell of fluid surrounding the nanotube via Lennard-Jones potential, plus a small contribution (10-20 %) of static pressure difference at the nanotube surface as compared with the bulk fluid induced by the curved interface. Then They proposed a model that fits their calculations, considering the RBM of a coupled system SWNT/environment composed by two spring constants: one coming from the C−C bond strength and the other coming

from the interaction strength between the SWNT and its surroundings. The problem of addressing the environmental effect on ω_{RBM} is now reduced to solve a simple harmonic oscillator for a cylindrical shell subjected to a inwards pressure ($p(x)$) given by:

$$\frac{2x(t)}{d_t^2} + \frac{\rho h}{Eh}(1-\nu^2)\frac{\partial^2 x(t)}{\partial t^2} = -\frac{(1-\nu^2)}{Eh}p(x)\,, \tag{5.2}$$

where $x(t)$ is the displacement in the radial direction, $p(x) = (24K/s_0^2)x(t)$, K (in eV/$\mathring{A}^2$) gives the Van der Waals interaction strength, s_0 is the equilibrium separation between the SWNT wall and the environment shell, E is the Young's modulus, ρ is the mass density per unit volume, ν is Poisson's ratio and h represents the thickness of the shell (see Subsection 2.1.2). If $p(x)$ is null, Eq.5.2 gives the fundamental ω_{RBM}^0 for pristine SWNT

$$\omega_{RBM}^0 = \left\{ \frac{1}{\pi c}\left[\frac{Eh}{\rho h(1-\nu^2)}\right]^{1/2}\right\}\frac{1}{d_t}\,, \tag{5.3}$$

where the term inside the curly bracket is established here as $227.0\,\mathrm{cm}^{-1}\mathrm{nm}$ (see appendix 2.1.2). For $p(x)$ non$-$null we have

$$\omega_{RBM}^{'} = 227.0\left[\frac{1}{d_t^2} + \frac{6(1-\nu^2)}{Eh}\frac{K}{s_0^2}\right]^{1/2}\,, \tag{5.4}$$

where $[6(1 - \nu^2)/Eh] = 26.3\,\mathring{A}^2/\mathrm{eV}$. The shift on $\omega_{RBM}^{'}$ due to the environment is given by:

$$\Delta\omega_{\mathrm{RBM}} = \omega_{\mathrm{RBM}} - \omega_{\mathrm{RBM}}^0 = 227/d_t\left[\sqrt{1 + C_e \cdot d_t^2} - 1\right]\,, \tag{5.5}$$

where $C_e = [6(1-\nu^2)/Eh][K/s_0^2]\,\mathrm{nm}^{-2}$.

The data in the Fig.5.2(b) is fitted (see black thick solid line) by considering C_e in Eq.5.5 as an adjustable parameter. The best fit is obtained with $C_e = (0.057 \pm 0.003)\,\mathrm{nm}^{-2}$. The d_t dependent behavior of the environmental effect in ω_{RBM} is then established up to $d_t = 3\,\mathrm{nm}$. Similar environmental effect is obtained for SWNTs in bundles [56, 13], surrounded by different surfactants [40, 57, 58, 41, 59, 42], in air suspended by posts [60] or sitting on a SiO$_2$ substrate [39], but absent in the "super-growth" SWNTs [34].

5.2 The effect of the environment on the $\omega_{\mathrm{RBM}}^{S.G.}$

The result discussed above gave rise to two different scenarios: one for the "super-growth" ($\omega_{\mathrm{RBM}}^{S.G.} = 227/d_t$) and another for all the other RBMs reported in the literature [39, 40, 41, 13, 42, 56, 57, 58, 59, 60, 61], which were shown to be fitted by

$\omega_{\text{RBM}} = (227/d_t)\sqrt{1 + (0.057) \cdot d_t^2}$. To understand why we have two scenarios, resonance Raman spectroscopy was used to study the ω_{RBM} of the "super-growth" SWNTs under three different conditions: I) an as-grown carpet-like sample, (II) in solution, dispersed with a surfactant and III) in bundles. Previously measured Raman maps, constructed by using different excitation laser energies, [10, 41, 42, 13] are here used as a guide for the (n, m) analysis which can be shown here by employing a single laser line [1]. The excitation laser energy chosen for this experiment was the most commonly found in worldwide laboratories, $E_{laser} = 2.41\,\text{eV}$ (514.5 nm) (For additional experimental details, see Appendix A). To quantify the changes in the RBM frequencies due to a change in the environment, Fig. 5.3 shows the spectrum for the "super-growth" SWNTs in a sodium dodecyl sulfate (SDS) solution (top), the Raman spectrum obtained for the bundled sample (middle) and the Raman spectrum for the as-grown "super-growth" SWNTs (bottom). In each spectrum, the raw spectra are fitted by Lorentzians representing the RBM features from SWNTs that are in resonance with the excitation laser and contribute to the spectra [73].

The arrows in Fig. 5.3 serve as a guide to the eyes, whereby we can easily realize that the frequencies for the solution and bundled samples, which from now on are called, respectively, $\omega_{\text{RBM}}^{solut.}$ and $\omega_{\text{RBM}}^{bundl.}$, are upshifted with respect to the as-grown values $\omega_{\text{RBM}}^{S.G.}$. In agreement with what is showed in the section 5.1, the larger the d_t value, the greater is the frequency upshift. Only a slight difference is observed between the $\omega_{\text{RBM}}^{solut.}$ and the $\omega_{\text{RBM}}^{bundl.}$, which suggests that the interactions between the tubes with their respective environments are in the same range of strength. Its worth to comment that the surfactant dramatically suppresses the Raman response of tubes with diameters higher than 0.9 nm ($d_t \geqslant 0.9\,\text{nm}$) when in solution. When drying the bundled sample, the RBM response for tubes with diameters ranging from 0.9 to 1.3 nm is recovered. This result is consistent with experiments of absorption, photoluminescence and Raman scattering in other SWNTs samples [74, 75, 76, 77, 78].

Figure 5.4 shows the differences between $\omega_{\text{RBM}}^{solut./bundl.}$ and $\omega_{\text{RBM}}^{S.G.}$ plotted as a function of d_t. The open circles stand for $\Delta\omega_{\text{RBM}}^{bundl.} = \omega_{\text{RBM}}^{bundl.} - \omega_{\text{RBM}}^{S.G.}$ and the down triangles stand for $\Delta\omega_{\text{RBM}}^{solut.} = \omega_{\text{RBM}}^{solut.} - \omega_{\text{RBM}}^{S.G.}$ (see Table 5.2). The black solid line in Fig.5.4, which fits the symbols, is given by Eq. (5.5) with $C_e = 0.056$. This result shows that the ω_{RBM} for both solution and bundles are upshifted in relation to the frequencies observed in the as-grown sample, following exactly the same van der Waals interaction model that describes all the ω_{RBM} in the literature, as shown in the section 5.1. The two scenarios

---

[1]The reader may interested to have a careful reading of Subsection 2.2.1where a complete discussion on how to properly make (n, m) is given.
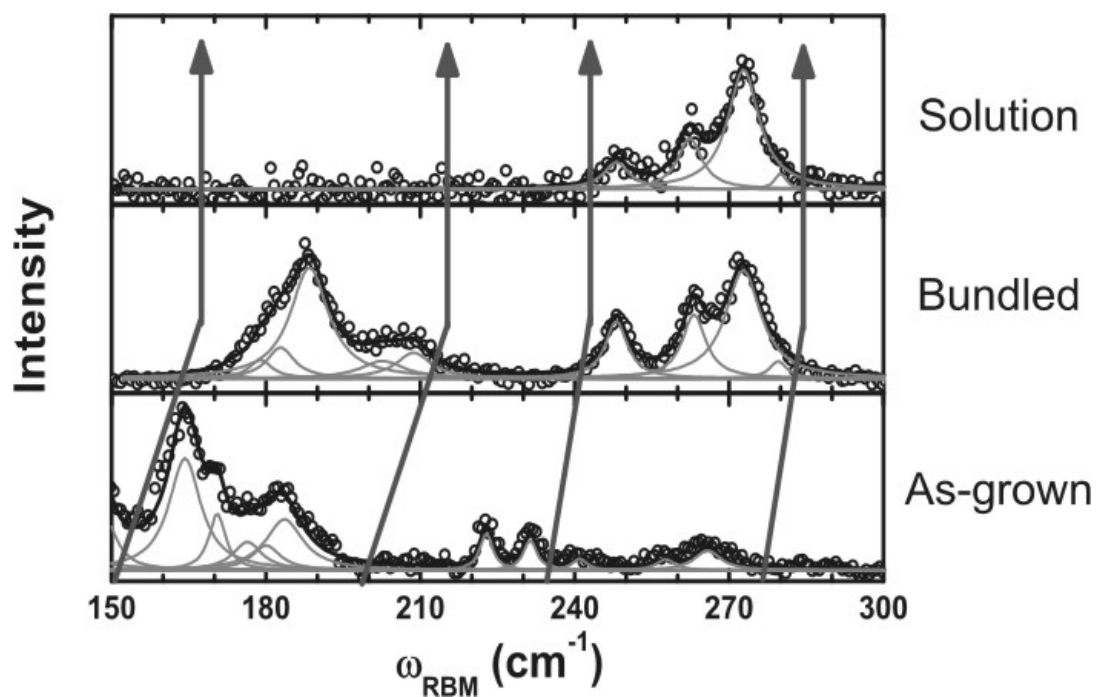
Figure 5.3: The Raman spectrum obtained for: (top) the solution of "super-growth" SWNTs in SDS, (middle) the bundled "super-growth" sample and (bottom) the as-grown sample. All the spectra were obtained by using $E_{laser} = 2.41\,eV$ (514.5 nm) and normalized to the highest intensity peak. The open circles represent the raw data and the solid gray curves are Lorentizians representing the RBMs from the SWNT species in resonance. The black solid line is the result obtained from the Lorentizian fitting procedure. The arrows are a guide to the eyes showing that the ω_{RBM} is upshifted for the solution and bundled samples, in comparison with the as-grown sample. [73]
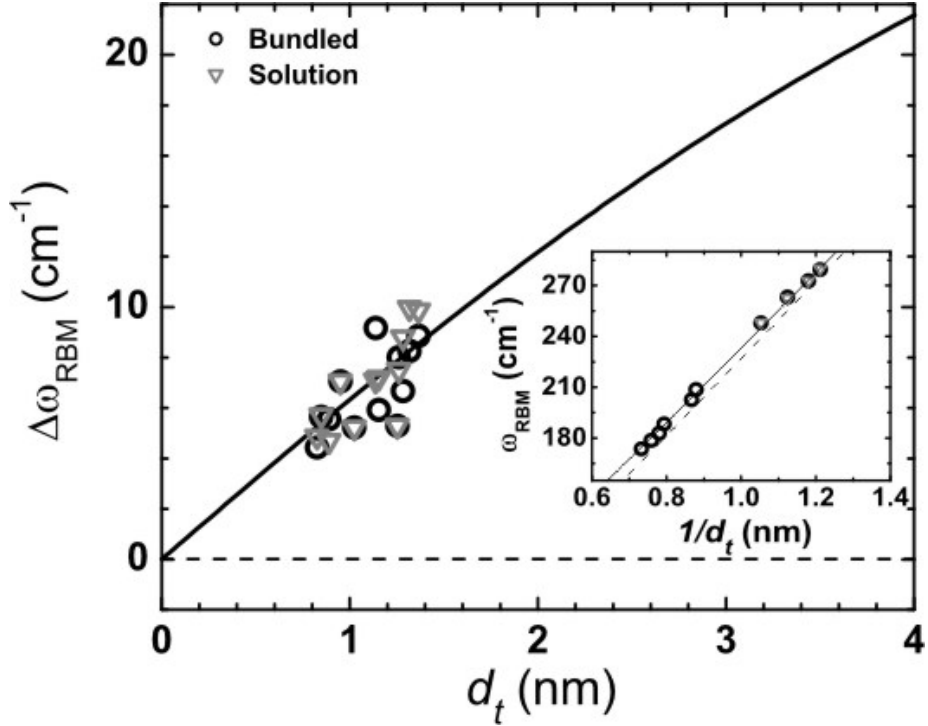
Figure 5.4: The as-grown super-growth frequencies ($\omega_{\text{RBM}}^{S.G.}$) are subtracted from the frequencies of both solution (∇) and bundled ($\bigcirc$) samples represented, respectively, by $\omega_{\text{RBM}}^{Solut.}$ and $\omega_{\text{RBM}}^{Bundl.}$, and plotted as a function of d_t. The solid curve describes the frequency shift behavior due to van der Waals interactions between the tube walls and their environment. Inset: $\omega_{\text{RBM}}^{solut./bundl.}$ plotted as a function of $1/d_t$, where the dashed line is given by $\omega_{\text{RBM}}^{S.G.} = 227/d_t$ and the solid line is given by $\omega_{\text{RBM}}^{solut./bundl.} = (227/d_t)\sqrt{1 + 0.056 \cdot d_t^2}$. [73]

are them merged indicating that the as-grown "super-growth" SWNTs are, somehow, free from environmental effects.

$\omega_{RBM}^{as-grown}$	$\omega_{RBM}^{bundl.}$	$\omega_{RBM}^{solut.}$	(n,m)	$\Delta\omega_{RBM}^{bundl.}$	$\Delta\omega_{RBM}^{solut.}$
275.1^a	279.5	279.9	$(10,1)$	4.4	4.9
267.1	272.8	272.8	$(9,3)$	5.6	5.7
257.6	263.2	262.3	$(8,5)$	5.6	4.7
240.9	248.0	248.0	$(7,7)$	7.1	7.1
222.8	228.0^b	228.0^b	$(9,6)$	5.2	5.2
199.5^a	208.7	206.6^b	$(14,1)$	9.2	7.1
196.7^a	202.7	203.9^b	$(13,3)$	5.9	7.2
183.6	188.9^b	188.9^b	$(16,0)$	5.3	5.3
180.4	188.4	187.9^b	$(15,2)$	8.0	7.5
176.2	182.9	185.0^b	$(14,4)$	6.7	8.8
170.5	178.7	180.4^b	$(13,6)$	8.3	10.0
164.8	173.7	174.7^b	$(12,8)$	8.9	9.9

Table 5.2: ω_{RBM} values and respective (n,m) assignments for the as-grown, solution and bundled SWNTs. Here $\Delta\omega_{RBM}^{solut./bundl.} = \omega_{RBM}^{solut./bundl.} - \omega_{RBM}^{S.G.}$
[a]Calculated using $\omega_{RBM} = 227/d_t$
[b]Calculated using $\omega_{RBM} = (227/d_t)\sqrt{1 + 0.056 \cdot d_t^2}$

5.3   Summary

We showed that the *S.G.* SWNTs present a relation $\omega_{RBM}=227.0/d_t$ that gives the fundamental spectroscopic signature of the SWNT d_t. This relation is in agreement with calculations using the velocity of sound in graphite and has $\omega_{RBM} \to 0$ as $d_t \to \infty$, recovering the 2D graphene (see Section 5.1). All of this make the *S.G.* sample an excellent prototype to understand the different RBM behavior of SWNTs. All the ω_{RBM} results in the literature are upshifted from the *S.G.* values due to Van der Waals interaction between the tube walls and the surrounding environment, and can be generally described by $\omega_{RBM} = 227/d_t(\sqrt{1 + C_e \cdot d_t^2})$ where C_e is an adjustable parameter. Additionally, when the *S.G.* tubes are exposed to some different environment, e.g. surfactant or bundles, they have their ω_{RBM} merged to the ones presented in the literature. The main contents of this chapter are published in *PhysicalReview* B **77**, 241403(R) (2008); and *AppliedPhysicsLetters* **95**, 261902 (2009).

Chapter 6

Environmental and Screening Effects on the SWNTs Energy Transitions E_{ii}

In chapter 5 we worked out the phenomena behind the changes on the ω_{RBM} due to a changing environment. In this chapter we are focused on understanding how a changing environment changes the SWNTs electronic properties, in special, how important is the environment on the screening of exciton's bounding and, therefore, how it influences the SWNTs optical transitions.

6.1   The effect of dielectric screening on E_{ii}

As mentioned in Chapter 5, 125 different laser lines were used to characterize the "super-growth" carbon nanotubes, giving us 125 different Raman profiles. In figure 6.1(a) the 125 resonance Raman spectra were used to generate a two-dimensional plot giving the Raman intensity as a function of the laser excitation energy (E_{laser}) and radial breathing mode frequency (ω_{RBM}). A Raman peak appears at a given ω_{RBM} whenever E_{laser} reaches the optical transition energy (E_{ii})[1], i.e. when resonance is established for a given carbon nanotube in the sample. Figure 6.1(b) is a plot of all the 197 $E_{ii}^{S.G.}$ extracted from the 2D map as a function of $\omega_{RBM}^{S.G.}$. Note that $E_{ii}^{S.G.}$ is ranging from E_{11}^{S} up to E_{66}^{S}, allowing a careful analysis of energy transition behavior (here S stands for semiconducting tube, otherwise M will be used for metallic tubes). Figure 6.1(c) gives the Kataura plot for SWNTs. All the ω_{RBM} values were obtained using the relation $\omega_{RBM} = 227/d_t$ (see

---

[1]Strictly speaking there is also resonance with the scattered light.

Chapter 5) and the E_{ii} values were obtained by the equation 6.1 (see it further in the text).
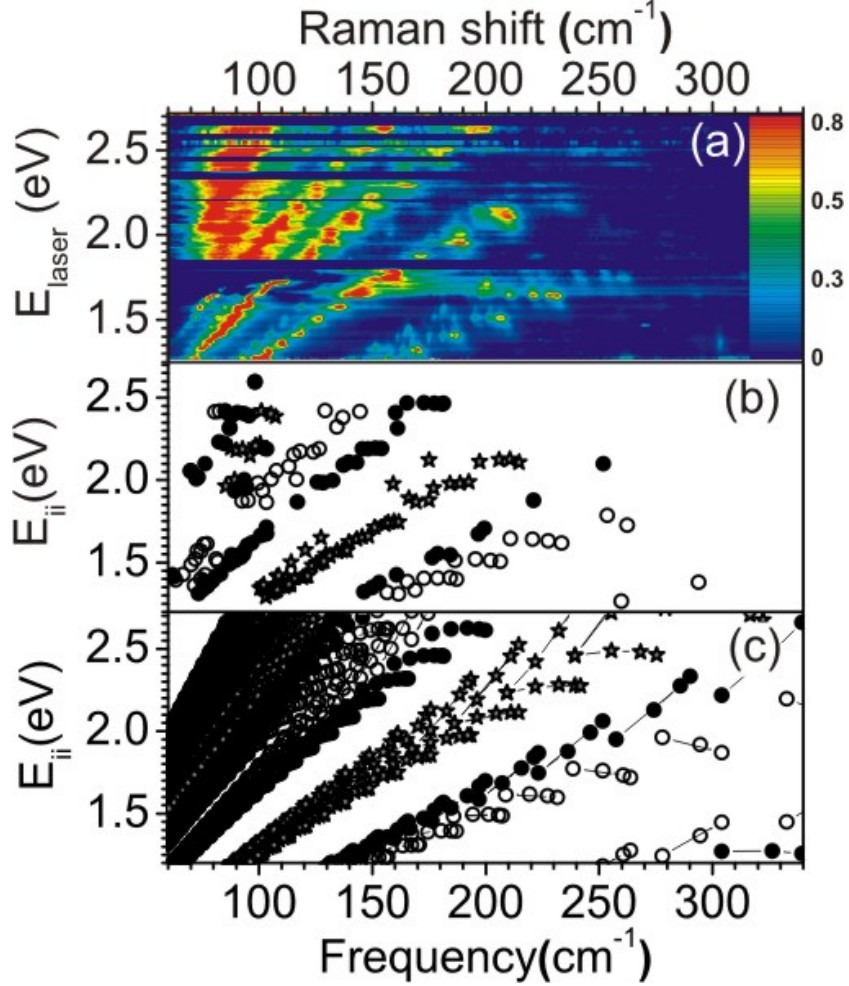
Figure 6.1: (a) 2D color map showing the $S.G.$ SWNT RBM spectral evolution as a function of excitation laser energy. The intensity of each spectrum is normalized to the strongest peak. (b) Plot of all transitions energies ($E_{ii}^{S.G.}$) experimentally obtained as a function of ω_{RBM}. (c) The Kataura plot for $S.G.$ SWNTs. The transition energies were calculated using Eq. 6.1, that is obtained by fitting the available $E_{ii}^{S.G.}$ (panel (b)) and plotted as a function of ω_{RBM}, given by $\omega_{RBM} = 227/d_t$ [34]. In (b) and (c) the gray stars stand for metallic tubes, the black bullets stand for type I semiconducting tubes and the opened bullets stand for type II semiconducting tubes. [35]

For a fixed SWNT chirality, the E_{ii} values are expected to exhibit a simple scaling behavior when plotted as a function of p/d_t, where $p = 1, 2, ..., 8$ for E_{11}^S, E_{22}^S,..., E_{66}^S,
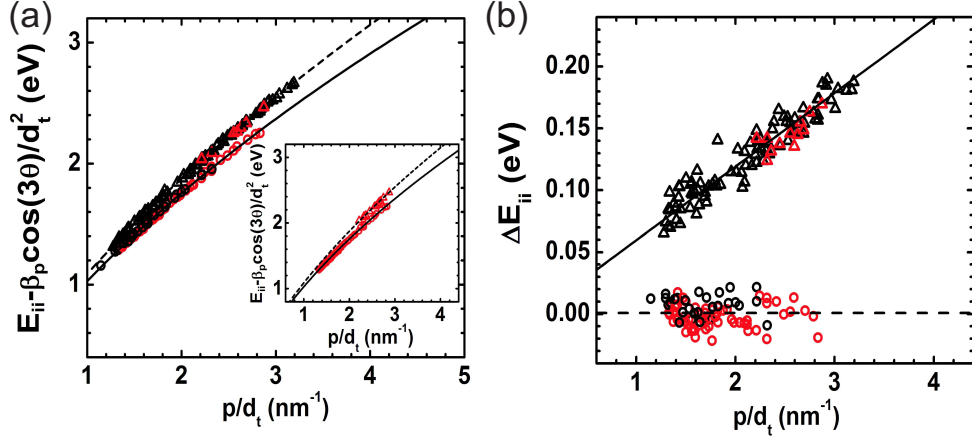
Figure 6.2: (a) Experimental optical transition energies as a function of p/d_t, after correcting for the chiral angle dependence ($E_{ii} - \beta_p \cos 3\theta/d_t^2$). The chirality dependence corrected E_{11}^S, E_{22}^S (open black circles) and E_{11}^M (open red circles) are fitted with Eq. 6.1 (see the black solid line). Inset: the metallic transitions (E_{11}^M and E_{22}^M) are in evidence. While E_{11}^M follows the same behavior as the lower semiconducting transitions (E_{11}^S, E_{22}^S) the E_{22}^M follows the higher semiconducting transitions (E_{33}^S,..., E_{66}^S). (b) Deviation (ΔE) of the ($E_{ii} - \beta_p \cos 3\theta/d_t^2$) data from the fitting curve in (a), versus $1/d_t$. The solid line ($\Delta E = 0.059p/d_t$) fits the ΔE_{ii}^S, for i = 1,..6 and ΔE_{22}^M (open black and red triangles, respectively). The dashed line in (a) is given by Eq. 6.1 plus $0.059p/d_t$.

respectively [12, 31]. The integer p corresponds to the distance ratio of the cutting lines from the K point [79]. Thus p/d_t represents the distance of the k point from the K point in the two-dimensional Brillouin zone of graphene. To a first approximation, considering the linear dispersion of the graphene close to the high-symmetry K-point and wavevector quantization along the circumference of the SWNT, the optical transition energies in carbon nanotubes are given by $E_{ii} = \hbar v_F (4p/3d_t)$ [10], where v_F is the Fermi velocity. For a fixed diameter, the E_{ii} values are expected to exhibit a comparably smaller dependence on the chiral angle θ (ranging from 0 to 30°) [10]. The chirality correction is null for armchair tubes ($\theta = 30°$) and is a maximum for zigzag tubes ($\theta = 0$), given approximately by $\beta_p \cos 3\theta/d_t^2$ [10].

Figures 6.2(a) and (b) shows a plot of the assigned transition energies as a function of p/d_t, after correction for their chirality dependence obtained by subtracting ($\beta_p \cos 3\theta/d_t^2$) from the experimentally obtained E_{ii} values. As largely discussed by Kane and Mele [12, 13, 31], the non-linear scaling is due to many-body effects and can be fit with a

logarithmic correction given by [2],

$$E_{ii}(p, d_t) = a\frac{p}{d_t}\left[1 + b\log\frac{c}{p/d_t}\right] + \beta_p\cos 3\theta/d_t^2 ,\qquad (6.1)$$

where $a = 1.074\,\text{eV}\cdot\text{nm}$, $b = 0.467$ and $c = 0.812\,\text{nm}^{-1}$. The β_p values for the lower(upper) E_{ii} branches are -0.07(0.09), -0.18(0.14), -0.19(0.29), -0.33(0.49), -0.43(0.59), -0.6(0.57), -0.6(0.73) and -0.65(not measured) for $p = 1, 2, 3, ..., 8$, respectively. To calculate E_{ii} higher than E_{11}^M ($p > 3$) the term $0.059p/d_t$ has to be added to the Eq. 6.1 [35]. It is worth to comment that such a nonlinear scaling relation results from a renormalization of the Coulomb energy that arises from treating the close-range many-body interactions of 2D graphene as a noninteracting quasi-particle. For the 1D SWNT system, long-range interactions strongly increase this quasi-particle gap, but in semiconductors the observed effect is significantly reduced due to the exciton binding energy. Thus, while the diameter dependence of the transition energies is defined by the logarithmic scaling, their absolute energy position is ultimately determined by the difference between the electron self-energy and the exciton binding energy. Its also important to note that this analysis gives results which are in complete accordance to the results we found in 2007 for a sample composed of vertically aligned SWNTs grown by an alcohol-assisted CVD method [13]. The higher $E_{ii}^{S.G.}$ ($E_{ii}^{S.G.} > E_{11}^M$) clearly do not follow the same scaling law as the E_{11}^S and E_{22}^S transitions, showing and enforcing once more the results obtained in 2007 that there is something fundamentally different between the first two semiconducting and first metallic energy optical transitions and the subsequent transitions in semiconducting and metallic SWNTs [13]. However, the adjustable coefficients of Eq. 6.1 are different due to different environmental conditions, as discussed further in Section 6.2.

6.1.1 The E_{11}^M and E_{22}^M transitions

Interestingly, while the higher energy branch of the E_{11}^M values was not observed for the measurements reported previously [56, 39, 40, 58, 41, 42, 13], the $S.G.$ sample provided a set of data for, both the higher and lower energies E_{11}^M for metallic nanotubes, besides giving information about the poorly investigated E_{22}^M, as highlighted in the Fig. 6.3.

As discussed further in the text, for comparison to theory, it is important to note that all transition energies determined from the $S.G.$ sample, for both semiconducting and metallic types, are found to be blue-shifted from energies previously found for other SWNT sample types [34]. The experimental points in Fig. 6.4(a) are in good agreement with their

---

[2]Chapter 2 brings a simple discussion about many-body calculations.
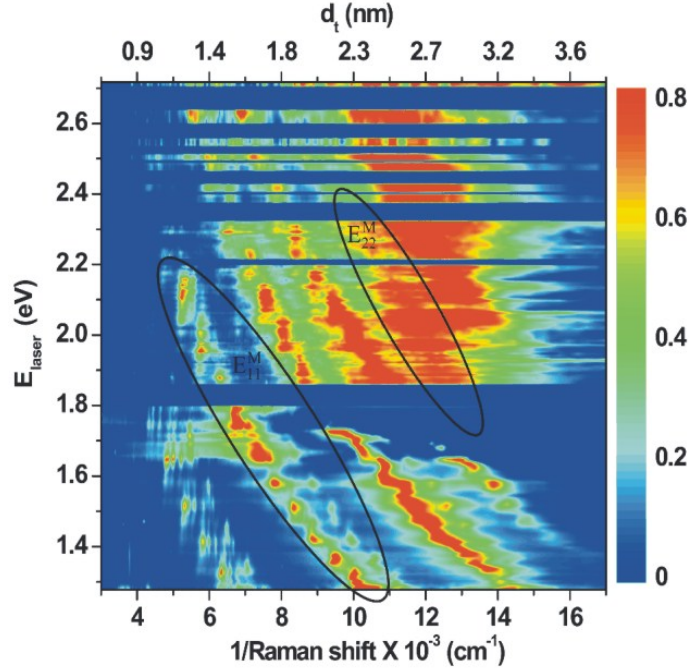
Figure 6.3: The 2D Raman excitation map showing the RBM intensity as a function of laser excitation energy and the inverse of the Stokes-Raman frequency (proportional to nanotube diameter). Each spectrum composing the plot has been normalized by the strongest peak for better clarity of the RBM resonances. The E11M and E22M features are highlighted. The upper axis is obtained considering $\omega_{RBM} = 227/d_t$. [34, 80]

theoretical counterparts and are found to match well to the expected family patterns. We find that there is a systematic deviation of the theoretical values from the experimental points, with values being underestimated at larger diameters and overestimated at smaller diameter. The difference between the experimental and theoretical values as a function of inverse diameter [Fig. 6.4(b)] shows a strong linear dependence possibly arising from how diameter-dependent exciton screening is treated within the theory (see section 6.2). For eight chiralities we are able to obtain sufficiently clear spectral features to allow the simultaneous extraction of energies for both the upper and lower branches (not simultaneously available for other metallic species for which the upper branches were observed) presenting the opportunity to directly evaluate the trigonal warping-induced splitting. In Fig. 6.4(c) we plot the difference between the available lower and upper-branches energies and compare values to the ETB expectations. Differences between theory and experiment range from 4 to 60 meV. The splitting shows a linear dependence with $1/d_t$ that approaches zero in the large-diameter limit, in agreement with expectations [80]. Although only one point in Fig. 6.4(c) is from E_{22}^M, there is a clear break in splitting behavior as one goes to

higher-order transitions. While further experimental data are necessary to explore this behavior, the increased splitting is expected as a result of the asymmetry of the trigonal warping effect in different directions within the Brillouin zone, which yields an increased dispersion along the $K - \Gamma$ direction (compared to that in the $K - M$ direction) as one moves further from the K-point for higher-order transitions. The E_{22}^{HM} energy thus increases faster than E_{22}^{LM} and results in an increased splitting relative to that found for E_{11}^{M}.

Finally, when the scaling law (Eq. 6.1) analysis is applied to the metallic E_{ii}, the data for both upper and lower branches closely match the semiconducting trendlines [80], *i.e.* E_{11}^{M} follows (E_{11}^{S}, E_{22}^{S}), while E_{22}^{M} follows (E_{33}^{S},..., E_{66}^{S}). Figure 6.2(a) and its inset show this trends very clearly. The excellent representation of the trend in the metallic transition energies by the semiconductor logarithmic scaling law is indirect evidence that the metallic transitions are also excitonic in nature. If one first assumes no exciton, then it is possible that significant metallic screening reduces the E_{11}^{M} self-energies sufficiently to allow for a coincidental overlap with the E_{11}^{S} and E_{22}^{S} scaling line. A simultaneous overlap of E_{22}^{M} with the E_{33}^{S},..., E_{66}^{S} scaling line, however, is unlikely in the absence of the exciton. Lack of a binding-energy stabilization for E_{22}^{M} would cause its scaling line to appear above the E_{33}^{S},..., E_{66}^{S} line, which is not the case. Thus, the existence of excitons in these 1D metals is strongly suggested over the full diameter and energy ranges measured [80].

6.1.2 The $E_{ii}^{S.G.}$ exhibits the highest E_{ii} values

As done to the ω_{RBM} frequencies, it is of fundamental importance to understand the effect of a changing environment on the $E_{ii}^{S.G.}$. The dielectric screening plays an important effect on the energy transitions mainly because it can dramatically change the strength of the exciton bounding. Changing the SWNTs environment is changing the dielectric screening phenomena. Here, we have compared our results with others available in the literature [40, 57, 41, 59, 42, 13, 67, 68, 69, 70]. Figure 6.5 shows the difference between E_{ii} from the literature ($E_{ii}^{Lit.}$) and $E_{ii}^{S.G.}$ as a function of tube diameter. The energy difference ($\Delta E_{ii} = E_{ii}^{Lit.} - E_{ii}^{S.G.}$) has an average dependence on d_t (see black solid curve in Fig. 6.5).

In Fig. 6.5, except for the star symbols that come from Rayleigh scattering [70], all the other ΔE_{ii} are negative, *i.e.* the E_{ii} values for the water-growth assisted sample measured here are higher than all the values published in the literature. This result suggests we measured the optical properties of pristine SWNTs in a dielectric constant environment of $\kappa_{env} \to 1$. As predicted by Y. Miyauchi *et al.* [44], an increase of the
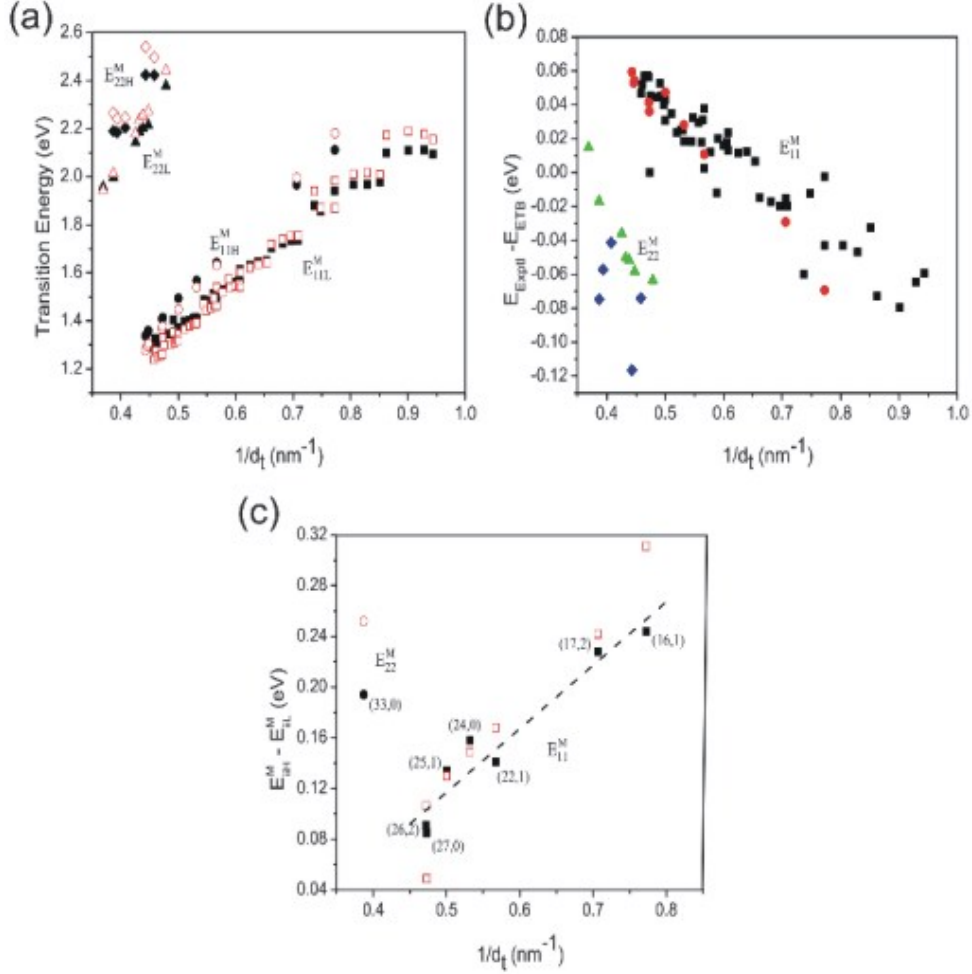
Figure 6.4: (a) A comparison of experimental (solid symbols) and ETB-determined (open symbols) metallic transition energies as a function of inverse nanotube diameter for E_{11}^{LM} (squares), E_{11}^{HM} (circles), E_{22}^{LM} (triangles), and E_{22}^{HM} (diamonds). (b) Difference in energy between experimental and ETB-determined results as a function of inverse nanotube diameter for E_{11}^{LM} (squares), E_{11}^{HM} (circles), E_{22}^{LM} (triangles), and E_{22}^{HM} (diamonds). (c) Energy splittings $(E_{ii}^{HM} - E_{ii}^{LM})$ for experimental (solid symbols) and ETB-determined (open symbols) transitions. Specific (n, m) species are identified. The dashed line is a linear fit to the E_{11}^{M} experimental data with $(E_{ii}^{HM} - E_{ii}^{LM}) = 0.5/d_t - 0.13$. [80]

dielectric constant of the environment generates a downshift in E_{ii}. The usually obtained results ($\varepsilon = 2.2$) generates a downshift of about ~ 40 meV, as roughly observed in Fig. 6.5. However, the downshift should depend on d_t, as suggested by the data in Fig. 6.5.

At this point we have two problems which merge into a unique physical effect. In the last discussion it is clear that when a environment is changed, the self-energy conection and the exciton's binding are also changed, yielding the downshift in most of the transitions
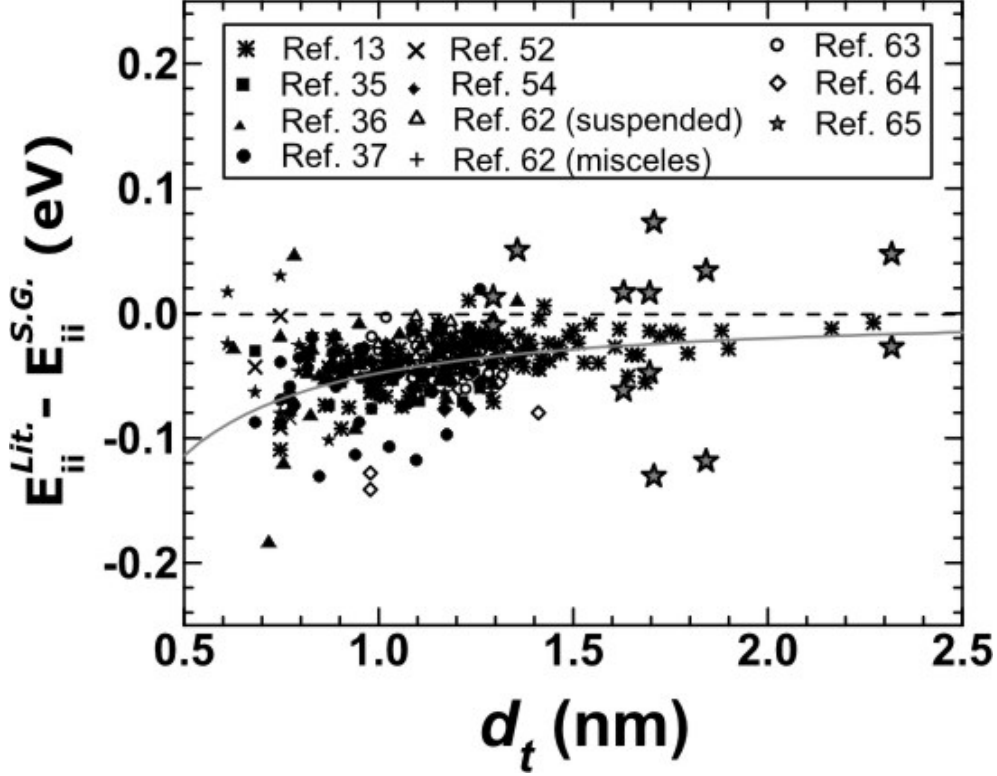
Figure 6.5: The difference between E_{ii} obtained from the literature ($E_{ii}^{Lit.}$) and E_{ii} from this work ($E_{ii}^{S.G.}$) are plotted as a function of d_t. Each symbol represents data from a different reference. The black solid line is a guide to the eye for the average value of ΔE_{ii}. The inset shows ΔE_{ii} as a function of chiral angle (θ). No dependence with chiral angle or $2n + m$ families are observed. [35]

in the literature [34]. As regards the energy scaling breakdown, discussed in Chapter 3, two explanations could be acceptable: (1) Quantum-chemistry calculations explain the scaling-law breakdown showing that the excitons related to higher transitions are weakly bound (or are even unbounded e-h pairs) [13, 11] due to the mixing of the DOS of E_{11}^S and E_{22}^S with E_{33}^S and so on and (2) Solid-state physics calculations, both tight binding and first-principles, that give an opposite picture, *i.e.* that the excitons which are related to the higher transitions are more strongly bound than the lower ones, and the stronger many-body effects cause the breakdown of the scaling law [15, 16]. The higher transitions exciton states would be strongly bounded because the effective mass of electron and hole in these higher transitions are heavier than in the lower transitions [15].

All these points clearly evidence that the experimental results themselves did not offer a conclusive answer towards one or the other theoretical model, as well as a proper model to predict changes in E_{ii} due to a changing environment. As told in Chapter 3 we

are, therefore, led to a deep search for the missing physics; i.e. the dielectric screening provided by a given medium.

6.2 The d_t dependence of the dielectric constant for the excitonic E_{ii}

The assignment of E_{ii} for SWNTs over a large region of both d_t (0.7-3.8 nm) and E_{ii} (1.2-2.7 eV) values and for a variety of surrounding materials are now available, thus making it possible to accurately determine the effect of the dielectric constant κ on E_{ii}, which is important for a general SWNT sample characterization and for the (n, m) assignment of individual tubes. Here we show d_t-dependent effective κ values for the exciton calculation that are needed to reproduce the experimental E_{ii} values consistently. The results thus obtained can be used by researchers in interpreting their optical experiments and environment effects.

Figure 6.6 shows a map of experimental E_{ii} values (black dots) from the SWNT S.G. sample. The resulting data for the E_{ii} transition energies are plotted as a function of ω_{RBM}, as obtained by resonance Raman spectroscopy (RRS), as explained in Chapter 2. In Fig. 6.6, the experimental values of E_{ii} vs. ω_{RBM} for the "super-growth" sample E_{ii}^{exp} are compared with the calculated bright exciton energies E_{ii}^{cal} (open circles and stars). Although E_{ii}^{cal} include SWNT curvature and many-body effects [16], clearly the E_{ii}^{exp} values are red shifted when compared with theory, and the red shift depends on ω_{RBM}, i.e., on d_t.

The E_{ii} values can be renormalized in the calculation by explicitly considering the dielectric constant κ, which represents the screening of the e-h (electron-hole) pair by core electrons and surrounding materials combined with the polarization function for π-electrons [16, 81]. The κ value that has been fitted to previously available E_{22}^{S} experimental values for bundled SWNTs, gives $\kappa = 2.22$ [16]. However, the constant κ value works only for the E_{22}^{S} transition and for the narrow d_t range $0.7 < d_t < 1.3$ nm. When we consider larger i values ($i \geq 3$) of E_{ii} and a broader d_t range (up to $d_t = 3.7$ nm), $\kappa = 2.22$ does not work anymore, since the κ value is sensitive to the exciton size.

The κ value can be understood as composed of two terms, κ_{env} and κ_{tube}, as explained in Chapter 3. First principles calculations show that κ_{tube} depends on the electron-hole charge separation in the excitonic state, and it exhibits an anti-screening behavior when this distance reaches d_t [43]. To fully account for the observed energy-dependent E_{ii} redshift, we fit the total κ values ($1/\kappa = 1/\kappa_{\mathrm{env}} + 1/\kappa_{\mathrm{tube}}$) to minimize $E_{ii}^{\mathrm{exp}} - E_{ii}^{\mathrm{cal}}$.
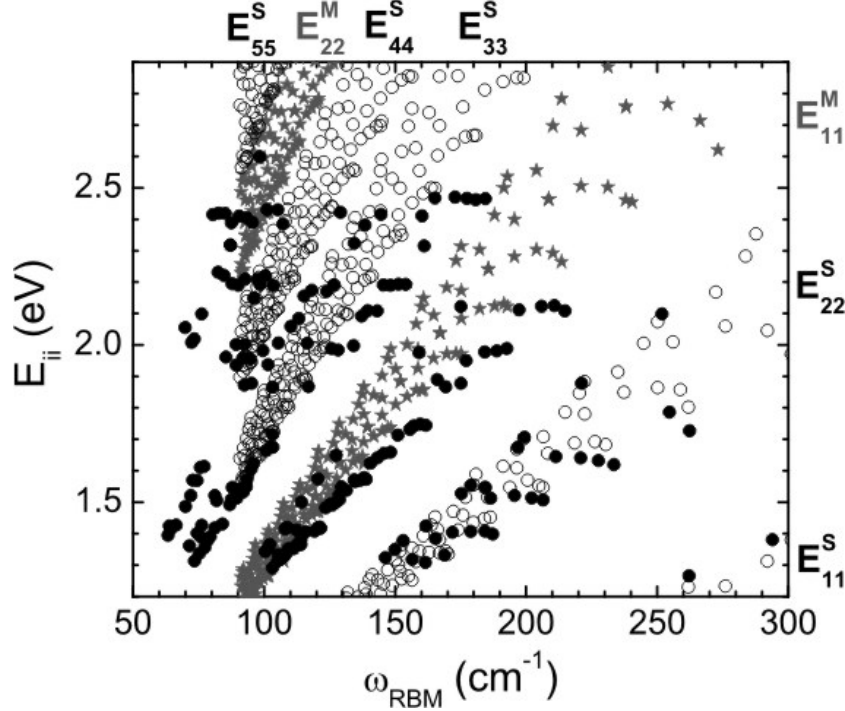
Figure 6.6: Black dots show E_{ii}^{exp} vs. ω_{RBM} results obtained from resonance Raman spectra taken from "super-growth" SWNT sample. The black open circles (semiconducting) and the dark-gray stars (metallic) give E_{ii}^{cal} for the bright exciton calculation with dielectric constant $\kappa = 1$ [34]. Along the x axis E_{ii}^{cal} are translated using the relation $\omega_{\text{RBM}} = 227/d_t$ [34]. E_{ii}^S ($i = 1 - 5$) stand for semiconducting and E_{ii}^M ($i = 1, 2$) stand for metallic transition energies. [17]

The bullets in Fig. 6.7 show the fitted κ values as a function of p/d_t which reproduce each experimental E_{ii} value for the assigned (n, m) SWNTs for the $S.G.$ SWNT sample [62]. The stars stand for a different SWNT sample, named "alcohol-assisted" ($A.A.$) [3] SWNTs [82], and it will be discussed in the next paragraph. We know from Chapter 2 that $p = 1, 2, 3, 4$ and 5 stands for E_{11}^S, E_{22}^S, E_{11}^M, E_{33}^S, and E_{44}^S, respectively [79]. Consideration of p/d_t allows us to compare the κ values of SWNTs with different d_t and different E_{ii} using the same plot. As seen in Fig. 6.7, the κ values increase with increasing p/d_t for different E_{ii} values. The κ values for E_{33}^S and E_{44}^S (Fig. 6.7(b)) appear in a smaller κ region than those for E_{11}^S and E_{22}^S (Fig. 6.7(a)), which is due to both the more localized

---

[3]As discussed previously, the nomenclatures "alcohol-assisted" ($A.A$) and "super-growth" ($S.G.$) carbon nanotubes will be employed throughout the text. The $A.A.$ tubes are grown by CVD method using Acetate Cobalt-Molybdenum as percussor and alcohol as catalyst. During the growth process the CVD chamber is kept under a Ar/H_2 flux. The $S.G.$ tubes are grown by CVD method using $Fecl_3$ (or Fe, Al/Fe, Al_2O_3/Fe, Al_2O_3/Co) as percussor and water as catalyst. During the growth process the CVD chamber is kept under a Ar/H_2 or He/H_2 flux.

exciton wavefunction (a larger exciton binding energy) for E_{33}^S and E_{44}^S compared with E_{11}^M and E_{22}^S, and to the lack of a κ_{env} dependence of the wavefunctions for the E_{33}^S and E_{44}^S excitons, as discussed bellow.
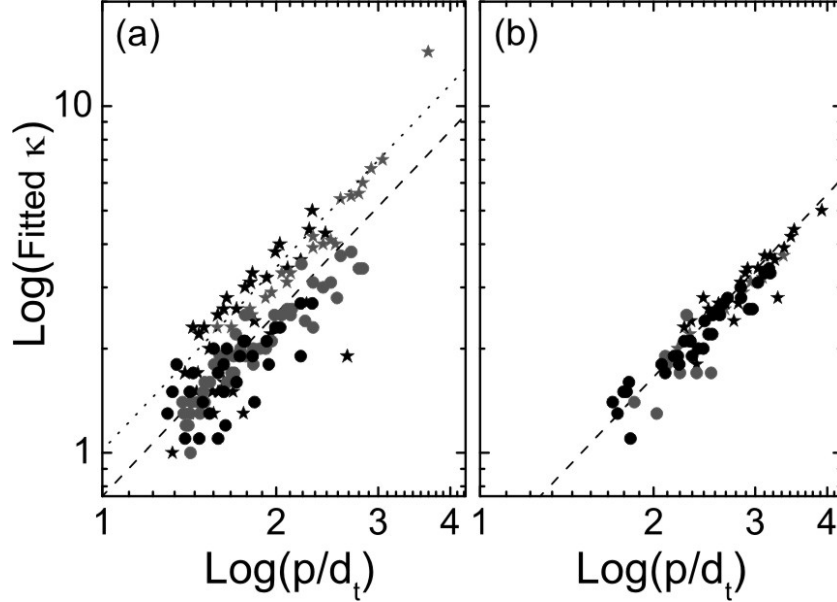

Figure 6.7: The calculated κ values as a function of p/d_t in a log-log plot, which are fitted to the experimental E_{ii} values from the "super-growth" (bullets) and "alcohol-assisted" (stars) samples. (a) E_{22}^S (black) and E_{11}^M (dark-gray). The dashed and dotted curves are obtained by fitting the circle and star data with Eq. 6.2, giving the values $C_\kappa = 0.75$ and 1.02, respectively. (b) E_{33}^S (black) and E_{44}^S (dark-gray). The dashed curve is for Eq. 6.2 with $C_\kappa = 0.49$. [17]

To gain more insights into the κ influence on the optical transition energies, Fig. 6.8 shows a comparison between the E_{ii}^{exp} from the "super-growth" SWNT sample (bullets) and from the "alcohol-assisted" SWNT samples (open circles). The "alcohol-assisted" SWNT sample is chosen for comparison for three reasons: (1) this sample also has a broad diameter distribution ($0.7 < d_t < 2.3\,\text{nm}$); (2) the observed E_{ii} are similar to many other samples in the literature [34, 35]; (3) the sample is morphologically similar to the "super-growth" sample (both are carpet-like free standing SWNTs) but the tubes are presented in small bundles, rather than isolated. From Fig. 6.8, we see that the E_{ii}^{exp} values from the "alcohol-assisted" SWNTs are generally red shifted with respect to those from the "super-growth" SWNTs. Assuming that κ_{tube} does not change from sample

to sample, since the structure of a given (n, m) tube should be the same, these results indicate that the "alcohol-assisted" SWNTs are surrounded by a larger κ_{env} value, thus increasing the effective κ and decreasing E_{ii}.
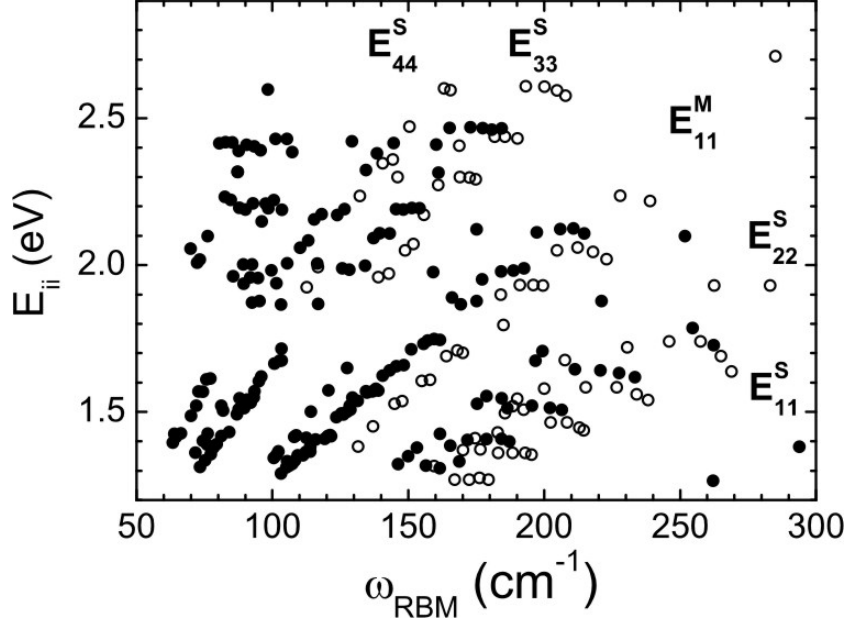
Figure 6.8: E_{ii}^{exp} vs. ω_{RBM} results obtained for the "super-growth" (bullets) and "alcohol assisted" (open circles) SWNT samples. [17]

Looking at Fig. 6.7 we can observe the difference in the κ values resulting from fitting the E_{ii}^{exp} to the *S.G.* (bullets) in comparison to the *A.A.* (stars) SWNT samples. For E_{22}^S and E_{11}^M (Fig.6.7(a)), we see a clear difference for κ up to $p = 3$ when comparing the two samples. However, for E_{33}^S and E_{44}^S (Fig.6.7(b)), no difference in κ between the two samples can be seen. This means that the electric field of the E_{33}^S and E_{44}^S exciton does not extend much outside the SWNT volume, in contrast to the E_{22}^S and E_{11}^M excitons for which the κ_{env} effect is significant. Since the effect of κ_{env} is relatively small for energies above E_{11}^M, it is possible to assign the (n, m) values from E_{33}^S and E_{44}^S if the dielectric constant of the environment is not known, even though the E_{33}^S and E_{44}^S values are seen within a large density of dots in the Kataura plot. In constructing Fig. 6.7 we fitted the κ values to the following function

$$\kappa = C_\kappa \left(\frac{p}{d_t} \right)^{1.7}, \tag{6.2}$$

where the exponent 1.7 works for all E_{ii}^{exp}, but different C_κ parameters are needed. For E_{11}^S, E_{22}^S and E_{11}^M, $C_\kappa = 0.75$ for the $S.G.$ SWNTs and $C_\kappa = 1.02$ for the $A.A.$ SWNTs (dashed and dotted curves in Fig. 6.7(a), respectively). The E_{33}^S and E_{44}^S are fitted using $C_\kappa = 0.49$ for both samples, as shown by the dashed line in Fig. 6.7(b).

Finally, Fig.6.9 summarizes the effect of our κ-based renormalization of E_{ii}. In Fig. 6.9 we plot the energy difference $\Delta E_{ii} = E_{ii}^{\mathrm{exp}} - E_{ii}^{\mathrm{cal}}$ as a function of d_t for (a) κ values fixed to be equal to 1 ($\kappa = 1$), (b) κ values fixed to be equal to 2.22 ($\kappa = 2.22$) and (c) the diameter dependent κ values using the function of Eq. 6.2, including both the $S.G.$ SWNTs and the $A.A.$ SWNTs. From Figs. 6.9(a) and (b) we observe that the fitting results using fixed values for κ are not good enough from a physical point of view, because the data in these figures are spread over a window of about $400\,\mathrm{meV}$, which is greater than the observed resonance window for a single (n, m) tube [10]. Besides, the spread of the ΔE_{ii} points in Figs. 6.9(a) and 6.9(b) increases for small d_t tubes. To address this physical inconsistency, we analyze the energy difference $\Delta E_{ii} = E_{ii}^{\mathrm{exp}} - E_{ii}^{\mathrm{cal}}$, where E_{ii}^{cal} is now calculated by considering κ given by Eq. 6.2. When the resulting ΔE_{ii} is plotted vs. d_t for all E_{ii} ($p = 1...5$), using the C_κ parameters given in the text, all the ΔE_{ii} in Fig. 6.9(c) deviates from zero by less than 70 meV, for both the $S.G.$ and the $A.A.$ SWNT samples, over the entire d_t region.
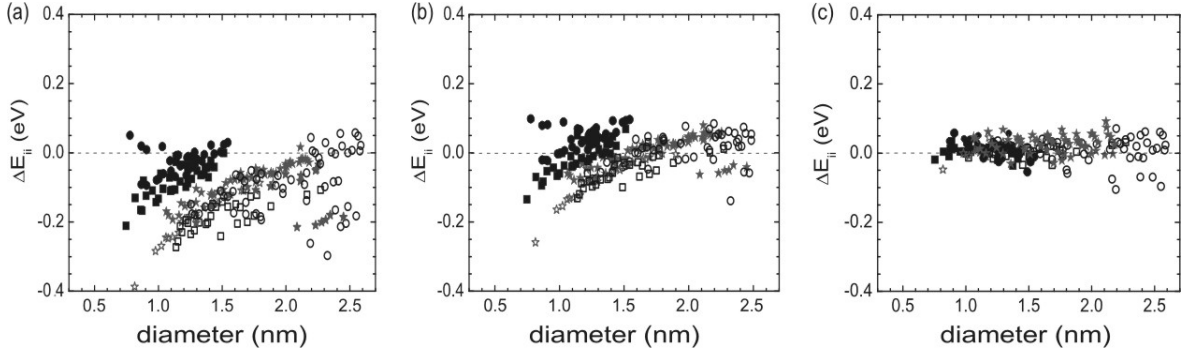
Figure 6.9: The difference $\Delta E_{ii} = E_{ii}^{\mathrm{exp}} - E_{ii}^{\mathrm{cal}}$ as a function of d_t for (a) $\kappa = 1$, (b) $\kappa = 2.22$ and (c) the diameter dependent κ given by Eq. 6.2. Filled stars (ΔE_{11}^M for metallic tubes), filled bullets (ΔE_{11}^S and ΔE_{22}^S for semiconducting tubes) and open bullets (ΔE_{33}^S and ΔE_{44}^S for semiconducting tubes) stand for $S.G.$ data, while open stars (ΔE_{11}^M for metallic tubes), filled squares (ΔE_{11}^S and ΔE_{22}^S for semiconducting tubes) and open squares (ΔE_{33}^S and ΔE_{44}^S for semiconducting tubes) stand for $A.A.$ data. [17]

6.3 The θ dependence of the dielectric constant for the excitonic E_{ii}

Nowadays the importance of excitons in the SWNTs electronic transitions is very clear from both an experimental and theoretical point of views [10, 13, 31, 12, 15, 16, 22, 37, 23, 38]. As showed by Jiang *et. al.* [16], the SWNTs excitonic levels show a considerable dependence on the SWNT chirality, which is shown by the so-called family dependence behavior [10]. As the interaction which maintains the SWNTs excitons stability are essentially Coulombic [10] and, therefore, κ dependent, it is necessary to verify how important it is to correct κ for the SWNT chiral angle (θ). As previously described, κ is composed of κ_{tube} and κ_{env}. However, κ_{tube} is totally dependent on the SWNTs structure and is also possibly θ dependent. In order to verify such a dependence, a term accounting for the chirality was introduced in eq. 6.2 that now reads,

$$\kappa = C_\kappa \left(\frac{p}{d_t} \right)^{1.7} + \beta_p \frac{\cos(3\theta)}{d_t^2} \,, \tag{6.3}$$

where β_p is weighting the chirality contribution for the different E_{ii}. Our analysis is again directed to the *S.G.* and *A.A.* samples [41, 13].

Figure 6.10 shows a plot of κ fitted to the *A.A.* (E_{22}^S, E_{11}^M) transitions as a function of p/d_t. All κ values were obtained and optimized in accordance with the explanation presented in section 6.2. In Fig. 6.10(a) κ has been chiral angle corrected using the second term in eq. 6.3 while in Fig. 6.10(b) it was not. By comparing Figs. 6.10(a) and (b) it is clear that the chirality correction has improved the κ's evaluation and, of particular importance, the κ fitted to E_{11}^M (black triangles) no longer collapses onto the same curve as those fitted to E_{22}^S (solid/open grey triangles), but rather appear on a curve higher than for E_{22}^S. This result is quite interesting since the dielectric screening for metallic tubes is more critical because of the presence of free-carriers, and this would make them to follow different scalings. The same behavior can be observed for the *S.G.* κ values, as exhibited in Fig. 6.11.

Similarly, in Figs. 6.11(a) and (b) the κ values are, respectively, corrected and not corrected for the chiral angle κ dependence for the *S.G.* SWNTs. Again, the κ values for E_{11}^M transitions (black bullets) appear higher than the values for E_{22}^S and both do not collapse onto the same curves. In both Fig. 6.10(a) and 6.11(a) the black and grey solid lines are fittings using Eq. 6.3. The curves in Figs. 6.10(b) and 6.11(b) are given in Ref.[17]. The values for C_κ and β_p are found in Tables 6.1 and 6.2, respectively.
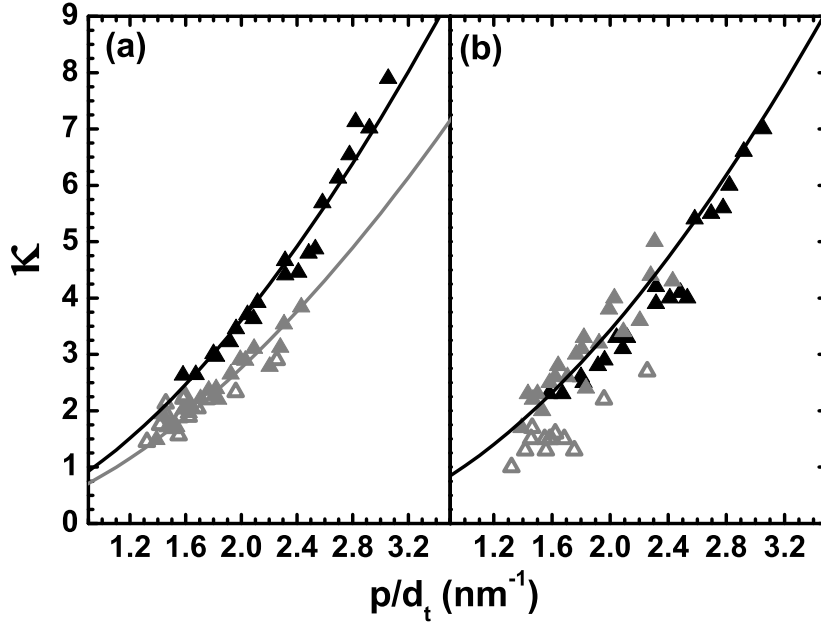
Figure 6.10: The κ values fitted to the *A.A.* E_{11}^M (black triangles) and E_{22}^S (solid/open grey triangles) transitions. (a) and (b) show, respectively, results for κ when the chirality correction is taken into account and when it is not. While the solid grey triangles stand for E_{22}^S type I the open grey triangles stand for E_{22}^S type II. In (a) the black and gray curves are obtained by fitting the data with eq. 6.3 and the curve in (b) is given by eq. 6.2. [17, 83]

A.A.'s C_κ	S.G.'s C_κ
$C_\kappa^{E_{11}^M} = 0.82$	$C_\kappa^{E_{11}^M} = 1.11$
$C_\kappa^{E_{22}^S} = 0.66$	$C_\kappa^{E_{22}^S} = 0.85$
$C_\kappa^{E_{33,44}^S} = 0.49$	$C_\kappa^{E_{33,44}^S} = 0.49$

Table 6.1: C_κ values found by fitting κ

Figure 6.12 shows a plot of κ fitted to the *A.A.* and *S.G.* (E_{33}^S, E_{44}^S) transitions as a function of p/d_t. Once more, Fig. 6.12(a) and (b) show, respectively, the κ values when the chirality correction is and is not taken into account. In this case, one can visibly see that the chirality correction slightly improves the data. It is interesting to note that the chirality correction, in fact, decreases only the spread around the fitting curve (black solid line in Fig. 6.12(a)). Then it connects that C_κ does not change from 0.49, in agreement
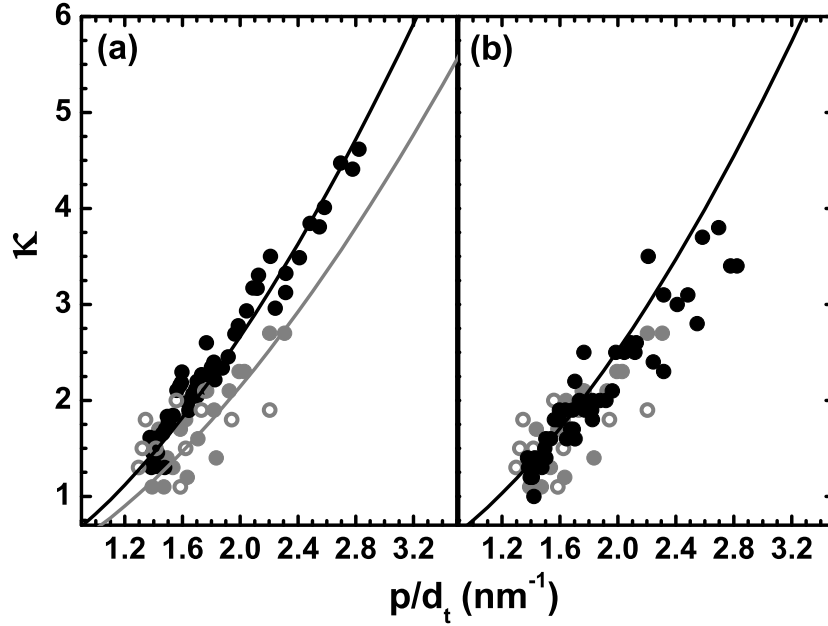
139

Figure 6.11: The κ values fitted to the $S.G.$ E_{11}^M (black bullets) and E_{22}^S (solid/open grey bullets) transitions. (a) and (b) show, respectively, results for κ when the chirality correction is taken into account and when it is not. While the solid grey bullets stand for E_{22}^S type I, the open grey bullets stand for E_{22}^S type II. In (a) the black and gray curves are obtained by fitting the data with eq. 6.3 and the curve in (b) is given by eq. 6.2. [17, 83]

A.A.'s β_p lower(higher)	S.G.'s β_p lower(higher)
$\beta_p^{E_{22}^S} = 1.2(-1.1)$	$\beta_p^{E_{22}^S} = 0.1(-0.1)$
$\beta_p^{E_{11}^M} = 1.3$(not measured)	$\beta_p^{E_{11}^M} = 1.4$(not measured)
$\beta_p^{E_{33}^S} = 0.95(-0.55)$	$\beta_p^{E_{33}^S} = 1(-0.2)$
$\beta_p^{E_{44}^S} = $ not measured(-0.3)	$\beta_p^{E_{44}^S} = $ not measured(-0.3)

Table 6.2: β_p values found by fitting κ. In the column's titles, lower(higher) stand for the lower(higher) E_{ii} branches in the Kataura's plot.

to the value given by ref. [17].

In figure 6.13 the chiral angle corrected κ values for higher and lower transitions of both *A.A.* and *S.G.* SWNTs are merged into an unique κ *vs* d_t plot, given a general picture of the dielectric screening problem. It is clear that two regimes still exist, one for the lower and another for the higher transitions (besides, of course, the natural separation
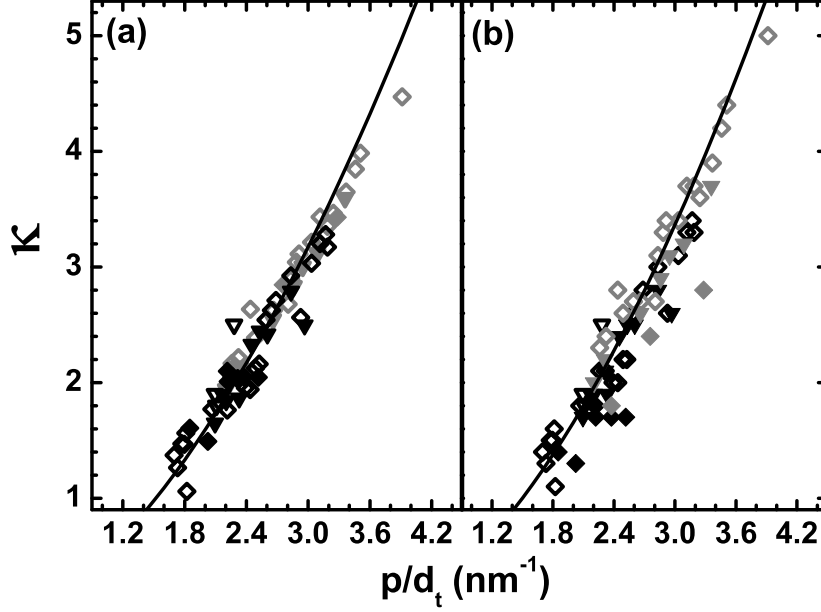
Figure 6.12: The κ values fitted to the *A.A.* and *S.G.* E_{33}^S and E_{44}^S transitions. (a) and (b) show, respectively, results for κ when the chirality correction is taken into account and when its not. The solid grey/black diamonds stand for the *A.A./S.G.* E_{33}^S type I transitions, the open grey/black diamonds stand for the *A.A./S.G.* E_{33}^S type II, the solid grey/black down-triangles stand for the *A.A./S.G.* E_{44}^S type I and the open black down-triangle stand for the *S.G.* E_{44}^S type II. In (a) the black curve is obtained by fitting the data with eq. 6.3 and the curve in (b) is given by eq. 6.2. [17, 83]

due to different κ_{env}). This is an indication that something more fundamental is needed to properly explain the screening behavior of κ.

6.4 Unifying the E_{ii}'s κ dependence: the importance of the exciton's size

In the last two sections we have discussed the d_t and θ dependence of the dielectric constant κ. However, by considering these two specific variables we saw that we cannot find a description for κ which is able to account for all E_{ii}. Our model was restricted to fit, separately, the lower (E_{11}^S, E_{22}^S, E_{11}^M) and higher (E_{33}^S, E_{44}^S) excitonic transitions. In the present section, we show that to consider the exciton's size l_z explicitly in κ's
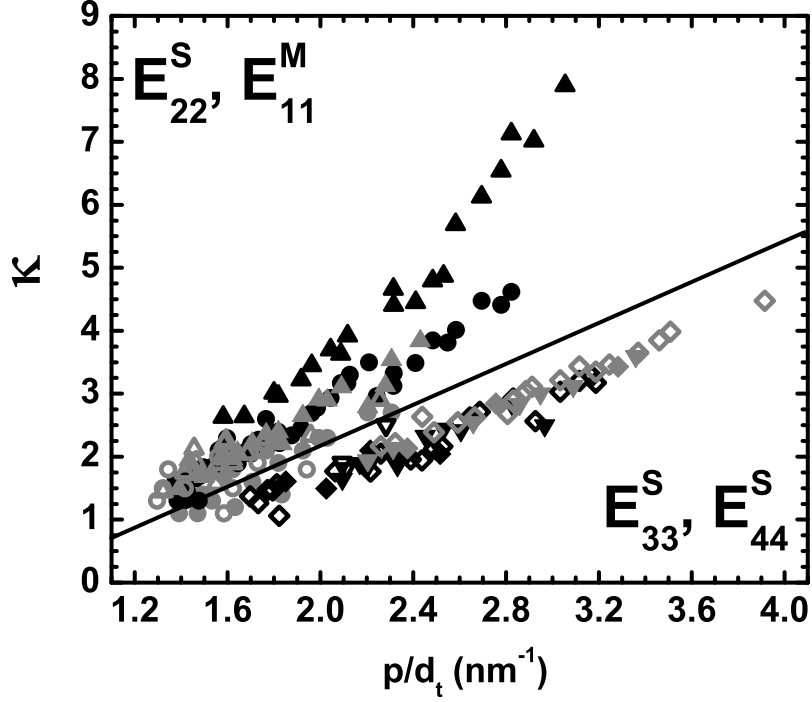
Figure 6.13: The chiral angle corrected κ values for higher and lower transitions of both *A.A.* and *S.G.* SWNTs are merged into an unique plot κ *vs* d_t, thus giving a general picture of the dielectric screening problem. The legend for the symbols is the same as used previously in the other figures. The black solid line is just a guide to the eyes showing a clear brake between higher and lower energy transitions. [17, 83]

formulation is of fundamental importance to properly describe the dielectric screening [18]. The exciton size is given by full-width at half maximum of the exciton wavefunction profile in 1D k-space. Considering l_z, the Eq. 6.2 now reads:

$$\kappa \approx C_\kappa \left[p^a \left(\frac{1}{d_t} \right)^b \left(\frac{1}{l_z} \right)^c \right] . \tag{6.4}$$

The variable l_k is involved in the κ function because of the screening by the different environments which modifies l_z. Besides this, l_z implicitly considers the chirality dependence of κ. The parameters (a, b, c) that are thus determined are common for all different samples so as to both optimize the correlation between κ and (p, d_t, l_k), and to minimize differences between theory and experiment. In Fig. 6.14, we show a series of results for the κ function for *A.A.*, *S.G.* and HiPco samples. For each sample, we

can unify the κ function for the lower transitions $(E_{11}^S, E_{22}^S, E_{11}^M)$ and higher transitions (E_{33}^S, E_{44}^S). Indeed, the exciton size is a key variable in the dielectric screening of excitons. Keeping d_t constant, the κ values for higher E_{ii} are smaller than that for lower E_{ii}. Thus l_k^{-1} (the exciton size in real space) is also smaller because only a small amount of the electric field created by an electron-hole pair will influence the surrounding materials. If l_k for a particular E_{ii} is kept constant, tubes with a smaller d_t will experience a stronger dielectric screening effect because the electric field lines from the electron-hole pair can easily go outside of the tube, thus explaining why both d_t and l_k are taken into account in the κ formulation [18]. The values of (a, b, c) from the best fitting result are found to be $(0.80 \pm 0.10, 1.60 \pm 0.10, 0.40 \pm 0.05)$, respectively. This result indicates another scaling relation of excitons similar to the previously reported scaling law which relates E_{bd} with d_t, κ, and the "effective mass" μ [84]. However, we found that the scaling relation involving μ works well only within S-SWNTs and another scaling function is needed for M-SWNTs. This is because E_{bd} for an M-SWNT is screened by free electrons even for a similar effective mass for the photo-excited carriers [84].

In Fig. 6.14 we can realize that the plots for each sample are different only by the constant C_κ whose values are 0.84, 1.19 and 1.28 for the $S.G.$, $A.A.$ and HipCo, respectively. Assuming that C_κ characterizes the environmental dielectric constant κ_{env} of each sample and taking into account that the $S.G.$ sample exhibits the highest values for E_{ii} (and therefore the lowest κ_{env}) we can normalize C_κ for the $S.G.$ sample in the way that $C_\kappa \longrightarrow \tilde{C}_\kappa(S.G.) = 1$. Thus, we have $\tilde{C}_\kappa = (1.00, 1.42, 1.52)$ for $(S.G., A.A.,$ HipCo$)$ samples. In principle, there is no physical mean which justifies $\tilde{C}_\kappa$. However, if we now plot the ratio $(\kappa - 1)/\tilde{C}_\kappa$ for each sample, it is found that all points collapse on to a single line, as shown in Fig. 6.14(e). This fact gives further support to the use of $\tilde{C}_\kappa$ as a unique parameter for each environment. This treatment has been checked to work for many surrounding materials, and the justification of the treatment will be reported elsewhere.

With the knowledge of $\tilde{C}_\kappa$ for several types of environments, we are now ready to use these results in practical applications. To a first approximation, we fit the energy shift $\delta E_{ii}^{\mathrm{env}}$ due to different environments (Fig. 6.15) by

$$\delta E_{ii}^{\mathrm{env}} = E_{ii}^{S.G.} - E_{ii}^{\mathrm{env}} \equiv \tilde{C}_\kappa \left[A + B \left(\frac{p}{d_t} \right) + C \left(\frac{p}{d_t} \right)^2 \right], \tag{6.5}$$

where A, B, C, are parameters common to all types of environments and E_{ii}^{env} is calculated with the κ function obtained previously. We find the best fit for $A = -42.8$ meV, $B =$
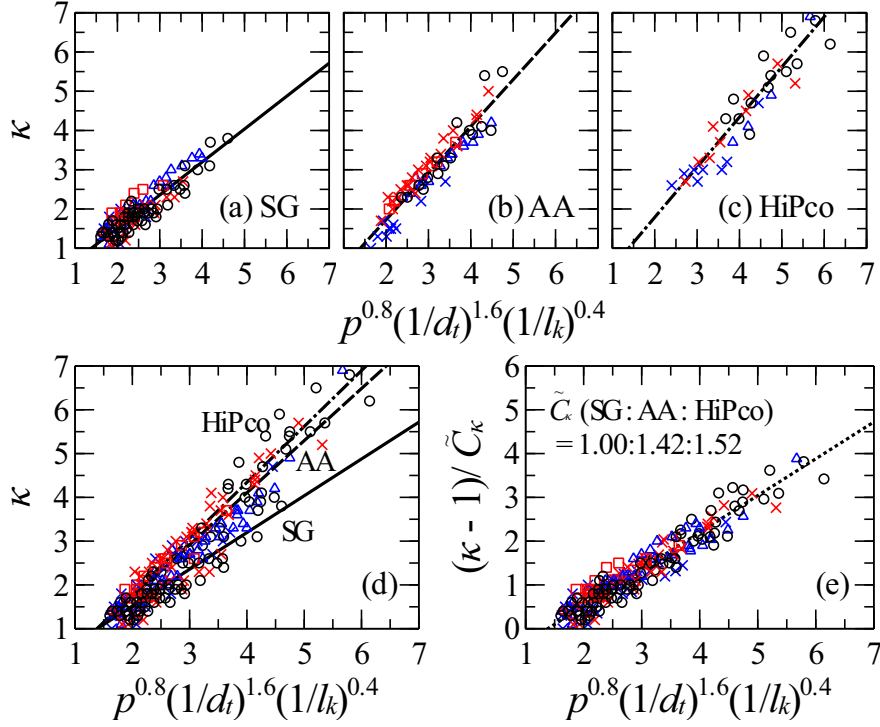
Figure 6.14: The κ function for: (a) *S.G.*, (b) *A.A.*, and (c) HiPco samples. (d) Data for the three samples are plotted on the same figure with fitted slope C_κ for each sample. (e) All the κ functions collapse on to a single line after dividing each function with the corresponding $\tilde{C}_\kappa$. The following symbols are used: $E_{11}(\circ)$, $E_{22}(\times)$, $E_{33}(\triangle)$, $E_{44}(\square)$. Black, red, and blue colors, respectively, denote metal $(\text{mod}(2n+m,3)=0)$, semiconductor type I $(\text{mod}(2n+m,3)=1)$, and type II $(\text{mod}(2n+m,3)=2)$ SWNTs. [18]

$46.34\ \text{meV}\cdot\text{nm}$, $C = -7.47\ \text{meV}\cdot\text{nm}^2$. The *S.G.* sample is then fixed as a standard, and all E_{ii} values for the other environments can be calculated simply by: $E_{ii}^{\text{env}} = E_{ii}^{S.G.} - \delta E_{ii}^{\text{env}}$. This treatment, together with the relation $\omega_{RBM} = 227/d_t(\sqrt{1 + C_e \cdot d_t^2})$, provides a general way to obtain the Kataura plot for SWNTs in any type of environment within an accuracy of 50 meV for all energy regions and d_t (See inset of Fig. 6.15).

6.5   Summary

We showed that the *S.G.* SWNTs exhibit the highest E_{ii} reported so far in the literature. We showed that all the E_{ii} values reported in the literature are downshifted of about $40\,\text{meV}$ with a slight diameter dependence. This different features of E_{ii} are directly related to the dielectric constant κ. We have modeled and discussed the diameter and chiral angle dependence of κ and concluded that, to provide an unique κ relation
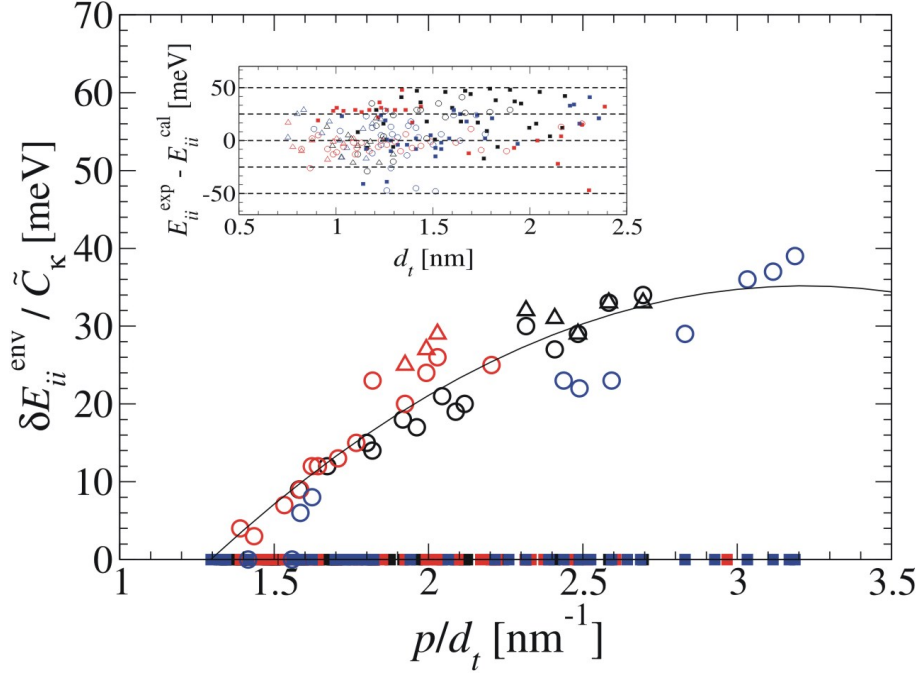
Figure 6.15: $\delta E_{ii}^{\mathrm{env}}$ versus d_t, scaled by $\tilde{C}_\kappa$. Circles and triangles, respectively, denote *A.A.* and HiPco samples. Many square symbols on the zero line denote the *S.G.* sample which is taken as the standard. The inset shows differences between experimental (exp) and calculated (cal) E_{ii} values for all samples, showing good agreement between experiment and our model. [18]

which describes the screening effect for all E_{ii}, it is of fundamental importance to include the exciton's size (l_z) in the treatment. We could then approach all E_{ii} of different environments by $E_{ii}^{\mathrm{env}} = E_{ii}^{\mathrm{SG}} - \delta E_{ii}^{\mathrm{env}}$ where $\delta E_{ii}^{\mathrm{env}}$ is given by Eq. 6.5 with $A = -42.8$ meV, $B = 46.34$ meV $\cdot$ nm and $C = -7.47$ meV $\cdot$ nm^2. With this formulation we are able to build a reliable Kataura's plot for any type of environment. Besides this, we directed a consistent discussion of the previously elusive higher and lower (E_{11}^M, E_{22}^M) comparing experimental data to theoretical data, and confirmed that the nature of metallic transitions is excitonic. The main contents of this chapter are published in *Physical Review Letters* **103**, 146802 (2009); *Physica Status Solid(b)* **245**, 2201 (2008); *Physical Review* B **78**, 165408 (2008); and *Physica Status Solid(b)* **247**, 2847 (2010). The results of the last section are published at *Applied Physics Letters* **97**, 091905 (2010).

Chapter 7

Manipulating the SWNTs Properties in the Nanometric Scale

As stated in Chapter 4, part of my PhD was directed to build a setup which is able to manipulate matter in the nanometric scale as well as perform, simultaneously, high-resolution optical spectroscopy (called Near-field spectroscopy). This chapter shows results using these two setup's trends where in the section 7.1 we used Near-Field spectroscopy to unravel the different optical responses of a SWNT segmented with different mediums surrounding it. In the section 7.2 we study changes in the vibrational structure of a SWNT submitted to a local pressure.

7.1 Visualizing the local optical response of semiconducting SWNTs: unraveling contributions from different environments

The emission energy of nanotubes is modulated by the environmental dielectric constant κ_{env}, which can be expected to be nonuniform along them, leading to nonuniform emission energies [57, 85, 86]. The use of DNA for hybridization of carbon nanotube sidewalls has facilitated sorting nanotubes and building chemical sensors [40, 87, 88]. Single-strand DNA-wrapping introduces DNA segments with finite length, while the details of the secondary DNA structure will be determined by a complex interplay between - stacking interactions between DNA bases and nanotube surface as well as electrostatic interactions of the phosphate backbone [89, 90]. The effect of helical wrapping by the charged DNA backbone was modeled by applying a helical potential causing symmetry breaking of the nanotube electronic structure and small energetic shifts for semiconducting

nanotubes (0.01 meV in water) [91, 92]. It is well-known that DNA-wrapping red-shifts the PL energy depending on the nanotube chirality by several tens of meV compared to the values reported for micelle-encapsulated nanotubes in aqueous solution [40, 93] which can be attributed to an increasing κ_{env} [17, 83, 18]. The surface coverage with DNA segments of finite length is expected to result in a nonuniform dielectric environment along the nanotubes [10, 93]. Limited by diffraction, the optical information collected in confocal microscopy contains the optical response from a nanotube length of about 300 nm, which is far too large to clarify details of individual DNA-nanotube interactions. To better figure out the different responses, tip enhanced spectroscopy (TES) becomes an ideal technique allowing us to study, step by step, small SWNT segments covered and uncovered by DNA.

The samples are composed of HiPCO nanotubes, DNA-wrapped HiPCO nanotubes spin-coated on glass, and (6,5) enriched DNA-wrapped CoMoCAT SWNTs spin-coated on a freshly cleaved thin mica layer glued on a glass cover slide. CoMoCAT SWNTs were sorted by using discriminating surfactants and wrapped by DNA after sorting. Density gradient ultracentrifugation isolates the narrow distributed, chirality enriched nanotubes. The mica layer was positively charged with Mg^{2+} ions by exposure to 1 M $MgCl_2$ to make the negatively charged DNA site of the hybrid adhere to the surface [93].

As a first step, we used confocal spectroscopy to study the photoluminescence PL responses from single DNA-wrapped and unwrapped SWNTs deposited on substrates. We found a strong red shift caused by DNA-wrapping of between 7 and 17 meV depending on the nanotube chirality. In the next step, TES was used to resolve PL variations along DNA-wrapped (6,5) and (6,4) nanotubes. Here two distinct emission bands are identified and assigned to emission from DNA-wrapped segments of the nanotube at E_{DNA} and unwrapped segments at E_0, distinguished by energy shifts of 18 meV for (6,5) and 30 meV for (6,4)-nanotubes, respectively. We were hereby able to spatially resolve the optical response of a nanotube to wrapping by a single DNA segment for the first time. Confocal emission spectra result from spatial averaging of the two peaks and show a peak at E_{conf} with a broadened spectral width of 40 meV. Figure 7.1 displays the histogram of PL emission energies from 203 HiPCO nanotubes (a), 235 DNA-wrapped HiPCO nanotubes spin-coated on glass (b), and 232 DNA-wrapped CoMoCAT nanotubes spin-coated on mica (c) obtained using confocal spectroscopy. The emission energies show a Gaussian distribution centered at energies that are assigned to different chiralities on the basis of literature data [40]. The emission energies of DNA-wrapped HiPCO nanotubes are red-shifted by 7-17 meV compared to unwrapped HiPCO nanotubes varying with nanotube

chiralities as discussed. DNA-wrapped CoMoCAT nanotubes on mica and DNA-wrapped HiPCO nanotubes on glass exhibit the same PL energies (Fig.7.1(b) and (c)) while the chirality distribution differs as a result of different catalytic growth and (6,5) enrichment in the case of the CoMoCAT material. The DNA-wrapped (6,5) nanotubes show an emission energy of $E_{conf} = 1.249\,\mathrm{eV}$, whereas unwrapped (6,5) nanotubes emit at $E_0 = 1.256\,\mathrm{eV}$.
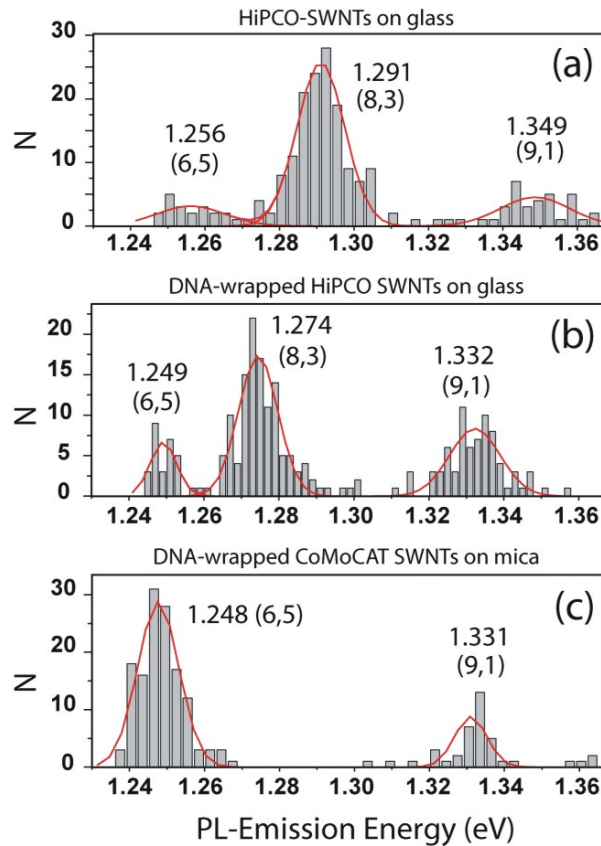

Figure 7.1: Histogram of PL emission energies from 203 HiPCO nanotubes (a), 235 DNA-wrapped HiPCO nanotubes spin-coated on glass (b), and 232 DNA-wrapped CoMoCAT nanotubes spin-coated on mica (c) upon laser excitation at 632.8 nm. The emission energies vary around center energies that are used for chirality assignment based on literature data. DNA-wrapping causes a red shift for all chiralities. DNA-wrapped HiPCO and CoMoCAT nanotubes on different substrates have almost the same emission energies, while the histogram reflects the chirality distribution. [94]

Next, we used TES to resolve the optical response coming form parts of a SWNT wrapped and unwrapped by DNA segments. Figure 7.2 presents the near-field PL measurement of a DNA-wrapped CoMoCAT (6,5) SWNT spin-coated on mica. Figure 7.2(a)

148

and (b) are the simultaneously recorded topography and near-field PL images, respectively. The scale bar indicates a lateral resolution of about 15 nm. The topographic height varies from 0.75 to 1.8 nm, indicating spatial transitions between DNA-wrapped and unwrapped nanotube segments. The PL image was obtained by measuring spectra at each pixel during the scan with an acquisition time of 0.4 s at a laser power of 100 μW. Figure 7.2(b) represents the integrated intensity from 970 to 1030 nm covering the emission range of (6,5) SWNTs. First, the center emission energies were obtained by fitting the spectra with a single Lorentzian line shape function shown in Figure 7.2(c) and (d). Apparently, the emission energy varies between 1.259 and 1.241 eV along the nanotube, as indicated by the two red dashed lines in Figure 7.2(c), while the average of all near-field spectra at 1.249 eV coincides with the value from confocal far-field measurements.

Figure 7.2(d) shows the variation of emission energy along the SWNT. Because the highest energy of 1.259 eV corresponds well to the value observed for unwrapped nanotubes of $E_0 = 1.256$ eV, we conclude that we detect parts of the nanotube that are not DNA-wrapped. In order to recover the average value observed in far-field measurements, DNA wrapping needs then to result in a larger red shift that can in fact be seen in the upper part of the nanotube with energies around 1.241 eV. Confocal measurements therefore underestimate the energy stabilization induced by DNA-wrapping by about a factor of 2. Similar near-field data obtained for (6,4) nanotubes indicates a DNA-induced energy shift of 30 meV (see Fig. 7.4). Limited by the spatial resolution of our experiment and the finite length of the DNA segments (∼20 nm), the probed nanotube length will mostly contain both unwrapped and DNA-wrapped segments, leading to a superposition of emission bands at 1.259 and 1.241 eV, as can be seen in Fig. 7.3(e). When fitting the spectra with two Lorentzian peaks fixed at 1.259 and 1.241 eV representing unwrapped and wrapped sections, Fig. 7.2(b) can be split into two PL images displaying the respective intensities of these sections (Fig. 7.2(f) and (g)).

Figure 7.3 compares the confocal and near-field PL spectra of the (6,5) nanotube in Fig. 7.2 obtained at position 150 and 750 nm as marked by gray circles in Fig. 7.2(c). Both confocal spectra (spectra (a) and (b)) show a single broad peak following a Gaussian line shape function with full width at halfmaximum (FWHM) of 40 meV caused by the superposition of emission from both DNA-wrapped and unwrapped nanotube segments in the focus area. The near-field spectra resulting from a wrapped segment at 1.241 eV (spectrum (c)) and an unwrapped segment at 1.259 eV (spectrum (d)) are significantly sharper with FWHM of 27 and 25 meV, respectively. Spectrum e taken at a position ∼80 nm on the other hand clearly shows two Lorentzian peaks (FWHM 25 meV) at 1.240
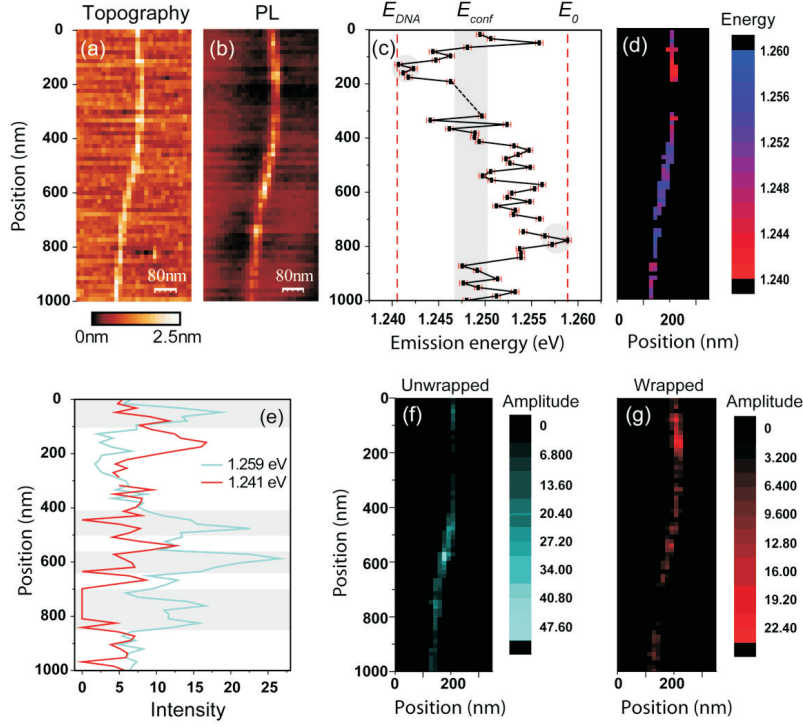
149

Figure 7.2: Simultaneously recorded topography (a) and near-field PL image (b) of a DNA-wrapped CoMoCAT (6,5) nanotube on mica. The PL image was obtained by measuring spectra at each pixel and represents the integrated intensity between 970 and 1030 nm covering the emission range of (6,5) nanotubes. For each pixel the emission spectrum was fitted with a single Lorentzian line shape function to extract the central emission energy that is plotted in (c) and (d). Strong energy variations occur between 1.259 and 1.241 eV on a length scale of about 20 nm (the error bar is about 0.7 meV indicated by the short red horizontal lines in (c)). The energy fluctuations occur around the confocal average $E_{conf} = 1.249$ eV that is marked by the vertical gray bar, while the maximum observed energy corresponds to the confocal average of unwrapped nanotubes $E_0 = 1.256$ eV marked by the dashed line. Apparently, some nanotube segments are not wrapped by DNA. (e) to (g) are fit results using two Lorentzian peak functions at E_0 and at E_{DNA}. The intensity profiles in (e) exhibit anti-correlation between the two peaks that can also be seen in the intensity images in (f) and (g). [94]

and 1.259 meV, reflecting the simultaneous detection of emission from wrapped and unwrapped segments. In agreement with the energy distribution in Fig. 7.2(c), we mostly observe spectra containing two peaks.

Figure 7.4 illustrates the gradual transition between confocal far-field and near-field spectra upon approaching the tip at two different positions along a single (6,4) nanotube. The emission energies marked with white dashed lines in Fig. 7.4(a) and (d) are from
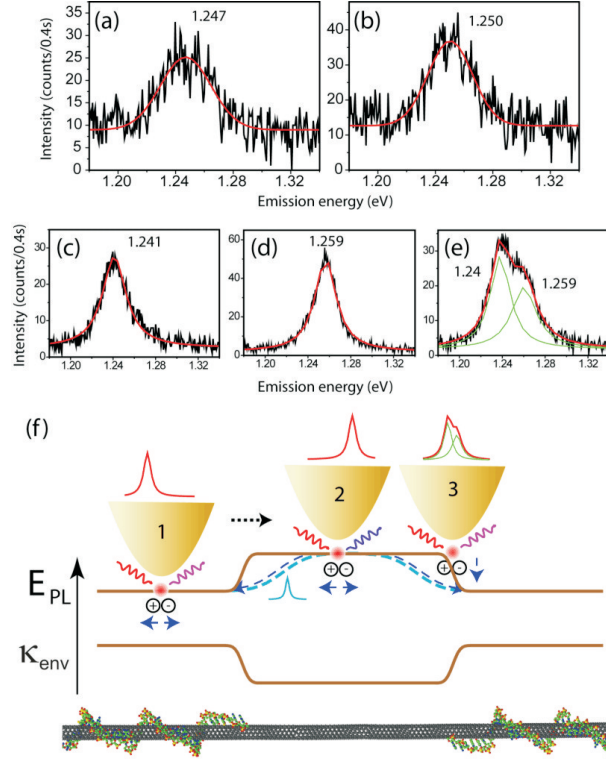
Figure 7.3: Confocal (a) and (b) and near-field ((c) to (e)) PL spectra of a DNA-wrapped CoMoCAT SWNT on mica together with Gaussian and Lorentzian fit curves for (a) and (b) and ((c) to (e)), respectively. Confocal and near-field spectra were detected at the locations along the nanotube in Fig. 7.2(c) marked by gray circles. Both confocal spectra (a, b) feature a full width at half-maximum (FWHM) of 40 meV, while the near-field spectra (c) and (d) are significantly sharper with a FWHM of 27 and 25 meV, respectively. In the near-field spectrum (e) on the other hand two distinct peaks are clearly resolved with FWHM 25 meV attributed to DNA-wrapped and unwrapped sections of the nanotube. (f) Schematic illustration of the exited state energy E_{PL} landscape (brown line) along the DNA-wrapped nanotube including two wrapped parts with an unwrapped part in between, as indicated by the nanotube below. κ_{env} denotes the dielectric constant of the local environment reflecting local DNA wrapping. For the tip probing at different positions (numbers 1, 2, 3) on the nanotube, the expected spectra are shown on top of each position. [94]

unwrapped and wrapped segments, respectively. For tip-sample distances larger than 20 nm, the detected signal represents the confocal spectrum resulting from spatial averaging. When the tip is closer within 10 nm distance, a strong signal enhancement occurs (Fig. 7.4(b) and (e)) and the near-field spectrum resulting from the nanotube section directly underneath the tip is detected. The peak energies during approaching observed
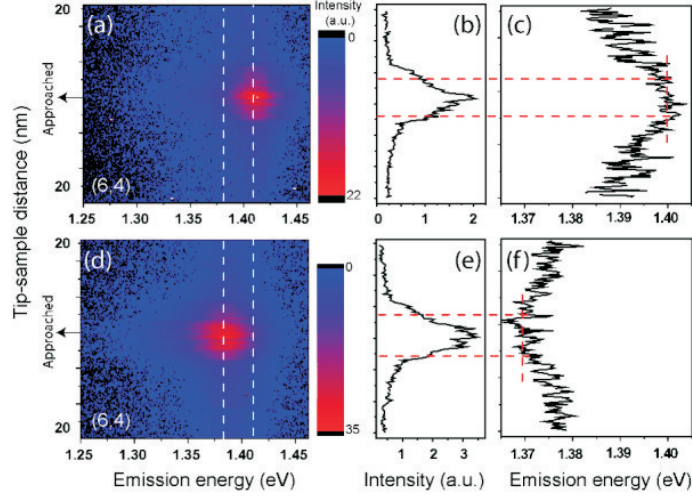
Figure 7.4: 2D photoluminescence maps taken at two different positions of a single (6,4) nanotube ((a) and (d)) as a function of tip-sample distance measured during tip approach and retracting. The difference between the two emission energies, marked by two white dashed lines, is due to DNA-wrapping. The PL intensity is strongly enhanced at small tip-sample distance and reaches the maximum when the tip is approached, marked by the arrows in (a) and (d), as shown in (b) and (e). The spectra are fit with single Lorentzian peak functions to determine the center emission energies at different tip-sample distances up to 20 nm and shown in (c) and (f) resolving the transition between confocal and near-field dominated peak energies. Within the near-field range, < 5 nm guided by the red dashed line, the emission energies are constant within the experimental precision (± 2 meV). [94]

for the two different positions along the nanotube are shown in Fig. 7.4(c) and (f) and clearly resolve the transition between confocal and near-field dominated peak energies. Importantly, in the near-field regime within the last 5 nm, marked with red dashed lines in Fig. 7.4, no spectral shift occurs within the precision of the measurement of about ± 2 meV. Hence, the observed emission energy variations reported in our work are not affected by the presence of the metal tip and are caused only by DNA-wrapping.

To understand the origin of the different PL spectra, we illustrated the energy landscape and its modulation induced by the dielectric environment along the DNA-wrapped nanotube in Fig. 7.3(f) schematically. The PL energy is lowered due to the increased dielectric constant κ_{env} associated with DNA-wrapping. Near-field scanning along the DNA-wrapped nanotube yields different optical responses when the tip is at different positions marked with numbers 1, 2 and 3. At position 1, the nanotube is locally excited on top of a DNA-wrapped segment and radiative exciton recombination occurs locally leading to low emission energy in the spectrum as shown in Fig. 7.3(c) and

152

indicated by the spectrum above the tip. At position 2 the tip probes the high emission energy of the bare nanotube as shown in Fig. 7.3(d). In the case of the tip probing on top of both DNA-wrapped and unwrapped parts depicted at position 3, the spectrum reveals double peaks including both low and high emission energies, as shown in Fig. 7.3(e). The simultaneous observation of two distinct emission peaks as in Fig. 7.3(e) demonstrates that the transition between the two emissive energy levels occurs rapidly with respect to our spatial resolution, i.e., within less than 15 nm. In contrast, slower changes as indicated by the blue dashed line in Fig. 7.3(f) would result in a single emission peak shifting in energy between high and low energy states.

7.2 Pressure-modulated G-band Raman frequencies in carbon nanotubes
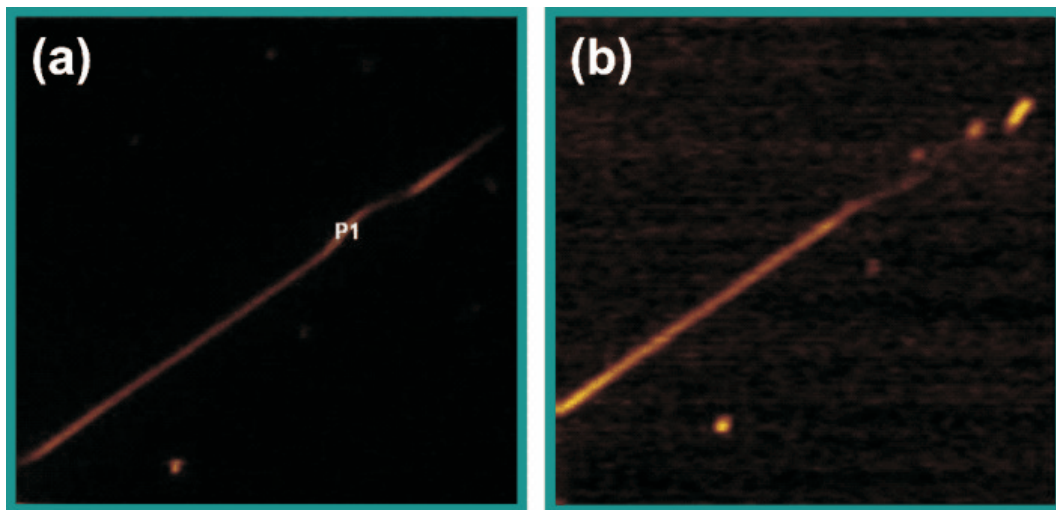
Figure 7.5: Spectral image of the G-band Raman mode of a serpentine carbon nanotube before (a) and after (b) pressing the tube with an AFM gold tip. The scan-area is $30 \times 30 \mu m^2$ and the APD's accumulation time was set at 20 ms. A band-pass filter centered at 700 nm was placed in front of the detector.

The images exhibited here were all measured with an APD device (see Chapter 2). A band-pass filter, centered at 700 nm, was placed in front of the the detector, in order to select only the scattered light correspondent to the G-band, which is composed by a first order Raman mode. In graphene systems, the G-band is a tangential vibration

mode of the carbon atom which is fitted with just one Lorentizian curve. In SWNTs systems, the G-band reveal several peaks[1] whose appearance is understood because of the confinement of the SWNTs in the radial direction. The APD's accumulation time was set at 20 ms. The laser power was 6.5 mW (measured just before the microscope rear entrance). The AFM together with the confocal system were, simultaneously, used for nano-manipulation, applying pressures to a carbon nanotube serpentine and take the respective Raman spectrum. The AFM probe used was a gold tip.

Figures 7.5(a) and (b) show images of the G-band of a single wall carbon nanotube on top of crystalline quartz[54]. The scan-area is $30 \times 30 \, \mu m^2$. In Fig. 7.5(a) the image was taken before applying pressure to the tube and Fig. 7.5(b) was taken after applying pressure to tube with an AFM gold tip. Fig. 7.5(b) shows clearly that the SWNT was damaged during the pressing. Fig. 7.6 plots the G-band Raman spectra as a function of tip-induced pressure. In both, Figs. 7.6(a) and (b), the arrows indicates an increase (Fig. 7.6(a)) or decrease (Fig. 7.6(a)) of pressure. A general comment is that the effect caused by tip is totally reversible. It is worth to comment that other experiments, not discussed here, show non-reversible effects.

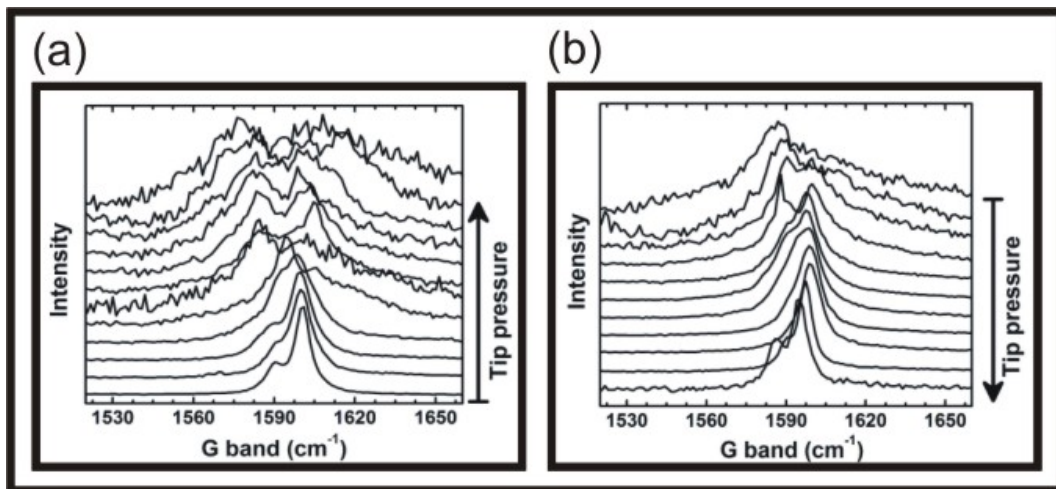**Figure 7.6**: The Raman spectra when the level of pressure is (a) increased and (b) decreased.

---

[1]Strictly speaking, these peaks will be symmetry dependent. Usually, as in our case, only two peaks rise: the transversal optical mode (TO) and the longitudinal optical mode (LO). The LO mode has a higher frequency when compared to the TO mode unless the kohn anomaly for metallic systems take place.

Saito *et. al.* explain that the frequency shift and broadening of the TO-phonon mode strongly depend on the curvature effect due to a special electron-phonon coupling in carbon nanotubes. This electron-phonon coupling could renormalize the TO and LO mode in order to make them split or cross each other [95, 96]. A deep understanding of this effect requires more data from different SWNTs. However, it is here demonstrated the effect of a controllable change of the G-band frequencies by applying external forces.
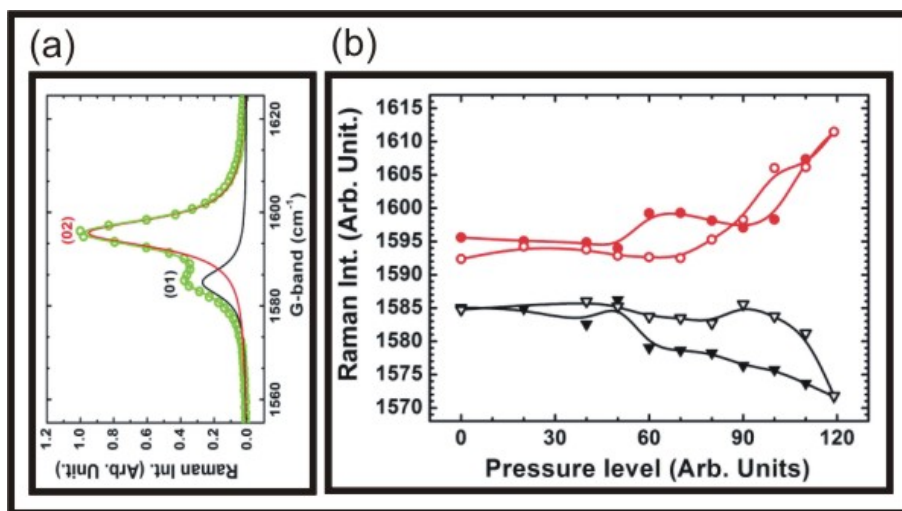

Figure 7.7: (a) An example of the Raman spectrum showing the two peaks feature. The color of the peaks are the same as the color of the curves in (b), yielding a color guide to the reader. (b) The frequencies of each Lorentizian were plotted as a function of the level of pressure. This illustrates the first hypothesis to explain the frequency changes. Here, the filled symbols means that the frequency is increasing while the open symbols means that the pressure is decreasing.

7.3   Summary

We showed a detailed analysis of DNA-wrapped SWNTs unraveling contributions from segments covered and not covered by DNA. The PL energy shift along SWNTs induced by DNA segments turns out to be a factor of 2 higher than the value determined from confocal measurements representing spatial averaging. Based on the simultaneous detection of PL bands from both DNA-wrapped and unwrapped segments, we conclude that the transition between the two energetic levels occurs on a length scale smaller than our spatial resolution of 15 nm. Tip-sample distance dependent PL spectra confirm that

the tip does not affect the emission energies within the near-field distance range. We also showed that, by pressing a SWNT with an AFM gold tip, it is possible to reversely modulate its G-band Raman frequencies. The Section 7.1 is published in *NanoLetters* **8**, 2706 (2008). The last section is being prepared for submission.

Chapter 8

Conclusions

Chapter 1 gave a brief introduction to the contents of this PhD thesis while Chapters 2 and 3 presented a historical overview of single wall carbon nanotubes (SWNTs) and their energy transition E_{ii}, together with its dielectric screening problem. Limitations in the capability of most of experimental setups to go beyond the micrometer scale has become a drawback to the advance of the research of mesoscopic systems. Nowadays, to perform experiments in the nanometer scale has become a major need, which gives rise to an important question: How and how easy is to build and implement experimental systems to perform experiments in the nanometer scale? Here, a detailed answer to this question was exposed. Part of this thesis was dedicated to perform the instrumentation needed to build a system for optical and mechanical manipulation in the nanometer scale. In Chapter 4, a very detailed description of the optical, mechanical and electronic devices necessary to implement a system for nano-spectroscopy and -manipulation was given. The purpose of this system is joining a confocal microscopy setup to an atomic force microscopy (AFM) setup.

With the confocal system, we are able to perform spectroscopy with optical resolutions coming close to $\lambda/2$, where λ is the light source wavelength. The AFM system allows us to photograph and manipulate nano-scaled systems. Both together allow simultaneous experiments of spectroscopy and nano-manipulation. The attempt is to make this chapter a start-point to whom desires to build a similar experimental scheme. The last section of the chapter exhibited several examples of confocal, topography and near-field images trying to guide the readers in how to obtain such an images. A brief description of the micro-Raman experimental setups I have used in my scientific work was also addressed in Appendix A.

In Chapter 5 we showed that a special class of SWNTs, called "super-growth", has

their ω_{RBM} related to the d_t by the $\omega_{\text{RBM}} = 227/d_t$ relation. This relation is noticeable because it recovers the SWNT graphene sheet limit which says that $\omega_{\text{RBM}} \longrightarrow 0$ when $d_t \longrightarrow \infty$. Furthermore, all the ω_{RBM} in the literature were found to be upshifted with relation to the "super-growth" $\omega_{\text{RBM}}^{S.G.}$. This upshift was explained with basis on the van der Waals forces which mediate the interactions between the tube wall and the surrounding environment. It was also shown that, by dispersing the "super-growth" tubes in sodium dodecyl sulfate (SDS) or bringing then into bundles, the "super-growth" ω_{RBM} is upshifted following the same behavior as the ω_{RBM} from the literature. Therefore, any measured $\omega_{\text{RBM}}(d_t)$ for an arbitrary experimental sample are fitted to the formula $\omega_{\text{RBM}} = (227/d_t)\sqrt{1 + C_e \cdot d_t^2}$ where only a single parameter (C_e) is used to account for the observed d_t-dependent environmental effects.

Chapter 6 showed that the "super-growth" SWNTs exhibit the highest E_{ii} reported so far in the literature. It was shown that all the E_{ii} values reported in the literature are downshifted of about $40\,\text{meV}$ with a slight diameter dependence. This different features of E_{ii} are directly related to the dielectric constant κ. It was modeled and discussed the diameter and chiral angle dependence of κ and concluded that to provide an unique κ relation which describes the screening effect for all E_{ii}, it is of fundamental importance to include the exciton's size (l_z) in the treatment. A universal approach to all E_{ii} of different environments could be described by $E_{ii}^{\text{env}} = E_{ii}^{\text{SG}} - \delta E_{ii}^{\text{env}}$ where $\delta E_{ii}^{\text{env}} = \tilde{C}_\kappa[A + B(\frac{p}{d_t}) + C(\frac{p}{d_t})^2]$ with $A = -42.8$ meV, $B = 46.34$ meV $\cdot$ nm and $C = -7.47$ meV $\cdot$ nm^2. With this formulation it is possible to build a reliable Kataura's plot for any type of environment. Besides this, a consistent discussion of the previously elusive higher and lower (E_{11}^M, E_{22}^M) comparing experimental data to theoretical data, was addressed and the general conclusion is that the nature of metallic transitions is excitonic.

The take home message given by both, Chapters 5 and 6, is summarized in Fig. 8.1. One must take the "super-growth" $(S.G.)$ carbon nanotubes as a standard so that their ω_{RBM} can be described by $\omega_{RBM} = 227/d_t(\sqrt{1 + C_e \cdot d_t^2})$ with $C_e = 0$. The ω_{RBM} for tubes in different types of environments can be described by the same equation where now the parameter C_e is appropriately adjusted to consider each environment. The $S.G.$ E_{ii}'s will be described by the empirically adjusted Eq. 2.19 (the values assumed by each parameter is showed in Fig. 8.1). To describe the E_{ii} for tubes in different types of environment, one must subtract the equation $\delta E_{ii}^{\text{env.}} = \tilde{C}_\kappa[-42.8 + 46.34(p/d_t) - 7.47(p/d_t)^2]$ from Eq. 2.19. Now, the parameter $\tilde{C}_\kappa$ must be appropriately adjusted to consider each environment.

Finally, Chapter 7 showed a detailed analysis of DNA-wrapped SWNTs unraveling

	ω_{RBM}	E_{ii}
S.G.	**(a)** $$\omega_{RBM} = \frac{227}{d_t}$$	**(b)** $$E_{ii}\left(\frac{p}{d_t}\right) = (1.049)\left(\frac{p}{d_t}\right)\left[1 + b(\kappa)\log\left(\frac{0.812}{\frac{p}{d_t}}\right)\right] + \beta_{ii}\frac{\cos(3\theta)}{d_t^2}$$ β_{ii} = lower (higher) $b(\kappa) = 0.416$ for E_{11} and E_{22} $\beta_{11} = -0.07\ (0.09)$ $b(\kappa) = 0.313$ for higher E_{ii} $\beta_{22} = -0.18\ (0.14)$ $\beta_{11M} = -0.31\ (0.49)$ $\beta_{33} = -0.43\ (0.59)$ $\beta_{44} = -0.60\ (0.57)$ $\beta_{55} = -0.60\ (0.73)$
S.G. + environment	**(c)** $$\omega_{RBM} = \frac{227}{d_t}\cdot\sqrt{1 + C_e \cdot d_t^2}$$	**(d)** $$E_{ii}^{env.} = E_{ii}^{S.G.} - \delta E_{ii}^{env.}$$ $$\delta E_{ii}^{env.} = \tilde{C}_\kappa\left(-42.8 + 46.34(p/d_t) - 7.47(p/d_t)^2\right)$$

Figure 8.1: The take home message given by both, Chapters 5 and 6, is: by considering the $S.G.$ tubes as a standard, their ω_{RBM} and E_{ii} will be described by the equations given in quadrants (a) and (b). Any other tubes, in any other type of environment will be described by an appropriate adjustment of C_e and $\tilde{C}_\kappa$ in the equations presented in quadrants (c) and (d), respectively.

contributions from segments covered and not covered by DNA. The PL energy shift along SWNTs induced by DNA segments turns out to be a factor of 2 higher than the value determined from confocal measurements representing spatial averaging. Based on the simultaneous detection of PL bands from both DNA-wrapped and unwrapped segments, it is concluded that the transition between the two energetic levels occurs on a length scale smaller than our spatial resolution of 15 nm. Tip-sample distance dependent PL spectra confirm that the tip does not affect the emission energies within the near-field distance range. Besides this, We also showed that, by pressing a SWNT with an AFM gold tip, it is possible to reversely modulate its G-band Raman frequencies.

Appendix A

Raman Spectroscopy: Experimental Details

A.1   The micro-Raman spectrometers

Three different comercial triple-monochromator spectrometers were used in this thesis: a Dilor XY system (at the Department of Physics - Federal University of Minas Gerais), a Horiba Jobin-Ivon T64000 system (at the Instituto Nacional de Metrologia, Normalização e Qualidade Industrial - Inmetro), and a SPEX system (at Los Alamos National Laboratory, USA), all of them equipped with a N_2 cooled Charge Coupled Device (CCD) detector (the CCD needs a temperature of -140°C to properly work), working in the backscattering configuration. The CCD can be understood as a large area of silicon photodiodes that form a bi-dimensional array of pixels. Through the photoelectric effect, the photodiodes convert photons into photoelectrons that are electronically processed. Each pixel delivers information compatible with the numbers of counts in it (in our setup, each count is approximately 1 to 16 photoelectrons).

These equipments can also be used in two modes: single- or triple-monochromator. The triple-monochromator systems are built by coupling three diffraction gratings that efficiently filter the information we are interested in. The incoming beam is reflected by the planar mirror (PM) 1 toward the spherical mirror (SM) 1 which reflects the beam toward the grating (Gr). As shown in Fig. A.1 each grating is in connection with other three mirrors. Next, the grating opens the beam's spectrum and part of a previously selected spectral range is focused by the SM2 into the monochromator exit slit.

In a triple-monochromator, two of these monochromators are coupled to form the
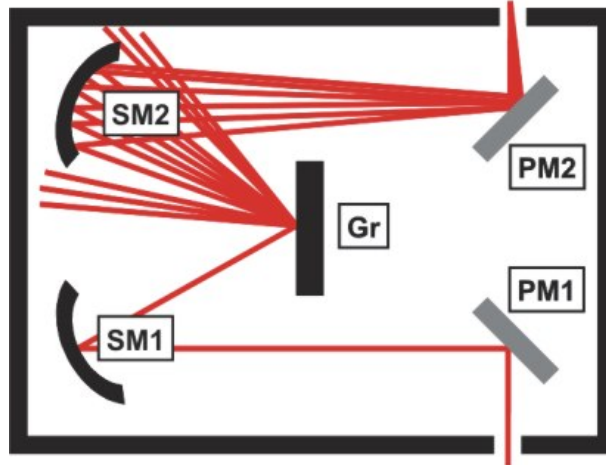
Figure A.1: In a monochromator scheme a grating (Gr) is geometrically connected to two spherical mirrors (SM1 and SM2) and two planar mirrors (PM1 and PM2). [97]

foremonochromator (see Fig. A.2) and the last monochromator forms the spectrograph. The foremonochromator can work in an additive or subtractive mode. In the subtractive mode, which is the one used in this work, the incoming beam reaches the Gr1 and this grating disperses the beam in a way that just a selected range of frequency (or, equivalently, wavelength) undergoes the slit 2 (S2). The range of frequencies depends on the grating position which can be conveniently chosen. Besides selecting a spectral frequency range, the slit S2 basically prevents the Rayleigh component of the light from propagating into the detection system. Next, the beam is focused by the grating Gr2 before undergoing the slit 3 (S3). Finally, it arrives at the spectrograph. Inside the spectrograph, the beam is dispersed by the grating Gr3. This dispersion covers a complete set of the CCD's pixels. In a triple-monochromator, the three gratings can be rotated simultaneously by a sine arm in order to chose the range of frequencies that will be covered by the CCD's pixels.

A.2 The excitation sources

In the last section, a brief introduction to the triple-monochromator spectrometers used in this work was given. This section addresses the technical details of the excitation sources used. At the Department of Physics - Federal University of Minas Gerais:

1. **Innova 70C Ion Laser from Coherent**: An Argon-Krypton laser, with the following emission lines: 647.1 nm, 568.2 nm, 528.7 nm, 520 nm, 514.5 nm, 501.7 nm,
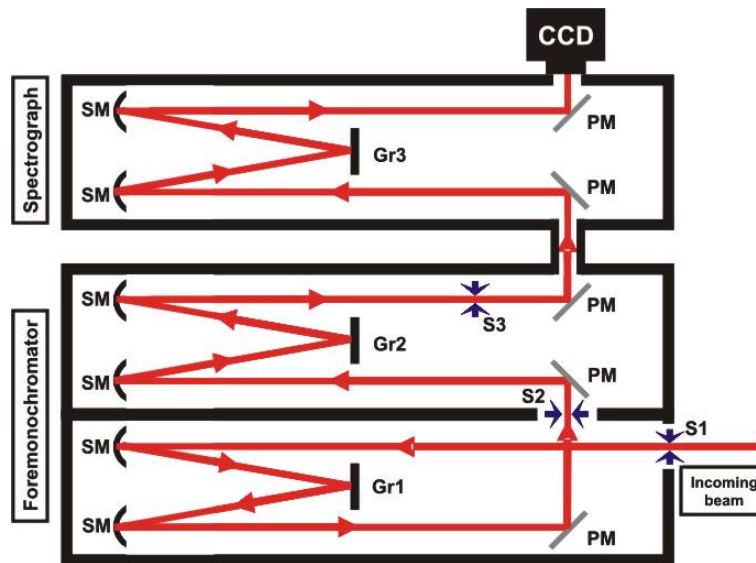
Figure A.2: The triple-monochromator is composed of a foremonochromator and a spectrograph. The foremonochromator is composed of two gratings that work harmonically in a configuration that basically filter the rayleigh component and select a specific spectral range. The other grating composes the spectrograph where the beam is dispersed and reach a set of CCD's pixels. [97]

496.5 nm, 488.0 nm, 476.5 nm, 472.7 nm, 465.8 nm, and 457.9 nm.

2. **899-01 Dye Ring Laser from Coherent**: A tuneable dye laser, with continuous light emission in the range from 380 nm to 880 nm (depending on the dye).

3. **Innova 90C Ion laser from Coherent**: An Argon laser, with the following lines: 528.7 nm, 514.5 nm, 501.7 nm, 496.5 nm, 488.0 nm, 476.5 nm, 472.7 nm, 465.8 nm, 457.9 nm, and 454.5 nm. It is usually used as a pump for the dye laser, operating in the multi-line mode, in which the output power emission can reaches values up to 7 W.

At the Instituto Nacional de Metrologia, Normalização e Qualidade Industrial - Inmetro:

1. **Melles Griot 35-LAP-431**: An Argon laser, with the following lines: 514 nm, 488 nm e 457 nm.

2. **Melles Griot 05-LHP-845**: A He-Ne laser with the line 632.8 nm.

At the Los Alamos National Laboratory, USA:

1. **Spectra-Physics Model 3900 S**: A tuneable Titanium:Sapphire laser, with continuous light emission in the range from 665 nm to 984 nm.

Appendix B

Publications

1. Araujo, P. T.; Nugraha, A. R. T.; Sato, K.; Dresselhaus, M. S.; Saito, R.; Jorio, A.. "Chirality dependence of the dielectric constant for the excitonic transition energy of Single-Wall Carbon Nanotubes". Physica Status Solidi. B, Basic Research, v. 247, p. 2847, 2010.

2. Araujo, P. T.; Pesce, P. B. C.; Dresselhaus, M. S.; Sato, K.; Saito, R.; Jorio, A.. "Resonance Raman spectroscopy of the radial breathing modes in carbon nanotubes". Physica E. Low-Dimensional Systems and Nanostructures, v. 42, p. 1251, 2010.

3. Araujo, P. T.; Jorio, A.; Dresselhaus, M. S.; Sato, K.; Saito, R.. "Diameter Dependence of the Dielectric Constant for the Excitonic Transition Energy of Single-Wall Carbon Nanotubes". Physical Review Letters, v. 103, p. 146802, 2009.

4. Araujo, P. T.; Fantini, C.; Lucchese, M. M.; Dresselhaus, M. S.; Jorio, A.. "The effect of environment on the radial breathing mode of supergrowth single wall carbon nanotubes". Applied Physics Letters, v. 95, p. 261902, 2009.

5. Araujo, P. T.; Maciel, I. O.; Pesce, P. B. C.; Pimenta, M. A.; Doorn, S. K.; Qian, H.; Hartschuh, A.; Steiner, M.; Grigorian, L.; Hata, K.; Jorio, A.. "Nature of the constant factor in the relation between radial breathing mode frequency and tube diameter for single-wall carbon nanotubes". Physical Review. B, Condensed Matter and Materials Physics, v. 77, p. 241403, 2008.

6. Araujo, P. T.; Jorio, A.. "The role of environmental effects on the optical transition

energies and radial breathing mode frequency of single wall carbon nanotubes". Physica Status Solidi. B, Basic Research, p. 2201, 2008.

7. Pesce, P. B. C.; Araujo, P. T.; Nikolaev, P.; Doorn, S. K.; Hata, K.; Saito, R.; Dresselhaus, M. S.; Jorio, A.. "Calibrating the single-wall carbon nanotube resonance Raman intensity by high resolution transmission electron microscopy for a spectroscopy-based diameter distribution determination". Applied Physics Letters, v. 96, p. 051910, 2010.

8. Qian, H.; Araujo, P. T.; Georgi, C.; Gokus, T.; Hartmann, N.; Green, A. A.; Jorio, A.; Hersam, M. C. ; Novotny, Lukas ; Hartschuh, A.. "Visualizing the Local Optical Response of Semiconducting Carbon Nanotubes to DNA-Wrapping". Nano Letters, v. 8, p. 2706-2711, 2008.

9. Doorn, S. K.; Araujo, P. T.; Hata, K.; Jorio, A.. "Excitons and exciton-phonon coupling in metallic single-walled carbon nanotubes: Resonance Raman spectroscopy". Physical Review. B, Condensed Matter and Materials Physics, v. 78, p. 165408, 2008.

10. Soares, J. S.; Barboza, A. P. M.; Araujo, P. T.; Neto, N. M. B.; Nakabayashi, D.; Shadmi, N.; Yarden, T. S.; Ismach, A.; Geblinger, N.; Joselevich, E.; Vilani, C.; Cancado, L. G.; Novotny, L.; Dresselhaus, G.; Dresselhaus, M. S.; Neves, B. R. A.; Mazzoni, M. S. C.; Jorio, A.. "Modulating the electronic properties along carbon nanotubes via tube-substrate interaction". Nano Letters, v. 10, p. 5043, 2010.

11. Nugraha, A. R. T.; Saito, R.; Sato, K.; Araujo, P. T.; Jorio, A.; Dresselhaus, M. S.. "Dielectric constant model for environmental effects on the exciton energies of single wall carbon nanotubes". Applied Physics Letters, v. 97, p. 091905, 2010.

12. Saito, R.; Sato, K.; Araujo, P. T.; Jorio, A.; Dresselhaus, G.; Dresselhaus, M. S.. "Exciton energy calculations for single wall carbon nanotubes". Physica Status Solidi. B, Basic Research, v. 246, p. 2581-2585, 2009.

13. Barboza, A. P. M.; Gomes, A. P.; Archanjo, B. S.; Araujo, P. T.; Jorio, A.; Ferlauto, A. S.; Mazzoni, M. S. C.; Chacham, H.; Neves, B. R. A.. "Deformation Induced Semiconductor-Metal Transition in Single Wall Carbon Nanotubes Probed by Electric Force Microscopy". Physical Review Letters, v. 100, p. 256804, 2008.

14. Gokus, T.; Hartschuh, A.; Harutyunyan, H.; Allegrini, M.; Hennrich, F.; Kappes, M.; Green, A. A.; Hersam, M. C.; Araujo, P. T.; Jorio, A.. "Exciton decay dynamics in individual carbon nanotubes at room temperature". Applied Physics Letters, v. 92, p. 153116, 2008.

15. Jorio, A.; Maciel, I. O.; Araujo, P. T.; Pesce, P. B. C.; Pimenta, M. A.. "The fundamental aspects of carbon nanotube metrology". Physica Status Solidi. B, Basic Research, v. 244, p. 4011-4015, 2007.

Bibliography

[1] C. Dekker. *Physics Today*, 52:22, 1999.

[2] A. Javey. *Nature*, 424:654, 2003.

[3] P. L. McEuen, M. S. Fuhrer, H. K. Park. *Nanotechnology*, 1:78, 2002.

[4] A. Bachtold, P. Hadley, T. Nakanishi, C. Dekker. *Science*, 294:1317, 2001.

[5] P. G. Collins, M. S. Arnold, P. Avouris. *Science*, 292:706, 2001.

[6] M. Endo, C. Kim, K. Nishimura, T. Fujino, K. Miyashita. *Carbon*, 38:183, 2000.

[7] E. Kimakis, G. A. J. Amaratunga. *Applied Physics Letters*, 80:112, 2002.

[8] E. Kimakis, G. A. J. Amaratunga. *Review of Advancede Materials Science.*, 10:300, 2005.

[9] M.S. Dresselhaus, G. Dresselhaus, R. Saito, A. Jorio. *Physics Reports*, 409:47, 2004.

[10] M. S. Dresselhaus A. Jorio and G. Dresselhaus. *Carbon Nanotubes: Advanced Topics in the Synthesis, Structure, Properties and Applications.* Springer-Verlag, Berlin, 2008.

[11] P. T. Araujo, P. B. C. Pesce, M. S. Dresselhaus, K. Sato, R. Saito, A. Jorio. *Physica E*, 42:1251, 2010.

[12] C. L. Kane and E. J. Mele. *Physical Review Letters*, 90:207401, 2003.

[13] P. T. Araujo, S. K. Doorn, S. Kilina, S. Tretiak, E. Einarsson, S. Maruyama, H. Chacham, M. A. Pimenta, A. Jorio,. *Physical Review Letters*, 98:067401, 2007.

[14] T. Michel, M. Paillet, J. C. Meyer, V. N. Popov, L. Henrard, J.-L. Sauvajol,. *Physical Review B*, 75:155432, 2007.

[15] K. Sato, R. Saito, J. Jiang, G. Dresselhaus, M. S. Dresselhaus. *Physical Review B*, 76:195446, 2007.

[16] J. Jiang, R. Saito, Ge. G. Samsonidze, A. Jorio, S. G. Chou, G. Dresselhaus, M. S. Dresselhaus. *Physical Review B*, 75:035407, 2007.

[17] P. T. Araujo, A. Jorio, M. S. Dresselhaus, K. Sato, R. Saito. *Physical Review Letters*, 103:146802, 2009.

[18] A. R. T. Nugraha, R. Saito, K. Sato, P. T. Araujo, A. Jorio, M. S. Dresselhaus. *Applied Physics Letters*, page accepted, 2010.

[19] G. Dresselhaus R. Saito and M. S. Dresselhaus. *Physical Properties of Carbon Nanotubes.* Imperial College Press, London, 1998.

[20] I. O. Maciel, N. Anderson, M. A. Pimenta, A. Hartschuh, H. Qian, M. Terrones, H. Terrones, J. Campos-Delgado, A. M. Rao, L. Novotny, A. Jorio. *Nature Materials*, 7:878, 2008.

[21] C. F. Leite. *Estudo de Propriedades Eletrônicas e Vibracionais de Nanotubos de Carbono por Espalhamento Raman Ressonante.* Department of Physics - Federal University of Minas Gerais, 2006.

[22] V. N. Popov. *New Journal of Physics*, 6:17, 2004.

[23] Ge. G. Samsonidze, R. Saito, N. Kobayashi, A. Grneis, J. Jiang, A. Jorio, S. G. Chou, G. Dresselhaus, M. S. Dresselhaus. *Applied Physics Letters*, 85:5703, 2004.

[24] M. S. C. Mazzoni and H. Chacham. *Applied Physics Letters*, 76:1561, 2000.

[25] B. Shan, W. G. Lakatos, Shu Peng, Kyeongjae Cho. *Applied Physics Letters*, 87:173109, 2005.

[26] Chan-Jeong Park, Yong-Hyun Kim, K. J. Chang . *Physical Review B*, 60:10656, 1999.

[27] A. P. M. Barboza, A. P. Gomes, B. S. Archanjo, P. T. Araujo, A. Jorio, A. S. Ferlauto, M. S. C. Mazzoni, H. Chacham, B. R. A. Neves. *Physical Review Letters*, 100:256804, 2008.

[28] M. Ishida, S. Mizuno, Y. Tani, Y. Saito, A. Nakamura. *J. Phys. Soc. Jpn.*, 68:3131, 1999.

[29] F. Wang, G. Dukovic, L. E. Brus, T. F. Heinz,. *Science*, 308:838, 2005.

[30] J. Maultzsch, R. Pomraenke, S. Reich, E. Chang, D. Prezzi, A. Ruini, E. Molinari, M. S. Strano, C. Thomsen, C. Lienau. *Physical Review B*, 72:241402(R), 2005.

[31] C. L. Kane and E. J. Mele. *Physical Review Letters*, 93:197402, 2004.

[32] L. D. Landau and E. M. Lifshitz. *Theory of Elasticity - Third Edition.* Pergamon Press, 1986.

[33] G. D. Mahan,. *Physical Review B*, 65:235402, 2002.

[34] P. T. Araujo, I. O. Maciel, P. B. C. Pesce, M. A. Pimenta, S. K. Doorn, H. Qian, A. Hartschuh, M. Steiner, L. Grigorian, K. Hata, A. Jorio. *Physical Review B*, 77:241403(R), 2008.

[35] P. T. Araujo and A. Jorio. *Physica Status Solid (b)*, 245:2201, 2008.

[36] P B. C. Pesce, P. T. Araujo, P. Nikolaev, S. K. Doorn, K. Hata, R. Saito, M. S. Dresselhaus, A. Jorio. *Applied Physics Letters*, 96:051910, 2010.

[37] V. N. Popov and L. Henrard. *Physical Review B*, 70:115407, 2004.

[38] C. D. Spataru, S. Ismail-Beigi, L. X. Benedict, S. G. Louie. *Physical Review Letters*, 92:077402, 2004.

[39] A. Jorio, R. Saito, J. H. Hafner, C. M. Lieber, M. Hunter, T. McClure, G. Dresselhaus, M. S. Dresselhaus,. *Physical Review Letters*, 86:1118, 2001.

[40] S. M. Bachilo, M. S. Strano, C. Kittrell, R. H. Hauge, R. E. Smalley, R. B. Weisman,. *Science*, 298:2361, 2002.

[41] H. Telg, J. Maultzsch, S. Reich, F. Hennrich, C. Thomsen,. *Physical Review Letters*, 93:177401, 2004.

[42] C. Fantini, A. Jorio, M. Souza, M. S. Strano, M. S. Dresselhaus, M. A. Pimenta,. *Physical Review Letters*, 93:147406, 2004.

[43] J. Deslippe, M. Dipoppa, D. Prendergast, M. V. O. Moutinho, R. B. Capaz, S. G. Louie,. *Nano Letters*, 9:1330, 2009.

[44] Y. Miyauchi, R. Saito, K. Sato, Y. Ohno, S. Iwasaki, T. Mizutani, J. Jiang, S. Maruyama,. *Chem. Phys. Lett.*, 442:394, 2007.

[45] R. Saito, K. Sato, P. T. Araujo, A. Jorio, G. Dresselhaus, M. S. Dresselhaus. *Physica Status Solidi (b)*, 246:2581, 2009.

[46] V. Perebeinos, J. Tersoff, P. Avouris,. *Physical Review Letters*, 92:257402, 2004.

[47] M. W. Davidson and M. Abramowitz. *Optical Microscopy.* Olympus - http://www.olympus.com.

[48] L. Novotny and B. Hecht. *Principles of Nano-Optics.* Cambridge University Press, 2006.

[49] K. Karraia, R. D. Grober. *Applied Physics Letters*, 66:1842, 1995.

[50] L. Billot, L. Berguiga, M. L. de la Chapelle, Y. Gilbert, R. Bachelot. *European Physical Journal (Applied Physics)*, 31:139, 2005.

[51] nanoSurf®. *Operating instructions, easyPLL plus version 3.0.* 2004.

[52] J. Wessel. *J. Opt. Soc. Am. B*, 2:1538, 1985.

[53] Huihong Qian. *Tip-enhanced Near-Field Optical Spectroscopy on Single-Walled Carbon Nanotubes.* Fakultaet fuer Chemie und Pharmazie der Ludwig-Maximilians-Universitaet Muenchen, 2008.

[54] N. Geblinger, A. Ismach, E. Joselevich. *Nature Nanotechnology*, 3:195, 2008.

[55] P. McEuen and C. Kittel. *Introduction to Solid State Physics.* John Wiley& Sons, 2005.

[56] M. Milnera, J. Krti, M. Hulman, H. Kuzmany,. *Physical Review Letters*, 84:1324, 2000.

[57] A. Hartschuh, H. N. Pedrosa, L. Novotny and T. D. Krauss,. *Science*, 301:1354, 2003.

[58] M. Strano, S. K. Doorn, E. H. Haroz, C. Kittrell, R. H. Hauge, R. E. Smalley,. *Nano Letters*, 3:1091, 2003.

[59] S. K. Doorn, D. A. Heller, P. W. Barone, M. L. Usrey, M. S. Strano,. *Applied Physics A*, 78:1147, 2004.

[60] M. Paillet, T. Michel, J. C. Meyer, V. N. Popov, L. Henrard, S. Roth, J. L. Sauvajol,. *Physical Review Letters*, 96:257401, 2006.

[61] A. Jorio, C. Fantini, M. A. Pimenta, R. B. Capaz, Ge. G. Samsonidze, G. Dresselhaus, M. S. Dresselhaus, J. Jiang, N. Kobayashi, A. Grneis, R. Saito,. *Physical Review B*, 71:075401, 2005.

[62] K. Hata, D. N. Futaba, K. Mizuno, T. Namai, M. Yumura, S. Iijima,. *Science*, 306:1362, 2004.

[63] D. N. Futaba, K. Hata, T. Yamada, K. Mizuno, M. Yumura, S. Iijima,. *Physical Review Letters*, 95:056104, 2005.

[64] D. N. Futaba, K. Hata, T. Namai, T. Yamada, K. Mizuno, Y. Hayamizu, M. Yumura, S. Iijima,. *Journal of Physical Chemistry B*, 110:8035, 2006.

[65] D. N. Futaba, K. Hata, T. Yamada, T. Hiraoka, Y. Hayamizu, Y. Kakudate, O. Tanaike, H. Hatori, M. Yumura, S. Iijima,. *Nature Materials*, 5:987, 2006.

[66] M. J. Longhurst, N. Quirke,. *Journal of Chemical Physics*, 124:234708, 2006.

[67] J. Lefebvre, J. M. Fraser, Y. Homma, P. Finnie,. *Applied Physics A*, 78:1107, 2004.

[68] Y. Ohno, S. Iwasaki, Y. Murakami, S. Kishimoto, S. Maruyama, T. Mizutani,. *Physical Review B*, 73:235427, 2006.

[69] H. Son, A. Reina, Ge. G. Samsonidze, R. Saito, A. Jorio, M. S. Dresselhaus and J. Kong,. *Physical Review B*, 74:073406, 2006.

[70] M. Y. Sfeir, T. Beetz, F. Wang, L. Huang, X. M. H. Huang, M. Huang, J. Hone, S. O'Brien, J. A. Misewich, T. F. Heinz, Lijun Wu, Yimei Zhu, L. E. Brus,. *Science*, 312:554, 2006.

[71] A. Jorio, C. Fantini, M. A. Pimenta, R. B. Capaz, Ge. G. Samsonidze, G. Dresselhaus, M. S. Dresselhaus, J. Jiang, N. Kobayashi, A. Grneis, R. Saito,. *Physical Review B*, 71:075401, 2005.

[72] V. N. Popov, P. Lambin,. *Physical Review B*, 73:085407, 2006.

[73] P. T. Araujo, C. Fantini, M. M. Lucchese, M. S. Dresselhaus, A. Jorio. *Applied Physics Letters*, 95:261902, 2009.

[74] S. Giordani, S. D. Bergin, V. Nicolosi, S. Lebedkin, M. M. Kappes, W. J. Blau, J. N. Coleman,. *J. Phys. Chem. B*, 110:15708, 2006.

[75] C. Fantini, A. Jorio, A. P. Santos, V. S. T. Peressinotto, M. A. Pimenta,. *Chem. Phys. Lett.*, 439:138, 2007.

[76] D. A. Tsyboulski, E. L. Bakota, L. S. Witus, John-David R. Rocha, J. D. Hartgerink, R. B. Weisman,. *J. Am. Chem. Soc.*, 130:17134, 2008.

[77] S. D. Bergin, V. Nicolosi, H. Cathcart, M. Lotya, D. Rickard, Z. Sun, W. J. Blau, J. N. Coleman,. *J. Phys. Chem. C*, 112:972, 2008.

[78] C. Fantini, J. Cassimiro, V. S. T. Peressinotto, F. Plentz, A. G. Souza Filho, C. A. Furtado, A. P. Santos,. *Chem. Phys. Lett.*, 473:96, 2009.

[79] R. Saito, G. Dresselhaus, M. S. Dresselhaus,. *Physical Review B*, 61:2981, 2000.

[80] S. K. Doorn, P. T. Araujo, K. Hata, A. Jorio. *Physical Review B*, 78:165408, 2008.

[81] V. Perebeinos, J. Tersoff, Ph. Avouris,. *Physical Review Letters*, 92:257402, 2004.

[82] Y. Murakami, E. Einarsson, T. Edamura, S. Maruyama,. *Carbon*, 43:2664, 2005.

[83] P. T. Araujo, A. R. T. Nugraha, K. Sato, M. S. Dresselhaus, R. Saito, A. Jorio. *Physica Status Solidi (b)*, page submmited, 2010.

[84] V. Perebeinos, J. Tersoff, P. Avouris. *Physical Review Letters*, 92:257402, 2004.

[85] A. Hartschuh, H. Qian; A. J. Meixner, N. Anderson; L. Novotny. *NanoLetters*, 5:2301, 2005.

[86] H. Htoon; M. J. OConnell, P. J. Cox, S. K. Doorn, V. I. Klimov. *Physical Review Letters*, 93:027401, 2004.

[87] M. Zheng, A. Jagota, E. D. Semke, B. A. Diner, R. S. Mclean, S. R. Lustig, R. E. Richardson, N. G. Tassi. *Nature Materials*, 2:338, 2003.

[88] K. Welsher, Z. Liu, D. Daranciang, H. Dai. *Nanoletters*, 8:586, 2008.

[89] R. R. Johnson, A. T. C. Johnson, M. L. Klein. *Nanoletters*, 8:69, 2008.

[90] S. Manohar, T. Tang, A. Jagota. *Journal of Physical Chemistry C*, 111:17835, 2007.

[91] P. J. Michalski, E. J. Mele. *Physical Review B*, 77:085429, 2008.

[92] V. I. Puller, S. V. Rotkin. *Europhysics Letters*, 77:27006, 2007.

[93] E. S. Jeng, A. E. Moll, A. C. Roy, J. B. Gastala, M. S. Strano,. *Nano Letters*, 6:371, 2006.

[94] H. Qian, P. T. Araujo, C. Georgi, T. Gokus, N. Hartmann, A. A. Green, A. Jorio, M. C. Hersam, L. Novotny, A. Hartschuh. *NanoLetters*, 8:2706, 2008.

[95] J. S. Park, K. Sasaki, R. Saito, W. Izumida, M. Kalbac, H. Farhat, G. Dresselhaus, M. S. Dresselhaus. *Physical Review B*, 80:081402(R), 2009.

[96] Ken-ichi Sasaki,1 R. Saito, G. Dresselhaus, M. S. Dresselhaus, H. Farhat, J. Kong. *Physical Review B*, 77:245441, 2008.

[97] L. G. Cancado. *Raman Spectroscopy of Nanographites*. Department of Physics - Federal University of Minas Gerais, 2006.